Ice-Climate Co-evolution During the Last Two Glacial Cycles: Characterization and Feedbacks via Ensemble Fully-coupled Earth System Modeling

by

© *Marilena Sophie Geng*

A thesis submitted to the

School of Graduate Studies

in partial fulfilment of the

requirements for the degree of

Doctor of Philosophy

Department of Physics and Physical Oceanography

Memorial University of Newfoundland

October 2024

St. John's Newfoundland

Abstract

Anthropogenic climate change, accelerating the melting glaciers and ice sheets resulting in future sea level rise, is a key concern for humanity. Over the past 700 thousand years, glacial-interglacial cycles have shaped Earth's climate. These are marked by relatively large, at times rapid system changes. As such, the past offers an albeit fuzzy perspective on possible ice and climate system interactions and transitions.

Constraints on ice-climate evolution beyond the Last Glacial Maximum, however, are sparse, and dating uncertainties increase with geologic time. Given the data limitations, the paleo community often looks to models to complement inferences from paleodata. Still, to date, no full glacial cycle simulations have been published with coupled ice and climate models of sufficient complexity to resolve synoptic scale atmospheric dynamics and ocean circulation.

This thesis explores the phase space of model simulations of transient ice-climate co-evolution in response to radiative forcing during the last two glacial cycles. The novelty of our study lies in three key aspects. Firstly, we employ LCice, a fully coupled Earth system model of intermediate complexity, which incorporates all key ice-climate feedbacks. Secondly, we utilize ensemble simulations instead of a single model realization. This approach moves beyond attempting to recreate the past as closely as possible with always imperfect models. It instead offers an exploration of plausible physically-self consistent scenarios. Thirdly, our study includes transient simulations of the last two glacial cycles, encompassing both ice growth and retreat phases.

This thesis documents the following contributions: 1) a detailed analysis of the potential phase space of the last two glacial inceptions, 2) a continuous record of climate fields derived from ensemble simulations across the last two glacial cycles, and 3) an analysis of the relative impact of the ice-climate feedbacks on ice evolution during the last glacial cycle.

Acknowledgements

Thanks to

My supervisor Lev - for the opportunity to immerse myself into this project for (too many) years, teaching my critical scientific thinking, and giving me a lot of freedom in my work

My committee of Joel Finnis and Entcho Demirov - for the ongoing encouragement, support and good recommendations

My lab mates Audrey, Matt, Kevin, and Alexis - for moral support, proofreading, coffee and treats

My parents - for continued support and pep talks and care packages

My previous lab mate and running partner Heather - for mental health runs and rants and recommendations

The ArcTrain project and the friends made through ArcTrain - for creative exchange and reassurance that we'll all come out on the other side

Caroline and Tanya - for being my after-hour writing partners and sharing my pain

Contents

List of Tables

List of Figures

Chapter 1

Introduction

One of society's primary concerns revolves around anthropogenic climate change and the consequential rise in sea levels from melting ice sheets. Climate models serve as critical tools for estimating future climatic scenarios. To ensure the reliability of these projections on long time scales, a comprehensive understanding of ice-climate feedback mechanisms and the Earth system's response to changes in radiative forcing is necessary. The Earth's climate has undergone numerous glacial cycles which display relatively large and (at times) abrupt system changes in response to varying radiative forcing. Therefore, they offer a great opportunity to increase our understanding of the Earth system. This thesis aims to do so by taking a significant step towards bounding the growth and decay of ice sheets over the last two glacial cycles, and the relative role of ice-climate feedbacks during the last glacial cycle using the fully-coupled Earth system model LCice.

This thesis is written in a manuscript format. Chapters 2-4 will be submitted to scientific journals. Each manuscript includes an individual introduction into the

specific topic. In the following, I give a short general introduction to past glacial cycles, observations that inform our knowledge of paleoclimate in general and the last two glacial cycles specifically, a brief review of glacial cycle modeling, and a description of the model LCice to situate my research.

1.1 Introduction to glacial cycles

The Earth's climate has been characterized by the quasi-periodic occurrence of glacials ("ice ages") and interglacials over the last $\sim$ 2.7 million years (Haug et al., 2005). During glacial stages, ice sheets cover North America, Northern Eurasia, Greenland, and Antarctica with small ice caps present in Tibet and Patagonia. In an interglacial stage, most ice, besides the ice sheets present today, Greenland and Antarctica, disappears. For the last 700 kyr, these have occurred in cycles of roughly 100 thousand years (100 kyrs, e.g. Clark et al., 2006). The buildup of ice sheets at the beginning of a glacial cycle, the glacial inception, is a successive process of ice advance and partial retreat, reaching glacial maxima in 70-90 kyrs. Deglaciations, also called terminations, happen much faster with the interglacial warm period lasting approximately 10-30 kyr (Berger et al., 2015).

Substantial changes in the climate system accompany the transition from interglacial to glacial conditions. The buildup of ice on land leads to a sea level lowering of 60 - 140 m depending on the strength of the glacial. This impacts ocean circulation through the opening and closing of key gateways connecting the Pacific, Arctic, and Atlantic oceans, as well as from reduced freshwater flux into the ocean. While the global mean temperature anomaly is inferred to be approximately 3.5 °C (Brook and

Buizert, 2018) from glacial to interglacial, temperatures anomalies of approximately 11.3 ± 1.8 °C (Brook and Buizert, 2018) and 23 °C (Dahl-Jensen et al., 1998) from Last Glacial Maximum to present-day have been inferred on the basis of borehole temperature records from Antarctica and Greenland respectively. This indicates a strong polar amplification of the cooling during glacials and warming during interglacials. Another characteristic of glacials is a reduction in atmospheric carbon dioxide (CO_2) of 60 - 120 ppm (see Figure 1.1). While CO_2 changes don't solely start or terminate glacial cycles, they play an important role in amplifying the cooling during glacials and warming during interglacials. The mechanisms behind CO_2 variations are largely known but not well-constrained. Likely, the Southern Ocean plays an important role, as CO_2 and Antarctic temperatures change nearly synchronously and the southern deep ocean can store large amounts of carbon.

Orbital changes in insolation are the external driver of glacial cycles. A decrease in incoming solar radiation cools the planet and leads to a glacial climate; an increase in insolation triggers termination of the glacial. The orbital parameters influencing insolation are obliquity, eccentricity and precession. Obliquity is the angle of Earth's spin axis and varies from 22.2 - 24.5° and has a periodicity of 41 kyr. Obliquity changes influence the seasonal amount of solar radiation reaching high latitudes; an increased obliquity intensifies the seasonality experienced on the planet (leading to particularly cold winters and warm summers). Eccentricity describes the shape of Earth's orbit: from more circular (small eccentricity) to more elliptic (large eccentricity). The several components of eccentricity cycles combine roughly to a periodicity of about 100 kyrs. Precession is the wobble of Earth's spin axis and determines where Earth experiences a specific season in the orbit. This, like obliquity, can intensify the sea-

sons, but unlike obliquity, it is not symmetric over the two hemispheres. When the Northern Hemisphere experiences summer at perihelion (closest in orbit to the sun), summers are especially warm but also short on the Northern Hemisphere, while at the same time, the Southern Hemisphere experiences an especially mild and short winter. Precession has a period of 26 kyr. The orbital parameters over the last two glacial cycles are displayed in Figure 1.1.

The orbital parameters and their regional influence on insolation were first computed by Milankovitch (1941). Following Milankovitch's theory, a low in summer insolation at approximately 65°N could trigger a Northern Hemisphere glaciation. Milankovitch recognized that mild summers rather than cold winters were needed to sustain perennial snow (contrary to former theories, for example, Croll, 1867). His calculations predicted glacial cycles with a periodicity of 41 kyr and/or 23 kyr, triggered by obliquity and (eccentricity modulated) precession, as these orbital parameters have the strongest influence on Earth's insolation. Records from tropical regions, for example proxies for monsoon strength, show clear obliquity and precession signals (Clemens et al., 1991; Bosmans et al., 2015). Before approximately 1 million years ago, glacial cycles had a dominant 41 kyr periodicity, too. However, the inferred sea level record over the last 700 kyr has a dominant spectral peak at 100 kyr (see Figure 1.2), with weaker signals at 41 kyr and 23 kyr (Ruddiman, 2003). While eccentricity periodicities of 100 kyrs would approximately match the observed lengths of glacial cycles, it has the most negligible influence on changing the overall insolation on Earth out of all orbital parameters. This gives rise to many hypotheses trying to explain the "100 kyr problem". While orbital factors are the primary driver, they do not explain all the variability and periodontics observed in climate records, hence

it is important to investigate multiple causal mechanisms. Generally, it is assumed that non-linearities and feedback mechanisms within the ice-climate system amplify and/or modify orbitally driven climate, leading to some obliquity or precession cycles being skipped (Imbrie et al., 1993; Ruddiman, 2003; Raymo and Huybers, 2008). While this thesis does not aim to solve the 100 kyr problem, I will investigate the role of ice-climate feedbacks in shaping ice evolution during the last glacial cycle.

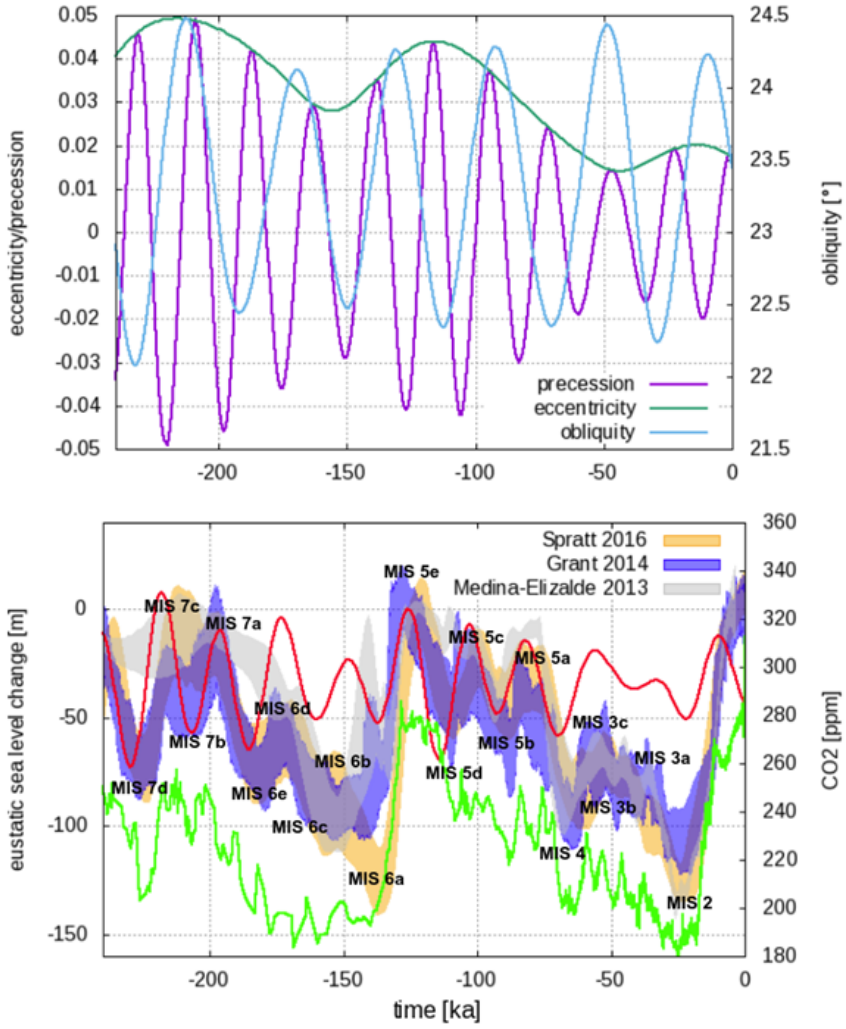

Figure 1.1: Orbital parameters (top, Berger and Loutre, 1991) and sea level reconstruction, insolation (red, Berger and Loutre, 1991) and CO_2 (green, Bereiter et al., 2015) for the last two glacial cycles. 95 % confidence range of sea level reconstruction by Spratt and Lisiecki (2016) (orange), Grant et al. (2014) (blue), and Medina-Elizalde (2013) (grey)

1.2 Examples of paleo-climate data that inform glacial cycle climate estimates

Our knowledge of past climate dynamics is (among others) based on geomorphological and sedimentological observations (Benn and Evans, 2010), direct measurements of atmospheric composition from air bubbles trapped in ice (Lüthi et al., 2008; Bereiter et al., 2015), pollen (Brewer et al., 2013), tree rings (LaMarche, 1978), and geochemical proxy data (Lisiecki and Raymo, 2005). The following gives a very short introduction to the data that will be discussed in the manuscripts.

Geomorphological observations include depositional landforms, e.g. moraines, that mark the maximum extent of an ice sheet at a time (in the case of lateral and terminal moraines), and erosional landforms like striations that indicate the flow direction of a glacier. More recent and more extensive glaciations overwrite glacial landforms from previous glaciations, therefore little data from pre-LGM glaciations is preserved.

To determine the age of a glacial landform, several dating techniques, each with their advantages and uncertainties can be used. Radiocarbon dating can be used to determine the age of organic matter buried under glacial sediments, thereby giving the approximate age of the sediment layer (Bowman, 1990). Due to the half-life of carbon-14 (^{14}C), radiocarbon dating can only be used to up to $\sim$ 40 ka, as the amount of remaining ^{14}C becomes too small to reliably measure in older materials. Cosmogenic nuclide dating can be used for older landforms (Balco, 2011). The nuclides are formed when high-energy cosmic rays interact with atoms in minerals. Therefore, the amount of cosmogenic nuclides gives information about when the rock became free of ice

cover. However, uncertainties in this dating method arise because nuclides from previous exposures may be present in the rock, post-depositional processes may alter nuclide concentrations, and because the cosmic ray flux varied through geologic time. Optically stimulated luminescence (OSL, Rhodes, 2011) dating, on the other hand, is used to determine the last time minerals, e.g. buried in glacial tills, have been exposed to sunlight. When minerals are buried, they accumulate energy from ionizing radiation in their surroundings which is released as luminescence when exposed to light. OSL dating assumes complete bleaching of minerals (setting the "clock" to zero) at the time of the last exposure. This assumption is likely broken to varying extents, thereby introducing a source of uncertainty in the dating method. Furthermore, uncertainties in the dose rate of ionizing radiation needs to be taken into account.

Geochemical proxy data are obtained from ice cores, marine or lake sediment cores, coral reefs, or speleothems (cave formations). The obtained data can be related to local or regional climate characteristics. Proxy data mentioned in this thesis are oxygen isotope ratios from marine sediment cores and ice cores, deuterium depletion from ice cores, and Mg/Ca and Pa/Th from marine sediment cores. A very short overview of these proxies is given in the following, the list is by no means complete.

The oxygen isotope ratio found in the shell of benthic foraminifera in marine sediment cores is the most commonly used record to characterize glacial cycles (see Figure 1.2). It is interpreted as the amount of water stored on land and is therefore used as an indicator for global sea level. Oxygen isotope 16 (^{16}O), the most common oxygen isotope, preferentially evaporates from water bodies to the atmosphere relative to the heavier ^{18}O isotope. ^{18}O preferentially precipitates out during transport of water vapor. In an equilibrium climate, the same amount of evaporating ^{16}O will

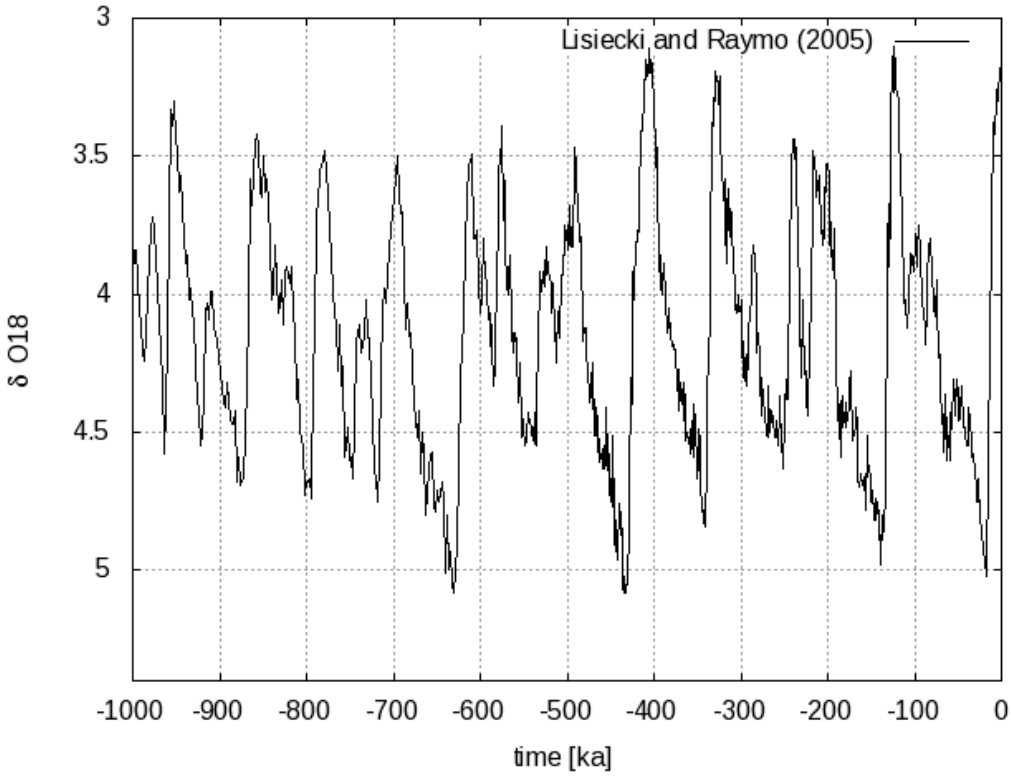

Figure 1.2: Stack of 57 globally distributed benthic ^{18}O records (Lisiecki and Raymo, 2005)

return to the ocean as it precipitates out. In a cooling climate, ice builds up on land, "traps" more of the lighter oxygen in the ice and leaves the oceans depleted in ^{16}O, leading to an increase in the $^{18}O/^{16}O$ (δ^{18}O) ratio. Therefore, the amount of δ^{18}O can be related to global sea level change. However, the ocean temperature in which the foraminifera shell is formed has a strong influence on the ratio of oxygen isotopes taken up into the shell. While deep ocean temperature variations are smaller than surface temperature variations, uncertainties in the sea level reconstructions still arise from the not clearly quantified temperature signal in the δ^{18}O record.

Oxygen isotope ratios are furthermore used to derive information from water

molecules in the ice core. Here, the isotopic ratio of δ^{18}O or δD (deuterium, the ratio of heavier to lighter hydrogen isotopes in H_2O) is in effect an albeit noisy metric of the cooling an air mass experienced on its way from evaporation source to deposition at the ice core location. The air arriving and precipitating over an ice sheet will be more depleted in D or ^{18}O during glacial periods as it experienced more cooling on its travel to polar regions. δD and δ^{18}O measurements also contain a signal of the temperature of the moisture source. However, they are found to correlate well with the cloud temperature at the precipitation site and are therefore a widely used temperature proxy (Holme et al., 2018).

Measurements from ice cores can be dated with high confidence if annual snow layers are visible and can be counted. Layer counting becomes more challenging with increasing depth in the ice core due to processes such as ice flow and ice deformation, which can compress and distort annual layers. Isotopic measurements and measurements from air bubbles from depths beyond layer counting are dated using depth-age models, and have higher dating uncertainties. The models are based on ice flow dynamics and tie points that can be dated absolutely (or otherwise globally synchronized) such as ash layers from volcanic eruptions.

Ocean temperature can be derived from the ratio of Mg/Ca from foraminifera in marine sediment cores. Calcium (Ca) is formed in foraminifera shells and incorporates Magnesium (Mg) in varying amounts depending on surrounding water temperature (Lowenstein and Hönisch, 2012). Measurements from benthic foraminiferas are related to deep ocean temperature and planktic foraminifera to sea surface temperature. Uncertainties in this proxy arise from factors such as changes in seawater chemistry and variations in the Mg/Ca ratio of different foraminifera species.

The ratio of Pa/Th in North Atlantic sediment cores is a proxy for circulation strength. Protactinium (Pa) and Thorium (Th) are daughter elements of uranium and produced at a fixed rate. Th is absorbed by marine particles and, therefore, accumulates on the sea floor more efficiently than Pa. As a result, Pa is transported to the Southern Ocean with the overturning circulation at higher rates than Th. Hence, an increase in Pa/Th in the North Atlantic indicates a weakened overturning circulation (less Pa transport to the Southern Ocean) and a decrease in Pa/Th a strong circulation (Robinson et al., 2019). Uncertainties arise from variations in sedimentation rates and biogeochemical processes.

Similar to ice cores, geochemical proxies from sediment cores are dated by assuming a sediment accumulation rate and correlating the sediment layer depth to age models, tied to specific marker horizons that can be absolutely dated.

In summary, data on past climate and ice is spatially and temporally limited, the interpretation of proxy data is associated with often unquantified uncertainties, and furthermore the dating of proxy observations has high uncertainties. Therefore, the collective knowledge of past ice-climate evolution is limited. I make use of paleoclimate modeling to fill in gaps in our understanding around the last two glacial cycles. Specifically, I examine differences between the ice-climate evolution over the penultimate and last glacial cycle that proxy and observational data cannot give.

1.3 The last two glacial cycles

The last two glacial cycles share similarities (similar insolation, CO_2 values and inferred global mean eustatic sea level change at glacial maximum), but also display

inferred differences (e.g. glacial inception strength and maximum ice sheet configurations). This makes the time frame useful to test Earth system models' feedback responses to changing radiative forcing, to compare two glacial cycles, and to explore ice-climate feedbacks.

The penultimate glacial cycle started at approximately 240 ka during Marine Isotope Stage (MIS) 7e (Figure 1.1). Global mean records indicate that eustatic sea level was slightly lower during this interglacial than present-day, so small relic ice sheets in Eurasian and/or North American must have been present. The last glacial cycle started approximately 120 ka during MIS 5e. During this last interglacial, eustatic sea level is inferred to have been 6-9 m higher than present-day (Dutton and Barlow, 2019). The exact contribution of the Greenland and Antarctic ice sheets to this sea level high-stand remains unclear.

The penultimate glacial cycle starts with a strong inception where sea level decreased to -80 mESL (m eustatic sea level) at MIS 7d over a relatively short time of 12 kyrs (Spratt and Lisiecki, 2016; Grant et al., 2014). However, as shown in Figure 1.1, there is a high uncertainty and some disagreement on penultimate inception among sea level records. During last glacial inception, sea level lowered to approximately -60 mESL at MIS 5d. Penultimate glacial inception had a more significant sea level drop than last glacial inception as insolation and CO_2 were lower (Figure 1.1).

The respectively following interstadials (warm periods of high sea level) MIS 7c and MIS 5c vary in strength as insolation is significantly higher during MIS 7c than 5c. The stadials (cold periods of low sea level) MIS 6e and 4 show a similar, substantial decrease in sea level although insolation at MIS 4 is higher than at MIS 6e (Figure 1.1).

By ∼140 ka the penultimate glacial maximum (PGM, MIS 6) is reached. Sea level estimates for this low-stand range from -107 to -163 mESL Rohling et al. (2017). The last glacial maximum (LGM, MIS 2) is reached at ∼21 ka with an estimated sea level low-stand of -98 to -130 mESL (Rohling et al., 2017). Greenhouse gases and insolation are of similar magnitude at both glacial maxima (see Figure 3.2). The orbital parameters displayed in Figure 3.2, however are different. Precession and eccentricity are higher during PGM than LGM. Therefore, PGM was warmer on a global annual average than LGM (Parrenin et al., 2013), but springs were cooler and longer, while summers were earlier and shorter during PGM compared to LGM.

While geomorphological observations for the LGM are abundant, data beyond that time frame is limited. Glacial landforms older than LGM are mostly overwritten by the last glacial advance. Yet, various glacial geological data indicate that during the PGM, the Eurasian ice sheet reached further eastwards and southwards than during the last glacial cycle. Astakhov (2004) finds that sea level during the last interglacial was unusually high at the Russian Arctic margin and concludes that this could be explained by a previous depression of the area. The depression would have been caused by a PGM ice sheet extending further to the east than the ice sheet during LGM. Svendsen et al. (2004) find that the Eurasian ice sheet extent during Late Saalian (the penultimate glaciation over Eurasia, 160-130 ka) was one of the most extensive of Quaternary glaciations and larger than LGM (Figure 1.3).The Late Saalian period includes several advances and retreats in different sectors of the ice sheet that may not have been synchronous (Svendsen et al., 2004).

On the other hand, little is known about the PGM North American ice sheets. This in itself suggests that the ice sheet was smaller or of similar size as the LGM ice

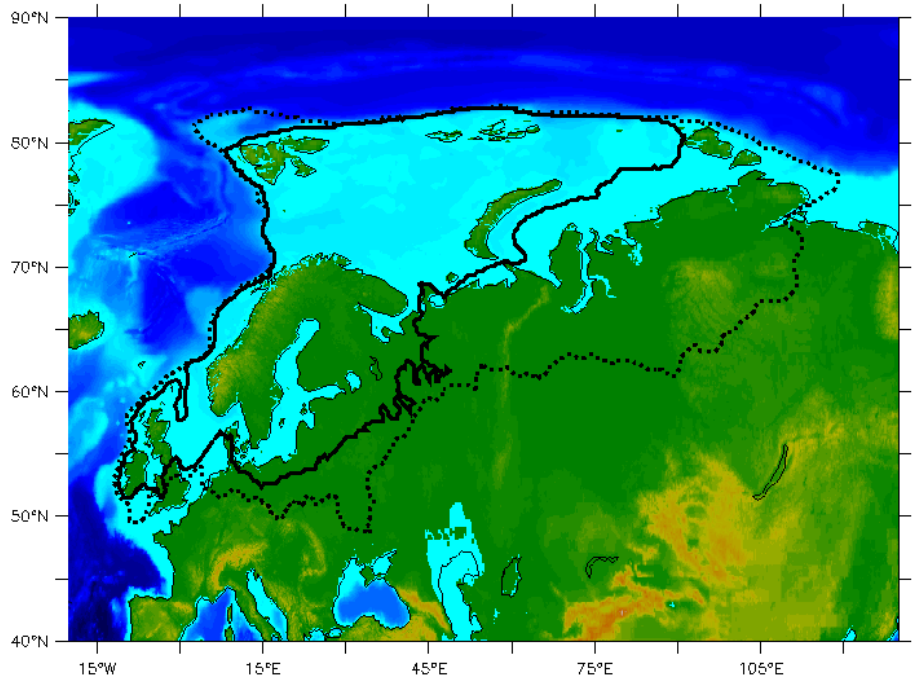

Figure 1.3: Reconstruction of maximum Eurasian ice sheet extent for LGM (solid black, Hughes et al., 2016) and Late Saalian (dashed black, Svendsen et al., 2004)

sheet as the latter effectively erased most prior glacial landforms.

As the North American and Eurasian ice sheets show opposite extent differences from PGM to LGM, the question arises how they react differently to the prevailing climate from one cycle to the other and if they possibly influence each other.

Since the last two glacial cycles started from interglacial conditions with ice configurations not too far from present-day, simulations of the glacial inceptions can be initialized with known present-day climate (Kubatzki et al., 2006). They offer an

opportunity to examine the rapid ice growth and subsequent retreat at the start of the last two glacial cycles. Specifically, I will investigate how ice area and volume differ between the last and penultimate glacial inception and how they compare to the limited available data.

1.4 Simulating the last two glacial cycles

Modeling has been used to fill in gaps in our knowledge of ice sheet evolution before the LGM. Simulating the rapid sea level decrease during glacial inceptions has been a challenge in numerous studies (Bahadory and Tarasov, 2018). Most attempts to simulate glacial inception with climate models have focused on steady-state simulations using general circulation models (GCMs) forced with constant 115/116 ka orbital and greenhouse gas (GHG) forcings (Khodri et al., 2001; Yoshimori et al., 2002; Vettoretti and Peltier, 2003; Otieno and Bromwich, 2009). Perennial snow cover was used as a proxy for ice sheet areas. Consequently, these simulations missed the influence of ice sheets (influencing the topography and freshwater fluxes) on the climate. On the other hand, Born et al. (2010) forced an ice sheet model with constant 115 ka climate model output. Here, the feedback loop between the growing ice sheet and the climate was missing, sea surface temperatures were too high, and the growth of a Eurasian ice sheet is consistently not generated.

In many fully coupled experiments incorporating GCMs coupled to ice sheet models, simulated ice sheets took significantly longer than expected to grow and remained below estimated sea level equivalents despite using constant 116 ka and 115 ka orbital and GHG forcings (Herrington and Poulsen, 2012; Gregory et al., 2012).

Early transient simulations of the entire last glacial cycle used two-dimensional energy balance models or climate models coupled to simple two or three-dimensional ice sheet models (Gallée et al., 1992; Peltier and Marshall, 1995; Tarasov and Peltier, 1997). While these models could capture the overall structure of ice growth and decay, they struggled to capture the deglaciation process (especially with respect to timing), the initial strong inception in the sub-stages of MIS 5, and the full extent and volume of the ice sheets at glacial maxima.

More recent work has employed Earth system models of intermediate complexity (EMICs) coupled to ice sheet models. Some studies simulated the last glacial inception from the interglacial to the first sea level low-stand, but the capacity of these models to melt the simulated ice from MIS 5d to 5c was not tested (Calov et al., 2005; Kageyama et al., 2004). As such, the possibility of a model cold-bias that facilitated inception was not ruled out. Studies to date that tested inception, including the ice retreat phase, did not include an interactive Antarctic ice sheet and often used a constant temperature bias correction (Willeit et al., 2023; Ganopolski et al., 2010) or constant precipitation bias correction (Bonelli et al., 2009). All studies struggle to simulate the ice sheet extent as estimated from geomorphological data. Alaska tends to be ice-covered in simulations (Bahadory et al., 2021; Ganopolski et al., 2010; Bonelli et al., 2009) contradicting evidence from geological studies (Kauman and Manley, 2004; Kaufman et al., 2011). Meanwhile, there is not enough ice simulated during inception and/or LGM over Quebec (Bonelli et al., 2009) or Eurasia (Ganopolski et al., 2010; Bonelli et al., 2009; Ganopolski et al., 2010).

Few studies have focused on the penultimate glacial inception or PGM. Patterson et al. (2024) make use of a coupled model (atmospheric component of the atmosphere-

ocean general circulation model FAMOUS coupled to the ice sheet model Glimmer) to simulate the North American ice sheet under equilibrium LGM and PGM conditions. Their ensemble simulations show a significantly smaller North American ice sheet during the PGM time slice than during LGM when FAMOUS is initialized with PGM and LGM ice sheet boundaries. However, their sensitivity analysis shows that the initial ice sheet boundary conditions in FAMOUS are the key driver for the differences in glacial maximum ice sheets.

Colleoni et al. (2014) used snapshots of climate model output and forced an ice sheet model offline to simulate the last two glacial inceptions. Their simulated ice sheet volumes only reached a maximum of 5 meters of sea level equivalent for both glacial inceptions, well below that inferred from sea level records. Choudhury et al. (2020) simulated penultimate glacial inception using the LOVECLIP model, capturing overall sea level change but lacking inferred sea level variability during the sub-stages following inception (see Figure 1.1).

Colleoni et al. (2009a,b, 2011) simulated the Late Saalian with an atmospheric general circulation model (LMDZ4) for 20 year equilibrium climate time slices. They prescribe LGM ice sheets for North America, Greenland, and Antarctica, while the Eurasian ice sheet boundary condition is based on PGM reconstructions (Svendsen et al., 2004). They found in a vegetation sensitivity study that albedo feedbacks over East Siberia resulting from changes from Taiga to Tundra cooled the regional climate and could have helped to sustain a larger Saalian ice sheet (Colleoni et al., 2009a). In an ocean sensitivity analysis, Colleoni et al. (2011) find that Northern Hemisphere sea surface temperatures are overall colder in a Late Saalian than in a LGM climate, which leads to less precipitation over Eurasia, but also helps sustain a perennial snow

cover over East Siberia, that was not sustained with LGM sea surface temperatures. Their findings highlight the importance of feedbacks between climate components and ice and that a fully coupled ice-climate model is necessary to capture ice evolution.

Colleoni et al. (2016), furthermore analyzed the influence of the PGM North American ice sheet topography on the downstream Eurasian ice sheet. Using a coupled Atmosphere-Ocean-Sea-Ice-Land model (CESM) and a fixed North American ice sheet extent to force an ice sheet model (GRISLI) off-line, they find that using a smaller-than-LGM ice sheet over North America changes the planetary wave pattern and therefore storm tracks downstream. This leads to higher temperatures and precipitation over the Eurasian ice sheet but a cooling over East Siberia, compared to a climate using a LGM-sized North American ice sheet. The smaller North American ice sheet furthermore leads to sea surface temperatures and precipitation in better agreement with PGM reconstructions than a LGM-sized ice sheet. These findings highlight that feedbacks triggered by one ice sheet influencing an ice sheet downstream play an important role in ice sheet evolution of the last two glacial cycles. Colleoni et al. (2011) further point out that there is a need for transient simulations of the penultimate glacial to understand the influence of the different orbital configuration leading up the PGM.

Summarizing previous work, we find that a fully coupled model is critical to capture the evolution of climate and ice sheets as uncoupled experiments will generally lack two-way consistency between ice and climate, leading to unrealistic climate or ice evolution. Coupled snapshot experiments, on the other hand, cannot display the dynamic reaction of the climate-ice system to changing forcing and cannot capture the growing and decaying phase of ice sheets. Fully coupled, transient simulations

can display wrong ice sheet configurations since a single (or few) simulation(s) can not account for parametric model uncertainty.

This thesis advances our understanding of ice evolution over the last two glacial cycles by (1) using a fully-coupled ice-climate model that includes all important ice-climate feedbacks (layed out in Section 1.5), (2) performing long transient simulations that cover glacial inception and termination, and (3) using ensemble simulations to partially address model parametric uncertainty. I furthermore test the role of initial conditions and ice-climate memory by comparing simulations covering two glacial cycles to simulations covering one glacial cycle.

1.5 Key ice-climate feedbacks and their representation in the model LCice

LCice is a fully-coupled ice-climate model. It combines the vegetation (VECODE), atmospheric (ECBilt) and ocean (CLIO) component of LOVECLIM with the glacial system model (GSM, see schematic 2.2 in Chapter 2). LOVECLIM is an EMIC, which allows for long paleo-climate simulations in reasonable calculation times while still including many components of the Earth system (Claussen et al., 2002; Weber, 2010).

In LCice, the atmospheric and especially the vegetation components have the least relative complexity compared to the current state of the art. ECBilt is a spectral global quasi-geostrophic model, with T21 truncation (32 x 64 Gaussian grid cells, 625 km resolution at equator), a time step of 4 h and only three vertical layers at

800, 500, and 200 hPa. The ocean component, CLIO, is a primitive equation model that includes dynamic/thermodynamic sea ice. The horizontal resolution is 3° x 3° and there are 20 vertical layers. The model accounts for turbulence by incorporating the effects of small-scale processes into the momentum equation through a harmonic operator and using parameterizations for vertical mixing. VECODE is a simple land vegetation model component that includes 3 types of surfaces: trees, grass and desert. Based on precipitation and growing degree-days, the plant functional type is calculated. The Saharan desert is hard-coded in and can not change to a plant type. A detailed assessment of LOVECLIM can be found in Goosse et al. (2010).

The LOVECLIM components are coupled to the glacial system model. The GSM (Tarasov, in prep.) is a 3D thermo-mechanically coupled ice sheet and a global visco-elastic bedrock deformation model. It includes all major ice sheets (Greenland, Antarctica, North America, Eurasia). The resolution of GSM in LCice is 0.5°- longitude by 0.25°-latitude in the northern hemisphere and a 20 km stereographic grid for Antarctica .

LCice includes all important ice-climate feedbacks, which are described in the following.

Climatic changes are initiated during a glacial cycle through changes in incoming radiation (via orbital parameters and atmospheric GHG concentration). Orbital parameters (Berger and Loutre, 1991) and GHG records (Bereiter et al., 2015) are the only prescribed forcings used by the model LCice in this thesis.

The climate variables necessary to calculate ice sheet growth or melt are passed from ECbilt to the GSM: monthly mean and standard deviation of temperature and wind, monthly means of precipitation, evaporation and atmospheric lapse rate. The

lapse rate is used to downscale temperature from the coarse LOVECLIM to the higher-resolution GSM grid. The wind fields are used in the orographic downscaling of precipitation to the finer GSM grid as per standard approaches (Roe, 2005). The vertical wind component along the slopes of the GSM topography can be calculated from the horizontal LOVECLIM wind components; precipitation forms from water vapor as the temperature decreases with increasing altitude.

The coupler applies a present-day bias correction to the LOVECLIM temperature and precipitation fields before they are passed to the GSM. The temperature bias correction decreases with increasing ice volume. At LGM sea level, the correction is zero, and at present-day sea level, the full correction is applied. The transition between these states depends on an ensemble parameter value. For each different LOVECLIM parameter vector, the corresponding base-line bias correction is set to the present-day monthly-mean discrepancy between simulation and present-day re-analysis (ERA5, Hersbach et al., 2020). The precipitation bias correction is imposed as a monthly regional scalar from the present-day continental (or sub-regions thereof) scale spatial mean anomaly. A common problem in glacial cycle modeling is excessive ice advance over Alaska and Siberia (e.g. Bahadory et al., 2021). LCice does not adequately resolve the atmospheric patterns that keep these regions ice free, therefore a crude temperature bias correction is needed to not distort results for adjacent regions. An ad-hoc bias correction increases temperature in these two regions (ranging from +1K to +9K).

Marine terminating ice sheets are additionally influenced by ocean temperature, which is important for sub-shelf melt. CLIO's bathymetry is fixed to present-day and ocean grid cells can not become land cells when sea level decreases during a glacial.

Furthermore, CLIO treats the present-day Antarctic ice shelf areas as land. Therefore, there is no ocean current underneath the Antarctic ice shelf from which ocean temperature and sub-self melt can be calculated. Instead, the upstream vertical ocean temperature field is passed from CLIO to the GSM for sub-shelf melt calculation.

The coupler passes updated ice sheet information from the GSM to the atmosphere and ocean. Ice sheets influence the atmosphere and ocean in various ways. Ice changes the albedo of the land. Due to the lighter surface colour of ice compared to vegetation or bedrock, more sunlight is reflected and local temperature decreases. This feedback is simply implemented by the coupler passing the updated ice mask calculated in the GSM to the atmosphere. Ice sheets furthermore alter the land topography, which is passed from GSM to LOVECLIM. The change in topography influences the atmospheric circulation. The jet stream can split around the North American ice complex and storm tracks are displaced, influencing temperature and precipitation downstream (Kutzbach and Wright, 1985; Andres and Tarasov, 2019; Liakka et al., 2016).

As ice sheets grow vertically, their load depresses the solid Earth underneath. The GSM calculates the glacial isostatic adjustment (GIA) and corrects ice sheet altitude and surface topography accordingly. Due to GIA, pro-glacial lakes form at ice sheet margins, which can enhance melting and calving. Pro-glacial lakes are resolved in the GSM. Ice sheets and GIA furthermore influence the routing of freshwater. The GSM calculates melt amounts and routing and the coupler passes them to the ocean component CLIO. The amount and location of freshwater injection into the ocean can have a significant influence on ocean circulation (especially on the Atlantic Meridional Overturning Circulation, Love et al., 2021).

When sea level decreases, the water flow through ocean gateways can be reduced. The land-sea mask cannot change in CLIO, however, Bering Strait through-flow is parameterized and dependent on the sea level calculated in the GSM. The Bering Strait connects the Pacific to the Atlantic via the Arctic Ocean. During Glacial Maxima, the Bering Strait formed a land bridge and ocean circulation from the Pacific into the Arctic and Atlantic was blocked. This potentially had a significant impact on ocean circulation and climate (Hu et al., 2015, 2012).

The un-accelerated model version couples LOVECLIM and GSM every 20 simulation years (based on sensitivity tests, Bahadory and Tarasov, 2018). In this thesis, the 4x accelerated ice-climate coupling is used, where 20 years of changing orbital and greenhouse gases are accelerated to span 5 years of forcing for LOVECLIM. Choudhury et al. (2020) found that ice sheet evolution is insensitive to up to 5x acceleration in coupling using LOVECLIM coupled to PSUIM. With our 4x acceleration setup, LCice can calculate $\sim$ 2000 yrs in 24 h on a single compute node.

Given the above described coupling between ocean, atmosphere and glacial components, LCice includes all key ice-climate feedbacks and is with its relatively short computation time well equipped to simulate glacial cycles.

1.6 Guiding research questions and thesis overview

As motivated above, I aim to simulate the last two glacial cycles using a fully-coupled EMIC to analyze the co-evolution of ice and climate in response to changes in radiative forcing. All chapters employ ensemble simulations, which let us partially account for parametric uncertainty. The goal is not to reconstruct past ice-climate evolution as

close to observations and proxy data as possible, but to bracket reality within the phase space of the ensemble. Due to ongoing model development, the ensembles used in each manuscript are not identical. The following research questions will be addressed in the manuscripts in Chapters 2-4:

- Chapter 2: What does glacial inception look like in the last two glacial cycles? How do ice area and volume differ between last and penultimate glacial inception and how do they compare to the limited available data? I present a detailed description of ice evolution during MIS 7 and 5, ranges of ice expansion and sea level change rates, and the relationship between timing of forcing and ice sheet maxima.

- Chapter 3: What are differences between the ice-climate evolution over the penultimate and last glacial cycle? How important is memory of the penultimate glacial ice evolution on the last glacial cycle ice-climate evolution? I present a continuous simulated record of climate fields of the last two glacial cycles in comparison to reconstructions. I assess differences in last glacial cycle ice evolution when simulated starting at MIS 7 and MIS 5.

- Chapter 4: How do ice-climate feedbacks shape ice evolution over the course of a glacial cycle? What is the relative role of ice sheets in the climate system for glacial cycle contexts? I performed sensitivity experiments where individual ice-climate feedbacks are turned off. I tested the influence of Bering Strait through flow, GIA, and the albedo and topographic effects of the North American and Eurasian ice sheet. The relative role of the feedback on ice evolution, the ice impact on itself and on other ice sheets is evaluated during glacial inception

and during the glacial maximum.

1.7 Bias correction bug

Shortly before completion of this thesis, a code bug was discovered concerning the temperature bias correction. When the bias corrections were created, the LOVECLIM present-day sea level temperature was inadvertently treated as 2 m air temperature on the LOVECLIM grid and as such had LOVECLIM lapse rate x LOVECLIM vertical elevation applied to the field. For present-day elevations above 0 m, this would have cold-biased the bias-correction on the order of 1-5 K for a grid elevation of 1000 m above sea level. Given the existing modeling uncertainties and sub 500 m surface elevation (on the LOVECLIM T21 grid) for most of North America and the gridded range of Europe and Siberia, this is arguably significant only for the North American Cordillera and the Greenland and Antarctic ice sheets. Furthermore, the latter two regions receive minimal attention in this study (given their much more limited response range over the glacial cycles). Another mitigating factor is that most of the simulations have bias-control parameter value that reduces the strength of the bias correction as a function of the global mean sea level anomaly from present.

Simulations with the correct bias correction have been tested. Not surprisingly, these simulations simulate a somewhat weaker inception, necessitating some re-tuning/re-sampling of model parameter vectors. A new ensemble recently started looks promising. The new simulations will be used for analysis in the manuscripts presented in this thesis before they will be submitted to journals. Simulation time is a minimum of 120 days to complete two glacial cycles, therefore the new simulations can not be

included in this thesis.

1.8 Co-authorship statement

This project was originally conceived and funding was acquired by Lev Tarasov, faculty in the Department of Physics and Physical Oceanography at Memorial University. The core of the GSM component of LCice was provided by Lev Tarasov. The core of the coupler of LCice was provided by Taimaz Bahadory and revised by Lev Tarasov and Marilena Geng. The thesis has been reviewed and edited by Lev Tarasov, Audrey Parnell, and Joel Finnis.

Lev Tarasov and Marilena Geng jointly developed the experimental design for all major project experiments.

Contribution to Chapter 2 were made as follows: experiments: Marilena Geng; model development: Lev Tarasov and Marilena Geng; analysis and interpretation of results: Marilena Geng, Lev Tarasov, and April Sue Dalton; manuscript preparation(initial drafting by Marilena Geng): Marilena Geng; Lev Tarasov, and April Sue Dalton.

Contribution to Chapter 3 were made as follows: experiments: Marilena Geng; model development: Lev Tarasov and Marilena Geng; analysis and interpretation of results: Marilena Geng, Lev Tarasov; manuscript preparation(initial drafting by Marilena Geng): Marilena Geng and Lev Tarasov.

Contribution to Chapter 4 were made as follows: experiments: Marilena Geng; model development: Lev Tarasov and Marilena Geng; analysis and interpretation of results: Marilena Geng, Lev Tarasov; manuscript preparation(initial drafting by

Marilena Geng): Marilena Geng and Lev Tarasov.

Chapter 2

A comparison of the last two glacial inceptions (MIS 7/5) via fully coupled transient ice and climate modeling

2.1 Abstract

Little is known about the evolution of continental ice sheets through the last two glacial inceptions. Here, we present the results of a perturbed parameter ensemble of transient simulations of the last two glacial inceptions and subsequent interstadials (Marine isotope stages, MIS 7e-6e, 240-180 ka and MIS 5e-4, 120-60 ka) with the fully coupled ice/climate model LCice. LCice includes all critical direct feedbacks between climate and ice. As shown herein, it can capture the inferred sea level change of the

last two glacial inceptions within proxy uncertainty. One key underlying question of paleoclimate dynamics is the non-linear state dependence of the climate system. Concretely, in a model-centric context, to what extent does the capture of one climate interval in an Earth systems model guarantee capture of another interval? For LCice, the capture of present-day climate is insufficient to predict capture of glacial inception climate, as only a small fraction of ensemble members that performed "well" for present-day captured inception. Furthermore, the capture of inferred sea level change in one inception has weak correlation with the same outcome for the other.

After partial history matching against present-day and past sea level constraints, the resultant NROY (not ruled out yet) ensemble of simulations have a number of features of potential interest to various paleo communities, including the following. (i) In correspondence with the inferred Last Glacial Maximum configuration, the simulated North American ice sheets are substantially larger than the Eurasian ice sheet throughout MIS 5d-MIS 4 and MIS 7d-MIS 6e. (ii) Hudson Bay can transition from an ice-free state to full ice cover (grounded ice) within 1000 years. (iii) North American ice sheets advanced southward on average at 170 $\pm$ 40 m/yr during both inceptions, while the Eurasian ice sheet advanced 50 $\pm$ 70 m/yr from MIS 5d-c and 100 $\pm$ 70 m/yr from MIS 7d-c. (iv) the Laurentide and Cordilleran ice sheets merge in their northern sectors in all NROY simulations for MIS 7d, contrary to what is assumed from limited geological data. (v) larger ice sheets display a larger lag in the timing of stadial maximum ice volume compared to that of the insolation minimum; the North American ice sheet maximum lags 3.7-4.5 kyrs behind the MIS 7d insolation minimum. Supplemental resources include a dynamic display of ice advance and subsequent retreat for a sub-ensemble of 15 NROY simulations from

MIS 5d-4 and MIS 7d-6e.

2.2 Introduction

On the basis of stacked benthic δ^{18}O sea level proxies, glacial inceptions are characterised by relatively fast transitions from interglacial to glacial conditions and a rapid drop of sea level. This is is clearly evident in the inferred up to 60 m eustatic sea level (mESL) drop during last glacial inception Marine Isotope Stages (MIS) 5e to 5d and even more clearly in the up to 80 mESL drop during the penultimate glacial inception, MIS 7e to 7d, over the course of approximately 12 kyrs (Spratt and Lisiecki, 2016). However, the associated rapid growth in terrestrial ice volume has been difficult to replicate by Earth system models (e.g. Calov et al., 2005; Bahadory et al., 2021). The subsequent strong interstadial and associated sea level rise imposes a further challenge for both modeling and understanding. As such, glacial inceptions and subsequent interstadials offer a potentially powerful test of whether the net feedback response of an Earth systems model (ESM) to radiative forcing is of appropriate magnitude, a key issue for building confidence in modeling future climate evolution. This relates to a broader motivation for testing Earth system models under paleo boundary conditions: the extent to which underlying state dependence of current ESM configurations might invalidate their predictive ability for simulating ongoing and future climate change. For the context herein, this issue can be addressed concretely as the extent to which the capture of a single glacial inception by an ESM correlates with its capture of a different glacial inception, and furthermore, the extent to which capture of present-day climate correlates with capture of ice and

climate over glacial inception.

The resolving power of the above test is dependent on the reliability of relevant paleo constraint data, which is especially challenging prior to the Last Glacial Maximum (LGM). Existing stacked sea level records provide insights into global ice volume changes but are subject to significant (often unquantified) uncertainties. Sea level estimates rely on δ^{18}O records, a convolution of eustatic sea level and deep ocean temperatures. A further source of uncertainty is the reliance on orbital tuning for the pre-^{14}C dating range. Two sea level records (Spratt and Lisiecki, 2016; Medina-Elizalde, 2013) published with uncertainty bounds are shown in Figure 2.1. Significant disagreements exist between the two, especially for the penultimate glacial cycle and both inceptions. Far-field and isotopic sea level proxy records, moreover, cannot offer information regarding the ice volume distribution between different ice sheets. Geomorphological data that could inform about individual ice sheet extent have very limited age control pre-^{14}C dating range. Furthermore, geological and geomorphological pre-LGM records are scarce since LGM ice overwrote most regions subject to episodic glacial cover during the Late Pleistocene.

A key ongoing challenge for paleoclimate modeling is computational cost. This challenge is addressed by invoking various approximations that limit accuracy. Uncoupled steady-state experiments (climate- or ice-only) lack key feedbacks and they therefore are not able to capture expected rates of sea level change (Khodri et al., 2001; Yoshimori et al., 2002; Vettoretti and Peltier, 2003; Otieno and Bromwich, 2009; Born et al., 2010; Colleoni et al., 2014). Early transient simulations of the entire last glacial cycle used two-dimensional energy balance or quasi-geostrophic climate models coupled to simple two or three-dimensional ice sheet models (Gallée et al., 1992;

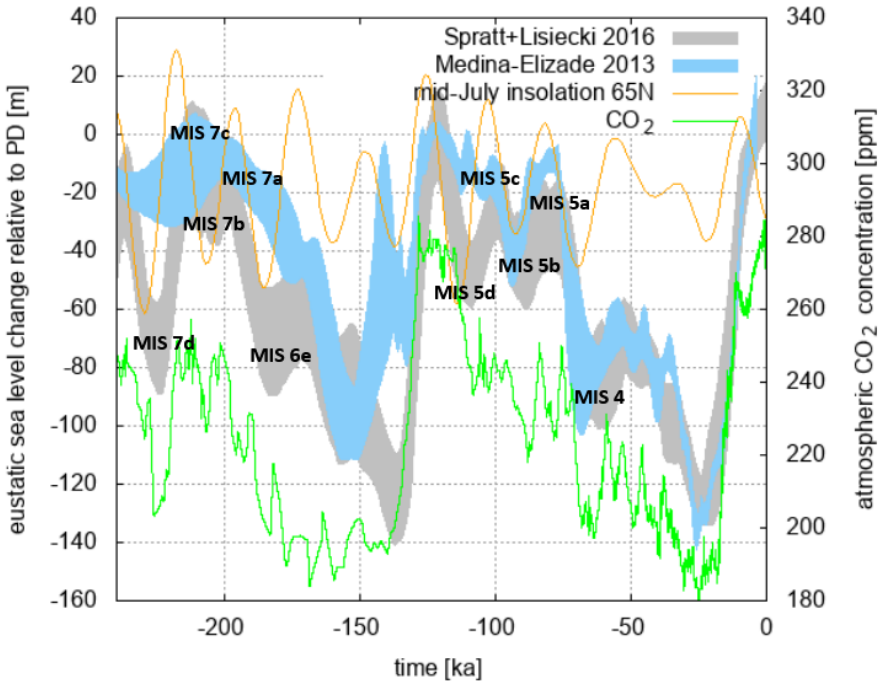

Figure 2.1: Sea level records (Spratt and Lisiecki, 2016; Medina-Elizalde, 2013), insolation and atmospheric CO_2(Bereiter et al., 2015) for the last two glacial cycles

Peltier and Marshall, 1995; Tarasov and Peltier, 1997). While these models could capture the overall structure of ice growth and decay, they were unable to capture the minimum ice volume required to explain proxy-based inferences for the last glacial inception sea level low-stand. More recent work has employed Earth system models of intermediate complexity (EMICs) coupled to ice sheet models. Such studies to date that tested inception and subsequent ice retreat did not include an interactive Antarctic ice sheet. Most such studies also have significant discrepancies between simulated and geologically-inferred ice extent. For example, Alaska tends to be nearly fully ice-covered (e.g. Bahadory et al., 2021; Bonelli et al., 2009; Willeit et al., 2023) contradicting geological records (Kauman and Manley, 2004; Kaufman et al., 2011).

Meanwhile, there is often not enough ice simulated over Quebec and Eurasia (EA) (e.g. Bonelli et al., 2009; Ganopolski et al., 2010, at least for LGM where geological data is available for comparison). Many models either poorly resolve critical feedbacks such as orographic forcing of precipitation (e.g. Bonelli et al., 2009; Ganopolski et al., 2010; Choudhury et al., 2020; Willeit et al., 2023) and/or simply lack feedbacks such as dynamic freshwater routing (e.g. Ganopolski et al., 2010; Bonelli et al., 2009; Choudhury et al., 2020).

The most successful attempts at simulating full glacial cycles with EMICs have to date relied on dust forcing (Ganopolski et al., 2010) or feedback (Willeit et al., 2023) to trigger ice retreat or keep areas ice-free. However, it remains unclear to what extent a reliance on dust forcing and or feedbacks is compensating for limitations in the utilized EMIC (the CLIMBER-2 EMIC used in Ganopolski et al., 2010, lacks a dynamical atmosphere). Dust process modeling is also subject to large uncertainties as regional dust input into the atmosphere and subsequent deposition is highly sensitive to regional aridity, winds, and turbulence. These characteristics are challenging for any EMIC to confidently capture. Atmospheric dust processes are therefore a potentially important but poorly constrained forcing and feedback.

Climate models have order 100 poorly constrained parameters (though for simpler EMICs many of these parameters are implicit). Furthermore, any computational model of a complex geophysical system will have significant trade-offs between fits to different tuning targets in parametric tuning. As such, analyzes based on just one or a few model simulations have very limited inferential value. We therefore present a perturbed-physics ensemble of transient simulations of the last two glacial inceptions and subsequent interstadials (MIS 5e to MIS 4 and MIS 7e to MIS 6e) with the

fully coupled ice/climate model LCice. The latter interstadial inclusion is important to ensure that an adequate simulation of glacial inception is not due to a cold bias in the model. We combine geological knowledge and model results to analyze the evolution of the last two glacial inceptions. This includes comparing the simulated ice advance and maximum and minimum ice sheet extents with available geological data.

The LCice model is described in Section 4.3.1. Section 4.3.2 lays out the experiment setup. In climate modeling, capturing present-day climate appropriately is often implicitly assumed to provide predictive confidence. In Section 2.4.1, we explicitly test this assumption for different interglacial/glacial stages during the penultimate and last glacial inception. In Section 2.4.2, we present the phase relationships between insolation and ice sheet response in ice volume and area. Sea level stacks are usually orbitally tuned, using a poorly constrained insolation-δ^{18}O lag parameter (Lisiecki and Raymo, 2005). Modeling enables an independent assessment of the impact of orbital tuning. Section 2.4.3 examines the simulated ice evolution over the last two glacial inceptions with a focus on the maximum extent at MIS 7d and 5d and the differences and similarities between them. Animations of ice sheet evolution are available (`https://doi.org/10.5446/66195`). We compare the available geological data against our simulations, and consider what insights the simulations can provide where there is limited geological information. Section 2.4.4 considers inter-ensemble variability and the extent to which different ice sheet configurations are possible with the same simulated sea level change. Finally, we discuss and summarize our findings in Section 2.5.

2.3 Methods

2.3.1 The Model LCice2.0

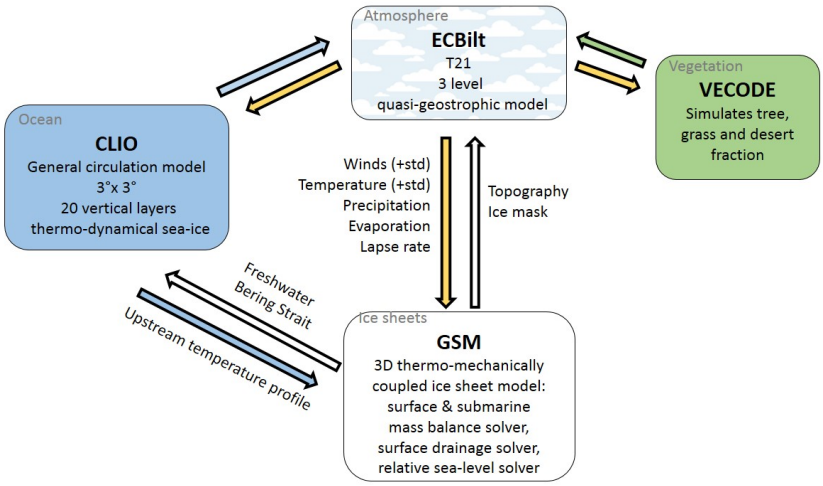

Figure 2.2: LCice components and couplings

LCice (visualized in Figure 2.2) consists of 3 components of the LOVECLIM model, including the atmosphere (ECBilt), ocean (CLIO) and vegetation (VECODE), coupled to an ice sheet systems model (GSM). LCice is forced by orbital parameters and greenhouse gas chronologies (Bereiter et al., 2015). LOVECLIM is an Earth system model of intermediate complexity (EMIC) capable of about 2.5 kyrs in 24 h on a single processor core with 4 x acceleration. LOVECLIM and its performance are discussed in detail by Goosse et al. (2010).

To enable interpretation of the simulation results, it is necessary to evaluate the strengths and weaknesses of the model. The key limitations are a combination of simplified process representation and limited spatial resolution. The vegetation com-

ponent VECODE has only 3 classes: trees, grass and deserts; however, the Saharan desert is hard-coded in and can not change to a vegetation type. The atmosphere ECBilt is quasi-geostrophic, on a T21 grid with 3 vertical levels. This means the model is suitable for capturing large (synoptic) scale mid-latitude atmospheric circulation but can't resolve small-scale, tropical or mesoscale convective systems. The limited spatial resolution of ECBilt will also significantly affect its ability to capture atmospheric stationary wave dynamics over Eurasia (EA) due to the North American (NA) ice sheet forcing, as well as associated changes in precipitation (with storm track displacement) and the amplitude of the seasonal cycle. In a suite of grid resolution sensitivity tests with the CAM3 atmospheric General Circulation Model (with full LGM boundary conditions) forcing an ice sheet model, Lofverstrom and Liakka (2018) find that T42 is the minimum resolution to grow inferred LGM ice extent though LGM NA ice extent can be reasonably captured at T21 (except for excessive glaciation of Alaska, which is not present in the T31 simulation). Goosse et al. (2010) find for default parameter values that LOVECLIM captures the present-day surface temperature pattern and the magnitude of precipitation of the mean climate "reasonably well" compared to observations appropriately smoothed to LOVECLIM resolution. However, a warm temperature bias exists in the tropics and the eastern Pacific, and the precipitation pattern is too symmetric between Northern and Southern Hemispheres. The extent of LGM annual mean cooling in LOVECLIM is in approximate agreement with other PMIP2 models (Goosse et al., 2010).

The ocean component CLIO is relatively complex compared to other EMICs. It is a full general circulation model (rather than e.g. the frictional-geostrophic model in the relatively new CLIMBER-X Willeit et al., 2022). The model simulates the

magnitude of the meridional overturning circulation in agreement with observations (Goosse et al., 2010). However, the 3°x 3°grid is too coarse to adequately resolve ocean circulation under ice shelves, and current Antarctic ice shelves are represented as land rather than ocean grid cells. Furthermore, the land-sea mask and bathymetry (except for the Bering Strait throughflow) are time-independent in the model. Although sea level changes, no ocean cells can be turned into land cells (or vice versa). To partially compensate, LCice has a sea level dependent parametrized Bering Strait through-flow in the ocean model.

The pre-existing LOVECLIM components are coupled to the Glacial Systems Model GSM (Bahadory and Tarasov, 2018). The coupler includes all important feedbacks between climate and ice for a glacial cycle context (Figure 2.2) except potentially dust (Willeit et al., 2022). It passes the monthly mean and standard deviation of temperature and monthly means of wind, precipitation, evaporation and lapse rate from ECBilt to the GSM. The downscaling scheme accounts for the orographic forcing of precipitation on the higher-resolution GSM grid. The temperature downscaling uses the LOVECLIM vertical atmospheric temperature gradient (lapse rate Bahadory and Tarasov, 2018). The GSM passes the ice mask and topography to the atmosphere, and a model parameter controls the topographic upscaling scheme (simple, envelope, or silhouette) from high to low-resolution grids. Furthermore, the GSM computes and passes topographically consistent freshwater fluxes to CLIO. Conversely, CLIO passes ocean temperature profiles to the GSM to calculate the submarine melting of marine-terminating ice sheets and ice shelves.

Since the first publication using LCice (Bahadory and Tarasov, 2018), we have updated the coupler, the most significant update of which is the inclusion of a dynamic

Antarctic ice sheet. The GSM has also been updated, including the conversion from pure shallow ice approximation to hybrid shallow ice/shallow shelf ice dynamics, and the introduction of a novel (and physically motivated) accounting for the impact of changing insolation forcing on surface mass-balance (Tarasov et al., in prep.).

A further significant change from Bahadory and Tarasov (2018) is the addition of temperature and precipitation bias corrections. Previous modeling efforts (Vettoretti and Peltier, 2003; Ganopolski et al., 2010; Willeit et al., 2023) have shown that model biases can have a significant impact on glacial cycle modeling. A key challenge is that there is no basis for assuming that present-day model biases would persist in total over a glacial cycle. Therefore, the bias correction used here decreases with increasing ice volume. At LGM sea level, the correction is zero, and at present-day (PD) sea level, the full correction is applied. The transition between these states depends on a parameter value. For each different LOVECLIM parameter vector, the corresponding base-line bias correction is set to the present-day monthly-mean discrepancy between simulation and ERA 5 (Hersbach et al., 2020). Since precipitation patterns will likely change much more drastically than temperature, the precipitation bias correction is imposed as a monthly scalar from the present-day continental scale spatial mean anomaly. To address the common problem of excessive ice advance over Alaska and Siberia, which would otherwise distort results for adjacent regions, (e.g. Bahadory et al., 2021), we impose further ad-hoc temperature increases in these two regions (ranging from +1K to +9K).

Given the possibility of inadequate capture of radiative feedbacks in LOVECLIM, we have also added a greenhouse gas radiative factor ensemble parameter, as suggested by Choudhury et al. (2020). The factor increases the atmospheric radiative sensitivity

to CO_2 variations with respect to the reference CO_2 value and ranges from 1.5 to 2.5. In total, every ensemble member has a parameter vector of 18 LOVECLIM and 23 GSM parameters that are varied.

2.3.2 Experiment Setup

We use fit to PD climate to select initial LCice parameter vectors for glacial inception simulations. To do so, plausible prior distributions for 18 LOVECLIM parameter values were defined. 2000 different LOVECLIM parameter vectors were then selected via Latin-hypercube sampling from these distributions. For each parameter vector, LOVECLIM was started with PD initial conditions at 1200 years before present and runs transiently uncoupled for 1 kyrs before activating coupling to the GSM.

We filter the simulations by comparison against ERA 5 (Hersbach et al., 2020) and ORAS 5 (Copernicus, 2021) reanalysis for the mean of 1980-2000. The metrics chosen for filtering are based on their importance for ice sheet growth and decay (summarized in Table 2.1). The metrics are as follows. 1) Mean 2 m temperature seasonality (June, July, August - December, January, February; JJA-DJF). This is motivated by the assumption that an ensemble member with the appropriate sensitivity to seasonal insolation cycling is also more likely to display the right sensitivity to insolation changes on glacial cycle time scales. 2) Mean annual precipitation, which is essential for ice sheet accumulation. 3) Southern Ocean temperature, which is important for Antarctic sub-shelf melt. Metrics 1 and 2 are evaluated over areas where ice sheet advance is expected during inception, such as Northern Canada (North America North, NAN), Hudson Bay region (North America South, NAS), West Eurasia (EAW), West

Antarctic Ice Sheet (WAIS), and East Antarctic Ice Sheet (EAIS); and in regions inferred to remain ice-free despite their high latitudes such as Alaska (NAAL) and Eastern Eurasia (EAE).

Ensemble members that simulate metrics within 4 sigma time variance of ERA 5 make up the not-ruled-out-yet (NROY) ensemble subset. We chose a 4-sigma range to partially compensate for limited sampling and an incomplete error model. The PD NROY ensemble subset narrows the parameter value ranges from which we re-sample to create a new ensemble to repeat the filtering process. In the end, 90 LCice parameter vectors result in simulations that pass the filtering process and are used for the last glacial inception simulations. The mean of the sub-ensemble that we will analyze later on (15 inception NROY ensemble members) shows a pronounced cold bias over the Arctic Ocean and a warm bias over North America (NA) winter for PD (Sup. Fig. A.1). These biases are much weaker in summer, however a warm bias over Labrador and Northern Siberia (ice inception areas) persist. In both seasons, there is a cold bias over West Antarctica and a warm bias over East Antarctica. Precipitation biases are most substantial in small-scale, high-elevation areas and the tropics. In northern hemisphere ice sheet regions, LCice displays a light wet bias over NA (except for the coastal mountain area) and a light dry bias over Scandinavia. Although far from complete, these biases give a crude initial estimate of the structural uncertainty of the model if one assumes that persistent biases proportionally reflect underlying model limitations.

The ensemble for each of the last and penultimate glacial inceptions consists of 90 PD NROY parameter vectors. Penultimate glacial inception simulations start at 240 ka, last glacial inception at 120 ka. Sea level records suggest that the last

(penultimate) interglacial likely had a higher (lower) than PD sea level. As the exact configuration of the Greenland and Antarctic ice sheets of the interglacial has high uncertainties, we opted to use the well-known PD conditions for initializing simulations for both time-frames. LOVECLIM is first spun up for 2 kyrs uncoupled at constant 240 ka (120 ka) forcing before full ice/climate coupling is activated. Choudhury et al. (2020) use LOVECLIM at 5 x acceleration and found that the ice sheet evolution is relatively insensitive to reduced acceleration. We choose a slightly more conservative 4 x acceleration in this study.

2.4 Results

Given the model limitations outlined in Section 4.3.1, the simulation results should not be interpreted as reconstructions. However, there is arguably inferential value in selective characteristics of ice sheet evolution consistently observed across the NROY ensemble.

In the following, we analyze the simulations with respect to global eustatic sea level change (Section 2.4.1), mean phasing of ice volume and area with insolation (Section 2.4.2), and ice area and geometry compared to geological and geomorphological evidence (Section 2.4.3).

2.4.1 Simulated Sea Level Performance

We use the Spratt and Lisiecki (2016) sea level stack as an additional implausibility filter to refine the NROY sub-ensemble. The stack consists of isotopic records and relative sea level records of the Red and Mediterranean seas. The stack has large age

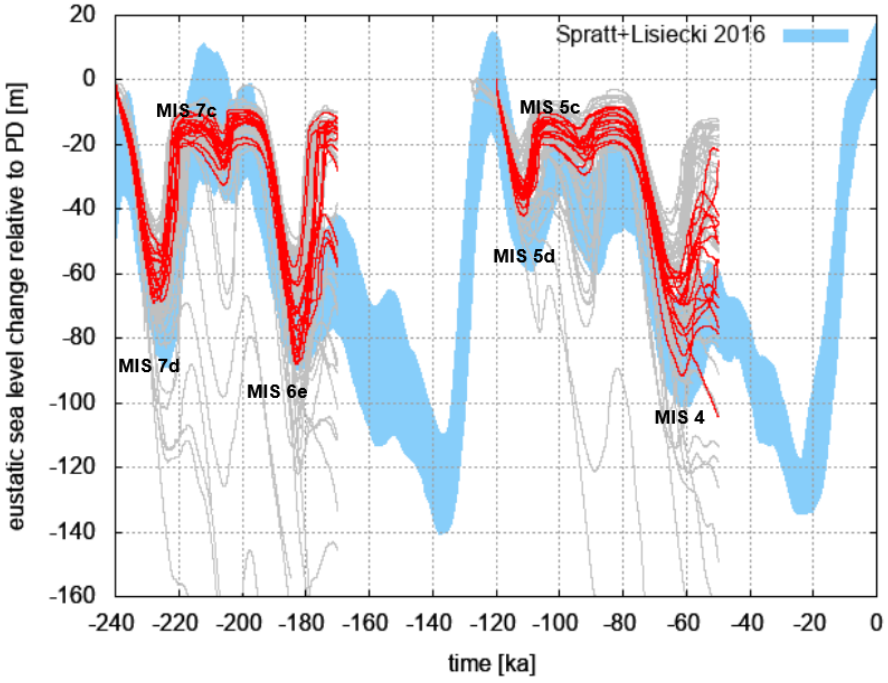

Figure 2.3: Sea level reconstruction in blue (Spratt and Lisiecki, 2016) and simulated sea level change for the 2 full ensembles of the penultimate and last glacial cycle. Grey: all ensemble members (which are NROY for present-day constraints), red: 15-member NROY sub-ensemble

uncertainties of at least 4 ka as it is based on tuning to the LR04 stack (tuned to a simple nonlinear ice volume model; Lisiecki and Raymo, 2005), and therefore ignores the potential for significant timing differences in the benthic δ^{18}O signal between the different ocean basins. However, it is one of the few continuous sea level estimates covering the last two glacial cycles that gives any uncertainty estimates (although likely underestimated). We chose this stack over Medina-Elizade (see both stacks in Figure 2.1), as they use corals not corrected for glacial isostatic adjustment, and corals may not be the best indicators of falling sea levels as the link between reef

growth and sea level is not always straightforward.

The two glacial inception ensembles are filtered for sea level high- and low-stands. Ensemble members are ruled out if their simulated sea level minima/maxima are not within the 95 percentile given by Spratt and Lisiecki (2016) for sea level low-/highstands during MIS 7d, 7e, and 6e in the penultimate as well as for MIS 5d, 5e, and 4 in the last glacial inception ensemble. Model-proxy match at these tie-points ensures an overall good simulation of eustatic sea level from MIS 7e-6e and MIS5e-4. MIS 4 and MIS 6e (the largest ice volume during the time intervals in question) pose the strongest constraint on each inception. Only 15 ensemble members pass the sea level filter (red in Figure 2.3), embodying the inception NROY sub-ensemble we analyze below.

The hypothesis that reasonable performance for PD climate predicts reasonable performance for glacial inception is not supported, as seen from the wide range of grey-coloured simulations in Figure 2.3. Furthermore, an ensemble member that performs well for the last glacial inception does not necessarily perform well for the penultimate glacial inception and vice versa. 43 of the 90 simulations pass the sea level filter for MIS 7d, 7e, and 6e only, 40 for MIS 5d, 5e, and 4 only, their overlap resulting in only 15 remaining ensemble members.

The NROY sub-ensemble shows that the NA ice sheet (combined Innuitian, Cordillerian, and Laurentide ice sheets) grows and melts ice volume faster than the EA ice sheet, where the fastest advancing ensemble member reached absolute growth rates of over 4 mSLE/kyr (meters of sea level equivalent per 1000 years) and melting rates of over 8 mSLE/kyr during MIS 7d. The EA ice sheet reached a maximum growth rate of over 2 mSLE/kyr for the fastest advancing ensemble member during the growth

towards MIS 7d and just under 4 mSLE/kyr of mass loss following the MIS 7d ice volume maximum. The sub-ensemble mean growth and decay rates and standard deviations per ice sheet can be found in Table 2.2.

We examine if any model ensemble parameter values separate ensemble members performing well in at least one of the glacial inception intervals from the rest of the ensemble. The mean cosine angle is used to quantify the similarity between the NROY parameter vectors with in the sub-ensemble of members passing MIS 7d-6e filters, members passing MIS 5d-4 filteres, and members passing both. No similarity is found within any of the ensemble subsets. This suggests that non-linearities between the interactions of the different parameters are at play and cannot be disentangled here. The only constraint established here for capturing the last two glacial inceptions is a greenhouse gas radiative factor between 2.0 and 2.5 (following Choudhury et al. (2020), tested values were 1.5, 2.0, and 2.5). All varied parameters and their value range can be found in Table A.1.

Table 2.1: NROY (not ruled out yet) conditions for a subset of ensemble members. Areas of evaluation are displayed in supplement Figure A.2

Metric	Area	acceptance range PD	acceptance range MIS 7d, 7c, 6e, 5d, 5c, 4
Mean 2m-temperature JJA-DJF 1981-2000	North America (NAN, NAS, NAAL), Eurasia (EAW, EAE), Antarctica (WAIS, EAIS)	4σ ERA 5 reanalysis time variance	-
Mean annual precipitation 1981-2000	North America (NAN, NAS, NAAL), Eurasia (EAW, EAE), Antarctica (WAIS, EAIS)	4σ ERA 5 reanalysis time variance	-
Mean ocean temperature profile 1981-2000	Southern Ocean	70 % within 4σ ERA 5 reanalysis time variance	-
Sea level	global	-	95 % confidence interval Spratt and Lisiecki (2016)

Table 2.2: Mean and standard deviation growth and melt rates for MIS 7d and 5d. Intervals for growth and melt are defined as 2 kyrs long and 1 kyr before and after the max volume is reached.

MIS	Growth rate NA	Growth rate EA	Melt rate NA	Melt rate EA
MIS 7d	2.6 ± 0.8 m/kyr	1.3 ± 0.6 m/kyr	7.0 ± 1.9 m/kyr	1.6 ± 1.0 m/kyr
MIS 5d	2.3 ± 0.4 m/kyr	1.1 ± 0.4 m/kyr	3.7 ± 1.7 m/kyr	0.3 ± 0.2 m/kyr

2.4.2 Phasing of Ice Sheet Volume and Area

To determine the phase relationship between ice area, volume and insolation, and differences in the phasing between the last two glacial inceptions, the inceptions are aligned by their insolation minima and maxima in Figures 2.4 and 2.5 (thin black line for penultimate, thick line for last glacial; note the two time axes at the top and bottom). Figure 2.4 provides the simulated mean ice area per ice sheet with the ensemble standard deviation of the 15 NROY ensemble members, and Figure 2.5 the mean ice volume. Light colours correspond to the penultimate glacial inception with time on the bottom x-axis, and dark colours correspond to the last glacial inception and corresponding time on the top x-axis.

The NA ice sheet (blue shades on left panel in Figures 2.4 and 2.5) is substantially larger than the EA ice sheet (orange shades on left panel in Figures 2.4 and 2.5) throughout MIS 5d-MIS 4 and MIS 7d-MIS 6e. The ice sheets are larger during the penultimate inception than during the last glacial inception, except for the NA ice sheet reaching about the same area and volume at MIS 4 and MIS 6e.

In accord with the relative direct control of maximal ice extent by summer temperature and insolation, the ice area maximum has a small lag behind the summer insolation minimum for the NA, Greenland, and EA ice sheets. The ensemble average ice area maximum lags no more than 500 yrs behind the MIS 5d insolation minimum and 1.4 ka behind the MIS 7d insolation minimum (see Table 2.3). The lag is larger at MIS 4 and 6e, and might be biased since these MIS mark the end of the filtering period, and a few ensemble members display run-away ice sheet behaviour afterward. Henceforth, we concentrate our analysis on MIS 7d and 5d, and to a lesser degree on

MIS 7c-b and 5c-b, leaving the subsequent intervals for a separate publication.

The ice volume maximum lags further behind the ice area maximum. Willeit et al. (2023) find a similar behaviour in their simulations: the ice sheets expand thinly at first, then the ice thickens. Ice thickening compensates for the early area retreat so that the maximum ice volume can be reached after the maximum ice area. This lag is nearly negligible for EA (0 kyrs at MIS 5d, 0.9 kyrs at MIS 7d) but significant for the larger NA ice complex (2 kyrs at MIS 5d, 2.7 kyrs at MIS 7d, Table 2.3). A strong correlation between ice volume and time lag of ice volume behind insolation forcing is especially evident for NA MIS 5d and 4 (see Figure 2.6). In accordance, the smaller EA ice sheet reaches its maximum volume before the NA and shows less lag between maximum ice volume and area.

The Greenland ice sheet's lag of about 2 kyr behind the insolation minimum does not match the corresponding relationship for the more ice-volume proximal EA ice sheet in Figure 2.6 (grey symbols). Instead, its lags approximate match those of the much larger NA ice sheet for MIS 6e, 5d, and 4. We reason that the fast response of the EA ice sheet compared to the NA and Greenland ice sheets to insolation forcing is mainly due to the increased ratio of potential ablation relative to accumulation as quantified by the larger ice margin length to ice sheet area ratio. Furthermore, for the majority of simulations, the EA ice sheet is not one coherent ice sheet. Instead, it consists of a minimum of 3 distinct ice sheets with extensive marine margins that can migrate more quickly than terrestrial margins. Finally the downstream proximity of NA to Greenland implies that the climate response to a large NA ice sheet will also strongly affect Greenland. The factors also likely explain the somewhat larger sub-ensemble variance in the timing of the EA ice sheet area and volume peaks compared

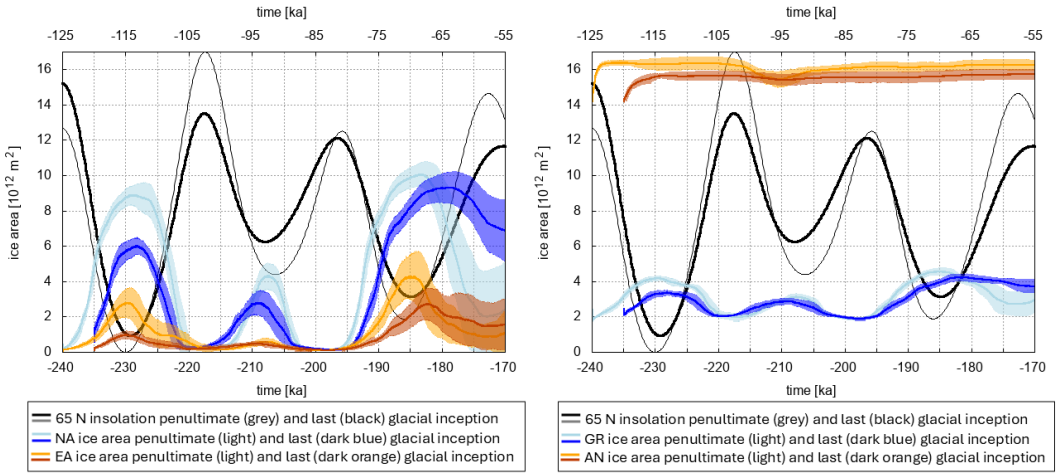

Figure 2.4: NROY ensemble ice area for NA and EA (left), and Greenland and Antarctica (right). Note the top and bottom time axis, aligning July insolation peaks at 65 N for the last two glacial inceptions.

to that of the NA ice sheet.

The Antarctic ice sheet, contrary to the Northern Hemisphere ice sheets, advanced for the first 10 thousand simulation years and then remained at a relatively constant area and volume. This may be due to the present-day tuning of subshelf ocean temperature bias corrections for Antarctica as well limitations in the GSM subshelf melt model. During the penultimate inception (light orange on right panel in Figures 2.4 and 2.5), the Antarctic ice volume and area show a small reduction at 210 ka. This coincides with the highest southern hemisphere summer insolation during the last two glacial cycles (551 W/m^2), which caused the WAIS to retreat.

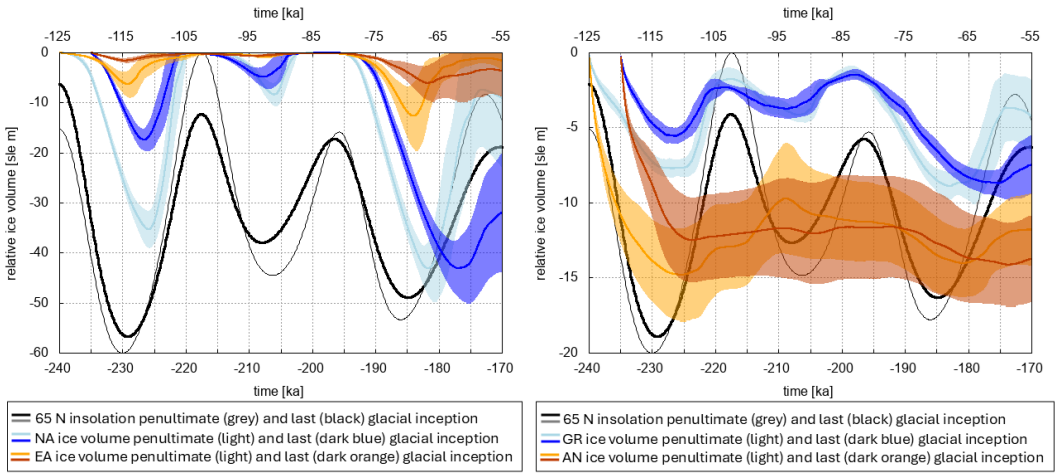

Figure 2.5: NROY ensemble ice area for NA and EA (left), and Greenland and Antarctica (right). Note the top and bottom time axis, aligning July insolation peaks at 65 N for the last two glacial inceptions.

Table 2.3: Timing of insolation minimum and ice area and volume maximum

MIS	insolation min.	EA ice area max.	NA ice area max.	EA ice volume max.	NA ice volume max.
MIS 7d	230 ka	229.8 ± 1.3 ka	228.6 ± 1.3 ka	228.9 ± 1.4 ka	225.9 ±0.4 ka
MIS 5d	114 ka	113.8 ±1.8 ka	113.5 ± 0.7 ka	113.8 ± 1.8 ka	111.5 ± 0.4 ka

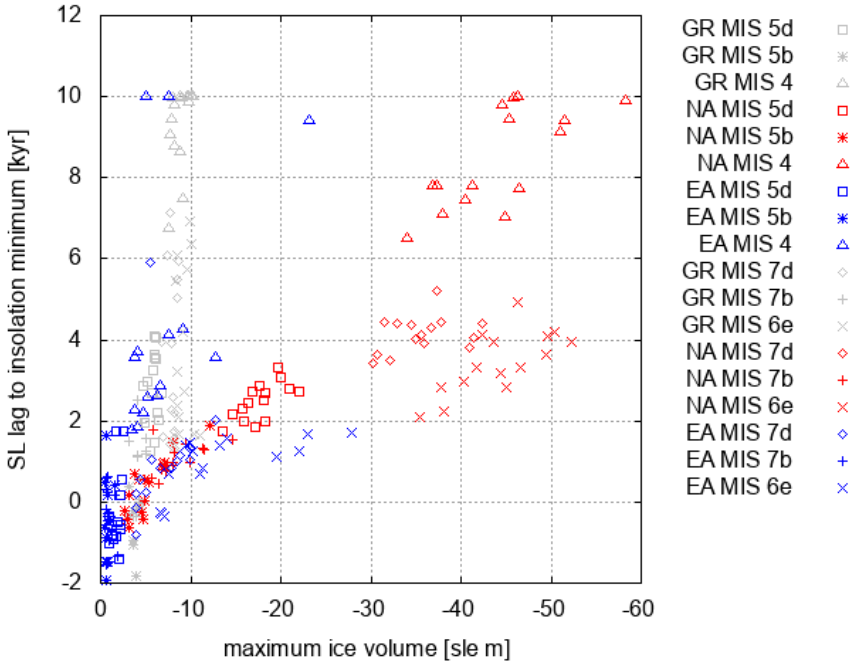

Figure 2.6: NA (red), EA (blue), and Greenland (grey) maximum ice volume for each of the 15 NROY ensemble members at MIS 5d, 5b, 4, 7d, 7b, and 6e and the according time lag between insolation minimum and timing of ice volume maximum

2.4.3 Evolution of extent, location and geometry of the Eurasian and North American ice sheets

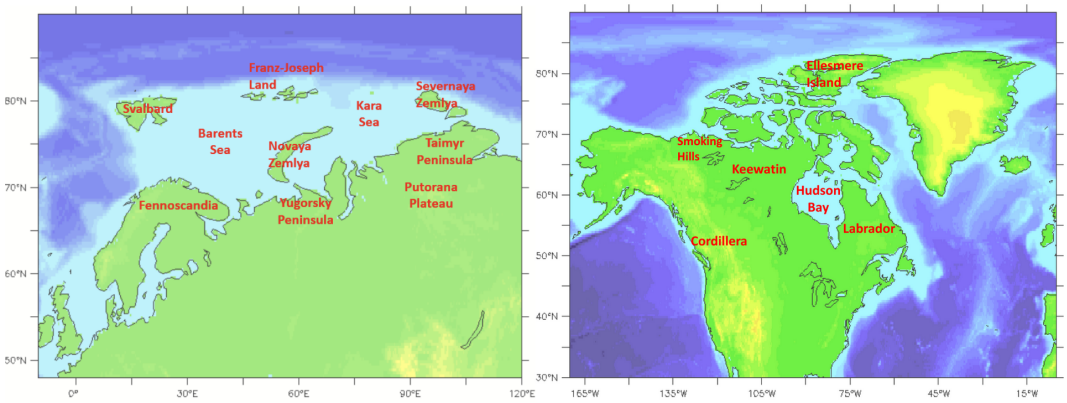

Figure 2.7: Overview of the study areas and names mentioned in EA (left) and NA (right)

While the present-day existing Greenland and Antarctic ice sheets grew during the last two glacial cycles, their advance was spatially restricted by the landmasses. Therefore, we focus solely on the EA and NA ice sheets in this section. For a dynamic display of ice advance and decay of all 15 members from MIS 5d-4 and MIS 7d-6e, see `https://doi.org/10.5446/66195`.

The relationship between ice margin location and summer isotherms is shown in Figures A.3-A.14. During the advance of the NA ice sheet, the simulated southern ice margin approximately aligns with the summer -2°C isotherm (specifically mean June-Aug, JJA, at sea level) in most regions (Figures A.3 - A.14). At maximum extent, the ice margin lies between the -2 and 0°C JJA isotherm. During the retreat phase, the ice margin aligns with or is south of the 4°C JJA isotherm. This warmer isotherm

during retreat is in accord with the varying combinations of thicker marginal ice and higher marginal ice flux during retreat. Ice margins of mountainous regions like the Cordilleran lie south of the aforementioned isotherms, as the isotherms are evaluated at sea level. The EA ice sheet has more extensive marine margins during advance and retreat phases and even during MIS 5d. For these, the simple relationship between ice margin and summer air temperature does not hold given the impact of calving and submarine melt. For the continental margins during MIS 7d ice advance, the same relationship as for the Laurentide ice sheet holds; the ice margin lies between the -2 and 0°C isotherm.

2.4.3.1 The onset of glaciation: Eurasian ice growth from simulation start to MIS 7d and 5d

At onset, the EA ice advance in the simulations begins over areas where ice persists to present-day, including Svalbard, Franz-Joseph Land), and Severnaya Zemlya (see locations in Figure 2.7 and dynamic ice advance in `https://doi.org/10.5446/66195`). The ice then expands beyond the present-day landmasses from the islands into the Barents and Kara Sea. The southernmost margin advances on average 50 m/yr southward from MIS 5e-d and 100 m/yr from MIS 7e-d with a NROY ensemble standard deviation of ± 70 m/yr in both periods (note all instances herein of ± are $\pm 1\sigma$). Following this initial onset of glaciation, the differences between MIS 7d and MIS 5d become evident, as described below.

MIS 7d: This southward spread of ice was more pronounced during MIS 7d, where the maximum ice area was reached at 230 ka in the NROY simulations. All ensemble members have some ice in the Scandinavian Mountains. Over 30 % of

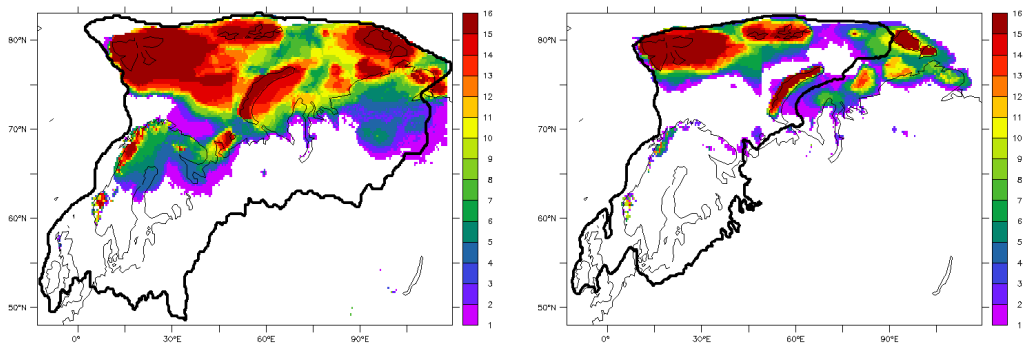

Figure 2.8: Density plot of maximum ice sheet extent over EA at MIS 7d (left) and MIS 5d (right). The colour indicates the number of NROY ensemble members (out of 15) simulating ice over the area. The bias correction over Alaska and Siberia can lead to "artificially" straight boundaries. Black contour lines give a maximum extent estimate. Due to a lack of maximum extent estimates for inception, the glacial maximum extent is displayed for EA: for MIS 7d, the Saalian maximum extent from Svendsen et al. (2004) as an upper limit; for MIS 5d, the LGM ice sheet extent from Hughes et al. (2016).

members have ice cover over the northern half of Fennoscandia and ice down to 65 N in the region of the Taymyr Peninsula (Figure 2.8, left).

Geological data constraining the MIS 7d interval of EA ice are sparse. Astakhov and Semionova (2021) describe marine records dated to MIS 7 in north-central Russia (Volma, Pupkovo settlement). Glaciomarine sediments from the Taimyr Peninsula have also been dated to MIS 7 (Möller et al., 2019b,a). However, age uncertainties for these geological data are, at minimum, ±16 ka, so it is unclear whether these sites date the onset of glaciation (as described in the simulations) or a time several

kyrs before/after. These sites are all situated at or south of the simulated MIS 7d ice margin.

MIS 5d: The simulated southward spread of ice from glacial inception centres over EA was less pronounced during MIS 5d. About 50 % of simulations have ice from Svalbard and Franz-Joseph Land merged, some ice in the north of Taymyr Peninsula, and a few spots in the Scandinavian mountains (Figure 2.8). Most ensemble members have an additional ice dome in the Kara Sea. Ice was largely absent from the Russian and Fennoscandian mainland, with the exception of some small glacial areas in high-latitude areas of Norway.

Geological data spanning MIS 5 are somewhat more abundant, however, precise constraints on the ice margin remain elusive. Geological investigations suggest that MIS 5d glacial initiation may have occurred in the Barents-Kara seas as well as on the Russian mainland, for example, on the high-elevation Yugorski Peninsula as well as the Putorana Plateau (Astakhov et al., 2016). The Barents-Kara ice sheet may have eventually spread southward, merging with the aforementioned ice masses on the Russian mainland as suggested by stratigraphic work from the Taimyr Peninsula, northern Russia and Fennoscandia, all of which have bracketed local ice advance during MIS 5d (Möller et al., 2019b, 2015, 2008). Overall, the most significant discrepancy between available geological data and the simulations is insufficient simulated ice on the Russian mainland. Further in-depth comparisons between our simulations and geological data are not possible given the shortage of geological data through the MIS 5d interval.

2.4.3.2 The onset of glaciation: North American ice growth from simulation start to MIS 7d and 5d

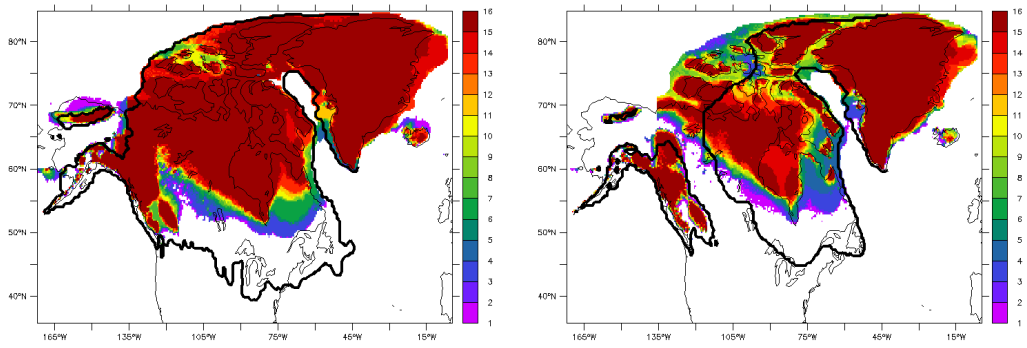

Figure 2.9: Density plot of maximum ice sheet extent over NA at MIS 7d (left) and MIS 5d (right). The colour indicates the number of NROY ensemble members (out of 15) simulating ice over the area. The bias correction over Alaska and Siberia can lead to "artificially" straight boundaries. Black contour lines give a maximum extent estimate. Due to a lack of maximum extent estimates for NA during MIS 7d, LGM maximum extent reconstruction from Dalton et al. (2022) is displayed. For MIS 5d, the reconstruction for 110 ka from Dalton et al. (2022) is shown.

Glaciation in NA starts on Ellesmere Island for all simulations consistent with the primary control of summer air temperature. From there, most simulations have ice subsequently advance over the Arctic Archipelago and Keewatin (see dynamic ice evolution in `https://doi.org/10.5446/66195`). A secondary controlling role for precipitation is partly evident in the few simulations that have additional nucleation over the much higher precipitation region of the Canadian Coastal Mountains.

The NA ice sheet advanced southwards rapidly, with NROY ensemble mean simulated advance rates of 170 ± 40 m/yr at the southernmost margin. Following this initial onset of glaciation, some differences between MIS 7d and MIS 5d become evident, as described below.

MIS 7d: In the simulations covering MIS 7d, the Keewatin Dome extended southward to approximately the boundary of the Canadian Shield and had a thickness of above 3 km (Figure 2.9, left). The maximum ice area is reached at 228 ka. During MIS 7d, all 15 NROY ensemble members simulate a completely ice-covered Hudson Bay and a merged Cordilleran and Laurentide ice sheet in the northernmost sector. Hudson Bay can glaciate very fast (see gif in video supplements: `https://doi.org/10.5446/66195`). Ice appears first in the North of Hudson Bay, including the connection to Hudson Strait, after which the rest of Hudson Bay can glaciate within 1 kyr.

There are presently very few geological data constraining the MIS 7d ice advance over NA. Geological evidence from north-central Alberta does support an active Keewatin ice dome during several parts of the Quaternary (e.g. Andriashek and Barendregt, 2017), but these ice advances are not constrained to specific intervals. The only terrestrial records spanning that interval are located well outside the glaciated region and therefore offer no precise constraint on ice sheet advance (Cheng et al., 2019; Winograd et al., 1992). Nevertheless, it is possible to make some broad comparisons between the simulations and geological inferences. A recent review of the Smoking Hills area, lying adjacent to the MacKenzie River, suggests that the majority of glacial sediments in this area are from the LGM (∼25 k), while some of the oldest constrained via cosmogenic burial dating to an ice advance at 2.9 ± 0.3 Ma

(Evans et al., 2021). Although these data constrain an ice advance significantly earlier than what is covered in this manuscript, they nevertheless support the presence of continental ice in this area prior to the LGM, and, presumably, the merging of the Cordilleran and Laurentide ice sheets at that time. The merging of these two ice sheets prior to the LGM is notable since the prevailing view is that they merged only at the LGM (see Discussion).

MIS 5d: The southward spread of ice from glacial inception centres over northern Canada is less pronounced during MIS 5d in the simulations. The maximum ice area was reached at 113.5 ka, and the simulated Keewatin ice sheet dome reached just below 3 km. During MIS 5d, all but one member have Hudson Bay completely ice-covered (Figure 2.9, right), and none of the 15 NROY members merge the Laurentide and Cordilleran ice sheets.

An estimate of the maximum ice area for this interval (around 110 ka) has been compiled by Dalton et al. (2022), however the measure of confidence in this ice reconstruction is low owing to a shortage of geological constraints. Areas of agreement between the simulation and geological data include ice-free conditions in Atlantic Canada (Vernal et al., 1986; Rémillard et al., 2017). A major area of contrast between the simulations and the geological data is the relative size of the Labrador and Keewatin domes. However, it is important to keep in mind the geological outline in Figure 2.9 represented the maximum ice area for this interval (around 110 ka). Only 4 ensemble members have ice cover over Labrador, but all have ice cover over a large swath of Keewatin. Geologists, however, traditionally suggest glacial inception started in broad high-altitude areas of Northern Labrador owing to prolonged snow cover and increased precipitation (Ives, 1957; Koerner, 1980). This hypothesis

is supported by glacial striae and flowlines indicative of a relatively early expansion of the Labrador Dome to almost the boundaries of the Canadian Shield (Kleman et al., 2010). However, very little of this evidence for glacial inception is directly dated – instead, most is inferential or constrained using indirect dating methods. The lack of a geological inference for early glaciation over Keewatin may simply reflect the paucity of field data over the broad Keewatin area, though recently, more attention has been paid to mapping and geomorphic work in these areas (Campbell et al., 2013; McMartin et al., 2021, 2023).

The 4 ensemble members that grow ice over Labrador during MIS 5d also grow ice furthest south over Labrador during MIS 7d. The ensemble members are characterized by above-average precipitation east of Hudson Bay compared to the rest of the sub-ensemble. Ensemble members with a glacial lobe over Labrador display a retreat pattern where the Laurentide ice sheet retreats from west to east from MIS 7/5d to MIS 7/5c, with the ice over northern Quebec and Baffin Island remaining last. This is similar to that long geologically-infered to have happened for the last deglaciation (e.g. Dyke, 2004). The rest of the ensemble retreats from all edges to the center, with the last ice remaining west of Hudson Bay.

2.4.3.3 Ice evolution through MIS 7c, 7b, and MIS 5c, 5b

The substages c-b during MIS 7 and 5 have minimal geological constraint aside from maximum extent for EA MIS 5b. When available (which is rare, especially for MIS 7), geological data can't be confidently assigned to a specific substage. Moreover, records purporting to document ice extent (ie. striation data) are inferentially dated or constrained using indirect dating methods. For this reason, the discussion of

geological data below is sparse.

Eurasia: During MIS 7c and MIS 5c, over EA, the simulated ice retreated to Svalbard, Severnaya Zemlya and October Revolution Island (Figure 2.10). The ice retreated on average 30 m/yr at the southern margin (with a high ensemble standard deviation of $\pm$ 30 m/yr) from MIS 5d to 5c and more than 3 times as fast from MIS 7d to MIS 7c (100 $\pm$ 70 m/yr). A retreat of ice northward of the Taimyr Peninsula during the MIS 5c interval is documented by the deposition of local glaciomarine sediments that were collected over various years in several studies, but recently reviewed by Möller et al. (2019b,a). Despite clear evidence of ice retreat, the timing of this retreat has low precision, and may have occurred at any time between MIS 5d and MIS 5b. A renewed expansion of ice sheets during MIS 7b and 5b is simulated, however, ice sheets are smaller due to the weak orbital forcing. MIS 7b has slightly larger ice sheets than MIS 5b, in accord with its lower JJA insolation and similar atmospheric pCO_2. The NROY ensemble underestimates global ice volume for MIS 5b compared to the sea level proxy record (Figure 2.3). Some geological studies suggest that the EA ice sheet was (at least in some areas) larger during MIS 5b than MIS 5d (or even infer no MIS 5d EA ice sheet, e.g. Svendsen et al., 2004), contradicting the simulations. However, the reliability of these inferences is unclear. The large majority of the ensemble members only simulate ice over Svalbard, Severnaya Zemlya, Novaya Zemlya and Franz-Joseph Land (Figure 2.12). Olsen et al. (2013) show a slightly larger Scandinavian ice sheet during MIS 5b than 5d (both larger than in simulations). They present no clear reasoning for this difference in size which might be based on geological data from a few sites as well as inferences from adjacent marine records. On the Taimyr Peninsula, on the other hand, Möller et al. (2019b) indicate that ice during MIS 5d was larger than

5b in this region with the ice configuration drawn using information from exposure dating of boulders as well as dating of marine sediments. In the Barents-Kara Sea, Svendsen et al. (2004) suggest a merged MIS 5b ice sheet from Svalbard to the Taimyr Peninsula in the East and Novaya Zemlya in the South, while these remain individual ice sheets in the simulations for both MIS 5d and 5b.

North America: During MIS 7c and 5c, most but not all of the simulated NA ice sheet retreated back (Figure 2.11). The larger NA ice sheet retreated faster than the EA ice sheet with rates of 100 $\pm$ 30 m/yr during MIS 5d-c and 190 $\pm$ 60 m/yr during MIS 7d-c. The retreat of the NA ice sheets during MIS 5c is supported by some geological data. From the periphery of the glaciated region, shoreline deposits on Banks and Victoria islands support ice-free conditions at $\sim$ 100 ka (Causse and Vincent, 1989) and similarly timed ice-free conditions are suggested for some areas of Baffin Island (Briner et al., 2007) as well as Atlantic Canada (Vernal et al., 1986; Rémillard et al., 2017). Evidence from the central region of the former ice sheet also supports ice-free conditions during MIS 5c between 105 ka and 95 ka (Allard et al., 2012; Dubé-Loubert et al., 2013). During MIS 7b, over NA, only 50 % of the NROY simulations have a continuous Laurentide ice sheet that includes Hudson Bay; during MIS 5b the majority of simulations only see ice in the Canadian Arctic islands and northern Nunavut (Figure 2.13). Geological evidence for NA is scant for MIS 5b, and any ice margin estimates for this interval are based largely on undated geomorphic data and/or inferences from the sea level record (Dalton et al., 2022).

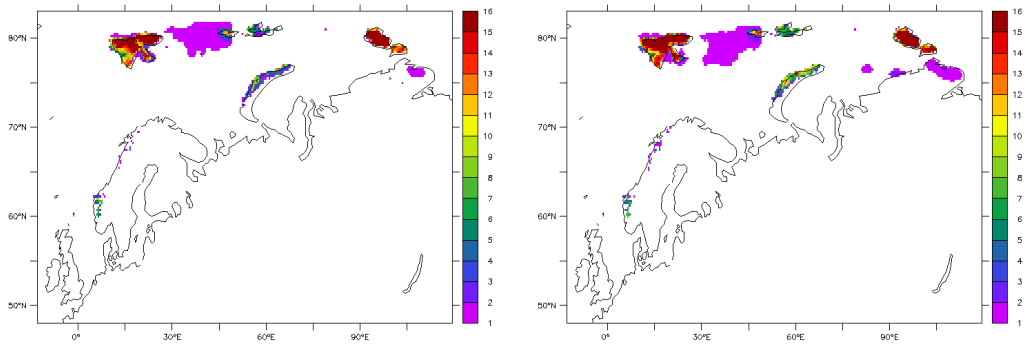

Figure 2.10: NROY ensemble EA ice sheet extent at MIS 7c (left) and MIS 5c (right).

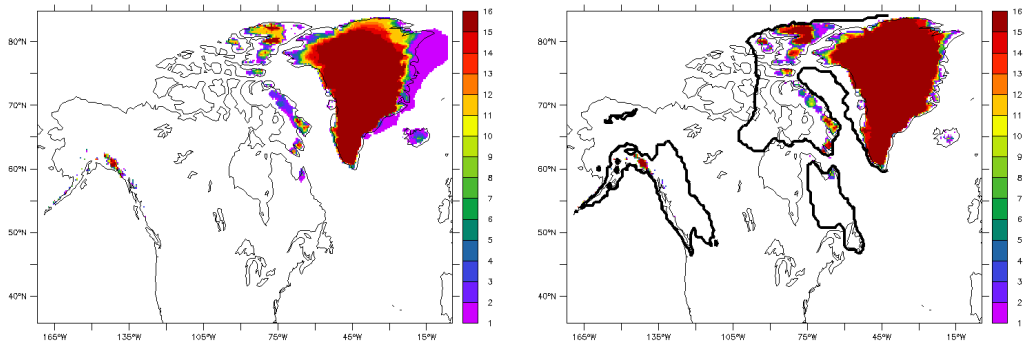

Figure 2.11: NROY ensemble NA ice sheet extent at MIS 7c (left) and MIS 5c (right). Black outline: Maximum ice extent at 100 ka from Dalton et al. (2022) (not available for other MIS).

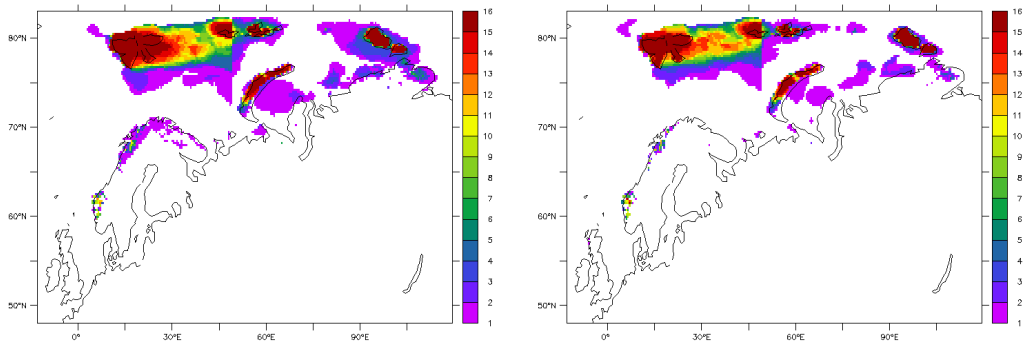

Figure 2.12: NROY ensemble EA ice sheet extent at MIS 7b (left) and MIS 5b (right).

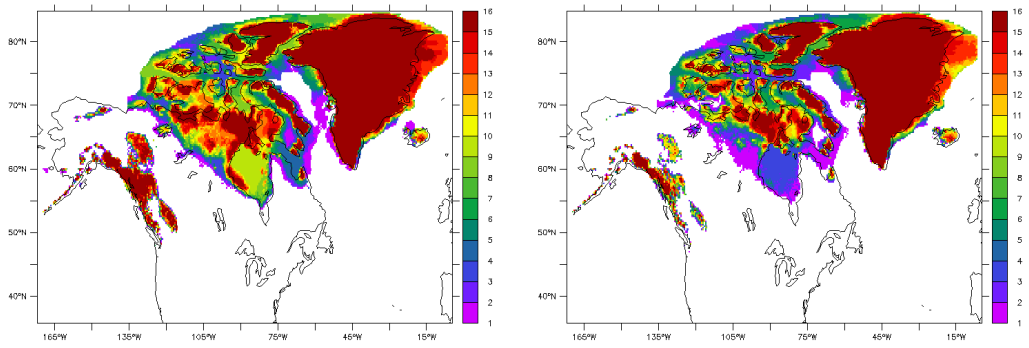

Figure 2.13: NROY ensemble NA ice sheet extent at MIS 7b (left) and MIS 5b (right).

2.4.4 Inter-ensemble variability

Selecting ensemble members with (nearly) the same global ice volume at MIS 7d reveals that different ice sheet configurations are possible for the same global eustatic sea level. Two example ensemble members in Figure 2.14 have the same maximum ice volume at MIS 7d, reached at slightly different times. One member (green) has a larger NA but a smaller EA ice area than the other. The characteristics persist through the last glacial inception. The two members display similar global ice volume at MIS 5d. The green line member shows more ice during MIS 5c,b, and a than the red line member; the same behaviour is displayed for MIS 7c, b, and a. By MIS 4 and MIS 6e, the red member has a larger ice volume than the green member.

Generally, ensemble members display the same behaviour in both glacial inceptions, as seen in the comparison of ice margins for 5 selected members in Figure 2.15. The green ensemble member has the southernmost ice extent in eastern NA and one of the smallest ice areas over EA in both inceptions. The cyan-coloured member has the most continuous ice extent over the Canadian Archipelago in both inceptions. The pink ensemble member has the northernmost ice extent for the Laurentide ice sheet, and the blue ensemble member has the most ice over Scandinavia for both inceptions.

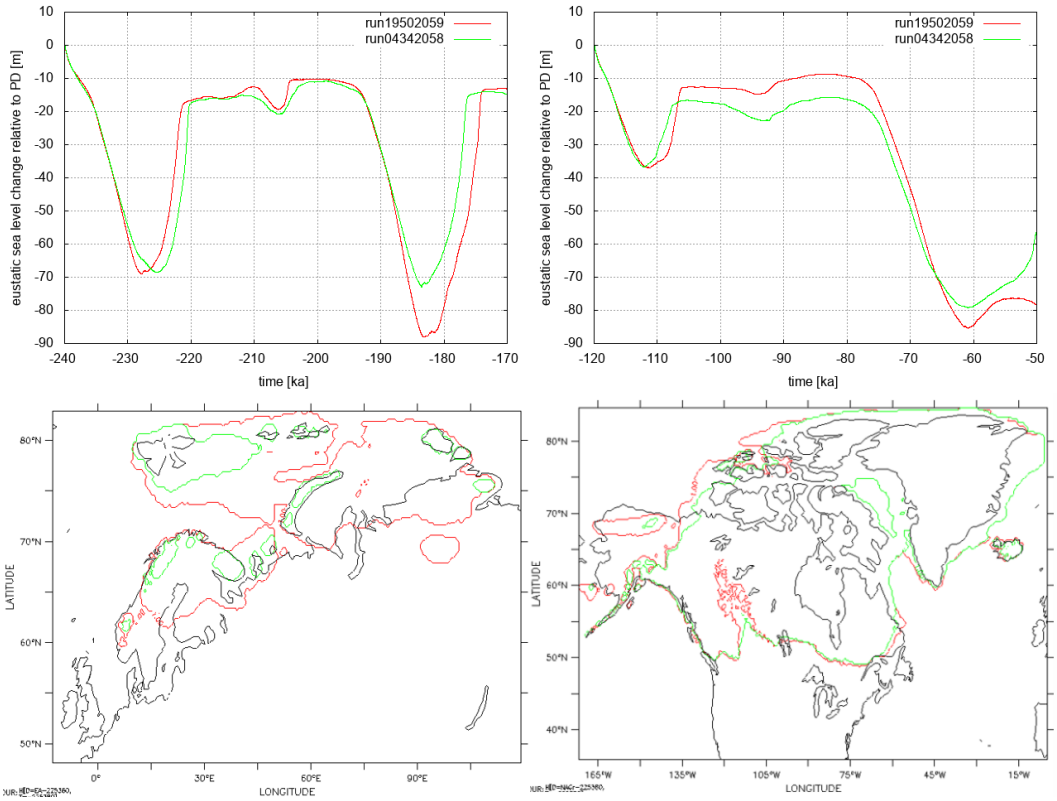

Figure 2.14: Two example NROY ensemble members with similar global ice volume (top) at MIS 7d (left) and MIS 5d (right) but different EA (bottom left) and NA (bottom right) ice sheet extent and geometry.

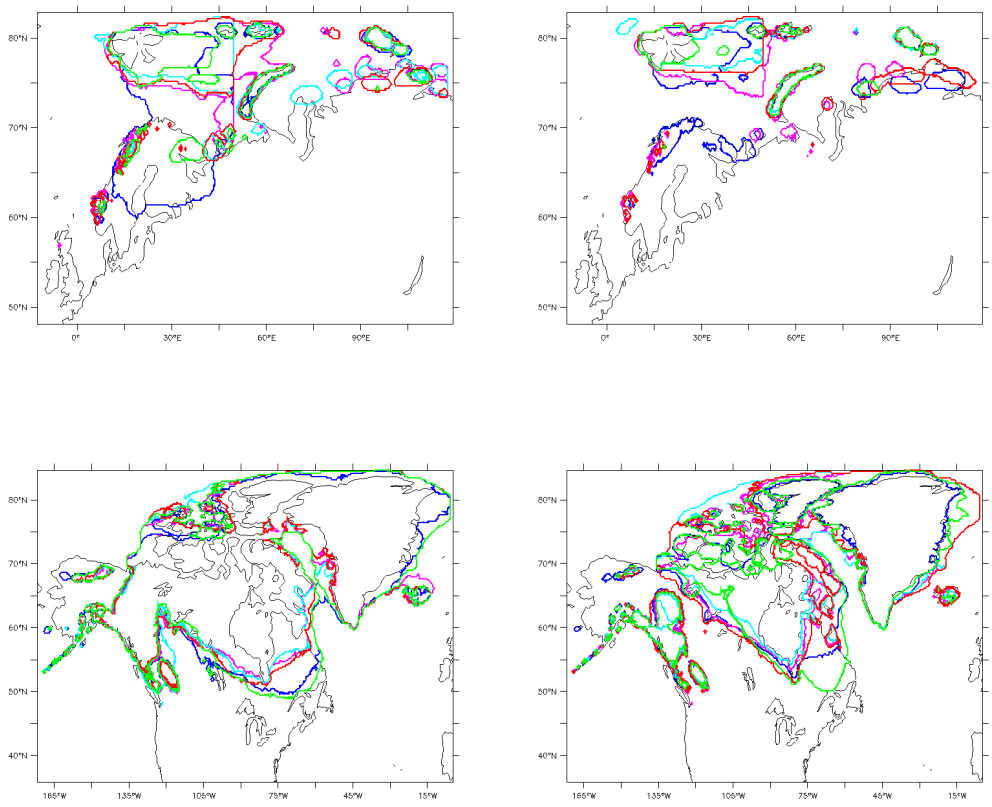

Figure 2.15: Ice margins of several NROY ensemble members indicated in the same colours for MIS 7d (left) and MIS 5d (right).

2.5 Discussion and Conclusion

Herein, we have tested the capability of a fully coupled Earth system model, LCice, to capture the last two glacial inceptions and subsequent interstadials when only forced with orbital parameters and greenhouse gases. We have identified and analyzed an NROY subset of ensemble members that simulate sea level change within the range of proxy uncertainty for MIS 7e-6e and MIS 5e-4. In the following, discussion of key features of the NROY ensemble is tailored to specific audiences.

2.5.1 Insights into ice sheet evolution

Presently, despite some recent efforts to compile geological data, little is known about the evolution of ice sheet extent through the last two glacial inceptions. One of the most extensive compilation efforts was Batchelor et al. (2019), who assembled a large amount of numerical and geological data to give estimates on ice extent in the Northern Hemisphere through various intervals during the Quaternary. Despite their efforts, Batchelor et al. (2019) acknowledge significant unknowns and data gaps in our collective knowledge of Quaternary ice configurations. Moreover, their ice extent estimates often rely on poorly constrained model results that were never designed to probe uncertainties. In another effort, Dalton et al. (2022) used a combination of chronostratigraphic records (often rare), geomorphic data (poorly dated), estimates of global mean sea level (potentially biased in a variety of ways) and previously published ice sheet models to derive outlines of pre-LGM NA ice sheet extent. Taking into account both the work of Batchelor et al. (2019) and Dalton et al. (2022), the reconstructions for MIS 5d, c, and d are all of "low confidence" and the onset of MIS

7 ice sheets are not investigated.

As LCIce has significant sources of unquantified uncertainty (especially on the climate side), the simulation results should not be interpreted as reconstructions. Instead, each individual simulation should be treated as a physically-self-consistent hypothesis. However, ice sheet evolution characteristics that are prevalent across the ensemble have some arguable inferential value albeit subject to the model limitations discussed in the model description above. Where model biases are large, results are more uncertain. The applied PD temperature bias correction is reduced as a function of simulated global mean sea level (relative to present) and model biases still play an unquantified role. This may especially influence results over Quebec (warm PD biases and little simulated ice) and Scandinavia (dry PD bias and little simulated ice). Furthermore, as discussed above, the limited spatial resolution of LOVECLIM will significantly affect its ability to fully capture atmospheric stationary wave changes over EA due to NA ice sheet forcing. This will in turn affect the fidelity of changes in precipitation (storm tracks) and the amplitude of the seasonal cycle, especially in Northern Russia.

2.5.1.1 Growth and retreat rates

Given that the simulations span intervals of ice sheet expansion (7d, 5d, 7b, 5b) and retreat (7c, 5c), the LCice ensemble can provide some physically self-consistent (though incomplete) bounds on rates of ice advance and retreat through the last glacial cycle.

Hudson Bay can transition from an ice free state to full ice cover (grounded ice) within 1000 years in the NROY ensemble (10 of 15 members glaciated Hudson Bay

during MIS 7d within 1000 years). This has relevance for both empirical and numerical workers studying the dynamics of the NA ice sheet evolution and buildup toward the LGM (Dalton et al., 2018; Gauthier et al., 2019; Kleman et al., 2010). Another instance where the rate of ice growth over Hudson Bay is of interest is for the debate surrounding the potential for, and timing of, ice-free conditions during MIS 3 (Dalton et al., 2019; Hodder et al., 2023; Miller and Andrews, 2019). A major concern with the ice-free hypothesis was the feasibility of rapid ice growth over Hudson Bay (along with concerns surrounding chronology, see Dalton et al., 2019). Since LCice simulates that Hudson Bay can glaciate fully in 1000 years, it lends some support to the hypothesis that Hudson Bay may have deglaciated at some point during MIS 3. The rate of deglaciation of Hudson Bay is less enigmatic, and geological deglaciation studies have shown that ice retreated in less than 1000 years (Brouard et al., 2021; Dalton et al., 2023; Gauthier et al., 2020).

Given dating uncertainties, ice sheet advance and retreat rates can only be inferred from geological data over extended time intervals with any confidence. Given the constraint of inception and subsequent interstadial inferred sea levels, the simulations offer plausible and physically-self-consistent estimates of past advance and retreat rates. The NROY ensemble has a mean NA ice sheet advance rate of 170 $\pm$ 40 m/yr at the southern margin during both inceptions, while the NROY EA ice sheet growth rate is 50 $\pm$ 70 m/yr for MIS 5d-c and 100 $\pm$ 70 m/yr for MIS 7d-c. Advance and retreat rates are derived from the latitude of the southernmost ice extent during growth and melt phase. The high standard deviation indicates that advance (retreat) from north to south (south to north) was by no means linear. While the over all ice area increased, the location of the southernmost ice extent can stagnate or even

retreat. Advance rates for ice sheets are not frequently reported in the literature, so it is difficult to compare these data with other studies. The mean NROY NA retreat rate is 100 m/yr during MIS5d-c, and 190m/yr at southern margin during MIS 7d-c (larger ice sheet, faster retreat). The mean NROY EA ice sheet retreat rate is 30 m/yr during MIS 5d-c and 100 m/yr during MIS 7d-c. These retreat rates are similar to the modern retreat of $>$ 100 m/yr seen in some areas of the Atlantic Arctic (Carr et al., 2017) and are comparable to the 50 to 80 m/yr estimate obtained for NA ice sheets by (Dalton et al., 2022).

2.5.1.2 Pre-LGM merging of the northern Laurentide and Cordilleran ice sheets

A characteristic of the NROY simulations is the tendency for the Laurentide and Cordilleran ice sheets to merge in their northern sectors in all of the simulations for MIS 7d (Figure 2.9). This coalescence of the Laurentide and Cordilleran ice sheets contradicts the traditional geological understanding of these ice masses. It is widely believed that they remained independent throughout the Quaternary and merged only during the LGM (Batchelor et al., 2019). Evidence in support of this assertion comes from the stratigraphic records over the Canadian Prairies. Moving westward across the Canadian Prairies, pre-glacial sediments (known as the Empress Group) are overlain only by fewer and fewer tills until they are overlain by only a single till west of Edmonton. In that area, pre-glacial tills date to 30 ka (Young et al., 1994). If one makes the big assumption that previous glacial expansions did not remove previous tills, this suggests that Laurentide ice only advanced to the Rocky Mountains once during the Quaternary, and this must have occurred after 30 ka. However, the results

herein, along with the work of Evans et al. (2021) suggests that the Cordilleran and Laurentide ice sheets may have merged farther northward prior to the LGM.

What could have been the cause of the long-standing separation of southern Laurentide and Cordilleran ice sheets? Herrington and Poulsen (2012), using an Atmospheric General Circulation Model, find that a glacial anticyclone established over their Laurentide ice sheet that transports warm air to the south-western ice margin and keeps the Laurentide ice sheet from merging with the Cordilleran. However, Herrington and Poulsen (2012) use steady-state simulations and lack critical ice-climate feedbacks (e.g. they use a slab ocean). Furthermore, their NA ice sheet doesn't extend south of Hudson Bay. These limitations leave unclear what the impact of such an anticyclone would be under full stadial ice extents. While a weak anticyclone develops over the Laurentide ice sheet in LCice, the strongest winds lie over the ice, and there is no transport of warm air to the south-western ice margin (Figure A.15). A caveat is that LCice's atmosphere might be too coarse and simplified to fully capture this potential phenomenon.

2.5.1.3 Ice sheet extent and isotherm correlation

The alignment of paleo-ice sheet margins with isotherms can help inform past ice sheet extent from temperature reconstructions where there are no geological constraints. During the advance of the NA ice sheet, the simulated southern ice margin aligns with the JJA-2°C isotherm in most areas. At maximum extent, the ice margin lies between the -2 and 0°JJA isotherm. During the retreat phase, the stronger margin ice flux pushes ice margin to or beyond the 4°isotherm. Mountainous regions like the Cordilleran lie south of the aforementioned isotherms, as the isotherms are evaluated

on sea level. The EA ice sheet has largely marine margins during advance and retreat phases and even during MIS 5d. For the continental margins during MIS 7d the same relationship as for the Laurentide ice sheet exists; the ice margin lies between the -2 and 0°JJA isotherms.

2.5.2 Implications for the sea level community

Rates of sea level change derived from proxy records have high uncertainties given the amplification of age uncertainties by the derivative operation. Given the filtering of simulations to be approximately consistent the approximate sea level record, our model derived rates of changes should have relatively high confidence. The simulated mean growth rates are 2.6 ± 0.8 mSLE/kyr for the NA ice sheet building up to MIS 7d and 2.3 ± 0.4 mSLE/kyr to MIS 5d. Net mass loss rates can be more than twice as large, with 7.0 ± 1.9 mSLE/kyr following MIS 7d and 3.7 ± 1.7 mSLE/kyr following MIS 5d. Melt and growth rates are smaller for the EA ice sheet (1.3 ± 0.6 mSLE/kyr and 1.1 ± 0.4 mSLE/kyr leading up to MIS 7d and 5d and 1.6 ± 1.0 mSLE/kyr and 0.3 ± 0.2 mSLE/kyr following MIS 7d and 5d respectively).

Age control prior to the ^{14}C calibration is an outstanding challenge, necessitating, for instance, a reliance on orbitial tuning of marine records. The impact of the age uncertainties are very evident in the different timing of MIS 7d and MIS 5b between the global mean sea level reconstructions of Medina-Elizalde (2013) and Spratt and Lisiecki (2016) shown in Figure 2.1. Given the incorporated physics, the timing of glacial stadial maxima and interstadials in LCIce should be relatively confident for NA and at most slightly advanced for EA given atmospheric grid resolution limitations.

The timing of simulated sea level high/low- stands matches that of the reconstructed sea level at MIS 7d, 7c, 6e, 5d, 5c, and 4 within proxy uncertainties.

The timing of maximum ice volume lags behind the insolation minimum. A correlation exists, where larger ice sheets display a larger lag. However, we reason that this is dependent not only on the size of an ice sheet but also on the ice sheet's geometry. The smaller EA ice sheet has a higher ratio of ice margin (and therefore calving and ablation zones) to ice volume as it consists of several smaller ice sheets during the periods examined here, while the larger NA (as well as Greenland) ice sheet consists of a more contiguous ice sheet. The size of the ice sheet will also come into direct play, given the larger impact of a larger ice sheet on regional climate. This along with geographic proximity to NA also partly explains the larger lag for Greenland compared to EA.

2.5.3 Implications for the modeling community

The fully coupled Earth system model of intermediate complexity LCice can simulate the evolution of ice volume within proxy uncertainty for MIS 7 and MIS 5. However, it is evident that a model's capability to simulate present-day climate is insufficient to predict its performance in simulating glacial inception, as only a small fraction of ensemble members performed well for both glacial inceptions. Furthermore, capturing sea level change well in one inception does not predict the same outcome for the other. Nevertheless, an ensemble member's overall behaviour (regarding ice sheet size and geometry) is similar in both simulation periods (Figure 2.15). Therefore, an ensemble member that displays excessive ice growth still within the bounds in one

inception might display the same behaviour slightly stronger in the other inception and miss the bounds of the accepted range. We do not see contrasting ice volume behaviour of one and the same ensemble member in the two inceptions. However, at the same simulated eustatic sea level, ensemble members can display different ice sheet configurations (Figure 2.14). This has high relevance for the selection of ice sheet boundary conditions for paleoclimate modeling, especially since deglacial ice sheet reconstructions are often used for pre-LGM boundary conditions by matching sea levels. Our ensemble results challenge the validity of this approach.

Simulating ice-free Alaska and Siberia during glacial inceptions remains difficult, as previous studies have shown (Bahadory et al., 2021; Ganopolski et al., 2010; Bonelli et al., 2009). Compared to previous studies employing an earlier version of LCice (Bahadory and Tarasov, 2018; Bahadory et al., 2021), this current model version improves the simulation of the expected NA ice sheet geometry, at least in part due to the imposition of present-day bias corrections. However bias corrections are a bitter pill, with limited justification for modeling climate response to large changes in radiative forcing and boundary conditions. This a core challenge for all coupled paleo ice-climate modeling as even the advanced General Circulation Models that participated in the recent CMIP6 have signficant regional present-day temperature and precipitation biases (e.g. Fan et al., 2020). It remains an open question how these biases should be addressed over glacial intervals for coupled ice and climate model at any level of computationally tractable complexity.

To build confidence in the detailed simulated evolution of coupled ice and climate, there is a need for effectively higher climate model resolution (equivalent to T42 or higher as discussed above) and complexity, which is beyond commonly avail-

able computational resources. A possible solution is the development of alternative fast climate models perhaps combining physics informed deep learning with reduced complexity climate models.

Chapter 3

Transient simulations of fully coupled global ice-climate evolution over the last two glacial cycles

3.1 Abstract

We present a small perturbed parameter ensemble of transient simulations for the last two glacial cycles with the fully-coupled ice sheet/Earth system model LCice. LCice has all key feedbacks between ice and climate (except dust), interactively simulates all major ice sheets (Greenland, Antarctica, North America, Eurasia), and is only forced by orbital parameters and greenhouse gases. This ensemble has been filtered according to consistency with present-day climate and capture of the last deglacial

interval. This is the first study with a model of this level of complexity that uses ensemble simulations and that transiently simulates ice-climate co-evolution for more than one glacial cycle.

The filtered ensemble of simulations approximately intersects (and in places fully covers) inferred eustatic sea level uncertainty bounds over time except for one key exception. At the Marine Isotope Stage 6d (MIS 6d) interstadial, the ensemble deviates significantly from the inferred sea level record: the ensemble simulates a near complete ice retreat to present-day configuration, while the sea level record suggests only a weak interstadial. Conversely, at the comparable MIS 3c (insolation is $\sim$ 20 W/m higher at 65°N but $CO_2 \sim 10$ ppm lower during MIS 6d than MIS 3c), the ensemble high-stand is somewhat lower than inferred from sea level proxies. All simulations that do capture the inferred MIS 6d sea level grow too much ice at glacial maximum and fail the MIS 1 filter. These results suggest a possible low sea level bias in the MIS 6d interval for inferences from benthic proxy records.

The temporal pattern of evolution of inferred temperature at ice core locations (NGRIP, EDC) and deep ocean temperature (at 3 well spaced marine sediment core sites) is largely captured by the simulations. Aside from insufficient amplitude, the main discrepancy is a lack of millennial scale (Dansgaard-Oeschger) variability for the NGRIP site with the model approximately following interstadial values of the NGRIP record when scaled to match the 20 ka to present interval. The annual simulated temperature with seasonal precipitation-weighting (reflecting the seasonal weighting in snow deposition and therefore associated isotopic signature) has a significantly higher amplitude ($\pm$ 4 °C) at NGRIP than the nominal (un-weighted) annual mean. The results can therefore aid deconvolution of ice core isotopic records for extraction

of mean annual regional temperature changes.

The Atlantic Meridional Overturning Circulation (AMOC) of the simulations has a higher variability during the penultimate than during the last glacial cycle likely due to higher rates of ice mass loss during some stadial to interstadial transitions. During the penultimate and last termination, AMOC collapses, comparable to Heinrich stadial 1. There are no signs of other Heinrich stadials or Dansgaard-Oeschger oscillations in the ensemble.

Our simulations also inform how internally robust the evolution of the last two glacial cycles is, as represented in a coupled model. A few key features emerge. First, just capturing last glacial inception with a fully coupled model does not guarantee capture of a subsequent glacial maximum and termination. Nor does capture of a full glacial cycle guarantee capture of the subsequent or preceding glacial cycle. Regionally, the most evident sensitivity is that of the whole last glacial cycle evolution of the Antarctic ice sheet to its internal state during the last interglacial.

3.2 Introduction

Glacial cycles are marked by relatively large and at times relatively abrupt system changes. Therefore, they pose a key challenge and opportunity for increasing collective understanding of the Earth system. However, prior to the Last Glacial Maximum (LGM), there are few high latitude terrestrial records of ice and climate (e.g. Batchelor et al., 2019) due to subsequent glacial erosion. For the Eurasian (EA) ice sheet there are geologically-based compilations of the maximum ice sheet extent for the last 4 major stadials (Svendsen et al., 2004), while for the North American (NA) ice extent,

little is confidently known about pre-LGM ice sheet states outside of interglacials (Batchelor et al., 2019).

Beyond the geographic bounds of the LGM ice extent, paleoclimate records are much more available. When considering transient evolution through a glacial cycle, continuous paleoclimate records from ice, marine, and lake cores are especially valuable. However, a long-known challenge in interpreting continuous paleoclimate records is the uncertain impact of the non-resolved changes in seasonality. Ice core records, for instance, are effectively weighted by precipitation seasonality but there is no direct means to infer changes in such seasonality (Persson et al., 2011). A further challenge is that orbitally forced changes in temperature seasonality are often not resolvable. And yet, the impact of changes in temperature on ice sheets and biological systems tends to have a strong seasonal dependence. Case in point, ice sheet evolution is most sensitive to summertime temperature and yet paleo ice sheet modelers have long relied on the use of nominally mean-annual glacial indices derived from ice core isotopic records for climate forcing (e.g. Buizert et al., 2018; Kageyama et al., 2021).

A key motivation for paleoclimatology is to understand the drivers of past Earth system change. This is partly inferred on the basis of relative phasing between paleoclimate records and Earth system forcings. However, beyond the carbon-14 calibration range (and the layer counting range for ice cores), dating uncertainties grow from the multi-kyr range onward. As such, it is for instance unclear when the stadial maximum ice volume occurred for last glacial inception, and even how close to synchronous it was between major ice sheets (Risebrobakken et al., 2007).

Given the data limitations, the paleo community often looks to models to comple-

ment inferences from paleodata. This has its own deep challenges. First, the required computational resources for a glacial cycle simulation with a current generation climate model is not presently feasible. Secondly, it is unclear to what extent even current generation climate models could capture the last glacial cycle when fully coupled with ice sheet models. Skepticism is justified given the large variance in PMIP 4 LGM simulation results (Kageyama et al., 2021) and ongoing challenges that current generation climate models have in accurately capturing present-day precipitation below continental scales (e.g. Ayugi et al., 2021; Li et al., 2022; Vicente-Serrano et al., 2022).

A reliance on modeling for inferring past ice and climate co-evolution can also go astray when certain assumptions are (generally implicitly) made. Crudely, this is the assumption that a high resolution full complexity Earth System Model that faithfully simulates present-day should capture the last glacial cycle. Concretely, if a climate model can "reasonably" capture present-day temperature seasonality and precipitation, how likely is it to capture the last glacial cycle when coupled to an ice sheet model? It is not even clear to what extent a "perfect" model would give the exact past, given that this assumes that past ice and climate evolution is dynamically robust and that some appropriately timed addition or subtraction of climate noise (e.g. the climate system perturbation from a major volcanic eruption) could not significantly change past ice-climate co-evolution.

It is also unclear to what extent capture of inferred ice and climate co-evolution (as represented by a few critical continuous ice core and marine records) can itself constrain a coupled ice and climate model.

Another challenge for pre-LGM paleoclimate modeling is the required specification

of ice sheet boundary conditions. The tendency in the community has been to match ice volumes as inferred from marine global mean sea level proxies against a much more constrained deglacial ice sheet chronology and use the latter (e.g. Merkel et al., 2010; Muri et al., 2012). To date, it is unclear to what extent such mix and matching is justifiable.

We aim to address the above context as follows. Firstly, the issues above imply that a modeling approach must be ensemble based. Rather than capturing "one reality" (this reality inferred from limited proxy data with high uncertainties), we aim to bracket reality. Secondly, given available resource limitations, we use the fully-coupled Earth System Model of Intermediate Complexity (EMIC) LCice. Given the use of an EMIC, we provide clear guidance on what aspects of our results have more confidence and which have less.

Few research groups have to date published transient simulations with fully-coupled intermediate to advanced complexity Earth system models covering time periods prior to the last glacial cycle. Ganopolski and Brovkin (2017) employed CLIMBER-2 to simulate the last 4 glacial cycles. CLIMBER-2, using a 2.5-dimensional statistical-dynamical atmosphere and a zonally averaged ocean, is significantly more simplified than the model used in this study. They only test two different model configurations with which they roughly capture the overall sea level and CO_2 change, but spend little time analyzing ice sheet extent and climate metrics in comparison to data. On the other hand, they achieve the to date only approximate capture of past glacial cycles by an Earth system model using its own carbon cycle to provide the required CO_2 forcing. Choudhury et al. (2020) used LOVECLIP (LOVECLIM-PSUIM) to simulate penultimate glacial inception from MIS 7e-6d. The sensitivity

to 2 parameters was tested but only the base parameter vector is analyzed in more detail. The simulation captures overall sea level change but lacks variability during MIS 7c-a compared to that inferred from sea level proxy records (e.g. Spratt and Lisiecki, 2016).

In this study, the fully-coupled EMIC LCice is employed for ensemble simulation of the last two glacial cycles. Simulations starting at MIS 7 and MIS 5 are both run to present-day.

Through this, we address the following questions: 1) To what extent is past ice and climate co-evolution robust, at least with respect to constrained model configuration? Furthermore, to what extent does memory of the penultimate glacial cycle affect subsequent last glacial cycle evolution? 2) To what extent does approximately capturing the glacial cycle sea level record constrain a coupled ice/climate model? Expanding this further, does capture of last glacial inception and subsequent retreat guarantee capture of the rest of the glacial cycle? 3) What is the likely timing of past (pre-LGM) major stadial stages of the last two glacial cycles? And how synchronous is each ice sheet to this timing? 4) Given the uncertainties in inferring past global mean sea level, to what extent may the mean inferences be biased, especially with regards to the nominal mean chronologies? 5) How does the seasonality of snow accumulation bias isotope-based inferences for regional mean annual temperature for the NGRIP and EDC ice core locations?

3.3 The model LCice 2.0

LCice (Bahadory and Tarasov, 2018) couples the Earth system model of intermediate complexity LOVECLIM (Goosse et al., 2010) with the Glacial System Model GSM (Tarasov, in prep.). The GSM is a 3-dimensional thermo-mechanically coupled ice sheet model with hybrid shallow ice and shallow shelf physics on a spatial resolution of 0.5^o longitude by 0.25^o latitude for the Northern Hemisphere and 20 km (polar stereographic grid) for Antarctica. All major ice sheets (Greenland, Antarctica, North America and Eurasia) are included. The LOVECLIM components used in LCice are the atmosphere ECBilt, the ocean CLIO and the vegetation VECODE.

VECODE has 3 land surface types, trees, grass and desert and is only coupled to the atmospheric component.

ECBilt is a quasi-geostrophic atmosphere at a spectral resolution/truncation of T21 and 3 vertical layers. The LCice coupler passes climatologies of monthly mean and standard deviation 2 m temperature and wind fields, along with monthly mean precipitation, evaporation and lapse rate to the GSM. The temperature climatologies are downscaled to the higher resolution GSM using the LOVECLIM derived lapse rate. Precipitation downscaling includes an orographic correction (Bahadory and Tarasov, 2018). A precipitation bias correction and a (glacial index based) transient temperature bias correction based on present-day (PD) simulations are added to the LOVECLIM fields. The coupler passes the updated GSM ice mask and topography back to ECBilt. Topography upscaling from the GSM to ECBilt grid is controlled by a model parameter (simple, envelope or silhouette upscaling scheme).

CLIO is a general circulation ocean model with a 3°x3° horizontal resolution and

20 vertical layers. The coupler passes the CLIO upstream ocean temperature profile to the GSM for sub-shelf melt calculation. The coupler passes GSM freshwater amounts and injection location back to CLIO. The coupler also controls the amount of water that flows through the Bering Strait as a function of GSM computed local sea level.

LCice is forced only by orbital parameters and greenhouse gas chronologies (Bereiter et al., 2015). Initialization starts with PD ice sheets. The simulations presented in this study use 4x accelerated coupling (5 simulation years in LOVECLIM, followed by 20 years in the GSM).

A key strength of LCice is the coupling between climate and ice components which includes all key feedbacks and its full complexity ocean model (in contrast to the zonally averaged or frictional geostrophic models more typical of EMICS, e.g. as in CLIMBER 2 Willeit et al., 2022). The model's main limitations are a combination of simplified process representation and limited spatial resolution. The atmosphere ECBilt is suitable for capturing large (synoptic) scale mid-latitude atmospheric circulation but cannot resolve small-scale, tropical or mesoscale convective systems (Goosse et al., 2010). The constrained spatial resolution of ECBilt will further limit its capacity to represent atmospheric wave dynamics which are important for the influence of NA ice sheet forcing on EA ice evolution and associated changes in precipitation (Andres and Tarasov, 2019; Lofverstrom and Liakka, 2018). As such, the detailed spatial evolution of Eurasian ice sheet in LCice likely has the largest errors.

Arguably the most confident aspect of the ensemble is the timing of ice sheet response, given the following reasons. Firstly, the uncertainties in orbital and greenhouse gas forcing are small and the model has the core physics to calculate ice-climate evolution. Secondly, the largest sources of phase lags to orbital forcing, i.e. the oceans

and ice sheets, are the most complete and advanced parts of LCice. Thirdly, the ensemble approach partly offsets model limitations, especially when designed to bracket system behavior.

3.3.1 Ensemble initialization

All ensemble members have previously been filtered for consistency with PD climate. Any member used here passed PD sieve conditions for simulated temperature seasonality, annual precipitation, and Southern Ocean temperature to lie within 4 standard deviations of ERA 5 (Hersbach et al., 2020) and ORAS 5 (Copernicus, 2021) reanalysis data.

Simulations covering the last glacial cycle (in the following referred to as "MIS 5 ensemble set") start at MIS 5e (122 ka). They undergo an uncoupled spinup, where LOVECLIM spins up for 2 kyrs under constant MIS 5e orbital and greenhouse gas conditions. Then, the GSM spins up for 7 kyrs using the constant MIS 5e LOVECLIM climate as boundary condition. Furthermore, the GSM has an internal thermodynamic iteration to partially spinup existing ice sheet temperature fields. Previous experiments have shown that the model has a tendency to grow slightly too much ice. The long GSM spinup gives an opportunity to immediately eliminate ensemble members that grow excessive amounts of ice (more than 20 m sea level change) under the interglacial 122 ka forcing. Ensemble members that have not been eliminated are used to simulate the full last glacial cycle as well as the last two glacial cycles. The 2 cycle simulations are in the following referred to as "MIS 7 ensemble set". The GSM spinup procedure is shortened for the MIS 7 set as ensemble parameter vectors

have already been pre-filtered in the MIS 5e spinup. LOVECLIM is spun up for 2 kyrs under constant MIS 7e (240 ka) orbital and greenhouse gas conditions and then instantly coupled to the GSM. The GSM initializes with PD ice sheets.

Each ensemble set consists of the same 56 perturbed physics members that passed PD filtering and GSM spinup bounds.

3.4 Results and Discussion

3.4.1 Eustatic sea level compared to reconstruction

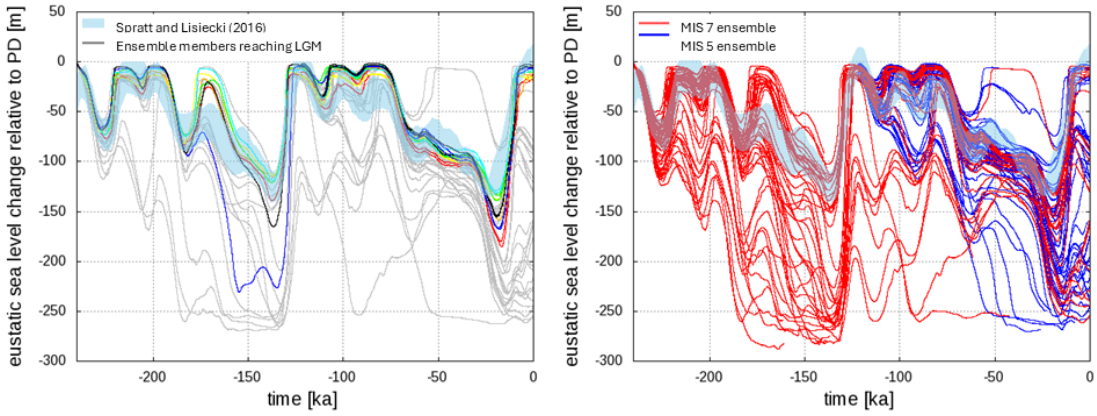

Figure 3.1: Eustatic sea level evolution. Left: the sub-ensemble that reaches LGM (gray) and that passed filtering for PD sea level (colours). Right:the full MIS 7 ensemble (red) and MIS 5 ensemble (blue). Light blue shading: 95 % confidence range of sea level reconstruction by Spratt and Lisiecki (2016)

The analysis only uses ensemble members that reach to at least 16 ka (to fully include LGM) in both the MIS 5 and the MIS 7 set. Many ensemble members become

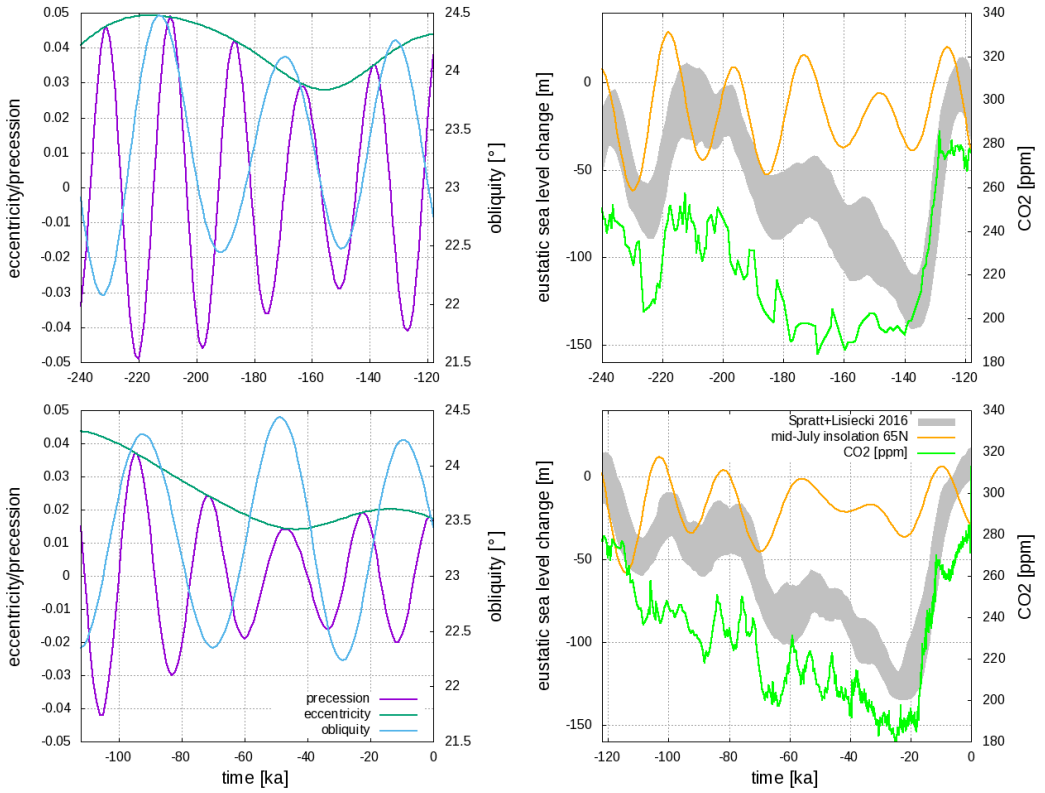

Figure 3.2: Left: Orbital parameters (Berger, 1978). Eccentricity and Precession on the left y-axis, obliquity [°] on the right y-axis. Right: 95 % confidence interval for sea level reconstruction (Spratt and Lisiecki, 2016) on the left y-axis [m], numbers indicating Marine Isotope Stages, 65 °mid-July insolation resulting from the variation in orbital parameters, and CO_2 record (Bereiter et al., 2015) on the right y-axis (right) [ppm] for the penultimate glacial cycle (top) and last glacial cycle (bottom)

unstable and crash, especially for the long MIS 7 set, therefore only 21 members (identical for the MIS 7 and MIS 5 ensemble set) are left for analysis. Subsequent application of a PD sea level filter (PD sea level at end of glacial cycle simulation $\leq$ -20 m) leaves only 7 members. Fig. 3.1 shows the complete ensemble to the left and the subsets of members reaching LGM (in gray) and PD-filtered members

(in colours) to the right. The majority of ensemble members are sieved out due to a too weak deglaciation after the LGM. The remaining 7 members capture the overall amplitude and timing of sea level low and high-stands according to sea level reconstructions (Spratt and Lisiecki, 2016). Compared to Choudhury et al. (2020), the stadial-interstadial variability during MIS 7 is captured well in the ensemble. Sea level evolution across the last glacial cycle is similar for the same ensemble members of the MIS 7 and the MIS 5 set (displayed in the same colour in Fig. 3.1). The mean LGM sea level simulated by the MIS 7 set (in the following referred to as "LGM 2") and by the MIS 5 set (referred to as "LGM") lies with -148 $\pm$ 18 mESL (meters eustatic sea level) and -153 $\pm$ 18 mESL, respectively, slightly below sea level reconstructions (-134 to -100 mESL, Spratt and Lisiecki, 2016). The PGM sea level lies with a mean of -129 $\pm$ 38 mESL well within sea level reconstructions (-140 to -109 mESL, Spratt and Lisiecki, 2016).

The gray lines in Fig. 3.1 (right) show that capturing the inferred glacial inception sea level change does not guarantee capture of the inferred glacial maximum. Many ensemble members capture sea level up to MIS 6e and MIS 4, respectively, but largely overestimate sea level change at PGM and LGM. On the other hand, outlier behavior for one time frame does not necessarily mean that the ensemble member will remain far off the expected sea level evolution for the remainder of the simulation. One excluded ensemble member in the MIS 7 set simulates about double the amount of sea level change than expected for PGM (blue in Fig. 3.1, right). By the following interglacial, however, this member simulates sea level in line with the other ensemble members.

The largest difference between the simulated and reconstructed sea level is the

interstadial MIS 6d around 170 ka. The ensemble displays a strong interstadial with sea level close to PD, while the sea level reconstruction suggests a maximum of -50 mESL. The "equivalent" interstadial in the last glacial cycle record, MIS 3c around 55 ka, is almost non-existent in the ensemble. This discrepancy is not explained by CO_2 values as they are low during both interstadials, and approximately 10 ppm higher during the weak interstadial at MIS 3c. The insolation forcing (at 65°N in summer), however, is 20 W/m^2 higher during MIS 6d than MIS 3c (see Fig. 3.2), triggering the near complete retreat of the NA and EA ice sheets. All simulations that would capture the weak MIS 6d interstadial as suggested by the sea level record grow significantly too much ice at PGM and LGM and cannot melt the ice at the interglacials MIS 5e and PD (see gray lines in Fig. 3.1). This suggests there may be a bias in the sea level reconstruction for this interval.

The nature of all persistent sea level differences between the filter ensemble and the Spratt and Lisiecki (2016) reconstruction (Fig. 3.1) are not collectively consistent with a strong model warm, or cold, bias. For instance, the MIS 6d discrepancy, previously discussed, precludes a dominant cold bias. Conversely, for both LGM and MIS 6e stadial, the ensemble is wholly biased to the low sea level side of the reconstruction uncertainty range and as such is not consistent with a dominant model warm bias. For a similar summertime insolation and about a 6 ppmv difference in CO_2, the ensemble fully covers the PGM uncertainty range but is biased to lower sea level at LGM, extending beyond the reconstructed lower bound. As such, this is inconsistent with a dominant over or under sensitivity to radiative forcing. A more definitive analysis would focus on the more relevant rates of sea level change, and more carefully separately factor out CO_2 and insolation. We therefore do not

rule out ensemble biases, only that whatever biases there are, they do not linearly dominate based on comparison to the Spratt and Lisiecki (2016) reconstruction.

3.4.2 Two glacial cycle continuous records

We present a comparison of modeled climate statistics against a selective representative set of proxy records. In Figure 3.3, ensemble mean and standard deviation are displayed in red, corresponding to the left y-axis, and proxy records in blue, corresponding to the right y-axis. As there are minimal differences for these specific records between the MIS 7 and MIS 5 ensembles, we only present the continuous, 2 cycle simulations of the MIS 7 ensemble (excluding the ensemble member that substantially overestimated PGM ice volume, blue in Fig. 3.1).

AMOC strength:

Ensemble AMOC strength significantly decreases or even collapses during terminations (after PGM and LGM). The collapse lasts approximately 5 kyrs. Besides the pronounced collapse after the LGM, there is little AMOC variability during the last glacial cycle. Individual events like the Younger Dryas or Heinrich Stadial 1 and 2 can not be identified during the last termination. The ^{231}Pa / ^{230}Th ratio from a North Atlantic sediment core off the coast of Florida (Süfke, 2019) is a proxy of circulation strength. The simulated AMOC collapse after LGM is in accord with the Pa/Th record. However, the record shows strong variability compared to that of the model. Furthermore, the proxy record suggests that AMOC strength was decreased during LGM compared to PD. In the simulations, AMOC is strengthened at glacial maxima. This agrees with the large majority of PMIP 3 and 4 models (Sherriff-Tadano and

Klockmann, 2021), but not proxy data (Lynch-Stieglitz, 2017). It remains unclear if this is a general model structural issue or a problem with the proxy-based inference.

During the penultimate glacial cycle, stadials and interstadials are more pronounced than during the last glacial cycle, causing higher AMOC variability during the penultimate than during the last glacial cycle. The ice sheet retreat between $\sim$ 225 - 215 ka and $\sim$ 180 - 170 ka adds about 60 m sea level equivalent of freshwater to the oceans, leading to a near-collapse of the AMOC. During the last glacial cycle, there is no ice retreat event of the same magnitude outside of the last glacial termination. The penultimate cycle also displays a larger inter-ensemble variability, especially during the periods of reduced AMOC strength.

NGRIP and EDC temperature:

The amplitude of temperature variations at NGRIP and EDC ice core locations from PD to glacial maximum is too small in LCice. Temperature reconstructions from boreholes suggest about 23 °C of variation for Greenland (Dahl-Jensen et al., 1998) and about 11.3 °C for Antarctica (Brook and Buizert, 2018). The LCice ensemble mean simulates approximately 16 and 5 °C respectively. However, LCice can capture the pattern of temporal evolution of temperature change within a glacial cycle compared to that of the temperature proxies δ^{18}O from the NGRIP ice core in Greenland and δD from the EDC ice core in Antarctica. The δ^{18}O record and to a smaller degree the δD record display temperature oscillations related to Heinrich and Dansgaard-Oeschger events during MIS 3. These are not evident in the simulated temperatures (not even for individual members). For Greenland, the ensemble mean precipitation-weighted temperature history follows the δ^{18}O interstadial values from MIS 4 to LGM. During MIS 5c-a the ensemble is relatively warmer than the δ^{18}O

record. Similarly, for Antarctica, the ensemble temperature follows the interstadial δD values for MIS 6. The last interglacial Antarctic temperature is underestimated in the ensemble.

The precipitation-weighted temperature and therefore the isotope record has a larger signal than the nominal annual mean (red vs. orange in Fig. 3.3). Last interglacial maximum and penultimate stadial temperatures are approximately 4 °C higher in the precipitation-weighted record. This therefore needs to be taken into account when using isotopic records from ice cores for annual mean temperature estimation.

Our results raise one further possible complication in interpreting regional climate variation from Greenland ice core records. Ensemble NGRIP temperature has limited sensitivity to AMOC strength. Simulated NGRIP temperature continues to increase during terminations even when AMOC strength is significantly reduced (e.g. around 220 ka) or even collapsed (e.g. 10 ka). However, as our simulations lack the requisite millennial scale variability in the isotopic record that is commonly understood to reflect AMOC variations, it is more speculative as to whether this discrepancy would carry over to such a context (especially given the lack of a plausible alternative to AMOC variations for driving the strong millennial scale variability in the ice core isotopic records).

Deep ocean temperature:

For both Pacific marine record locations in Fig. 3.1, the last interglacial relative warming of the deep ocean is underestimated in the model compared to reconstructions. Furthermore, the records show a temperature "overshoot" in the Holocene that is not seen in the model. The relative warming of the equatorial Atlantic site

is captured by the ensemble, however this is with a phase delay resulting in the ensemble warming only peaking at the end of the Eemian at approximately 120 ka. The only other main relative discrepancy is an ensemble warm bias for the equatorial site during most of the first 40-50 kyr of each glacial cycle. Conversely, the relative temperatures for the ensemble are mostly consistent with the 3 marine records for the MIS 6 and MIS 4 to MIS 2 intervals.

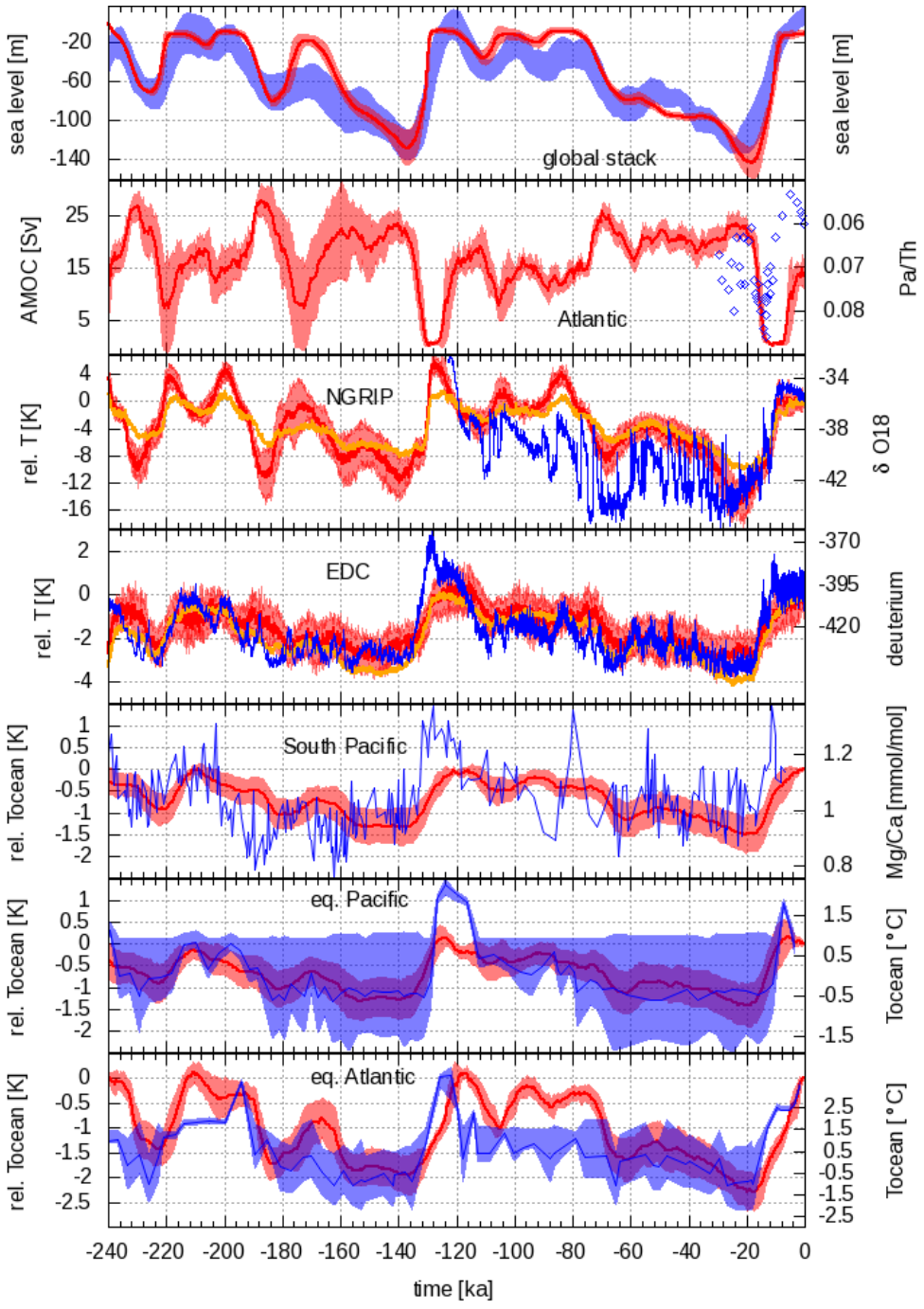

Figure 3.3: Caption on next page

Figure 3.3: Simulated (red, with ensemble standard deviation, relative to left y-axis) and reconstructed (blue, relative to right y-axis) climate indicators, from top to bottom: eustatic sea level change [m] relative to PD and sea level stack (Spratt and Lisiecki, 2016). AMOC strength and Pd/Th ratio from a sediment core off the coast of Florida (Süfke, 2019). Relative temperature weighted by precipitation at NGRIP ice core location (and relative annual temperature in orange) and NGRIP δ^{18}O record (Members, 2007). Relative temperature weighted by precipitation (and relative annual temperature in orange) at EDC ice core location and EDC deuterium record (Jouzel and Masson-Delmotte, 2007). Relative mean deep ocean temperature off of New Zealand and Mg/Ca benthic record (41°47.15'S, 171°29.94'W, Elderfield et al., 2012). Relative mean deep ocean temperature off of Costa Rica (Pacific) and temperature reconstruction with upper and lower estimate (0°10'N, 110°31'W, Bates et al., 2014a). Relative mean deep ocean temperature off the West Sahara (Atlantic) and temperature reconstruction (18°4'N,21°1'W, Bates et al., 2014b). All continuous records have been scaled to approximately match ensemble mean LGM and present-day.

3.4.3 PGM and LGM ice sheets compared to reconstructions

Fig. 3.4 displays a density plot of the number of ensemble members simulating ice over the given area during the glacial maxima of the last two glacial cycles. Presented are PGM and LGM as simulated in the long MIS 7 ensemble set (LGM 2), and in the MIS 5 set (LGM). Black contour lines show reconstructions of maximum ice extent where available. The simulated EA PGM ice sheet is for most simulations smaller than reconstructions suggest (Svendsen et al., 2004). A caveat is that the reconstruction represents the inferred maximum extent during the Saalian (Eurasian penultimate maximum glaciation period), which was unlikely to be synchronously reached along the entire ice margin. The eastern extent matches the reconstruction well. Two ensemble members (blue in Fig. 3.4) furthermore capture the southern extent well, but no member grows enough ice towards the west. One ensemble member (purple) grows an unrealistically large ice sheet reaching the borders of the GSM ice sheet domain. There is less variability in EA ice sheet extent during LGM and LGM 2. The simulated EA ice sheet brackets the reconstruction but reaches too far east compared to the reconstructed extent (Hughes et al., 2016).

The NA PGM ice sheet is nearly identical to the LGM and LGM 2 ice sheet extent. During all glacial maxima, the NA ice sheet approaches the maximum possible extent of the NA continental shelf break. Four simulations also reach the GSM southern grid bound (straight southern ice margin line in Fig. 3.4). The simulated ensemble ice extent largely brackets the geological inferences. Simulated ice reaches slightly further south over western NA than the LGM reconstruction suggests (Dalton et al., 2022). A distinct difference between simulations and reconstruction is the south-western

ice lobe over in the Cordillera mountain range that all ensemble members simulate. The applied temperature bias correction has too strong an impact on high elevation regions, likely driving ice growth in the Cordillera.

One small but persistent feature is the existence of a narrow ice shelf bridging the glacial maximum Greenland and Icelandic ice sheets. This may be an artifact from not accounting for the impact of the strong eastern boundary current on ice shelf formation. To date, there is no clear geological records that could either support or refute such an ice bridge. Further examination of this bridge is relegated to an ongoing history matching exercise for the Icelandic ice sheet.

Geological evidence indicates that EA was significantly larger during PGM than LGM (Svendsen et al., 2004; Astakhov, 2004) and NA likely smaller or of similar size (Dyke et al., 2002). LCice cannot fully capture these specific changes in relative ice sheet sizes, which has also proven to be difficult in other studies. Patterson et al. (2024), e.g., used the atmospheric general circulation model FAMOUS coupled to the ice sheet model Glimmer for PGM and LGM equilibrium simulations of the NA and Greenland ice sheets. With their setup, they can simulate a smaller NA ice sheet during the PGM time slice than during LGM when the climate is initialized with PGM and LGM ice sheet boundaries. When the same initial ice sheet is used, the NA PGM ice sheet is larger than the LGM ice sheet.

A large part of the explanation for differences in simulated ice sheet extent and reconstruction is the low resolution of the LCice atmosphere. Lofverstrom and Liakka (2018) have found that an atmospheric horizontal resolution of T85 (nominal 1.4°, versus 5.6° for LOVECLIM T21 according to models' Gaussian grids, but respectively about 2.1° and 8.6° based on the number of spherical harmonic basis functions

employed) is needed to accurately capture the LGM EA ice sheet (with the NCAR CAM3 atmospheric model and equilibrium forcing). They found the NA ice sheet to be less sensitive to atmospheric resolution. In an analysis with the same LCice model as present (Geng and Tarasov, in prep.), the simulated EA ice sheet does not have the sensitivity to NA ice sheet evolution observed in higher resolution climate models (Ullman et al., 2014; Liakka et al., 2016, using ModelE2-R and CAM3, respectively, in equilibrium simulations). Examination of simulated wind fields (not shown) further confirms that LCice lacks the capability to adequately simulate changes to the atmospheric stationary wave field that are observed in higher resolution climate models due to the NA ice sheet evolution.

Glacial cycle scale simulations at T85 resolution are not computationally feasible in the foreseeable future. As such, the coupled ice/climate modeling community would benefit from the development of approaches to compensate for limited climate model resolution, be it via some sort of dynamic bias correction or machine learning.

3.4.4 Influence of memory of the penultimate glacial cycle on last glacial cycle evolution

Fig. 3.5 shows that the ensemble mean of PGM ice sheets has a different configuration compared to that for LGM ice sheets. Regardless of whether they were simulated starting from MIS 5e or MIS 7e, the LGM ice sheets are nearly identical. The difference between PGM and LGM/LGM 2 is more pronounced over EA than NA. The NA PGM ice sheet is slightly thicker ($\sim$ 200 m) over Northern Canada and slightly thinner over Alaska ($\sim$ 500 m) and the south-eastern margin ($\sim$ 200 m) in compar-

ison to the LGM NA ice sheet. There is scarcely any difference in ice sheet extent. Conversely, the ensemble mean EA PGM ice sheet is significantly smaller than the LGM/LGM 2 ice sheet in extent and ice height (up to 2000 m over the North Russian coast).

Looking at individual ensemble members confirms the similarity between LGM and LGM 2 and the difference to PGM: the difference between NA and EA ice sheet size is smallest between LGM and LGM 2 and larger between PGM and LGM/LGM 2 (see Fig. 3.6). This holds for all ensemble members (that ran long enough, empty square in Fig. 3.6), not just for the PD-filtered subset (filled squares in Figure). There is little variability in ice volume and area for the NA ice sheet between LGM/LGM 2 and PGM but also within the ensemble, as the ice sheets are at or close to maximum possible extent especially since the GSM imposes complete ice calving when ice reaches the continental shelf break (Fig. 3.4). The EA ice sheets display a distinct difference between LGM/LGM 2 and PGM and a large inter-ensemble variability. For the Greenland ice sheet (GR), no difference between PGM and LGM/LGM2 is visible, the ice sheet presents a similar ice volume in all 3 simulated maxima. This is in large part again due to all GR glacial maximum fully reaching the continental shelf break GSM imposed limit for ice. Antarctic ice volume (AN), however, has more similarity between glacial maxima for PGM and LGM2, the glacial maxima of the same continuous simulation (MIS 7 ensemble set), rather than LGM and LGM2.

Fig. 3.7 displays the individual ice sheet volume evolution. NA and EA ice sheets in the PD-filtered MIS 7 ensemble set have nearly fully retreated by MIS 5e, therefore the last glacial cycle starts with nearly identical (non-existent) ice sheets in both ensemble sets. As such, outside of the climate system the main signatures of previous

ice sheet presence are in the altered bed temperature profile (impacting subsequent geothermal heat flux at the base of the ice sheet) and residual GIA disequilibrium. The GR ice sheet in the MIS 7 set has not completely retreated to PD ice volume by MIS 5e. In the MIS 5 set, the uncoupled GSM spinup leads to varying sizes of the GR ice sheet at the start of the coupled simulation. The same ensemble members from the two sets show small differences in GR ice volume evolution from MIS 5d-5b, however by MIS 5a they are mostly converged. Conversely, there are significant differences in Antarctic ice volume between the ensemble members with the same parameter vector in the two (MIS 5 to 1 and MIS 7 to 1) ensembles from MIS 5e to the end of the simulation at PD. Even when removing the PD bias (Fig. 3.8), differences between the two sets persist. A simple scale analysis based on ice sheet mean accumulation rates, aspect ratios, and length scales would support this extended Antarctic ice sheet response timescale. Furthermore, history dependency of simulated ocean temperatures could also play a significant role given the presence of extensive marine ice components and potentially high grounding line sensitivity to changes in ocean temperature (driving submarine melt).

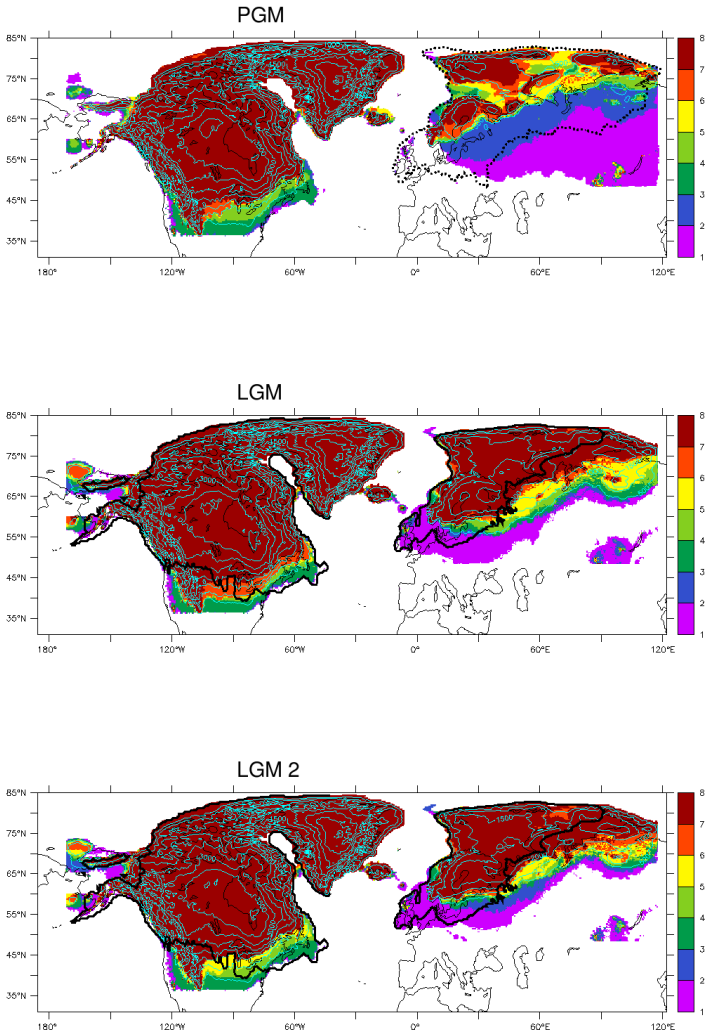

Figure 3.4: Number of runs covering the area with ice in rainbow shading at PGM (top) with EA Saalian maximum extent following Svendsen et al. (2004) in black; LGM (middle) and LGM 2 (bottom) with NA maximum extent from Dalton et al. (2022) and EA maximum extent from Hughes et al. (2016) in black. Light blue contours indicate ensemble mean ice height (in steps of 500 m). "Artificially" straight lines in western Alaska, southern NA, and eastern EA are GSM grid bounds (chosen to be outside of maximum geological bounds for the last two glacial cycles)

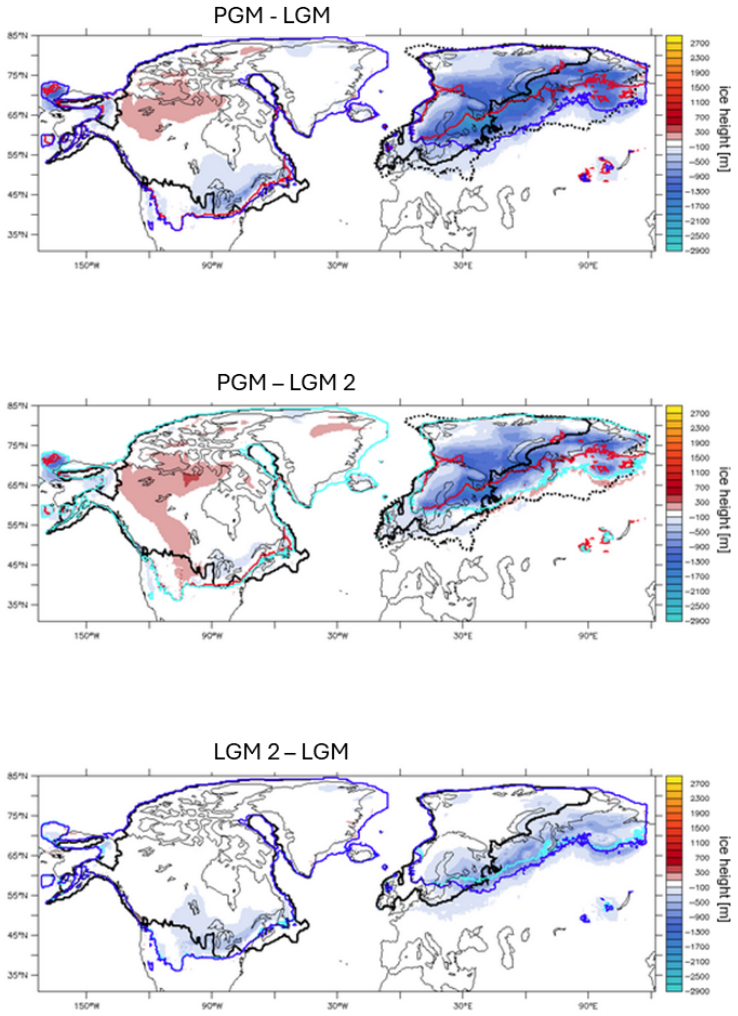

Figure 3.5: Mean ice height differences between PGM, LGM 2 and LGM of the sub-ensemble (excluding one member with excessive EA ice volume, blue in Fig. 3.1 right). Red contour: mean PGM ice extent; cyan contour: mean LGM 2 ice extent; blue contour: mean LGM ice extent; black contour: LGM reconstruction maximum extent by Dalton et al. (2022) over NA and Hughes et al. (2016) over EA; black dashed contour: maximum Saalian extent by Svendsen et al. (2004).

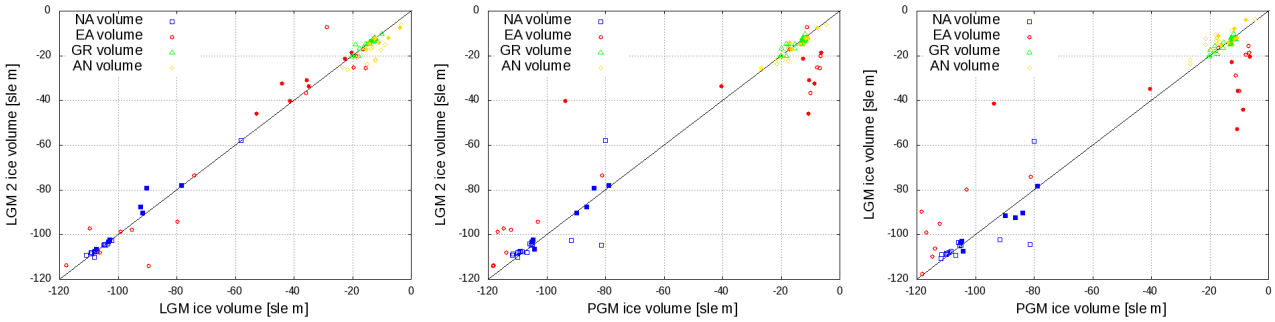

Figure 3.6: Maximum ice volumes as eustatic sea level contribution at LGM and LGM 2, PGM and LGM 2, and PGM and LGM in comparison. Filled squares are members of the sub-ensemble that passed the PD sea level filter. Empty squares are ensemble members that reached 16 ka.

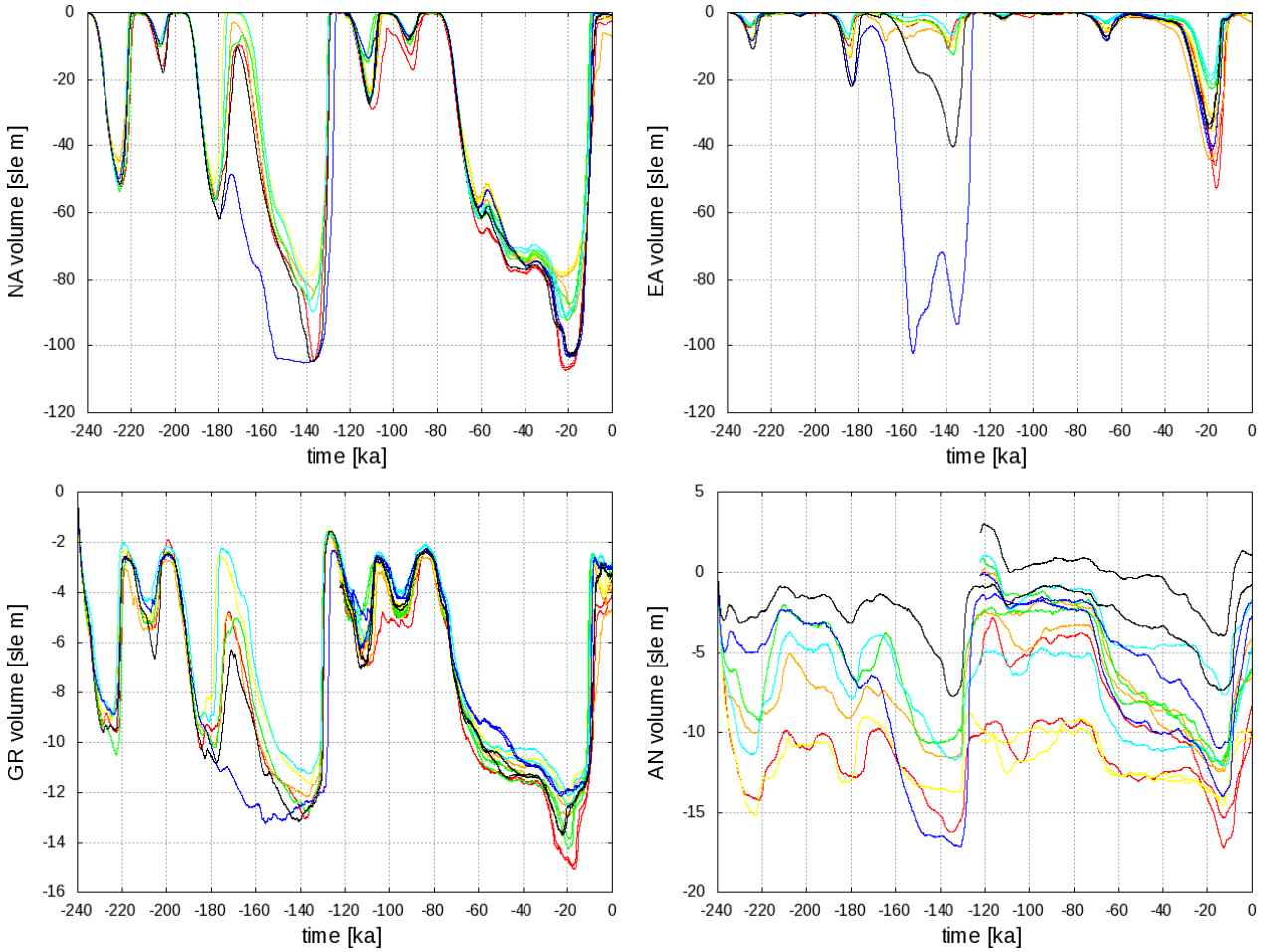

Figure 3.7: Ice volume as eustatic sea level contribution for individual ice sheet and PD-sea level filtered ensemble member

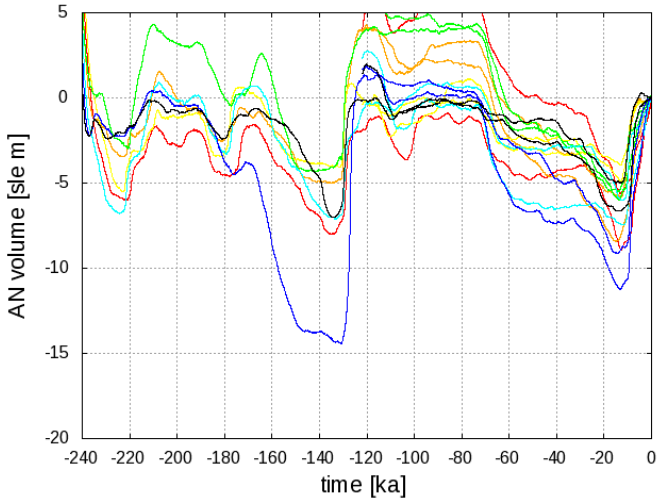

Figure 3.8: Ice volume as eustatic sea level contribution for AN PD-sea level filtered ensemble member shifted to reach 0 m PD sea level

3.4.5 Timing of maximum ice volume during stadials and phasing with insolation

The timing of maximum ice volume globally and for all 4 major ice sheets for the stadials of the last two glacial cycles are summarized in Tables 3.1 and 3.2. MIS 6c and 3b are not listed as they are short, weak stadials and their timing is indeterminable in the simulations.

As expected, ice volume generally lags insolation forcing; only GR reaches its maximum volume before the insolation minimum is reached during MIS 7b, PGM, and MIS 5b. This is likely partly due to the hard continental shelf break limit on ice sheet extent that bounds nearly the whole margin of the maximal GR ice sheet. This GR phase lead is furthermore smaller than inter-ensemble variability for MIS 7b and PGM. For all listed stadials, the ensemble mean phase difference between GR and NA is within 1.5 kyr, reflecting strong climatic impact of the NA ice sheet on GR. On the other hand, the ensemble mean stadial phase difference ranges up to the 8 kyr lead of EA compared to GR at MIS4.

The timings of ice volume maxima for the stadials of the last glacial cycle agree between MIS 7 and MIS 5 ensembles for all ice sheets, but the inter-ensemble variability is significantly increased at MIS 5d in the MIS 7 set (bold in Table 3.4). The timing of mean sea level minima is dominated by the NA ice sheet (cf. similarities in timing in the first two rows in Tables 3.1, 3.2). EA has the smallest lag behind insolation. This is in accord with its relatively large ice perimeter to ice area ratio and has long been evident in the higher sensitivity of simulated EA ice sheets (compared to NA) in simplified coupled ice and climate models (e.g. Tarasov and Peltier, 1997).

Table 3.1: Timing of 65 °N mid-July insolation minimum, eustatic sea level (SL) minimum, and ice sheet volume maxima during stadials of the penultimate glacial cycle in ka

maximum	MIS 7d [ka]	MIS 7b [ka]	MIS 6e [ka]	PGM [ka]
insolation	230	207	185	137
global SL	226.0 ± 1.2	206.3 ± 0.5	182.7 ± 0.6	136.8 ± 0.8
NA volume	225.1 ± 0.4	206.3 ± 0.5	181.1 ± 1.0	138.1 ± 1.6
EA volume	228.8 ± 0.5	206.9 ± 0.2	184.0 ± 0.7	137.0 ± 1.5
GR volume	225.0 ± 2.5	207.5 ± 1.6	180.8 ± 2.3	138.7 ± 2.8
AN volume	224.0 ± 2.8	197.1 ± 6.3	180.0 ± 1.1	134.5 ± 3.3

AN has the largest lag relative to northern summer insolation but also the largest intra-ensemble variability in lags.

The largest lag between insolation and ice volume for each ice sheet is highlighted in bold in Table 3.3. For all but EA this is at MIS 4. The smallest lag for each ice sheet is underlined in Tables 3.3 and 3.4. The lag is small at weak stadials like MIS 7b and 5b but also at PGM. Therefore, the lag is not necessarily related to the strength of the stadial nor the total ice sheet volume.

Table 3.2: Timing of 65 °N mid-July insolation minimum, eustatic sea level (SL) minimum, and ice sheet volume maxima during stadials of the last glacial cycle from the MIS 5 ensemble (from the MIS 7 ensemble)

maximum	MIS 5d (MIS 5d 2) [ka]	MIS 5b (MIS 5b 2) [ka]	MIS 4 (MIS 4 2) [ka]	LGM (LGM 2) [ka]
insolation	114	93	70	22
global SL	111.3 ± 0.7 (110.8 ± 0.6)	92.9 ± 0.4 (92.5 ± 0.7)	60.8 ± 0.8 (60.8 ± 0.8)	18.7 ± 1.0 (18.4 ± 0.7)
NA volume	111.3 ± 0.7 (110.9 ± 0.6)	93.0 ± 0.3 (92.5 ± 0.6)	60.8 ± 0.7 (60.8 ± 0.9)	20.3 ± 1.4 (20.6 ± 1.6)
EA volume	114.5 ± 0.8 (112.3 ± 4.4)	94.0 ± 1.5 (94.8 ± 2.4)	66.9 ± 0.3 (67.0 ± 0.5)	18.4 ± 1.0 (18.0 ± 0.9)
GR volume	112.9 ± 0.8 (110.4 ± 1.3)	94.5 ± 1.0 (94.3 ± 1.2)	59.0 ± 0.1 (59.1 ± 0.2)	20.4 ± 2.1 (20.4 ± 1.6)
AN volume	107.5 ± 2.4 (106.3 ± 4.0)	95.7 ± 7.0 (94.5 ± 7.1)	59.1 ± 0.1 (59.0 ± 0.1)	13.5 ± 0.9 (13.1 ± 0.5)

Table 3.3: Lag between insolation minimum and maximum ice volume for stadials of the penultimate glacial cycle. Negative values indicate ice sheet volume lags behind insolation, positive ice sheet volume leads before insolation. Underlined values indicate smallest lag for each ice sheet

ice sheet	MIS 7d lag [kyrs]	MIS 7b lag [kyrs]	MIS 6e lag [kyrs]	PGM lag [kyrs]
global SL	-4.0 ± 1.2	-0.7 ± 0.5	-2.3 ± 0.6	-0.2 ± 0.8
NA volume	-4.9 ± 0.4	-0.7 ± 0.5	-3.9 ± 1.0	1.1 ± 1.6
EA volume	-1.2 ± 0.5	-0.1 ± 0.2	-1.0 ± 0.7	<u>0.0 ± 1.5</u>
GR volume	-5.0 ± 2.5	<u>0.5 ± 1.6</u>	-4.2 ± 2.3	1.7 ± 2.8
AN volume	-6.0 ± 2.8	-9.9 ± 6.3	-5.0 ± 1.1	<u>-2.5 ± 3.3</u>

Table 3.4: Lag between insolation minimum and maximum ice volume for stadials of the last glacial cycle. Negative values indicate ice sheet volume lags behind insolation, positive ice sheet volume leads before insolation. Underlined values indicate smallest lag for each ice sheet. Bold values indicate maximum lag for each ice sheet. Bold standard deviation points out high inter-ensemble variability during MIS 5d

ice sheet	MIS 5d (MIS 5d 2) lag [kyrs]	MIS 5b (MIS 5b 2) lag [kyrs]	MIS 4 (MIS 4 2) lag [kyrs]	LGM (LGM 2) lag [kyrs]
global SL	-2.7 ± 0.7 (-3.2 ± 0.6)	-0.1 ± 0.4 (-0.5 ± 0.7)	**-9.2 ± 0.8 (-9.2 ± 0.8)**	-3.3 ± 1.0 (-3.6 ± 0.7)
NA volume	-2.7 ± 0.7 (-3.1 ± 0.6)	-0.0 ± 0.3 (-0.5 ± 0.6)	**-9.2 ± 0.7 (-9.2 ± 0.9)**	-1.7 ± 1.4 (-1.4 ± 1.6)
EA volume	0.5 ± 0.8 (-1.7 ± **4.4**)	1.0 ± 1.5 (1.8 ± 2.4)	-3.1 ± 0.3 (-3.0 ± 0.5)	**-3.6 ± 1.0 (-4.0 ± 0.9)**
GR volume	-1.1 ± 0.8 (-3.6 ± **1.3**)	1.5 ± 1.0 (1.3 ± 1.2)	**-11.0 ± 0.1 (-11.0 ± 0.2)**	-1.6 ± 2.1 (-1.6 ± 1.6)
AN volume	-6.5 ± 2.4 (-7.7 ± **4.0**)	2.7 ± 7.0 (1.5 ± 7.1)	**-10.9 ± 0.1 (-11.0 ± 0.1)**	-8.5 ± 0.9 (-8.9 ± 0.5)

3.5 Conclusions

We present simulations of a small ensemble covering the last two glacial cycles. Out of 56 ensemble parameter vectors that passed a PD filter for temperature seasonality, annual precipitation, and mean Southern Ocean temperature, only seven members can capture global eustatic sea level change within uncertainty ranges. Therefore, capturing PD climate does not predict capture of glacial cycle climate. Even capturing glacial inception eustatic sea level change cannot predict capture of full glacial cycle sea level within reconstruction uncertainty bounds. Deglaciation after stadials poses the strongest constraint.

The small ensemble captures the timing and the relative overall temporal pattern of air temperature at the Greenland NGRIP and Antarctic EDC sites, and the deep ocean temperature from 3 sites in equatorial Atlantic, and equatorial and Southern Pacific is captured in the simulations. However, the total amplitude of glacial cooling and interglacial warming is underestimated in the ensemble. There are furthermore no centennial to millennial Dansgaard-Oeschger like oscillations visible in the simulated NGRIP temperature. AMOC, however, presents a Heinrich-stadial-like collapse after PGM and LGM, but no further variability during the last termination. NGRIP temperature is not directly linked to AMOC strength, as the temperature increases during phases of AMOC collapse. AMOC overall displays a larger variability during the penultimate glacial cycle than during the last glacial cycle.

Precipitation weighted temperature has a significantly ($\pm$ 4 °C) larger amplitude for NGRIP location compared to nominal mean temperature. Though imperfect, our simulations results provide a previously absent physically-based dataset for decon-

volving seasonal biasing of paleo proxy data time series for the last 2 glacial cycles.

A notable deviation of the ensemble from the inferred eustatic sea level record is MIS 6d. In the ensemble, MIS 6d is a strong interstadial with near full retreat, while the sea level record indicates a weak interstadial. The equivalent MIS 3c in the last glacial cycle is a weak interstadial in the ensemble. July insolation at 65 °N is $\sim$ 20 W/m higher during MIS 6d but CO_2 $\sim$ 10 ppm lower compared to MIS 3c. As no ensemble member can capture a weak MIS 6d interstadial without strongly deviating from the sea level record for the following glacials and interglacials, this suggests that the sea level record might be biased too low for this interstadial.

On a global scale, there is little ice-climate memory of the penultimate glacial cycle in the last glacial cycle ice evolution. Antarctica, however, is sensitive to ice sheet history and displays significant differences between simulations started at MIS 5 and MIS 7, leading to large PD biases. This is a reminder that modeling the future Antarctic ice sheet will be highly dependent on (uncertain) initial conditions (Seroussi et al., 2019; Nowicki et al., 2016).

The 4 major ice sheets do not reach maximum ice volume synchronously. Maximum ice volume generally lags behind insolation minimum. MIS 4 displays the largest lag (of 9.2 $\pm$ 0.8 kyrs) for global mean sea level. The lag not only varies for the different ice sheets but also temporally from stadial to stadial. There is no clear relationship between the amount of lag and the strength of the stadial, likely in part due variations in CO_2. At MIS 4, where a large lag between insolation and ice volume exists, CO_2 values are relatively high and decrease just as the insolation minimum is reached. At PGM, where the lag between insolation and ice volume is small, CO_2 is already at a minimum. Our results therefore suggest that proxy records tuned to

orbital phasing may have age errors of up to ~ 9 kyrs.

Overall, the presented simulated ensemble of ice-climate evolution over the last two glacial cycles brackets the temporal pattern of reconstructed sea level, polar air temperature, and deep ocean temperature. This on top of the seasonal resolution of temperature and precipitation can therefore aid deconvolution of paleo proxies over this time span.

Chapter 4

The role of feedbacks between ice and climate in driving the last glacial cycle

4.1 Abstract

We examine the dynamical role of the North American and Eurasian ice sheets during the last glacial cycle. We specifically compare the main atmosphere, ocean, and solid Earth mediated feedbacks of ice sheets on themselves and with each other during glacial inception and MIS 3-1. This is via an ensemble-based sensitivity analysis using the fully-coupled Earth system model LCice to isolate the impact of ice sheet topography and albedo, glacial isostatic adjustment (GIA), Bering Strait through flow, and freshwater storage and routing.

All tested sensitivities result in ice volume changes of more than 10 m eustatic sea

level equivalent for both the North American and Eurasian ice sheet for most if not all ensemble members. There is a high variability in response to the tested feedbacks depending on ensemble member parameter vector, highlighting the importance of ensemble simulations. The North American sheet evolution is especially variable during MIS 3, where behavior varies between a weak interstadial and a strong interstadial with near-full ice retreat. The intra-ensemble variability during MIS 3 is reduced in all sensitivity experiments, indicating that all tested feedbacks play a critical role during this interval. GIA exhibits the strongest mean influence on ice sheet evolution and is necessary for complete deglaciation for both major ice sheets. AMOC collapses during last glacial termination and resumes after approximately 5 kyrs in the control ensemble. A consistently closed Bering Strait inhibits AMOC resumption.

4.2 Introduction

During the last glacial cycle, orbitally forced changes in the climate system, amplified by changes in greenhouse gas concentration, drove large scale glaciation and subsequent deglaciation. The evolving ice sheets in turn exerted potentially significant influence on the climate system through changes in albedo, topography, and freshwater fluxes. The influence of orbital and greenhouse gas forcing on ice and climate evolution has been tested for various model complexities and times scales (e.g. Vettoretti and Peltier (2004) for last glacial inception and Yoshimori et al. (2001) for last termination). What to date remains unclear is the extent to which the ice to climate system couplings feed back to in turn drive further ice sheet growth and decay. Put simply, to what extent does ice sheet evolution over a glacial cycle depend on ice

sheet forcing of the climate system? And how does the relative influence of these ice-climate feedbacks evolve through a glacial cycle?

Ice sheets directly influence the atmospheric and ocean systems via changes in albedo, topography, freshwater, and sea level. The influence of ice sheets on surface albedo is straight forward. In addition to directly changing local surface elevation, ice sheets influence adjacent topography through glacial isostatic adjustment (GIA). During the Last Glacial Maximum (LGM), the major Laurentide ice domes reached more than 3 km above sea level (e.g. Tarasov et al., 2012), posing an obstacle that reorganized atmospheric circulation (Liakka et al., 2016). This could result in splitting the jet stream around the ice sheet (Kutzbach and Wright, 1985; Andres and Tarasov, 2019). Changes in atmospheric circulation will influence both local and global climate. Moisture and energy transport can be altered, affecting precipitation patterns, air temperature, sea surface temperature (SST), and therefore potential ice growth or decay. Furthermore, the presence of an ice sheet obstructing atmospheric circulation can have a direct impact on global ocean circulation by influencing wind stress and the water vapor transport from one ocean to another (Schmittner et al., 2011). Changes in ice and ocean load drive GIA, i.e. deformation of the surface of the solid Earth. The ice sheets depress the solid Earth beneath and proximal to them. Consequently, the ice sheet itself experiences a reduction in elevation, resulting in elevated near surface air temperatures. As the ice subsequently retreats, the surface of the solid Earth has a delayed relaxed return to ice free elevation.

Freshwater fluxes to the ocean are modified by ice sheet storage and subsequent release of freshwater along with direct (e.g. ice dam) and indirect (via GIA) induced changes to river routing. The amount, timing, and location of freshwater input into

the ocean plays a role modifying global meridional circulation (Love et al., 2021). This, in turn, affects ocean heat transport, especially to Northern Europe (e.g. Oldenburg et al., 2018).

Ice sheets further modify ocean circulation by changes in sea level. Shallow ocean gateways, such as the Bering Strait, are closed during glacial times when the sea level is lowered due to water storage in ice sheets. The Bering Strait is critical for global ocean circulation as it connects the Pacific with the Arctic Ocean and delivers relatively fresh water through the Arctic Ocean to the North Atlantic. Presently, the Bering Strait is about 50 m deep, and the mean through flow is about 0.8 Sv northward (Roach et al., 1995; Woodgate et al., 2006). Most General Circulation Models do not have a dynamic land mask and therefore cannot simulate the effect of ocean gateways closures on ice and climate evolution.

The climate drivers of ice sheet evolution are well known and have long been used to force paleo ice sheet models though with limited feedback of the evolving ice sheet on climate.

Herein we undertake a sensitivity analysis of ice sheets and climate dynamics across the last glacial cycle to test the relative influence of the above mentioned feedbacks. We use the fully coupled Earth system model LCice, which includes all key couplings between ice and climate, resolves atmospheric circulation at synoptic scales, and includes a fully coupled ocean general circulation model. Though our analysis is focused on the North American and Eurasian ice complexes, for global dynamical consistency, the simulations dynamically include the other two main paleo ice sheets (Greenland and Antarctica).

4.3 Methods

4.3.1 The Model LCice2.0

LCice couples the Glacial System Model GSM (Tarasov, in prep.) to the Earth system model of intermediate complexity LOVECLIM (Goosse et al., 2010). All major ice-climate couplings are included (Bahadory and Tarasov, 2018). Climatologies of temperature, lapse rate, precipitation, and wind are calculated in LOVECLIM's atmospheric component, ECBilt, and passed to the GSM. ECBilt has a quasi-geostrophic atmosphere on a T21 spectral grid with 3 vertical layers. ECBilt's precipitation is downscaled to the finer GSM grid with accounting for orographically forced precipitation on the higher resolution GSM surface slopes. Temperature and precipitation fields are subsequently corrected for present-day (PD) biases. The strength of the bias correction is a function of global mean sea level under ensemble parameter control. The coupler passes the updated ice mask and topography from GSM back to ECBilt.

Ocean and near surface atmospheric temperatures respectively drive or control submarine melt and calving. CLIO is the primitive equation ocean component of LOVECLIM that includes dynamic/thermodynamic sea ice. It has 20 vertical layers and a horizontal resolution of 3x3°. Upstream ocean temperature profiles from CLIO are passed to the GSM for determining sub-shelf melt. The GSM computes topographically-self-consistent surface freshwater runoff and ice calving fluxes (simplistically included in the runoff flux) for CLIO input. GSM determined local sea level controls Bering Strait throughflow in CLIO. However, LOVECLIM otherwise has the common paleoclimate model limitation of ocean landmask fixed to PD. LOVECLIM has a fully coupled land vegetation component consisting of three surface types (trees,

grass, and desert).

The GSM is a thermo-mechanically coupled ice sheet model with hybrid shallow ice and shallow shelf physics. It includes all major ice sheets (Greenland, Antarctica, North America, Eurasia). The GSM operates on a 0.5° longitude by 0.25° latitude grid for the Northern Hemisphere and a 20 km polar stereographic grid for Antarctica. Glacio-isostatic adjustment in the GSM is visco-elastic with a radially inhomogeneous and spherically symmetric earth rheology and linear approximation for Geoidal deflection (Tarasov, in prep.).

The default LCice version has a coupling step of 20 years (based on sensitivity tests, Bahadory and Tarasov, 2018). We use a 4x acceleration (20 years pass in the forcing conditions and the GSM, 5 years in LOVECLIM). This is slightly more conservative than Choudhury et al. (2020) who find that ice sheet evolution is relatively insensitive to up to 5x acceleration in ice sheet model and LOVECLIM coupling.

A key strength of LCice lies in its coupling of climate and ice components, incorporating all crucial feedback mechanisms. A further advantage is that LCice features a ocean general circulation model in contrast to zonally averaged or frictional geostrophic models common in Earth system models of intermediate complexity (e.g. in CLIMBER Willeit et al., 2022). The model's primary drawbacks stem from simplified process representations and constrained spatial resolution, especially in the atmospheric component. ECBilt is capable of capturing large-scale mid-latitude atmospheric circulation, but it lacks the resolution to accurately represent small-scale tropical or mesoscale convective systems (Goosse et al., 2010). The limited spatial resolution further hampers its ability to depict atmospheric wave dynamics.

4.3.2 Experiment Setup

The sensitivity analysis uses a small 7 member baseline ("ctrl") ensemble with all feedbacks active. The parameters values that are varied include 19 LOVECLIM (14 related to atmosphere, 3 to vegetation, 1 to the ocean, and 1 to the down-scaling scheme) and 23 GSM parameters.

These members were selected from a larger pool of 90 perturbed parameter ensemble members as follows. To ensure that the sensitivity ensemble accurately represents the sea level changes during the last glacial cycle, filtering criteria were applied to the larger ensemble. In detail, the filters were: 1) glacial inception (sea level ranging from -30 to -60 m between -115 and -105 ka, 2) subsequent rise to between -9 and -36 m between -130 and -95 ka), 3) LGM (sea level decrease to 110 to 150 m between -30 and -15 ka), and 4) PD (sea level above -30 m in the year 1950). Following this filtering process, only 7 ensemble members remained, as illustrated in Figure 4.1.

The analysis involved eight different leave-one-feedback-out experiments (see Table 4.1). To isolate the influence ocean gateways have on glacial climate and ice evolution, Bering Strait throughflow is kept constantly closed (Bering Strait closed, "bsc") or at PD values (Bering Strait open, "bso"). In the ctrl experiment, the throughflow changes depend on local sea level. To isolate the influence of individual ice sheets on climate and the other ice sheet, the coupling between GSM and LOVECLIM is partially turned off. In experiments "flatNA" and "flatEA" the North American and Eurasian ice masks evolve and are passed from GSM to LOVECLIM, respectively, but LOVECLIM is continually forced with PD topography. Therefore, the change in albedo produced by the ice sheet is still present, but its influence on atmospheric

circulation through changes in topography is removed. In experiments "noNA" and "noEA" LOVECLIM is continually forced with the corresponding PD icemask and orography. All sensitivity experiments retain the key temperature and surface mass balance elevation feedback for the GSM, the information is just not passed to LOVECLIM. To test the influence of GIA on ice sheet evolution and climate, GIA is simply turned off ("noGIA").

A final experiment considers the ice to ocean freshwater coupling. In the "PDdrain" experiment, the stand-alone LOVECLIM freshwater treatment is applied, for which all precipitation is immediately returned to the ocean. In the GSM, the precipitation is still stored in the ice sheets. In ctrl, precipitation can be stored in ice sheets and the meltwater routing is dynamically consistent with the evolving topography. The influence of Antarctic melt water on the ice-climate system was also tested, but there was negligible change in NA and EA ice sheet evolution, therefore these results are not included.

We examine two sea level lowstands and the transition in and out of them: MIS 5d and MIS 2 (LGM). The MIS 5d analysis time frame is 120 - 100 ka, and the analysis time frame encompassing LGM ("MIS 3-1") is from 50 - 0 ka.

4.4 Results and Discussion

The analysis focus is on the North American (NA) and Eurasian (EA) ice volume (and to a lesser degree in ice area) during MIS 5d and LGM. The Greenland and Antarctic ice sheets are given limited attention as their areal extent and mean elevation have a much more limited range over the course of the last glacial cycle.

Table 4.1: Description of experiments

Name	Description
ctrl	baseline experiment, all couplings turned on
bsc	Bering Strait constantly closed
bso	Bering Strait constantly open
flatNA	no topography change due to NA ice sheet in LOVECLIM
noNA	no NA ice sheet in LOVECLIM
flatEA	no topography chnage due to EA ice sheet in LOVECLIM
noEA	no EA ice sheet in LOVECLIM
noGIA	GIA turned of
PDdrain	precipitation returned to ocean via PD drainage routes

Below, we analyze temperature (SST and land temperature at sea level) and precipitation, given their direct influence on the growth and retreat of ice sheets. Additionally, the assessment includes sea ice extent, which impacts precipitation availability, wind patterns affecting heat and moisture transport, and the strength of AMOC due to its influence on heat transport to the North Atlantic region. The metrics are presented either at the time of maximum ice volume and area (wind field, ice height, sea ice and ice sheet extent) or a few thousand years prior to the sea level lowstand (SST, air temperature, and precipitation), depending on when their effects are most pronounced. All metrics for all experiments are displayed in Appendix B. The main

body of the paper only displays the most influential metrics.

4.4.1 Baseline ensemble (ctrl)

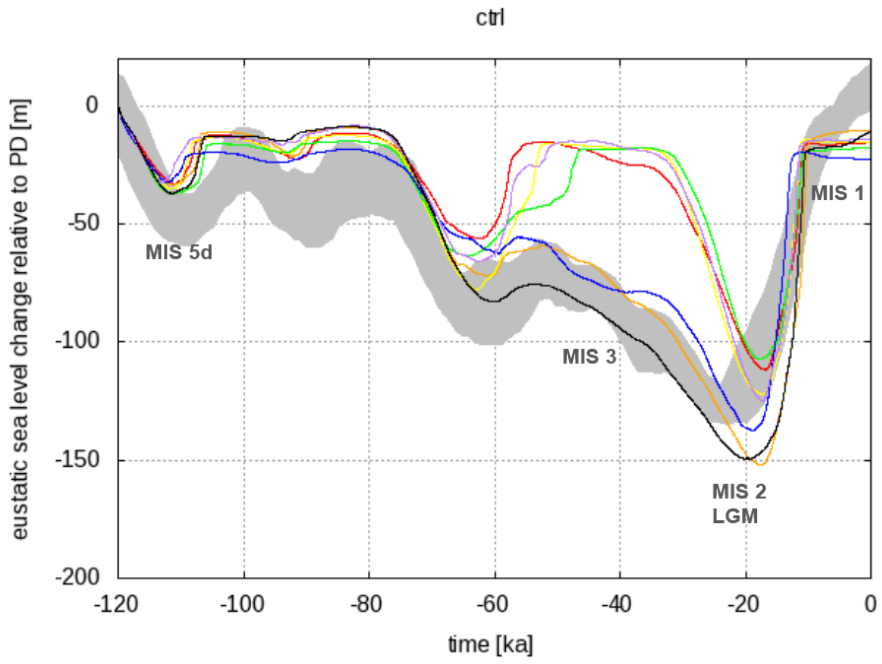

Figure 4.1: Eustatic sea level evolution of the ctrl ensemble (coloured lines). Grey shading: 95 % confidence range of sea level reconstruction by Spratt and Lisiecki (2016)

Though not a selection criterion, the ctrl ensemble brackets the inferred global mean eustatic sea level for MIS 3 and 2. MIS 5d sea level lowstand is reached at around year 112 ka, where the sea level dropped to -34.1 m ± 2.5 m. Ice builds up in North America over the Canadian Archipelago, the Cordilleran, Laurentides, and Hudson Bay (see Figure 4.2). In Eurasia, ice expands over Svalbard, Franz-Joseph-Land, the Taymyr Peninsula, Novaya Zemlya, and the Scandinavian mountains. Following MIS

5d, the ice sheets retreat, and the sea level returns to near-interglacial level by 105 ka.

During LGM, the sea level lowstand was reached around 18 ± 1 ka (slightly later than suggested by the sea level record, Spratt and Lisiecki, 2016) with -132 ± 20 m. The ensemble exhibits two different sea level trajectories during MIS 3. As shown in Figure 4.1, three simulations follow the Spratt and Lisiecki (2016) sea level record, displaying a weak interstadial with a mean sea level of -67 m. Four simulations display a higher mean sea level of about -21 m at 50 ka. This latter result is perhaps consistent with recent studies suggesting significant southern margin retreat of the North American ice sheet during at least one sub-interval of MIS 3 (Weiss et al., 2022; Antonioli et al., 2021; Dalton et al., 2019).

During the extensive glaciation at LGM, the Laurentide, Cordilleran, and Greenland ice sheets merge, and ice reaches as far south as 45 °N. Equally, there is one large Eurasian ice sheet covering Fennoscandia and the Barents-Kara Sea. For all but two simulations, the southern extent of the Eurasian ice sheet is well beyond that inferred on the basis of glacial geology (Hughes et al., 2016).

AMOC strength, calculated as the maximum of the stream function in the region 20 to 80 °N, -500 to -5500 m depth in the North Atlantic, is constant at the beginning of the simulations (see yellow shading e.g. in Figure 4.10). As the ice sheets first retreat during the MIS 5d interval, AMOC decreases by about 40 %. By 100 ka AMOC is stronger but not fully returned to the strength at simulation start. Towards the LGM, the AMOC strengthens and deepens. The North Atlantic deep water formation (NADW) cell reaches nearly 5 km, displacing the Antarctic bottom water cell (see Appendix B.3). This matches PMIP 3 and 4 results (Muglia and Schmittner, 2015;

Sherriff-Tadano and Klockmann, 2021) but not proxy reconstructions which suggest a shoaled AMOC during glacial conditions (Lippold et al., 2012; Pöppelmeier et al., 2021). As the ice sheets retreat after 20 ka, the AMOC collapses for about 5 kyrs. By the end of the simulation, pre-LGM AMOC strength is reached. For one ensemble member, AMOC has already collapsed at the beginning of the MIS 3-1 interval; this member is therefore excluded from the LGM analysis (blue in Figures 4.3 and 4.4).

Sea ice extent increases from MIS 5d to LGM, reaching South of Newfoundland in winter and covering the GIN (Greenland, Island, Norwegian) Seas year round at LGM (see green dashed line in e.g. Figure 4.11). Sea ice does not reach further south than the simulated location of deep water formation ($\sim$ 60 °N, Appendix B.3). The location of deep water formation does not change over the course of the glacial cycle (except for AMOC collapse).

4.4.2 Sensitivity ensembles

Figures 4.3 and 4.4 show the difference in global eustatic sea level between the corresponding sensitivity and the ctrl ensemble members. The most apparent feature is the large variability in response to a tested sensitivity among the ensemble members. Differences in NA ice sheet volume between sensitivity experiments and ctrl are largest during MIS 3. This is also the interval of highest ctrl ensemble variance. Sensitivity ensemble members switch back and forth between following the strong MIS 3 interstadial trajectory where the NA ice sheets retreat nearly completely, and the weak MIS 3 trajectory of the sea level stack (Figure 4.1). NA ice volume differences between sensitivity experiments and ctrl are rather small at LGM. This is in part due

to the hard limit of the NA southern grid edge at 35.75^o N, and the saturated marine boundary (all ice at the continental shelf break has imposed complete calving in the GSM).

The EA ice sheet is small during MIS 5d in ctrl and restricted to the low precipitation Barents-Kara Sea region (and adjacent mainland coast). Therefore, EA will has a limited potential to respond to tested sensitivities at MIS 5d. Differences in EA volume are largest at LGM. Note that a small phase shift in model response between two ensembles can lead to a large difference in Figures 4.3 and 4.4. The response of nominal "outliers", ensemble members that respond contrary to the rest of the ensemble, is not consistent. An ensemble member that acts as an outlier for the MIS 5d time frame is not necessarily an outlier for the MIS 3-1 frame.

Given the high variance in simulation response, differences in ensemble means can easily under-represent ensemble response (cf Figures 4.5 and 4.6). Our primary reference for characterizing sensitivities is therefore the ESL contribution timeseries of ensemble member sensitivity response (Figures 4.3 and 4.4). As evident in these plots, all of the sensitivity experiments have a significant ($>$ 10 mESL) impact for most if not all ensemble members for both NA and EA. Furthermore, all experiments have at least one ensemble member with a sensitivity response of more than 50% of the glacial maximum baseline ESL. Therefore, all the tested feedbacks have the potential to be highly important for ice sheet evolution, but simultaneously it is very unclear even what sign the feedback has in many cases.

The high variance in ensemble member response, especially with most experiments having ensemble members with opposite ESL responses (Figures 4.3 and 4.4) for at least some time intervals, presents a challenge in deciphering the associated feedback

components. To address this and isolate the more consistent characteristics of the response, our analysis below is focussed on ensemble means and standard deviations. Furthermore, a few runs with AMOC collapse are excluded from the ensemble statistical analysis. Specifically, when there is no obvious physical reason for the collapse (e.g. a collapse during ice growth phase when freshwater forcing is reduced) and the ensemble members are outliers in their response compared to the rest of the ensemble, we exclude the ensemble member to better isolate the dominant ensemble signal. Moreover, simulations that crash during or before an analysis time frame (MIS 5d of MIS 3-1) are excluded from mean ensemble analysis. For the purposes of this narrower ensemble analysis below, a "significant" change is defined as a change in NA or EA ice volume where the mean of the sensitivity ensemble lies outside the 1 sigma range of the ctrl ensemble as displayed in Figures 4.5 and 4.6.

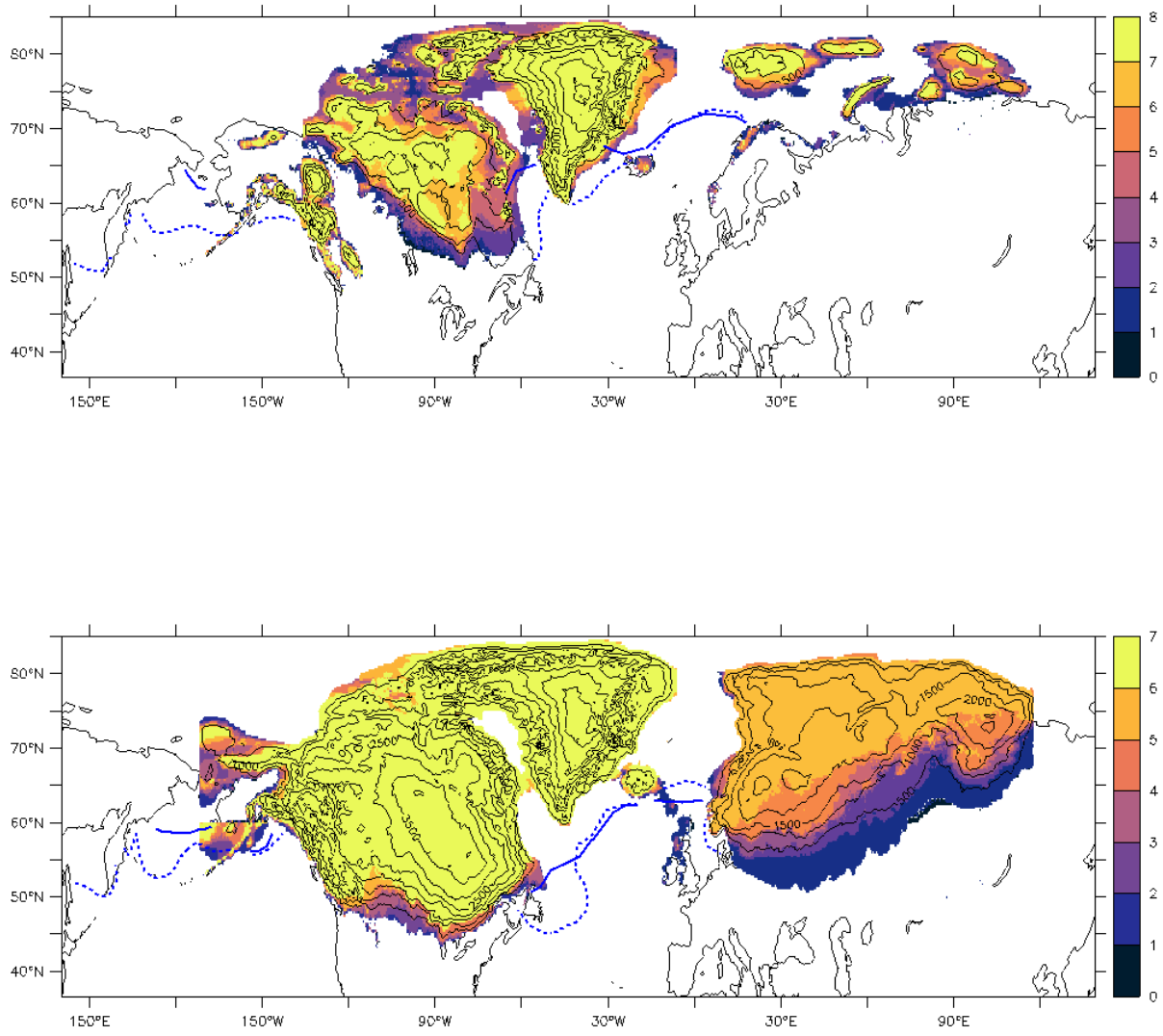

Figure 4.2: Ctrl ensemble ice cover at MIS 5d (left) and LGM (right). Maximum ice area shaded, colour indicating the number of runs out of the 7 (6 for LGM) member ensemble covering the area with ice. Contour lines indicating the ensemble mean ice sheet elevation at maximum volume (500 m steps). Blue contour lines indicating mean sea ice cover edge in October and April (dashed)

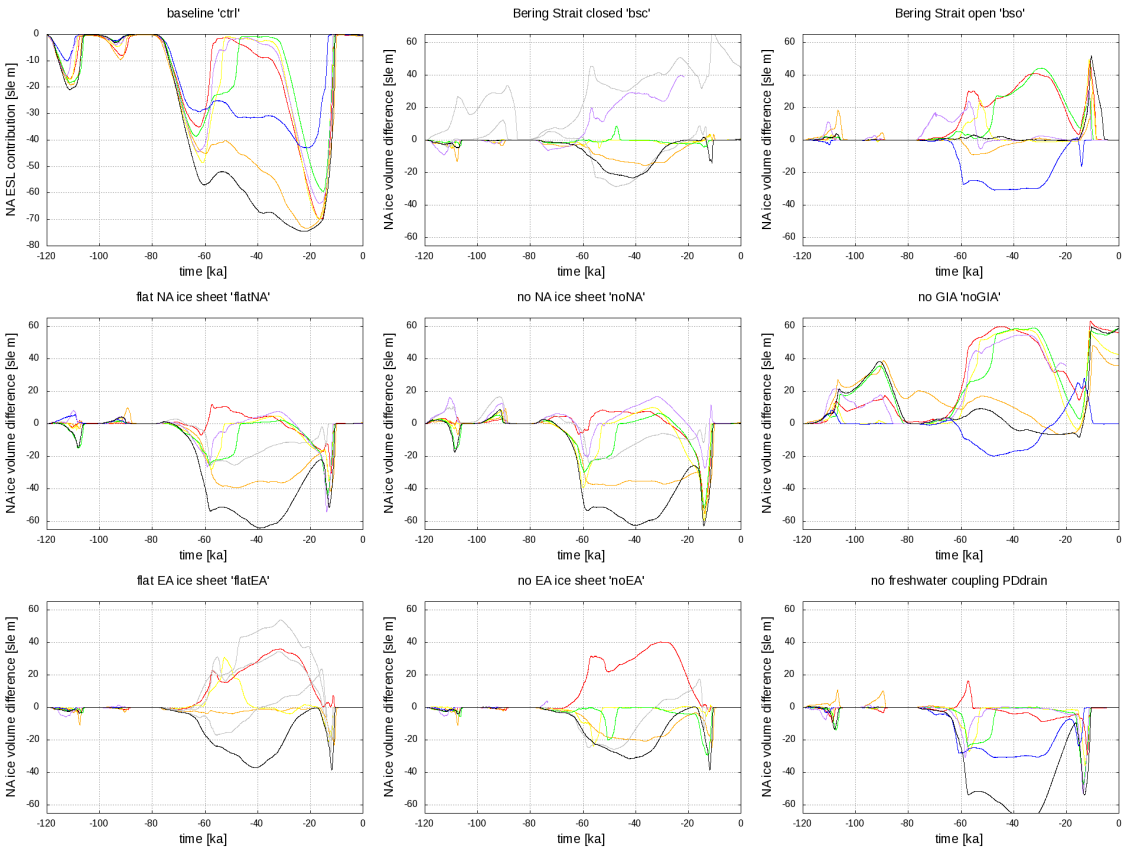

Figure 4.3: NA ice volume as eustatic sea level contribution for ctrl ensemble members (top left) and absolute difference between sensitivity-ctrl. Grey-coloured ensemble members were excluded from the analysis due to AMOC outlier behavior. Ensemble members can be included in analysis for the MIS 5d interval and excluded for the MIS 3-1 interval for said reason, then the line colour changes to gray after the MIS 5d interval

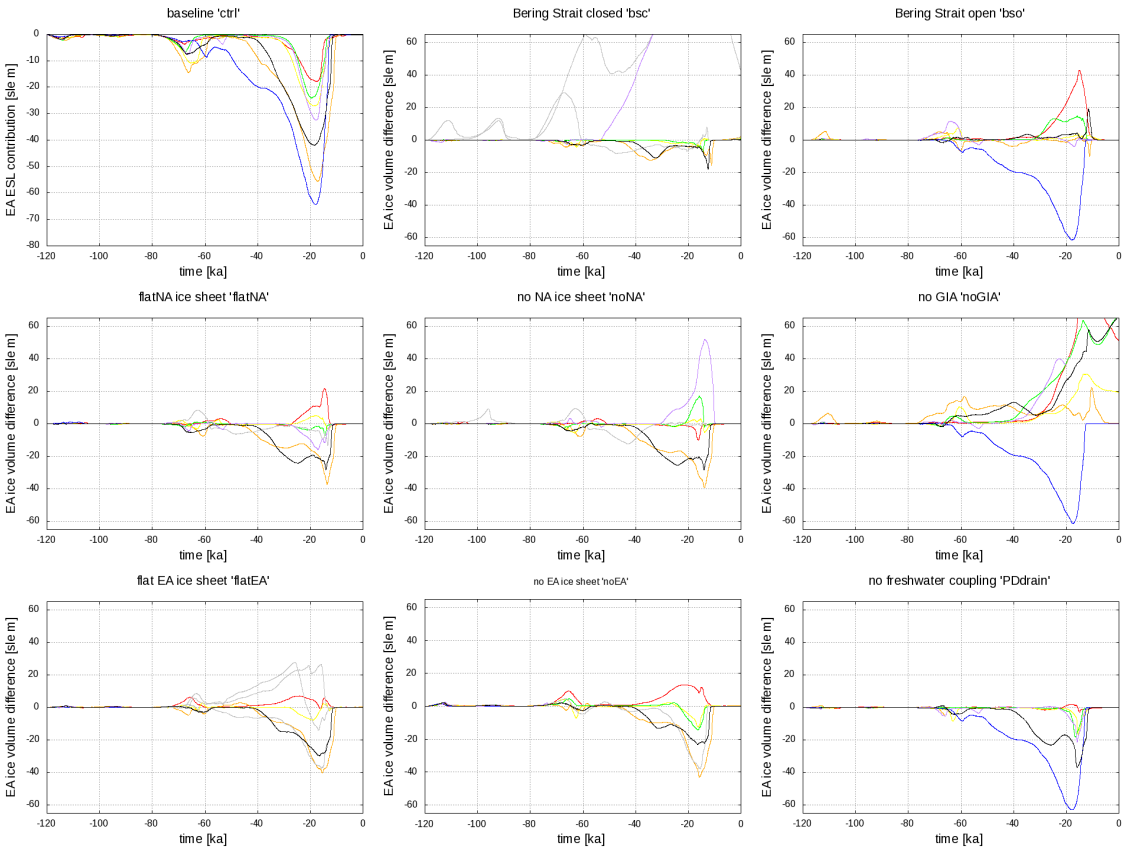

Figure 4.4: EA ice volume as eustatic sea level contribution for ctrl ensemble members (top left) and absolute difference between sensitivity-ctrl. Grey-coloured ensemble members were excluded from the analysis due to AMOC outlier behavior. Ensemble members can be included in analysis for the MIS 5d interval and excluded for the MIS 3-1 interval for said reason, then the line colour changes to gray after the MIS 5d interval

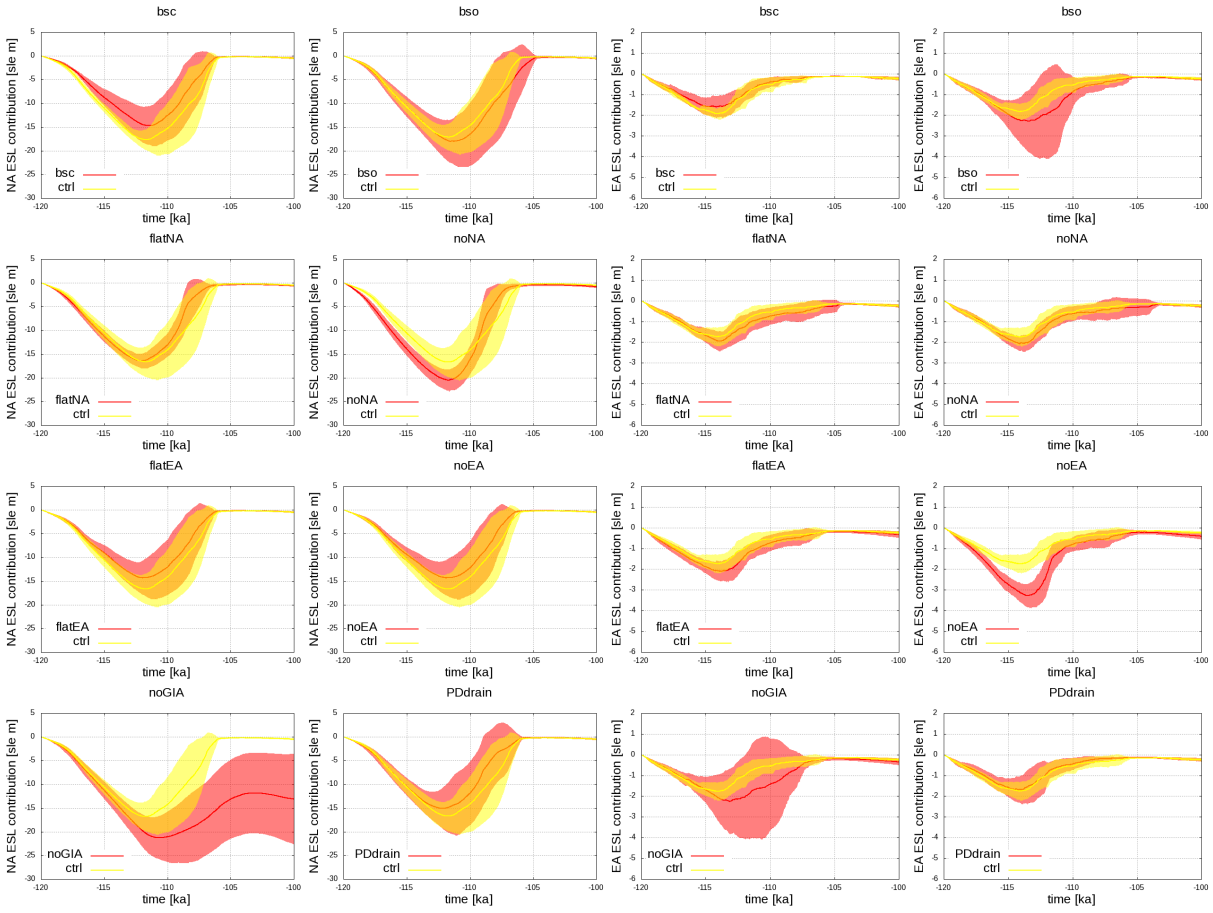

Figure 4.5: Mean NA (2 left columns) and EA (2 right columns) ice volume as contribution to global eustatic sea level and standard deviation for ctrl (yellow) and sensitivity (red) ensembles during MIS 5d

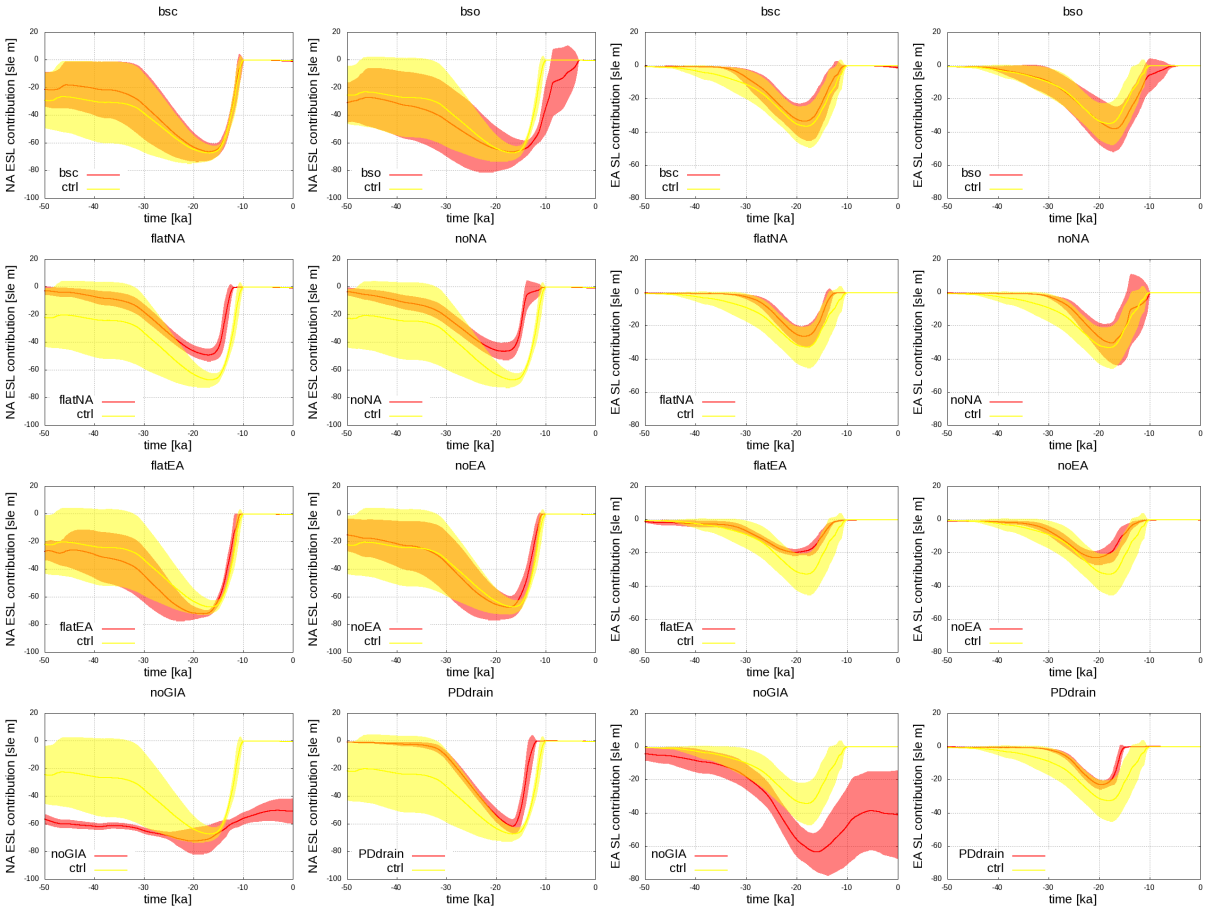

Figure 4.6: Mean NA (2 left columns) and EA (2 right columns) ice volume as contribution to global eustatic sea level and standard deviation for ctrl (yellow) and sensitivity (red) ensembles during MIS 3-1

4.4.2.1 Bering Strait closed (bsc)

To isolate the impact of Bering Strait throughflow, this experiment keeps Bering Strait continuously closed, typical of glaciated conditions. Two ensemble members are identified as nominal outliers for MIS 5d and not included in the ensemble means (displayed as thin gray lines in Figures 4.3 and following). AMOC collapses instantly at simulation start for one member, and for another after MIS 5d. AMOC collapse after MIS 5d is not implausible (as seen below for AMOC collapse after LGM); however, since AMOC does not recover for the rest of the simulation, inclusion in ensemble mean climate analysis during the MIS 3-1 interval would complicate the interpretation. Though not considered in our mean analysis, shutdown of AMOC in two of 7 simulations points to the critical role that Bering Strait throughflow can play in large scale ocean circulation. One ensemble member grows large NA and EA ice sheets towards LGM, while the rest of the ensemble has less ice than the ctrl experiments. As this large ice simulation crashed before reaching LGM, it is not included in the ensemble mean analysis of MIS 3-1.

With no Bering Strait throughflow throughout MIS 5e-c, NA and EA ice volume is decreased on average relative to ctrl (Figure 4.5). In ctrl, Bering Strait throughflow ceased at MIS 5d as sea level is low, therefore Bering Strait closure in bsc compared to ctrl mainly has an influence leading up to and after the sea level lowstand.

The cessation of Pacific water inflow to the Arctic Ocean reduces export of cold, low salinity Arctic water into the North Atlantic. There is a small increase in AMOC strength from MIS 5e-5d (Figure 4.9). This leads to increased SST (over 2 degrees in October at 115 ka, see green shading in Figure 4.7, left) in the North Atlantic

and Labrador Sea and less sea ice coverage in the Labrador Sea (see pink vs. green dashed lines in Figure 4.7, left). This influence of Bering Stait closure on AMOC and increased heat transport to the North Atlantic is also found in experiments with high resolution atmosphere-ocean models (CCSM2, 3, Hu et al., 2015, 2012). However, they furthermore find an Atlantic-Pacific seesaw behavior, where the North Pacific cools, as the Pacific southward meridional freshwater transport increases. This is not the case in our simulations. Contrarily, SST in the North Pacific just south of the Bering Strait increased over 4 degrees in bsc compared to ctrl. The Northern shallow cell of the Pacific meridional overturning circulation (PMOC) slightly strengthens in the bsc experiments compared to ctrl (see red contour vs. shading in Figure 4.8). Warmer water masses that are usually exported from the Kuroshio Current into the Arctic build up in the North Pacific, leading to increased SST (Menviel et al., 2014). Besides the increased SST in the North Pacific and North Atlantic, temperatures slightly increase over North America and Scandinavia. Due to the increased North Atlantic SST, precipitation is slightly increased over Svalbard (Appendix B.10), however, the increased temperatures outweigh the increased precipitation, leading to decreased ice volume and area. There is little change in the overall wind field (Figure in Appendix B.4).

During and leading up to LGM, there is no significant change in mean ice volume, SST, temperature, precipitation, wind field and sea ice extent. The Bering Strait is closed for half of the ensemble members already at the start of the interval at 50 ka. By 25 ka, throughflow is shut down for all ctrl ensemble members. AMOC intensity in the bsc experiment is similar to ctrl up to 10 ka, where AMOC is collapsed. Contrary to the ctrl ensemble, however, AMOC does not recover from the collapse until the

end of the simulation (see Figure 4.9). When Bering Strait is closed, fresh water from the melting ice sheets is not efficiently transported out of the North Atlantic and buoyancy forcing accumulates (Hu et al., 2015), leading to the collapse of AMOC. When the Bering Strait opens up (in ctrl), the influx of Pacific water from the Arctic diminishes the impact of the fresh melt water (Pöppelmeier et al., 2021) while melt water keeps accumulating in the bsc experiments. In freshwater hosing experiments, Pöppelmeier et al. (2021) found that AMOC recovery (after the freshwater hosing decreased) took significantly longer when Bering Strait was closed than when it was open.

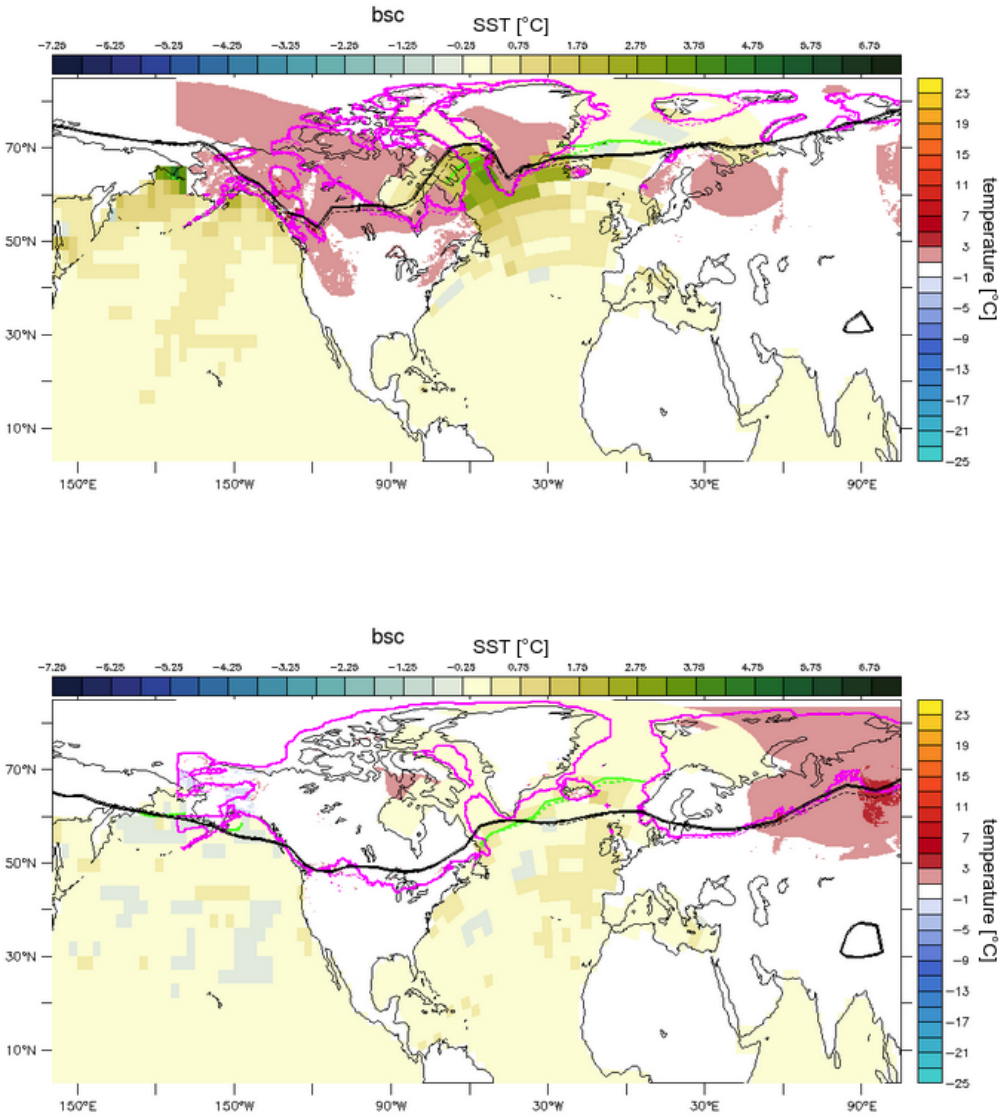

Figure 4.7: Difference bsc-ctrl ensemble mean of October SST (blue-green shading) and GSM JJA temperature over ice sheet domains scaled down to sea level (cyan-yellow shading) at 115 ka (top) and 21 ka (bottom), about 2-3 kyrs before reaching sea level minimum. Black contour lines: ensemble mean LOVECLIM summer (JJA) 0° isotherm, green contour lines: ensemble mean October sea ice extent, pink contour line: ensemble mean ice sheet extent, solid lines: bsc, dashed lines: ctrl

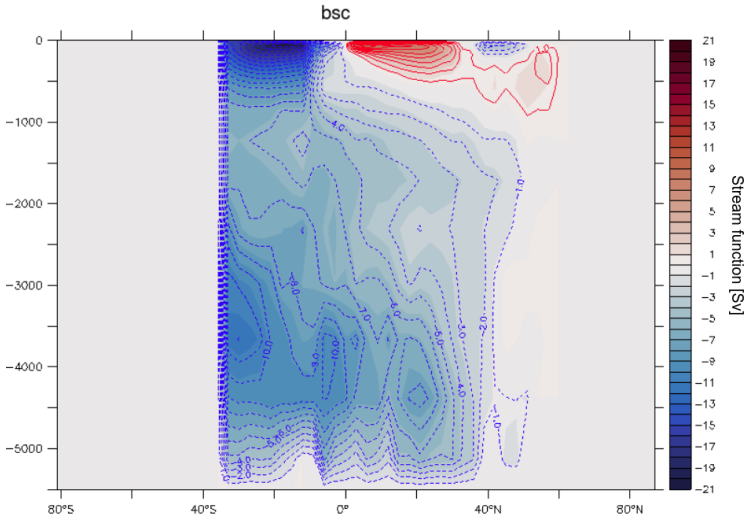

Figure 4.8: PMOC streamfunction for ctrl (shading) and bsc (contour) experiments at 115 ka

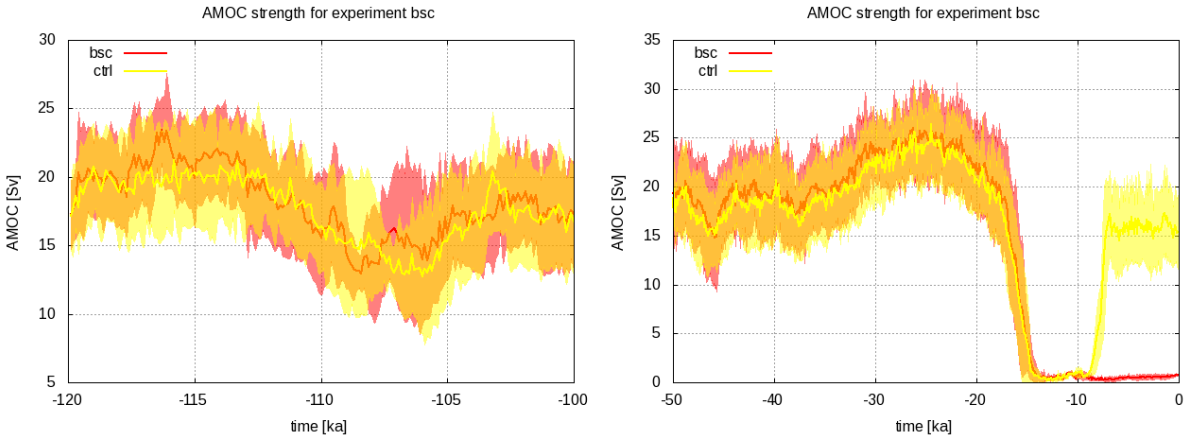

Figure 4.9: Ensemble mean and standard deviation of AMOC strength for the MIS 3-1 interval. Red: bsc, yellow: ctrl

4.4.2.2 Bering Strait open (bso)

In the bso experiment, the constant input of Pacific water into the Arctic Ocean leads to enhanced export of relatively fresher water from the Arctic into the North Atlantic Ocean. Therefore, AMOC strength is decreased compared to ctrl during inception (see Figure 4.10). With decreased AMOC strength, SST are decreased during MIS 5d in the bso experiment in both the North Atlantic and GIN (Greenland-Iceland-Norwegian) Seas (see blue shading in Figure 4.11), and sea ice extends further south. This leads to a small decrease in temperature over EA and to a larger EA ice sheet. However, intra-ensemble variance is strongly increased. One outlier displays a very large increase, distorting the mean; the other ensemble members only display small increases.

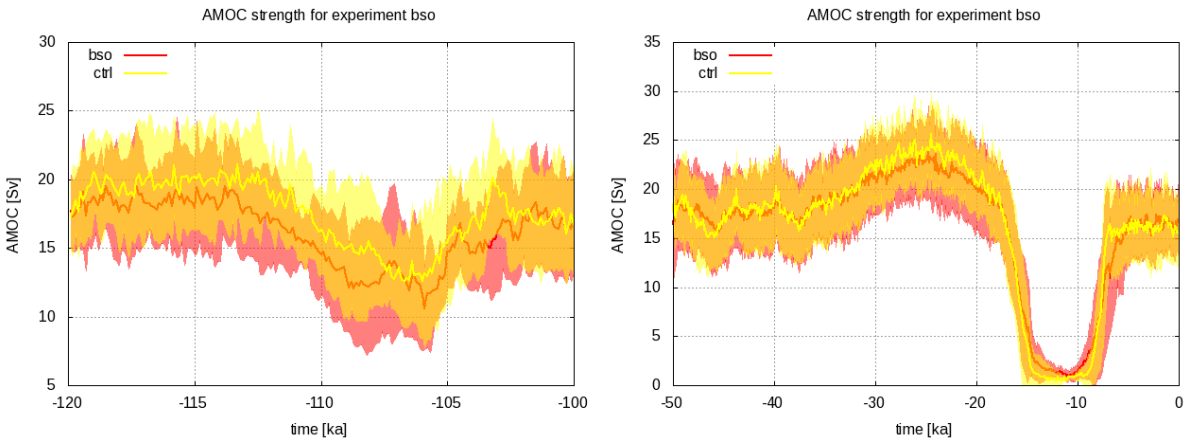

Figure 4.10: Ensemble mean and standard deviation of AMOC strength for the MIS 5d (left) and MIS 3-1 (right) interval. Red: bso, yellow: ctrl

At LGM, there is a large variability in ice volume (Figure 4.3,4.4) and climate metric responses which cancel each other out in the ensemble mean (Figure 4.6). Half

of the ensemble displays a decrease in AMOC strength and an associated cooling in the North Atlantic region; half of the ensemble shows little change in AMOC and a variety of temperature responses. In the ensemble mean, there is no significant change in AMOC (Figure 4.10). Analyzing individual ensemble members is beyond the scope of this paper. We speculate that the export of Arctic water into the Atlantic might be slowed down in some experiments due to the increased perennial sea ice cover in the North Atlantic; and/or the transport of freshwater out of Arctic Ocean is tightly held in Greenland boundary current thereby avoiding mixing into the GIN Seas.

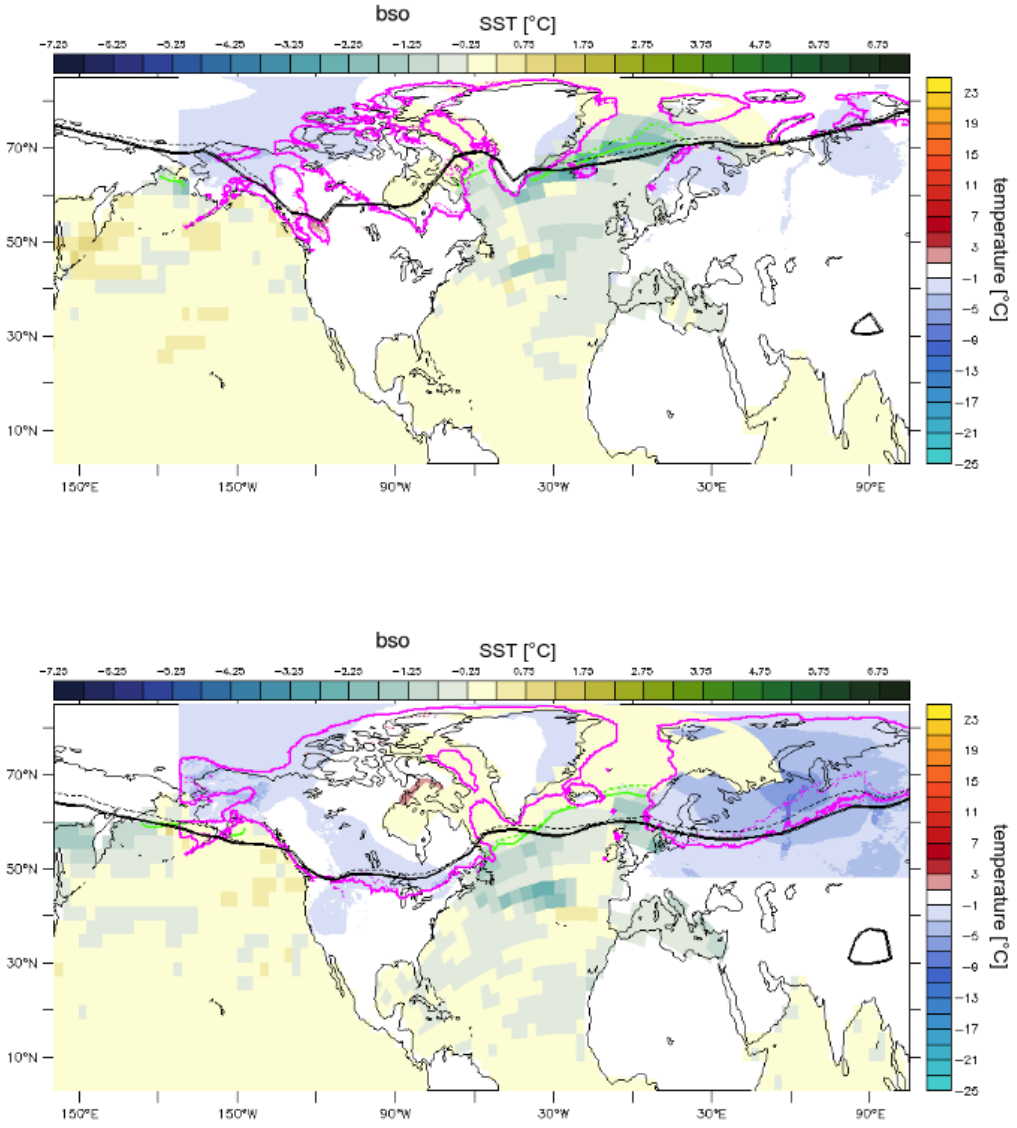

Figure 4.11: Difference bso-ctrl ensemble mean of October SST (blue-green shading) and GSM summer (JJA) temperature over ice sheet domains scaled down to sea level (cyan-yellow shading) at 115 ka (top) and 21 ka (bottom), about 2-3 kyrs before reaching sea level minimum. Black contour lines: ensemble mean LOVECLIM summer (JJA) 0° isotherm, green contour lines: ensemble mean October sea ice extent, pink contour line: ensemble mean ice sheet extent, solid lines: bso, dashed lines: ctrl

4.4.2.3 Flat and removed NA ice sheet (flatNA, noNA)

The configuration difference between the flat and no-ice experiments is a constant PD LOVECLIM ice mask in the latter. This primarily impacts surface albedo. However, even in the no-ice experiments seasonal snow coverage will overlap most if not all of the ice sheet area in the flat-ice experiments, rendering limited isolation of albedo response. Therefore, we analyze the two sensitivity experiments flatNA and noNA (and flatEA and noEA below) in part together. Of particular interest is the mutual influence of the NA and EA ice sheets.

The temperature response over EA to the flat or removed NA ice sheet is highly variable across the ensemble (not shown), leading to only minimal changes on average (Figure 4.12). During MIS 5d, the mean EA ice volume increases slightly (not significantly) for both flat NA and noNA (Figure 4.5, right). During LGM, on the other hand, the mean EA ice sheet volume is slightly decreased compared to ctrl (Figure 4.6, right). Again the response is highly variable across the ensemble as shown in Figure 4.4. For flatNA (noNA), two out of six ensemble members show an increase in EA ice volume, three (two) a decrease, and one (two) little to no change. Ensemble members displaying one response in the flatNA experiment do not necessarily display the same response in the noNA experiment. As such, for at least some of the ensemble members, as such the whole system response to the imposed changes in surface albedo is potentially very non-linear.

Other sensitivity studies that tested the influence of the NA on the EA ice sheet in higher resolution models have found that especially at LGM, the Laurentide ice sheet changes the atmospheric stationary wave pattern (Ullman et al., 2014) and

therefore influences EA ice sheet growth. The eastward growth of the EA ice sheet is restricted as the NA ice sheet triggers an anomaly in the summer stationary wave field leading to a warming over Siberia and a cooling over Europe, causing the EA ice sheet to migrate westward (Liakka et al., 2016). LCice's atmospheric resolution is too coarse to fully capture this phenomena. While there is a small change in the wind field downstream of the NA ice sheet, the impact does not reach far enough to cause a significant relocation of the EA ice sheet. Three out of seven ensemble members simulate an increase in temperature over Europe when the NA ice sheet is flat or removed, which would match the above mentioned studies. The other ensemble members simulate no change or even a decrease in temperature.

At MIS 5d, there is virtually no change of the 800 hPa wind field directly over EA aside from a more southerly flow over central and eastern Fennoscandia (Figure 4.13, top). There is a change in the mean wind over NA and the North Atlantic during both MIS 5d and LGM which impacts AMOC. The winter winds (generally stronger than summer winds, see supplements Figure B.5) over the Atlantic are decreased. This will weaken the Gulf Stream and thereby decrease AMOC strength (see Figure 4.14) and depth of the NADW formation cell (supplement Figure B.3) in the flat/noNA experiments compared to ctrl. At MIS 5d, this leads to slightly decreased SST in the GIN Seas (blue shading in Figure 4.12, top).

Leading up to LGM, SST changes are dominated by a consistent warming in the Labrador Sea (Figure 4.12). In the ctrl experiment, the extensive NA ice sheet deflects the polar front and the strong winter wind around the Greenland high pressure system to the south (black arrows in Figure 4.13, bottom). This brings cold Arctic air to the Labrador Sea region. In the flat/noNA experiment, the deflecting ice sheet is

missing and there is no southward component in the wind field in the area, leaving the Labrador Sea about 5 °C warmer. Therefore, sea ice cover is decreased (dashed pink line in Figure 4.12 and 4.13). In ctrl winter, sea ice on the west side of the North Atlantic reaches south to 45 °N. In the noNA experiments, sea ice only extends from the northern edge of Newfoundland to the southern edge of Iceland. SSTs are furthermore decreased in the north Pacific off the North American coast. In summer, the noNA wind field has a stronger north-south component along the North American west coast than in ctrl (Appendix B.7). This leads to upwelling along the coast and decreased SST.

The influence of the NA ice sheet on itself is not straight forward. The atmosphere is uncoupled from the evolving ice sheet topography (and partially albedo changes). Therefore, the ice sheet does not experience the self-induced local cooling of its surroundings as in ctrl beyond that due to surface elevation gain. On the other hand, due to that lack of cooling, moisture fluxes can be increased and more precipitation is available for ice growth. Furthermore, wind fields and therefore precipitation patterns over the ice sheet area will be different. A large ice sheet can deflect winds southward, and the flanks of the ice sheet can force orographic precipitation. The changed precipitation and temperature patterns can oppose each other's effect on ice sheet evolution.

For the flatNA experiments, the influence of the NA ice sheet on its own ice volume evolution at MIS 5d is mixed across the ensemble so that there is no change in NA ice volume on average. However, there is a uniform change in ice sheet geometry. The flatNA ice sheet reaches less far south but covers more of the Canadian archipelago and Baffin island (see red and blue shading in Figure 4.13) due to the removal of

precipitation shadowing. In a fully coupled system, precipitation will mainly fall at the west flank of an ice sheet due to topographic forcing (under westerly wind influence as is largely the case in mid-latitudes). In the noNA and flatNA experiments, more precipitation reaches the north-eastern section of the uncoupled ice sheet (see Figure 4.15 for noNA ensemble, left).

There is a similar geometry shift in the noNA experiments as the flatNA. Additionally, the NA ice sheet volume increases. The expected key difference between noNA and flatNA is the extent of summer snow cover in the noNA versus ice sheet extent in the flatNA experiments (black contour lines in Figure 4.12 representing 0 °JJA isotherm, which should be proximal to the snow line). However, there is no significant difference between the southern extent of the 0 °isotherm between flat and noNA experiments (not shown). There is also no change in wind patterns between noNA and flatNA experiments (Appendix B.4). The increase in ice volume for noNA compared to flatNA is largely due to an increased ice thickness over the Canadian archipelago and a thin merger between the northern Laurentide and Cordilleran ice sheet (merged only for one ensemble member, see pink solid and dashed contour lines in Figure 4.13). In these areas, the noNA ensemble has slightly higher precipitation rates than the flatNA experiments (see Figure 4.15, right). The increased warmth due to the missing albedo cooling must lead to this small increase in precipitation and increased ice volume.

During MIS 3, the intra-ensemble variability is significantly reduced in the noNA and flatNA experiments; all ensemble members follow the trajectory of a strong interstadial where NA ice sheets are close to completely retreated (Figure 4.6).

At LGM, the noNA and flatNA experiments have significantly decreased NA ice

volume and a lower mean ice height, displayed in Figure 4.13, bottom. Sea level temperatures are significantly increased, even for the flatNA case. Changes in atmospheric circulation likely play a role in this warming as well as in precipitation changes. In ctrl, a strong anticyclone builds over the NA ice sheet (black arrows in Figure 4.13). For noNA and flatNA, this is not the case and the ice sheet area is under weak jetstream influence (red arrows in Figure 4.13). Less precipitation reaches the south and south of the margin of the Laurentide ice sheet in the sensitivity experiments than in ctrl (Figure 4.16). As described above, the NA ice sheet in the ctrl experiment deflects the polar front leading to a mean north-easterly wind from the Labrador Sea towards the south-eastern ice margin. For the uncoupled ice sheet, this region is under the undeflected impact of the westerlies. These will carry less humidity to this region than the onshore winds in ctrl. Furthermore, there is no orographic forcing of precipitation at the ice margin in LOVECLIM for the no/flat NA experiments. Therefore, precipitation at the south-eastern margin is decreased and the ice extent less far south. Precipitation is increased, on the other hand, over the Cordillera. The jet stream is not deflected by the ice sheet topography in no/flatNA and air masses reach the mountain range directly from the Pacific (Figure 4.16).

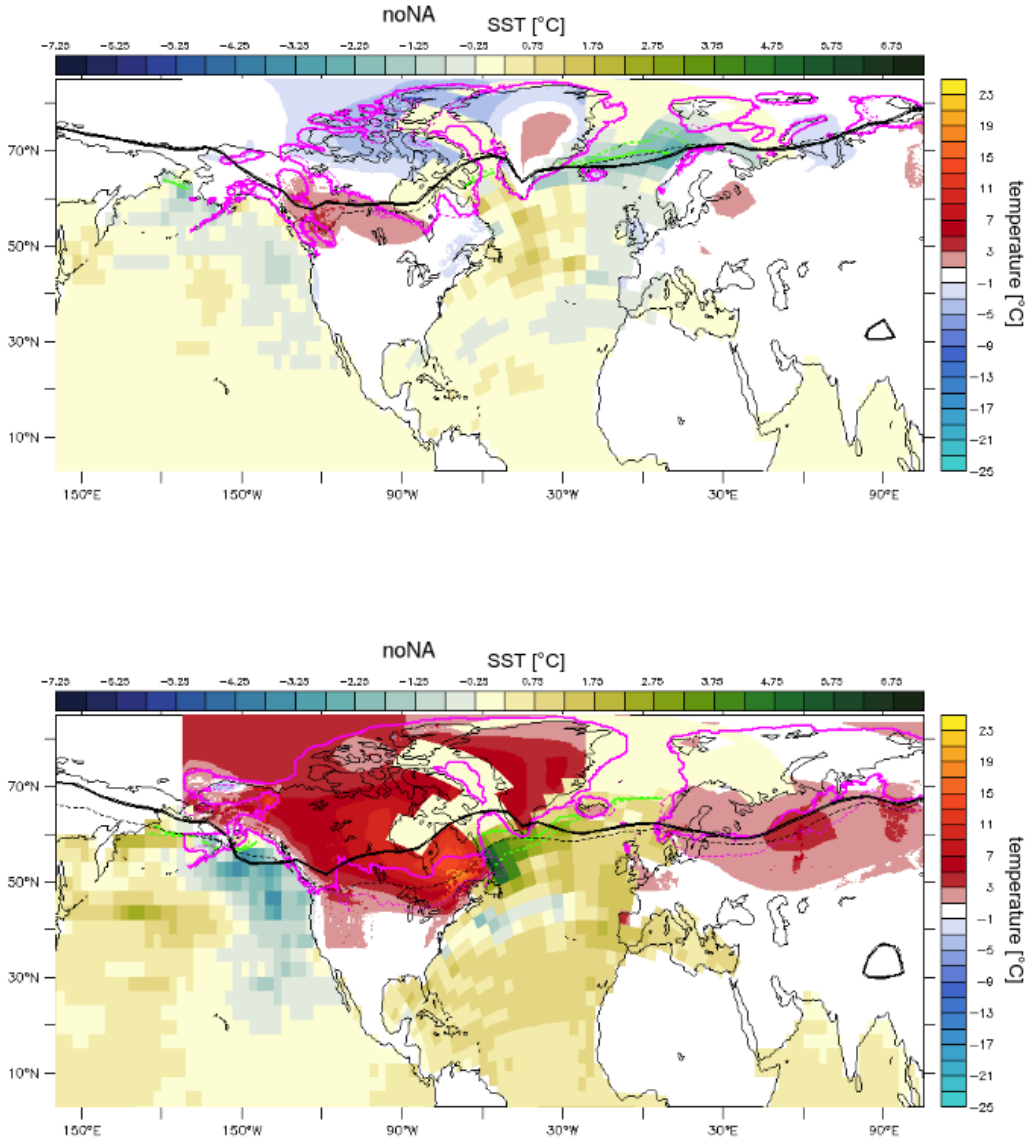

Figure 4.12: Difference noNA-ctrl ensemble mean of October SST (blue-green shading) and GSM summer (JJA) temperature over ice sheet domains scaled down to sea level (cyan-yellow shading) at 115 ka (top) and 21 ka (bottom), about 2-3 kyrs before reaching sea level minimum. Black contour lines: ensemble mean LOVECLIM summer (JJA) 0° isotherm, green contour lines: ensemble mean October sea ice extent, pink contour line: ensemble mean ice sheet extent, solid lines: noNA, dashed lines: ctrl

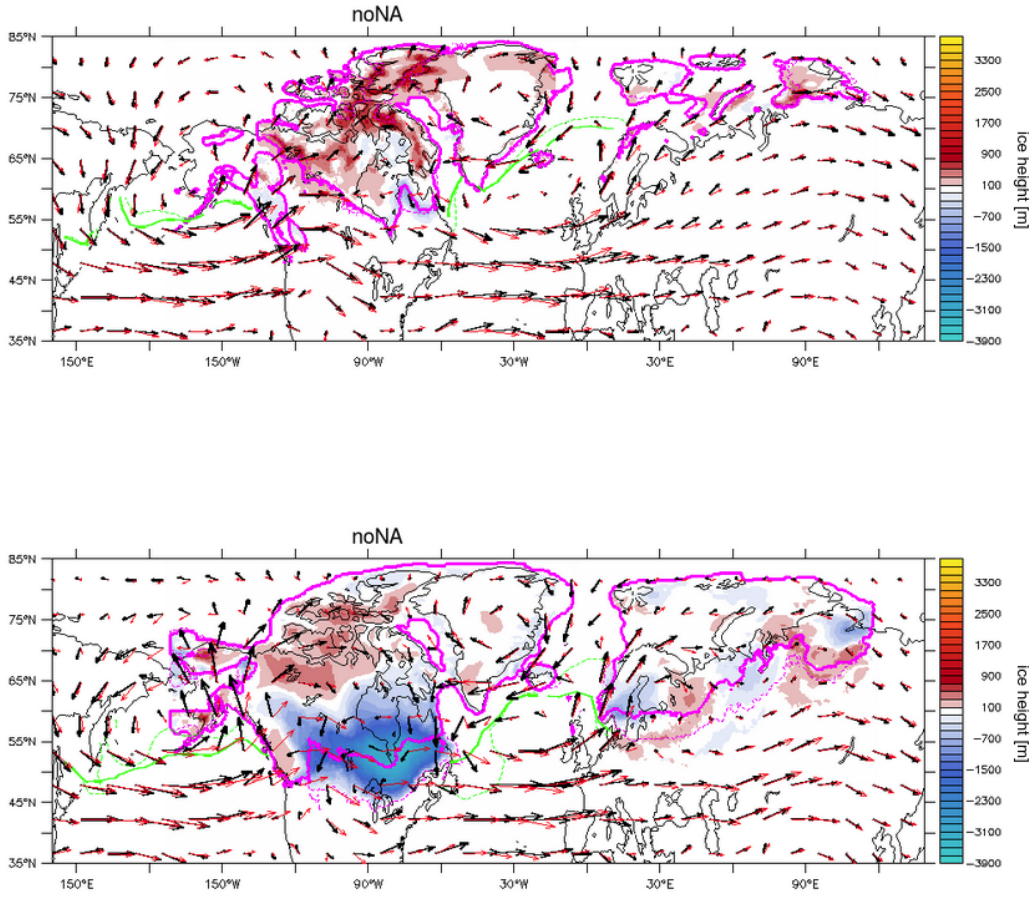

Figure 4.13: DJF 800 hPa ensemble mean wind field and difference in mean ice height (noNA-ctrl) at the time of EA maximum ice volume during MIS 5d (left) and LGM (right). Black arrows: ctrl, red arrows: noNA. Green contour lines: ensemble mean October sea ice extent, pink contour line: ensemble mean ice sheet extent, solid lines: noNA, dashed lines: ctrl.

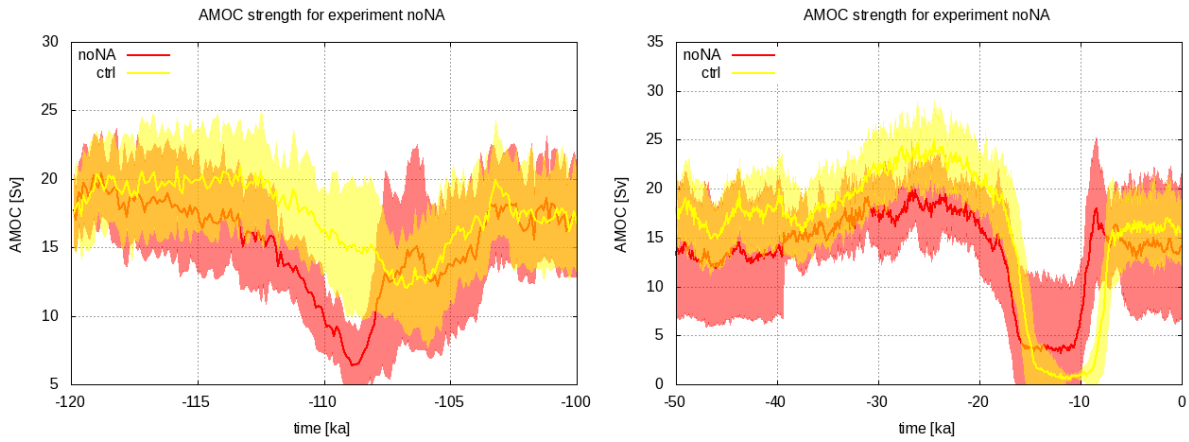

Figure 4.14: Ensemble mean and standard deviation of AMOC strength for the MIS 5d (left) and MIS 3-1 (right) interval. Red: noNA, yellow: ctrl

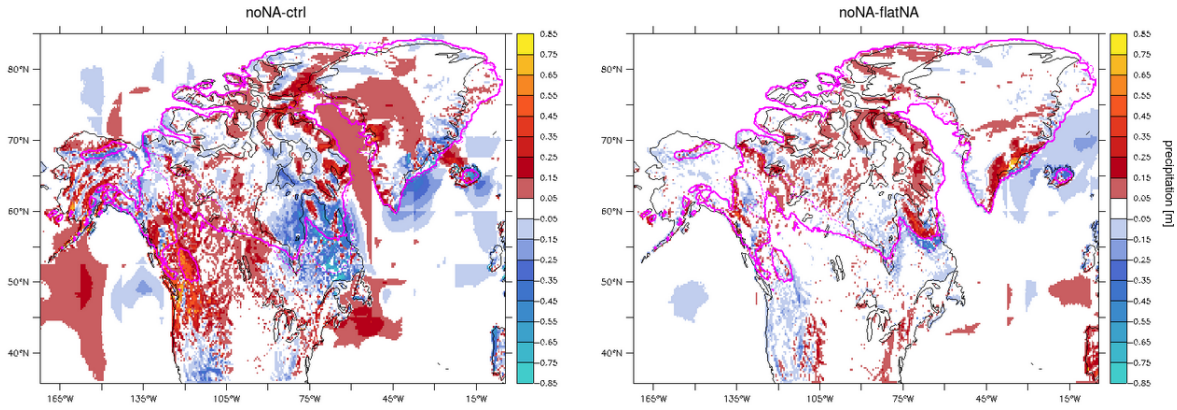

Figure 4.15: Difference in precipitation at 114 ka. Left: noNA-ctrl, green (pink) contour line: ctrl (noNA) ice sheet extent; right: noNA-flatNA ensemble mean. Black (cyan) contour line: mean noNA (flatNA) ice sheet extent

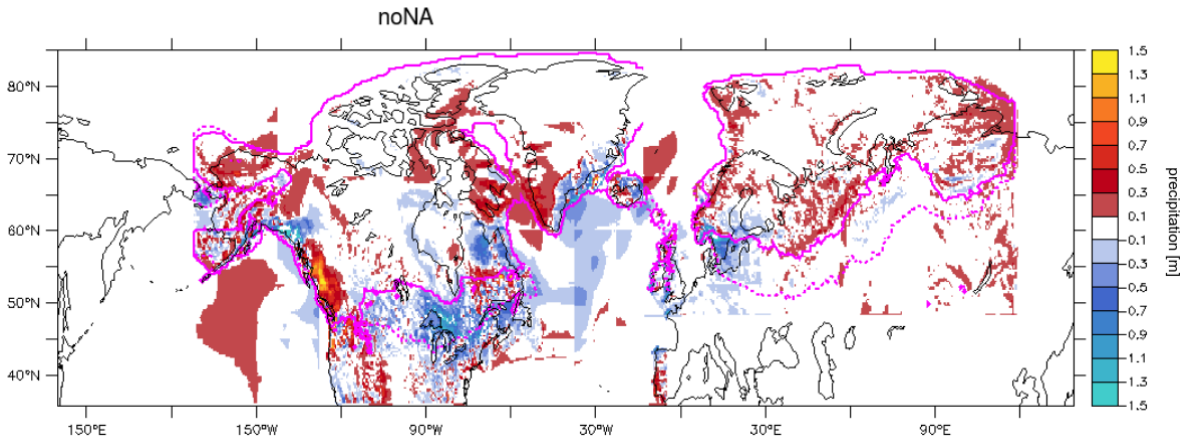

Figure 4.16: Mean difference noNA-ctrl in precipitation at 21 ka. Pink contour line: ensemble mean ice sheet extent, solid: noEA, dashed: ctrl

4.4.2.4 Flat and removed EA ice sheet (flatEA, noEA)

The EA ice sheet has on average no significant influence on NA ice volume at MIS 5d and LGM (Figure 4.5 and 4.6). There is a small increase in temperature over Alaska and northern Canada during MIS 5d in both the noEA and flatEA ensemble, which leads to a small decrease in NA ice volume compared to ctrl. During MIS 3, the impact on NA ice volume is large and highly variable for individual ensemble members, which cancels out in the mean ice evolution.

The influence of the EA ice sheet on itself is highly variable across the ensemble. During MIS 5d, over the North Atlantic and parts of Eurasia, ensemble members display both warming and cooling, precipitation increases and decreases, which cancel each other out in the ensemble mean. A semi-consistent feature of the flat/noEA ensemble compared to ctrl is an increase in precipitation over Franz Josef Land. The EA ice volume increases in this area (Figure 4.18). In the flatEA ensemble, the majority of ensemble members displays a light warming over Siberia compared to ctrl (Appendix B.8). In the noEA ensemble, on the other hand, the majority of ensemble members display a light cooling in Siberia (Figure 4.17). Although the changes are small, the noEA ice sheet gains significant volume in these regions at MIS 5d while the flatEA ensemble shows only a small ice volume increase compared to ctrl. There is virtually no change in the mean wind field outside of the EA ice sheet (Appendix B.4).

At LGM, EA ice volume is decreased in both noEA and flatEA experiments compared to ctrl. Due to the uncoupled EA ice sheet and the lack of its cooling effect, temperature over EA increases significantly during LGM (similar to flat/noNA), and

the signal extends to the NA ice sector over Alaska (Figure 4.17). Parts of the northern sector of the EA ice sheet have more precipitation for flat/noEA compared to ctrl while the southern sector generally has less (Figure 4.18). The ice sheet extends less far to the south but further west, covering parts of Great Britain.

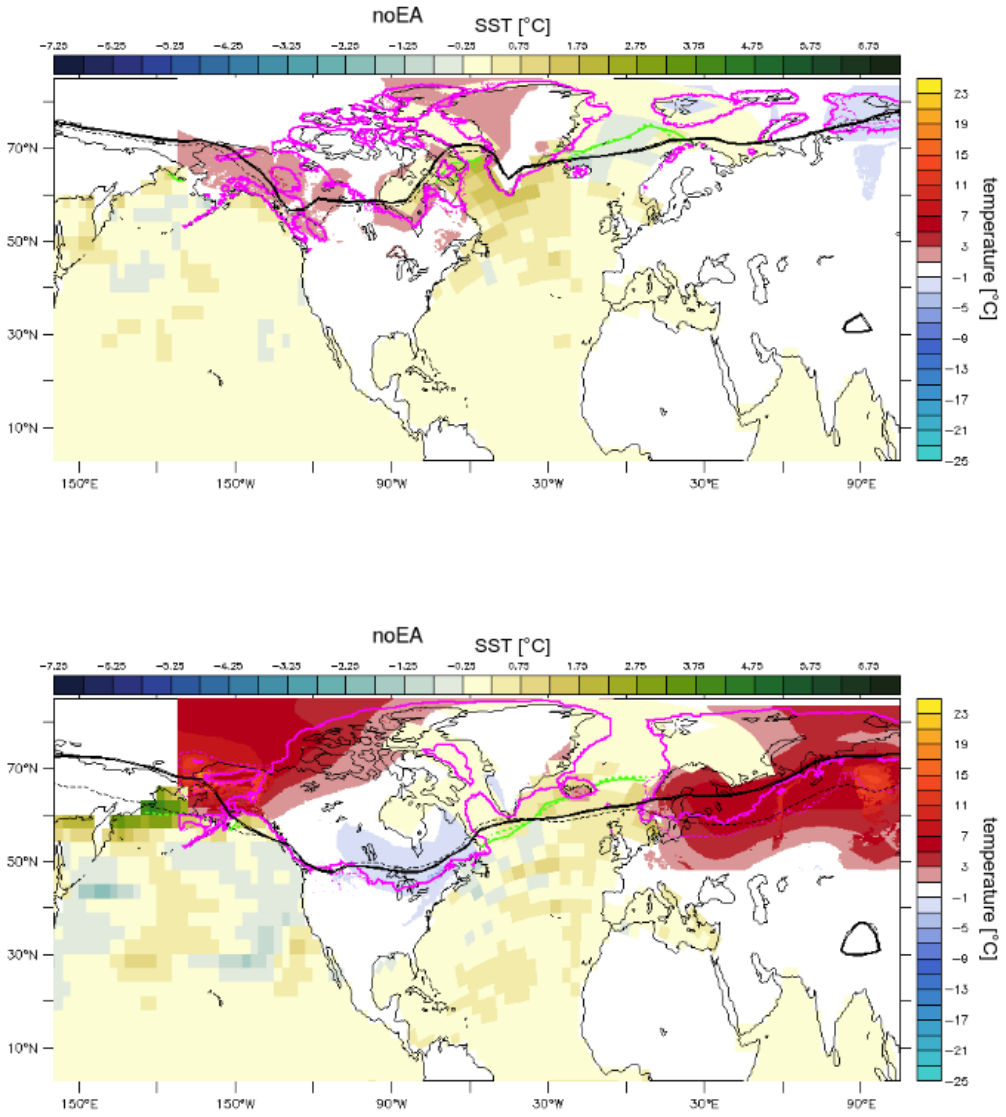

Figure 4.17: Difference noEA-ctrl ensemble mean of October SST (blue-green shading) and GSM summer (JJA) temperature over ice sheet domains scaled down to sea level (cyan-yellow shading) at 115 ka (top) and 21 ka (bottom), about 2-3 kyrs before reaching sea level minimum. Black contour lines: ensemble mean LOVECLIM summer (JJA) 0° isotherm, green contour lines: ensemble mean October sea ice extent, pink contour line: ensemble mean ice sheet extent, solid lines: noEA, dashed lines: ctrl

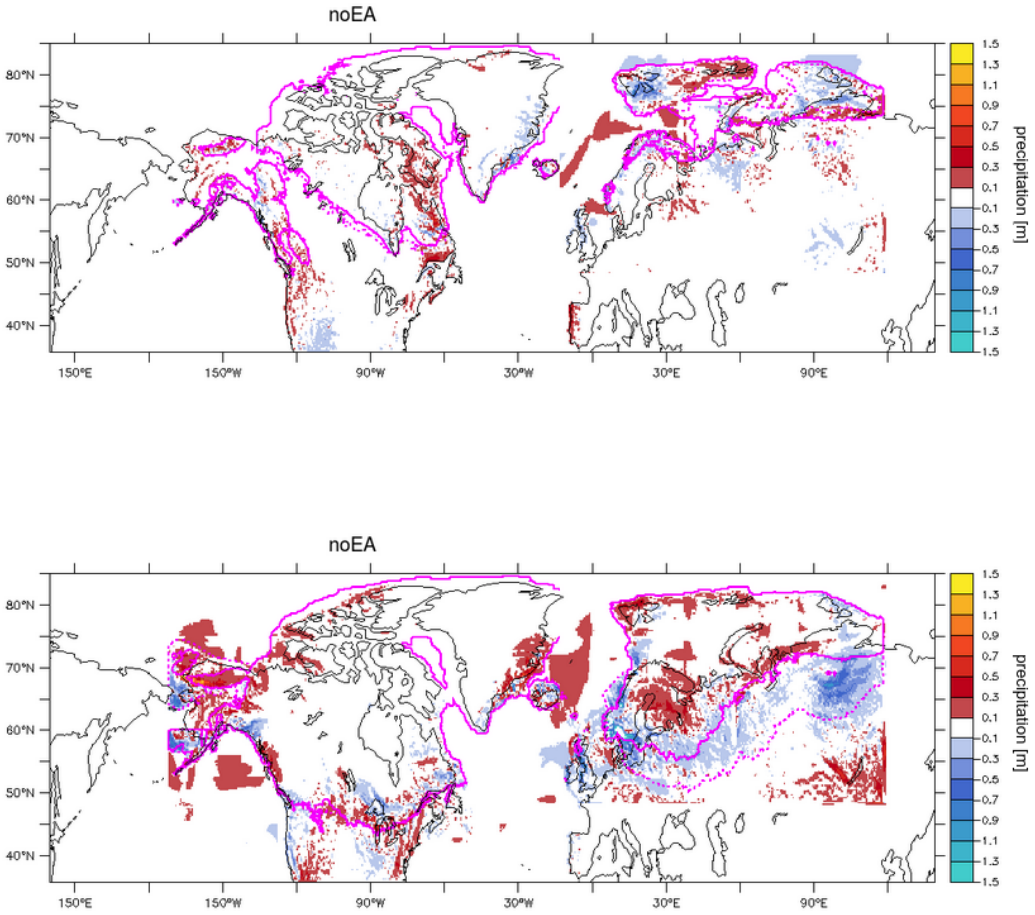

Figure 4.18: Mean difference noEA-ctrl in precipitation at 114 ka (top) and 21 ka (bottom). Pink contour line: ensemble mean ice sheet extent, solid: noEA, dashed: ctrl

4.4.2.5 No GIA (noGIA)

During MIS 5d, both NA and EA ice sheet volumes significantly increase in the noGIA experiments compared to ctrl (Figure 4.5). This is largely due to increased ice thickness as opposed to increased ice extent (Figure 4.21). There is no significant change in SST and sea ice cover during the MIS 5d maximum (Figure 4.21).

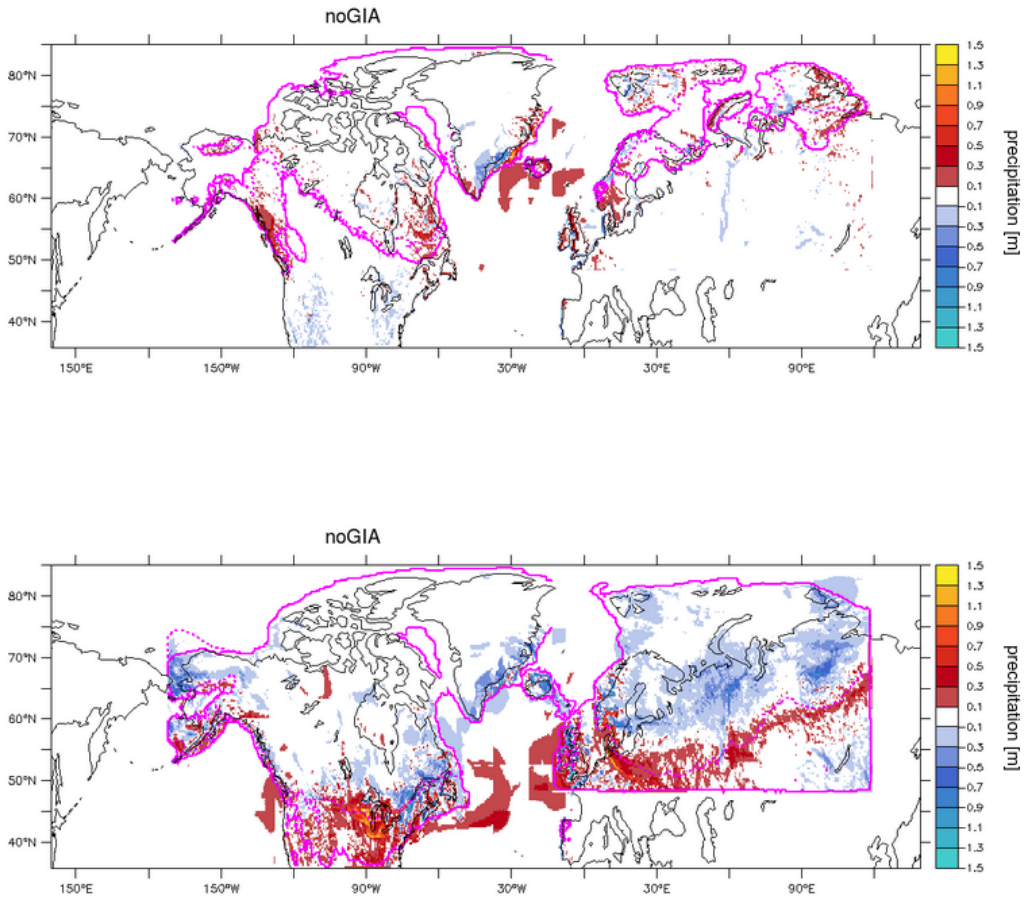

Figure 4.19: Mean difference noGIA-ctrl in precipitation at 114 ka (top) and 21 ka (bottom). Pink contour line: ensemble mean ice sheet extent, solid: noGIA, dashed: ctrl

The MIS 5d noGIA EA ice sheet displays a large ensemble variance, as one ensemble member increases its EA ice volume massively while the others have small to moderate increases (Figure 4.4).

The noGIA NA ice sheet growth towards LGM is limited as it already has the volume of ctrl LGM at 50 ka. Only one ensemble member grows additional ice towards LGM, while the others have plateaued.

Figure 4.20 shows that the northern sector of the NA ice sheet has a lower ice thickness in the noGIA experiments than in ctrl. However, the ice sheet reaches further south and therefore ice thickness in the southern sector is higher. The noGIA ice sheet reaches about 500 m higher elevations than the ctrl NA ice sheet in the ice sheet center around Hudson Bay. Figure 4.19 shows that at these high elevations, precipitation is slightly decreased compared to ctrl. Absolute precipitation (not shown) is close to zero over the northern half of the ice sheet at 21 ka and becomes the limiting factor for further ice growth in noGIA. Only south of 50 °N precipitation in noGIA is increased compared to ctrl, leading to the increased ice extent.

Over EA, the changes in precipitation are similar to NA, a decrease in the northern and an increase in the southern sector. The increase in precipitation and the decrease in temperature has such a large impact over EA that the ice sheet extents to the maximum boarders of the GSM domain.

Due to the large ice sheets, all of the northern Hemisphere experiences a cooling compared to ctrl (Figure 4.21). Sea ice extends significantly further south in the North Atlantic. This does not impact the location of NADW formation (Figure in Appendix B.3).

As long ago shown in GIA sensitivity experiments with a much simpler coupled

climate model (Tarasov and Peltier, 1997), the removal of GIA strongly weakens glacial retreat. For ctrl, a positive feedback loop is triggered as the ice starts to retreat. Due to GIA, the ice margins sit at lower elevation. When the ice starts melting, the overall ice sheet elevation decreases further, as the isostatic uplift is not instantaneous. Due to the low altitude, temperatures are mild and the ice sheet keeps retreating. Furthermore, the ice slope becomes increasingly steeper as the ice retreats into the GIA-induced bed depresssion. Increased slopes increase the ice flux into the ablation zone and therefore melting. The thicker LGM ice in ctrl will also drive warmer basal temperatures which will decrease ice viscosity and increase the fraction of ice subject to streaming. Without GIA, the ice surface elevation will tend to be higher in noGIA experiments than in ctrl, keeping the ice at colder temperatures due to the high altitudes. Compared to NA, the EA ice sheet has a smaller impact on continental scale climate and also a larger ice margin to ice area ratio making it more sensitive to climate forcing. This is evident in the complete noEA deglaciation during MIS 5c. At LGM, however, the noGIA EA ice sheet displays the same behavior as NA during MIS 5d. Over 50 % of both ice sheets remains up to PD. Since the freshwater flux into the North Atlantic is decreased due to the limited ice sheet retreat after LGM, AMOC decreases, but does not completely collapse as in ctrl (Appendix Figure B.2).

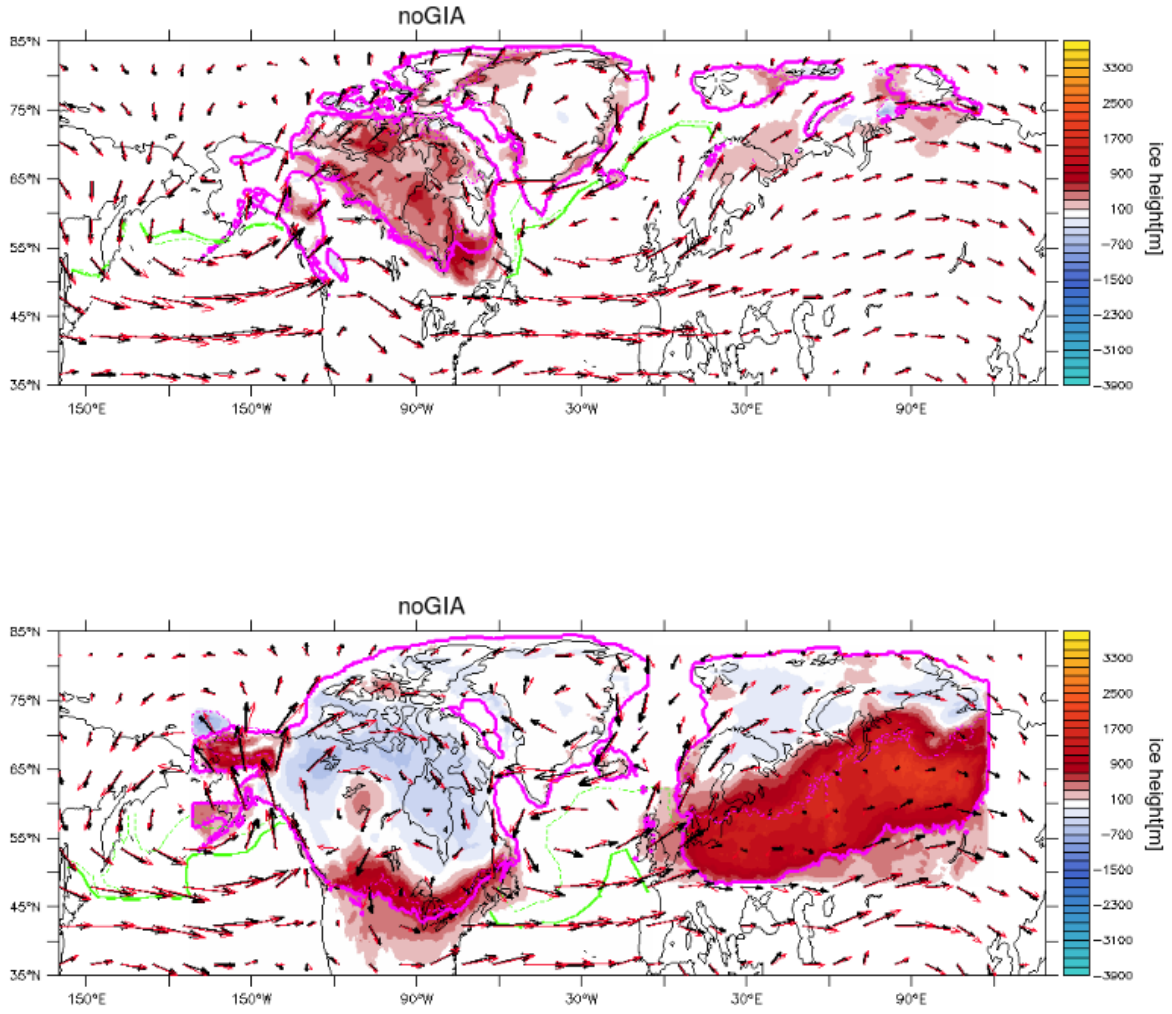

Figure 4.20: DJF 800 hPa ensemble mean wind field and difference in mean ice height (noGIA-ctrl) at the time of EA maximum ice volume during MIS 5d (left) and LGM (right). Black arrows: ctrl, red arrows: noGIA. Green contour lines: ensemble mean October sea ice extent, pink contour line: ensemble mean ice sheet extent, solid lines: noGIA, dashed lines: ctrl.

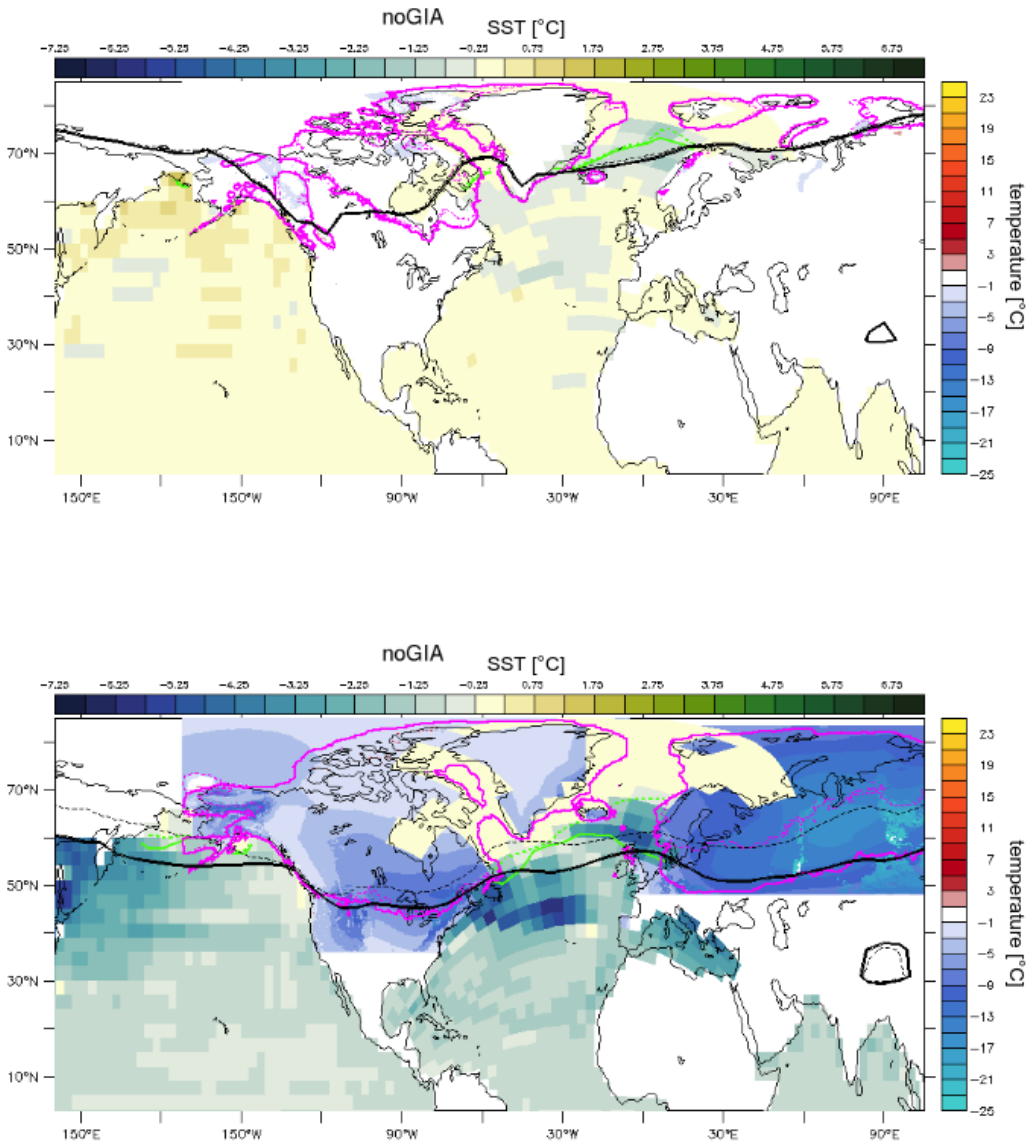

Figure 4.21: Difference noGIA-ctrl ensemble mean of October SST (blue-green shading) and GSM summer (JJA) temperature over ice sheet domains scaled down to sea level (cyan-yellow shading) at 115 ka (top) and 21 ka (bottom), about 2-3 kyrs before reaching sea level minimum. Black contour lines: ensemble mean LOVECLIM summer (JJA) 0° isotherm, green contour lines: ensemble mean October sea ice extent, pink contour line: ensemble mean ice sheet extent, solid lines: noGIA, dashed lines: ctrl

4.4.2.6 PD drainage routes (PDdrain)

In the PDdrain experiments, GSM freshwater storage and induced river routing changes are decoupled from LOVECLIM for which all precipitation is immediatedly routed to the oceans using its internal constant PD river routing mask. Therefore, during ice growth phases, the ocean in PDdrain experiments should receive more freshwater input than ctrl. Conversely, during ice sheet retreat phases, ctrl will have enhanced freshwater fluxes into the oceans compared to PDdrain.

In spite of these changes, during MIS 5d, there is no change in mean EA ice volume and only a small mean decrease in NA ice volume in PDdrain compared to ctrl experiments (Figure 4.5). More clear (though still not significant by our stated criterion) is a more rapid post MIS 5d maximum NA retreat by the PDdrain ensemble.

The high ensemble variance in NA ice volume during MIS 3 and high EA ice volume variance during MIS2 are strongly decreased in PDdrain (see Figure 4.6). All PDdrain ensemble members follow the trajectory of a strong MIS 3 interstadial with NA ice sheets nearly completely retreated (see Figure 4.3). As evident in comparing ctr in Figures 4.1 and 4.4 the ctrl runs with strong NA MIS 3 retreat, also have the smallest EA LGM ice volumes. The results of the system dynamics driving this relationship are even more strongly evident in the PDdrain experiments: the EA MIS 3-1 ensemble mean and standard deviation volume is confined to the low boundary of the corresponding range of ctrl values.

The AMOC response to PDdrain is not proportional to the above ice volume responses. MIS 5d to 5c AMOC strength is strongly increased compared to ctrl (Figure 4.23). The increase in AMOC strength during the MIS 5d ice growth phase is unex-

pected given the PDdrain increase in total discharge of water to the ocean compared to ctrl. By process elimination, especially given the minimal MIS 5d PDdrain ice volume response, changes in the spatial pattern of freshwater injection into the ocean must account for the increased AMOC response. The increase in MIS 5d AMOC strength leads to increased SSTs in the North Atlantic especially near southern Greenland (Figure 4.22). However, this does not translate into significant changes in North Atlantic mean October sea ice extent nor terrestrial summer sea level temperatures.

The most significant AMOC impact of PDdrain is the weak post LGM reduction in strength as opposed to the complete shutdown in ctrl (Figure 4.23). This propagates as a continued enhanced PDdrain AMOC right to 0 ka. This does not impact ice evolution during termination.

During LGM, the PDdrain impact on climate is stronger as compared to MIS 5d, with reduced mean North Atlantic October sea ice extent, more widespread increase in SSTs, and warmer terrestrial temperatures (Figure 4.22). This is consistent with the strongly reduced LGM EA ice volume for PDdrain (Figure 4.6).

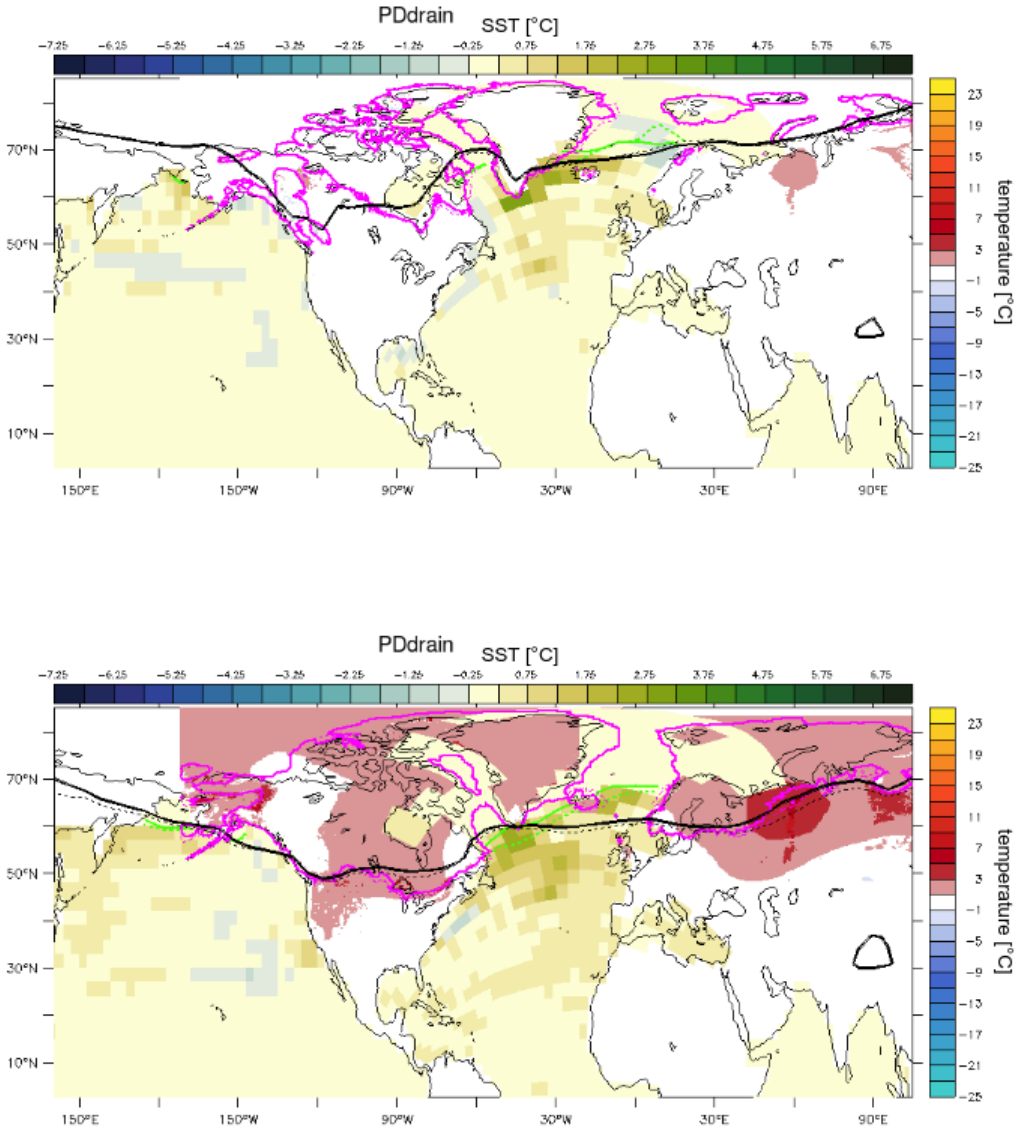

Figure 4.22: Difference PDdrain-ctrl ensemble mean of October SST (blue-green shading) and GSM summer (JJA) temperature over ice sheet domains scaled down to sea level (cyan-yellow shading) at 115 ka (top) and 21 ka (bottom), about 2-3 kyrs before reaching sea level minimum. Black contour lines: ensemble mean LOVECLIM summer (JJA) 0° isotherm, green contour lines: ensemble mean October sea ice extent, pink contour line: ensemble mean ice sheet extent, solid lines: PDdrain, dashed lines: ctrl

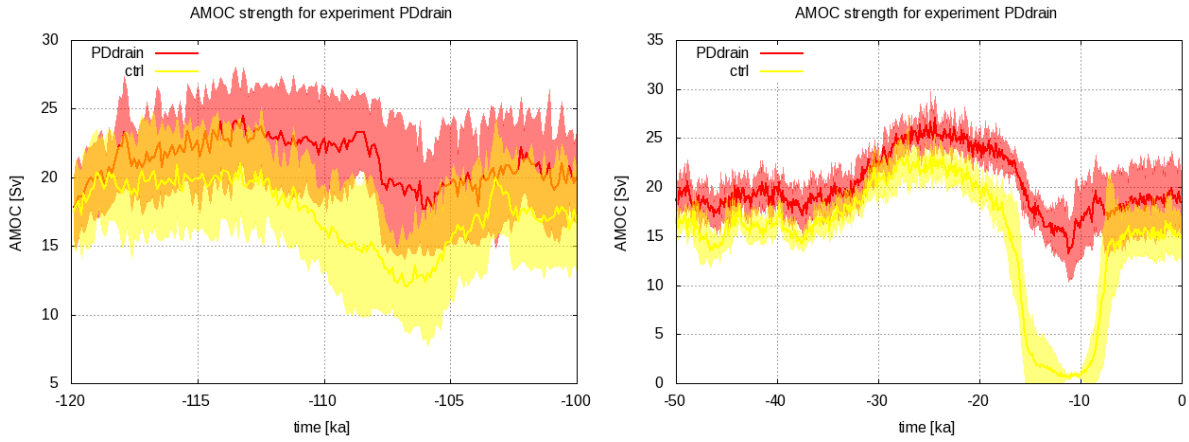

Figure 4.23: Ensemble mean and standard deviation of AMOC strength for the MIS 5d (left) and MIS 3-1 (right) interval. Red: PDdrain, yellow: ctrl

4.5 Conclusions

With the glacial Earth system model LCice we have isolated the impact of the key ice-Earth system feedbacks on NA and EA ice sheet evolution during the last glacial cycle. Specifically, the following ice sheet to climate system couplings were removed in one at time sensitivity experiments: orographic, radiative, freshwater storage and routing, Bering Strait throughflow dependence on depth, and GIA.

A key feature of the experimental design was a small ensemble based analysis to lightly probe sensitivity dependence on the model parameter vector. The ensemble parameter vectors are a high variance sub-sample from a larger 90 member set that pass constraints for glacial inception, subsequent interstadial, LGM, and PD based on inferred sea level. A resultant key take-away is that removal of all but one of the above couplings results in ice volume anomalies for each of the two ice sheets of greater than half of the LGM ice volume for at least two of the 7 ensemble parameter vectors.

Though the high intra-ensemble variance in responses limits confident summary statements of specific feedbacks, a few noteworthy results clearly stood out. Firstly, the ctrl ensemble divides into two different MIS 3 NA ice volume trajectories, one with only a weak interstadial, and one with close to complete deglaciation. The resultant high ensemble variance of NA ice volume for this interval was collapsed for four of the sensitivity experiments (flatNA, noNA, noGIA, and PDdrain) and reduced for the remaining experiments. This suggests that all the associated feedbacks play an especially critical role during this interval which is also evident in the high intra-ensemble variance in the ice volume response for each of the experiments (Figure

4.3).

A likely related feature is an ensemble mean reduction of AMOC by approximately 5 Sv for the noNA (no NA ice sheet to atmospheric coupling) experiment relative to ctrl for most of the MIS 3 interval. This is also the interval of most concentrated Dansgaard-Oeschger oscillations during the last glacial cycle in the Greenland ice core records (e.g. Johnsen et al., 2001). As Dansgaard-Oeschger oscillations are generally inferred to involve changes in AMOC strength (e.g. Menviel et al., 2020), this result supports an important role for NA ice sheet and atmosphere feedbacks in the Earth system dynamics underlying Dansgaard-Oeschger behavior.

A third consistent result is confirmation of previous studies using simpler climate models (e.g. Tarasov and Peltier, 1997) that GIA is required to simulate deglaciation. However, unlike the results of Tarasov and Peltier (e.g. 1997), which only found this to be critical for the NA ice sheet, both EA and NA sheets failed to deglaciate in the noGIA experiments. The residual PD ice volumes were at least two thirds of their LGM values for all noGIA simulations except for two extremal simulations with ctrl LGM ice volumes well outside of ranges inferred by separate history matching projects (Tarasov et al, in prep.).

During the last glacial termination, AMOC collapsed in ctrl and closed Bering Strait experiments, but did not recover when Bering Strait was kept closed. The Pacific to Arctic throughflow into the North Atlantic effectively acts as an "engine starter" in the ctrl experiments.

Finally, for all but one of the experiments (PDdrain) there are ensemble members with significant ice volume anomalies of opposite signs for each ice sheet. Even for a single parameter vector, the sign of the feedback can change between different

major stadial intervals. This strong non-linear parametric dependency of the model feedbacks is an important caution against reliance on a single parameter vector for feedback analysis of Earth system models. It also suggests that separate ice sheet and Earth systems models will generally need re-tuning when coupled.

Our core take away is that 1) all of the main ice sheet-climate feedbacks described above can play a critical role in ice-climate co-evolution and 2) the feedbacks are non-linear and dependent on climate model configuration. This provides further motivation for full coupling of ice sheet models to advanced paleoclimate models.

Chapter 5

Conclusions

In this thesis, I have employed the model LCice for simulations of the last two glacial cycles. This is the first study with a model of this level of complexity that uses ensemble simulations and that transiently simulates ice-climate co-evolution for more than one glacial cycle. This thesis is taking a significant step towards bounding the growth and decay of ice sheets over the last two glacial cycles, and the relative role of ice-climate feedbacks during the last glacial. LCice is a fully-coupled Earth system model of intermediate complexity. Its resolution and complexity is significantly higher than that of the only EMIC previously used for simulations of more than one glacial cycle (CLIMBER-2, Ganopolski and Brovkin, 2017). Using ensemble simulations, the model parametric uncertainty is partially addressed. The ensemble offers a range of potential histories rather than a single simulation tuned to reproduce history based on limited data with high uncertainties.

After extensive ensemble sieving against chosen constrain, the resultant small ensembles intersect and in a large part cover the inferred eustatic sea level bounds for

the last two glacial inceptions (Chapter 2), the last two glacial cycles (Chapter 3) and the last glacial cycle (Chapter 4). The rapid growth in terrestrial ice volume during glacial inception been difficult to replicate by Earth system models (e.g. Calov et al., 2005; Bahadory et al., 2021) and the subsequent generally strong interstadial and associated sea level rise imposes a further challenge for both modeling and understanding. The appropriate magnitude of net feedback response to radiative forcing of Earth system models is a key issue for building confidence in modeling future climate evolution. LCice has shown here to capture the overall sea level response to forcing. Furthermore, the temporal pattern of air and deep ocean temperature (though not the signal full amplitude) as inferred from ice and marine sediment cores is captured in the ensemble (Chapter 3). Chapters 2 and 3 show a range of possible ice sheet configurations during glacial inceptions and maxima, some bracketing reality (if reality is known). Therefore, the simulations can fill in gaps in our knowledge of ice-climate evolution since little (especially confidently dated) data is available pre-LGM. However, the simulations should not be misunderstood as reconstructions, they rather offer physically self-consistent histories of potential ice-climate evolution.

Ice-climate evolution can be sensitive to history/initial conditions, this is the case at least for Antarctic ice evolution in simulations presented here (as Chapter 3 has shown). Initial conditions always have uncertainties. Earth system and climate models, no matter how sophisticated and of high resolution they are, are always simplifications of reality and will therefore have errors. Furthermore, Chapter 4 has shown that small changes (like varying parameter values) can lead to large differences when testing the response to feedbacks, reminiscent of a butterfly effect. When analyzing a single simulation, these uncertainties are not accounted for and no indication of con-

fidence in the results can be made. The ensemble simulations used here, on the other hand, can at least partially account for parametric uncertainty. Model structural uncertainty still remains.

Ensemble members that pass PD filtering (here: temperature seasonality, annual precipitation, and Southern Ocean temperature within 4 standard deviations of reconstructions) will not necessarily capture glacial cycle climate. Even capture of glacial inception sea level evolution does not predict capture of sea level evolution across the full glacial cycle. This suggests that Earth system models can have a state dependency that might invalidate their predictive ability, especially if only one simulation is analyzed.

The lag in timing of maximum ice volume behind insolation minimum is not constant but varies between ice sheets and between the different stadials. Therefore, maximum ice volume is not reached synchronously for all ice sheets. There is no clear relationship between strength of the stadial (amount of sea level decrease) and the amount of ice volume-to-insolation lag. Therefore, orbitally tuned proxy records can likely display age errors of over $\sim$ 9 kyrs (based on ensemble mean lags of the last two glacial cycles).

Using an Earth system model of intermediate complexity, like LCice, has the advantage that ice-climate evolution can be simulated over relatively long periods in a relatively short time (120 days for two glacial cycles). However, this comes at the trade off of reduced process and spatial resolution. The atmospheric component of LCice is not capable of simulating the changes in atmospheric wave dynamics to capture the ice extent of the EA ice sheet in response to the NA ice sheet (Chapter 4), and to capture the inferred differences in EA ice extent between LGM and PGM

(Chapter 3).

The main research questions were addressed in the three manuscripts as follows:

Chapter 2: What does glacial inception look like in the last two glacial cycles? How do ice area and volume differ between last and penultimate glacial inception and how do they compare to the limited available data?

- Due to the stronger forcing during penultimate compared to last glacial inception, the NA and EA ice sheets are larger during MIS 7 than MIS 5.

- For both inceptions, ice growth and decay is not a gradual process but relatively rapid. The larger NA ice sheet generally advanced and retreated faster than the smaller EA ice sheet: NA advanced 170 ± 40 m/yr at the southern margin during both inceptions, EA 100 ± 70 m/yr. Mean eustatic sea level rise due to melt reached 7.0 ± 1.9 m/kyr (7 mm /yr) from the NA ice sheet and 1.6 ± 1.0 m/kyr from EA ice sheet contributions during MIS 7d to 7c.

- Given the rapid growth and retreat, Hudson Bay transitions from an ice free state to full ice cover within 1000 years in the simulations. This has relevance as there is a debate surrounding the potential for, and timing of, ice-free conditions over Hudson Bay during MIS 3, where a major concern was the feasibility of rapid ice growth.

- The Laurentide and Cordilleran ice sheets merge in their northern sectors in all analyzed simulations for MIS 7d, contrary to what is assumed from limited geological data.

- During ice sheet advance, the simulated southern ice margin approximately

aligns with the summer -2°C isotherm. At maximum extent, the ice margin lies between the -2 and 0°C JJA isotherm. During the retreat phase, the ice margin aligns with or is south of the 4°C JJA isotherm.

- Different simulated ice sheet configurations are possible for the same global eustatic sea level.

Chapter 3: What are differences between the ice-climate evolution over the penultimate and last glacial cycle? How important is memory of the penultimate glacial ice evolution on the last glacial cycle ice-climate evolution?

- The ensemble brackets the NA and EA ice sheet extent during LGM. During PGM, the eastern extent of the EA ice sheet is captured and 2 ensemble members capture the southern extent, but the simulated ice sheet does not reach as far west as reconstructions suggest.

- The ensemble captures the timing and the relative overall temporal pattern of air temperature at the Greenland NGRIP and Antarctic EDC sites, and the deep ocean temperature at 3 sites in equatorial Atlantic, and equatorial and Southern Pacific. However, the total amplitude of glacial cooling and interglacial warming at the ice core sites is underestimated in the ensemble. The warming of the last interglacial is furthermore underestimated for the Pacific deep ocean temperature sites.

- Precipitation weighted temperature has a significantly (± 4 °C) larger amplitude than nominal mean temperature at NGRIP ice core site. The simulations

provide a physically-based dataset for deconvolving seasonal biasing of paleo proxy data time series.

- There is a higher variability in AMOC strength during the penultimate than during the last glacial cycle, likely due to higher rates of ice mass loss during some stadial to interstadial transitions.

- The North American, Eurasian, and Greenland ice sheets are not significantly sensitive to ice history. However, the whole last glacial cycle evolution of the Antarctic ice sheet is sensitive to its internal state during the last interglacial. This indicates the importance of assessing the (uncertain) initial conditions when modeling the future Antarctic ice sheet.

Chapter 4: How do ice-climate feedbacks shape ice evolution over the course of a glacial cycle? What is the relative role of ice sheets in the climate system for glacial cycle contexts?

- All tested sensitivities (impact of Bering Strait open/closed, ice sheet topography and albedo, GIA, fresh water storage and routing) have an impact on both major ice sheets and result in ice volume anomalies greater than half of the LGM ice volume for at least two out of seven ensemble members.

- The response to a tested feedback is highly variable depending on the ensemble member parameter vector with ensemble members displaying ice volume anomalies of opposite signs.

- For all but one of the experiments (PDdrain) there are ensemble members with significant ice volume anomalies of opposite signs for each ice sheet. Even for a

single parameter vector, the sign of the feedback can change between different major stadial intervals.

- In the ctrl experiments, MIS 3 has the largest intra-ensemble variability, where ensemble members either follow the trajectory of a weak interstadial or a strong interstdial with near complete NA ice retreat. This variability is reduced in all sensitivity experiments, but especially for noGIA, PDdrain, and no/flatNA, indicating that all tested feedbacks play a critical role during this interval.

- GIA has the largest average impact on ice sheet growth out of the tested feedbacks and is necessary for complete deglatiation of the NA and EA ice sheet.

- The opening of Bering Strait plays an important role for AMOC recovery during glacial termination, as AMOC does not recover in experiments where Bering Strait is kept closed.

5.1 Future work

The sensitivity analysis in Chapter 4 has left some questions open that I would like to address before submitting this manuscript to a journal. Specifically the "bso" (Bering Strait constantly open) and "PDdrain" (constant present-day drainage routing) experiments had surprising results (to me).

The behavior of the bso experiments during LGM is surprising as some ensemble members show a decrease and others an increase in AMOC strength compared to the ctrl simulations. Re-running some simulations to extract more output from the ocean component (like salinity and velocities in the North Atlantic) might offer an

explanation as to where the water flowing through Bering Strait is being mixed into North Atlantic waters and its impact on AMOC.

The PDdrain experiments showed a surprising increase in AMOC strength during glacial inception. Given that during inception, in the PDdrain experiments more water is injected in the oceans than in ctrl experiments, where water is stored on land, a decrease in AMOC strength would have been expected. Further sensitivity experiments are needed to disentangle the impact of freshwater amount and location of inception into the ocean. I will set up experiments where only the freshwater routing is kept at PD, but the ice sheet storage of water is allowed.

While there is no direct coupling between vegetation and ice sheets, there are feedbacks between the two components via the atmosphere that I have not tested. A change in vegetation cover from Tundra to Taiga influences albedo (especially when snow covered) and can therefore influence local temperature. While the vegetation component in LCice only has 3 functional types (trees, grass, desert), it might be worth testing the impact of constant PD vegetation cover on ice sheet evolution in the future.

Chapter 3 has potential for collaboration with proxy experts. My simulated climate fields could be compared to more reconstructions. Other metrics than the ones shown can be extracted from the model and might be of interest to geologists and paleontologists.

In the future, dust feedbacks should be accounted for in LCice. Other glacial cycle studies with coupled models (Ganopolski et al., 2010; Willeit et al., 2023) profited from a combination of simulating glaciogenic dust and dust forcing. However, I want

to avoid the usage of an ad hoc, potentially nonphysical dust forcing. Dust increases during glacial climates due to increase in available surfaces as sea level decreases, aridity, and erosion. Transport of dust in the atmosphere and deposition in of dust on ice can have an impact on glacial climate, ice sheet extent and can accelerate glacial termination (Bar-Or et al., 2008; Bauer and Andrey, 2010).

As addressed in the introduction, I have accidentally created a high elevation cold-biased ensemble. This will be corrected in the future. There may be something to learn from a comparison of the ensembles presented herein with the newly re-tuned ensemble.

Bibliography

G. Allard, M. Roy, B. Ghaleb, P. J.H. Richard, A. C. Larouche, J. J. Veillette, and M. Parent. Constraining the age of the last interglacial–glacial transition in the hudson bay lowlands (canada) using u–th dating of buried wood. *Quaternary Geochronology*, 7:37–47, 2 2012. ISSN 1871-1014. doi: 10.1016/J.QUAGEO.2011.09.004.

Heather Andres and Lev Tarasov. Towards understanding potential atmospheric contributions to abrupt climate changes: Characterizing changes to the north atlantic eddy-driven jet over the last deglaciation. *Climate of the Past*, 15:1621–1646, 8 2019. ISSN 18149332. doi: 10.5194/cp-15-1621-2019.

Laurence D Andriashek and René W Barendregt. Evidence for early pleistocene glaciation from borecore stratigraphy in north-central alberta, canada. *Canadian Journal of Earth Sciences*, 54:445–460, 2017. doi: 10.1139/cjes-2016-0175. URL `https://doi.org/10.1139/cjes-2016-0175`.

Fabrizio Antonioli, Lucio Calcagnile, Luigi Ferranti, Giuseppe Mastronuzzi, Carmelo Monaco, Paolo Orrù, Gianluca Quarta, Fabrizio Pepe, Giovanni Scardino, Giovanni Scicchitano, Paolo Stocchi, and Marco Taviani. New evidence of mis 3 relative

sea level changes from the messina strait, calabria (italy). *Water*, 2021. doi: 10.3390/w13192647. URL https://doi.org/10.3390/w13192647.

Valery Astakhov. Middle pleistocene glaciations of the russian north. *Quaternary Science Reviews*, 23:1285–1311, 6 2004. ISSN 0277-3791. doi: 10.1016/J.QUASCIREV.2003.12.011. URL https://www.sciencedirect.com/science/article/pii/S0277379103003457.

Valery Astakhov and Liudmila Semionova. The penultimate interglaciation of northern russia. *Quaternary International*, 605-606:142–154, 2021. ISSN 10406182. doi: 10.1016/j.quaint.2020.12.034. URL https://doi.org/10.1016/j.quaint.2020.12.034.

Valery Astakhov, Valentina Shkatova, Andrei Zastrozhnov, and Margarita Chuyko. Glaciomorphological map of the russian federation. *Quaternary International*, 420:4–14, 10 2016. ISSN 1040-6182. doi: 10.1016/J.QUAINT.2015.09.024.

Brian Ayugi, Jiang Zhihong, Huanhuan Zhu, Hamida Ngoma, Hassen Babaousmail, Karim Rizwan, and Victor Dike. Comparison of cmip6 and cmip5 models in simulating mean and extreme precipitation over east africa. *International Journal of Climatology*, 41:6474–6496, 2021. doi: https://doi.org/10.1002/joc.7207. URL https://rmets.onlinelibrary.wiley.com/doi/abs/10.1002/joc.7207.

Taimaz Bahadory and Lev Tarasov. Lcice 1.0-a generalized ice sheet system model coupler for loveclim version 1.3: Description, sensitivities, and validation with the glacial systems model (gsm version d2017.aug17). *Geoscientific Model Development*, 11:3883–3902, 2018. ISSN 19919603. doi: 10.5194/gmd-11-3883-2018.

Taimaz Bahadory, Lev Tarasov, and Heather Andres. Last glacial inception trajectories for the northern hemisphere from coupled ice and climate modelling. *Climate of the Past*, 17:397–418, 2021. ISSN 18149332. doi: 10.5194/cp-17-397-2021.

Greg Balco. Contributions and unrealized potential contributions of cosmogenic-nuclide exposure dating to glacier chronology, 1990–2010. *Quaternary Science Reviews*, 30:3–27, 1 2011. ISSN 0277-3791. doi: 10.1016/J.QUASCIREV.2010.11.003.

Rotem Bar-Or, Carynelisa Erlick, and Hezi Gildor. The role of dust in glacial-interglacial cycles. *Quaternary Science Reviews*, 27:201–208, 2008. ISSN 02773791. doi: 10.1016/j.quascirev.2007.10.015.

Christine L. Batchelor, Martin Margold, Mario Krapp, Della K. Murton, April S. Dalton, Philip L. Gibbard, Chris R. Stokes, Julian B. Murton, and Andrea Manica. The configuration of northern hemisphere ice sheets through the quaternary. *Nature Communications*, 10:1–10, 2019. ISSN 20411723. doi: 10.1038/s41467-019-11601-2. URL `http://dx.doi.org/10.1038/s41467-019-11601-2`.

Stephanie L Bates, Mark Siddall, and Claire Waelbroeck. Sea level records and deep ocean temperatures from odp site 138-849, 2014a. URL `https://doi.org/10.1594/PANGAEA.854799`.

Stephanie L Bates, Mark Siddall, and Claire Waelbroeck. Sea level records and deep ocean temperatures from odp site 108-659, 2014b. URL `https://doi.org/10.1594/PANGAEA.854797`. In supplement to: Bates, SL et al. (2014): Hydrographic variations in deep ocean temperature over

the mid-Pleistocene transition. Quaternary Science Reviews, 88, 147-158, https://doi.org/10.1016/j.quascirev.2014.01.020.

Eva Bauer and A. Ganopolski Andrey. Aeolian dust modeling over the past four glacial cycles with climber-2. *Global and Planetary Change*, 74:49–60, 2010. ISSN 09218181. doi: 10.1016/j.gloplacha.2010.07.009. URL `http://dx.doi.org/10.1016/j.gloplacha.2010.07.009`.

D. Benn and D. J.A. Evans. *Glaciers and Glaciation*. Routledge, 2nd ed. edition, 2010. URL `https://doi.org/10.4324/9780203785010`.

Bernhard Bereiter, Sarah Eggleston, Jochen Schmitt, Christoph Nehrbass-Ahles, Thomas F. Stocker, Hubertus Fischer, Sepp Kipfstuhl, and Jerome Chappellaz. Revision of the epica dome c co2 record from 800 to 600-kyr before present. *Geophysical Research Letters*, 42:542–549, 2015. ISSN 19448007. doi: 10.1002/2014GL061957.

A. Berger and M. F. Loutre. Insolation values for the climate of the last 10 million years. *Quaternary Science Reviews*, 10:297–317, 1991. ISSN 02773791. doi: 10.1016/0277-3791(91)90033-Q.

A Berger, M Crucifix, DA Hodell, C Mangili, JF McManus, B Otto-Bliesner, K Pol, D Raynaud, LC Skinner, PC Tzedakis, EW Wolff, QZ Yin, A Abe-Ouchi, C Barbante, V Brovkin, I Cacho, E Capron, P Ferretti, A Ganopolski, JO Grimalt, NV Honisch, K. Kawamura, A. Landais, V.Margari, B. Martrat, V.Masson-Delmotte, Z.Mokeddem, F. Parrenin, A. A. Prokopenko, H. Rashid, M. Schulz,

and N. Riveiros. Interglacials of the last 800,000years. *Reviews of Geophysics*, 54: 162–219, 2015. doi: 10.1002/2015RG000482.Received.

Andre Berger. Long-term variations of daily insolation and quaternary climatic changes. *Journal of the Atmospheric Sciences*, 35:2362–2367, 1978. URL https://doi.org/10.1175/1520-0469(1978)035%3C2362:LTVODI%3E2.0.CO;2.

S Bonelli, S Charbit, M Kageyama, G Ramstein, C Dumas, and A Quiquet. Investigating the evolution of major northern hemisphere ice sheets during the last glacial-interglacial cycle. *Climate of the Past*, pages 329–345, 2009. doi: 10.5194/cp-5-329-2009. URL https://doi.org/10.5194/cp-5-329-2009.

A. Born, M. Kageyama, and K. H. Nisancioglu. Warm nordic seas delayed glacial inception in scandinavia. *Climate of the Past*, 6:817–826, 2010. ISSN 18149324. doi: 10.5194/cp-6-817-2010.

J H C Bosmans, F J Hilgen, E Tuenter, and L J Lourens. Obliquity forcing of low-latitude climate. *Climate of the Past*, 11:1335–1346, 2015. doi: 10.5194/cp-11-1335-2015. URL https://www.clim-past.net/11/1335/2015/.

Sheridan Bowman. *Radiocarbon Dating*. London : Published for the Trustees of the British Museum by British Museum Publications, 1990.

S. Brewer, J. Guiot, and D. Barboni. Pollen methods and studies — use of pollen as climate proxies. *Encyclopedia of Quaternary Science: Second Edition*, pages 805–815, 1 2013. doi: 10.1016/B978-0-444-53643-3.00180-1.

J. P. Briner, Y. Axford, S. L. Forman, G. H. Miller, and A. P. Wolfe. Multiple

generations of interglacial lake sediment preserved beneath the laurentide ice sheet. *Geology*, 35:887–890, 2007. ISSN 00917613. doi: 10.1130/G23812A.1.

Edward J. Brook and Christo Buizert. Antarctic and global climate history viewed from ice cores. *Nature*, 558:200–208, 2018. ISSN 14764687. doi: 10.1038/s41586-018-0172-5.

Etienne Brouard, Martin Roy, Pierre Marc Godbout, and Jean J. Veillette. A framework for the timing of the final meltwater outbursts from glacial lake agassiz-ojibway. *Quaternary Science Reviews*, 274:107269, 12 2021. ISSN 0277-3791. doi: 10.1016/J.QUASCIREV.2021.107269.

C. Buizert, B. A. Keisling, J. E. Box, F. He, A. E. Carlson, G. Sinclair, and R. M. DeConto. Greenland-wide seasonal temperatures during the last deglaciation. *Geophysical Research Letters*, 45:1905–1914, 2018. ISSN 19448007. doi: 10.1002/2017GL075601.

Reinhard Calov, Andrey Ganopolski, Martin Claussen, Vladimir Petoukhov, and Ralf Greve. Transient simulation of the last glacial inception. part i: Glacial inception as a bifurcation in the climate system. *Climate Dynamics*, 24:545–561, 2005. ISSN 09307575. doi: 10.1007/s00382-005-0007-6.

J. E. Campbell, E. C. Little, D. Utting, and I. McMartin. Surficial geology, nanuraqtalik lake, nunavut; geological survey of canada, canadian geoscience map 60. 2013. doi: 10.4095/292009.

J. Rachel Carr, Chris R. Stokes, and Andreas Vieli. Threefold increase in marine-

terminating outlet glacier retreat rates across the atlantic arctic: 1992–2010. *Annals of Glaciology*, 58:72–91, 2017. ISSN 02603055. doi: 10.1017/aog.2017.3.

C Causse and J S. Vincent. Th–u disequilibrium dating of middle and late pleistocene wood and shells from banks and victoria islands, arctic canada. *Canadian Journal of Earth Sciences*, 26:2718–2723, 1989. doi: 10.1139/e89-231. URL `https://doi.org/10.1139/e89-231`.

Hai Cheng, Gregory S. Springer, Ashish Sinha, Benjamin F. Hardt, Liang Yi, Hanying Li, Ye Tian, Xianglei Li, Harold D. Rowe, Gayatri Kathayat, Youfeng Ning, and R. Lawrence Edwards. Eastern north american climate in phase with fall insolation throughout the last three glacial-interglacial cycles. *Earth and Planetary Science Letters*, 522:125–134, 9 2019. ISSN 0012-821X. doi: 10.1016/J.EPSL.2019.06.029.

Dipayan Choudhury, Axel Timmermann, Fabian Schloesser, Malte Heinemann, and David Pollard. Simulating marine isotope stage 7 with a coupled climate-ice sheet model. *Climate of the Past*, 16:2183–2201, 2020. ISSN 18149332. doi: 10.5194/cp-16-2183-2020.

Peter U. Clark, David Archer, David Pollard, Joel D. Blum, Jose A. Rial, Victor Brovkin, Alan C. Mix, Nicklas G. Pisias, and Martin Roy. The middle pleistocene transition: characteristics, mechanisms, and implications for long-term changes in atmospheric pco2. *Quaternary Science Reviews*, 25:3150–3184, 2006. ISSN 02773791. doi: 10.1016/j.quascirev.2006.07.008.

M. Claussen, L. Mysak, A. Weaver, M. Crucifix, T. Fichefet, M. F. Loutre, S. Weber, J. Alcamo, V. Alexeev, A. Berger, R. Calov, A. Ganopolski, H. Goosse,

G. Lohmann, F. Lunkeit, I. Mokhov, V. Petoukhov, P. Stone, and Z. Wang. Earth system models of intermediate complexity: Closing the gap in the spectrum of climate system models. *Climate Dynamics*, 18:579–586, 2002. ISSN 09307575. doi: 10.1007/s00382-001-0200-1.

Steven Clemens, Warren Prell, David Murray, Graham Shimmield, and Graham Weedon. Forcing mechanisms of the indian ocean monsoon. *Nature*, 353:720–725, 1991. ISSN 1476-4687. doi: 10.1038/353720a0. URL `https://doi.org/10.1038/353720a0`.

F. Colleoni, G. Krinner, and M. Jakobsson. Sensitivity of the late saalian (140 kyrs bp) and lgm (21 kyrs bp) eurasian ice sheet surface mass balance to vegetation feedbacks. *Geophysical Research Letters*, 36:1–5, 2009a. ISSN 00948276. doi: 10.1029/2009GL037200.

F. Colleoni, G. Krinner, M. Jakobsson, V. Peyaud, and C. Ritz. Influence of regional parameters on the surface mass balance of the eurasian ice sheet during the peak saalian (140 kya). *Global and Planetary Change*, 68:132–148, 2009b. ISSN 09218181. doi: 10.1016/j.gloplacha.2009.03.021. URL `http://dx.doi.org/10.1016/j.gloplacha.2009.03.021`.

Florence Colleoni, Johan Liakka, Gerhard Krinner, Martin Jakobsson, Simona Masina, and Vincent Peyaud. The sensitivity of the late saalian (140 ka) and lgm (21 ka) eurasian ice sheets to sea surface conditions. *Climate Dynamics*, 37: 531–553, 2011. ISSN 09307575. doi: 10.1007/s00382-010-0870-7.

Florence Colleoni, Simona Masina, Annalisa Cherchi, and Doroteaciro Iovino. Impact

of orbital parameters and greenhouse gas on the climate of mis 7 and mis 5 glacial inceptions. *Journal of Climate*, 27:8918–8933, 2014. ISSN 08948755. doi: 10.1175/JCLI-D-13-00754.1.

Florence Colleoni, Claudia Wekerle, Jens Ove Näslund, Jenny Brandefelt, and Simona Masina. Constraint on the penultimate glacial maximum northern hemisphere ice topography (140 kyrs bp). *Quaternary Science Reviews*, 137:97–112, 2016. ISSN 02773791. doi: 10.1016/j.quascirev.2016.01.024.

Climate Change Service Copernicus. Oras5 global ocean reanalysis monthly data from 1958 to present. *Climate Data Store*, 2021.

James Croll. On the change in the obliquity of the ecliptic, its influence on the climate of the polar regions, and level of the sea. *Transactions of the Geolocial Society of Glasgow*, 2:177–198, 1867. URL `https://doi.org/10.1144/transglas.2.3.177`.

D. Dahl-Jensen, K. Mosegaard, N. Gundestrup, G. D. Clow, S. J. Johnsen, A. W. Hansen, and N. Balling. Past temperatures directly from the greenland ice sheet. *Science*, 282:268–271, 1998.

April S. Dalton, Sarah A. Finkelstein, Peter J. Barnett, Minna Väliranta, and Steven L. Forman. Late pleistocene chronology, palaeoecology and stratigraphy at a suite of sites along the albany river, hudson bay lowlands, canada. *Palaeogeography, Palaeoclimatology, Palaeoecology*, 492:50–63, 3 2018. ISSN 0031-0182. doi: 10.1016/J.PALAEO.2017.12.011.

April S. Dalton, Sarah A. Finkelstein, Steven L. Forman, Peter J. Barnett, Tamara Pico, and Jerry X. Mitrovica. Was the laurentide ice sheet significantly reduced

during marine isotope stage 3? *Geology*, 47:111–114, 2019. ISSN 19432682. doi: 10.1130/G45335.1.

April S. Dalton, Chris R. Stokes, and Christine L. Batchelor. Evolution of the laurentide and innuitian ice sheets prior to the last glacial maximum (115 ka to 25 ka). *Earth-Science Reviews*, 224:103875, 2022. ISSN 00128252. doi: 10.1016/j.earscirev.2021.103875. URL https://doi.org/10.1016/j.earscirev.2021.103875.

April S. Dalton, Helen E. Dulfer, Martin Margold, Jakob Heyman, John J. Clague, Duane G. Froese, Michelle S. Gauthier, Anna L.C. Hughes, Carrie E. Jennings, Sophie L. Norris, and Benjamin J. Stoker. Deglaciation of the north american ice sheet complex in calendar years based on a comprehensive database of chronological data: Nadi-1. *Quaternary Science Reviews*, 321:108345, 12 2023. ISSN 0277-3791. doi: 10.1016/J.QUASCIREV.2023.108345.

Hugo Dubé-Loubert, Martin Roy, Guillaume Allard, Michel Lamothe, and Jean J Veillette. Glacial and nonglacial events in the eastern james bay lowlands, canada. *Canadian Journal of Earth Sciences*, 50:379–396, 2013. doi: 10.1139/cjes-2012-0065. URL https://doi.org/10.1139/cjes-2012-0065.

Andrea Dutton and Natasha L M Barlow. What do we know about last interglacial sea level? *Past Global Changes Magazine*, 27:6–7, 2019. ISSN 2411605X. doi: 10.22498/pages.27.1.6.

A S Dyke. An outline of north american deglaciation with emphasis on central and northern canada. In J Ehlers and P L Gibbard, editors, *Quaternary Glaciations-Extent and Chronology, Part II*, volume 2b, pages 373–424. Elsevier, 2004.

A S Dyke, J T Andrews, P U Clark, J H England, G H Miller, J Shaw, and J J Veillette. The laurentide and innuitian ice sheets during the last glacial maximum. *Quaternary Science Reviews*, 21:9–31, 2002. ISSN 0277-3791. doi: https://doi.org/10.1016/S0277-3791(01)00095-6. URL `http://www.sciencedirect.com/science/article/pii/S0277379101000956`. EPILOG.

H. Elderfield, P. Ferretti, M. Greaves, S. Crowhurst, I. N. McCave, D. Hodell, and A. M. Piotrowski. Evolution of ocean temperature and ice volume through the mid-pleistocene climate transition. *Science*, 337:704–709, 2012. ISSN 10959203. doi: 10.1126/science.1221294.

D. J.A. Evans, I. R. Smith, J. C. Gosse, and J. M. Galloway. Glacial landforms and sediments (landsystem) of the smoking hills area, northwest territories, canada: Implications for regional pliocene – pleistocene laurentide ice sheet dynamics. *Quaternary Science Reviews*, 262:106958, 6 2021. ISSN 0277-3791. doi: 10.1016/J.QUASCIREV.2021.106958.

Xuewei Fan, Qingyun Duan, Chenwei Shen, Yi Wu, and Chang Xing. Global surface air temperatures in cmip6: Historical performance and future changes. *Environmental Research Letters*, 15, 10 2020. ISSN 17489326. doi: 10.1088/1748-9326/abb051.

H. Gallée, J. P. Van Yperselb, T. Fichefet, I. Marsiat, C. Tricot, and A. Berger. Simulation of the last glacial cycle by a coupled, sectorially averaged climate-ice sheet model: 2. response to insolation and co 2 variations. *Journal of Geophysical Research*, 7:7(D14), 15713–15740., 1992. URL `https://doi.org/10.1029/`

92JD01256. problems: not enough ice (southern extent), needed to apply an ageing snow parameter to NH to get deglaciation. That same aging snow parameter would have made AN melt.

A Ganopolski, R Calov, and M Claussen. Simulation of the last glacial cycle with a coupled climate ice-sheet model of intermediate complexity. *Climate of the Past*, pages 229–244, 2010.

Andrey Ganopolski and Victor Brovkin. Simulation of climate, ice sheets and co2 evolution during the last four glacial cycles with an earth system model of intermediate complexity. *Climate of the Past*, 13:1695–1716, 2017. ISSN 18149332. doi: 10.5194/cp-13-1695-2017.

Michelle S. Gauthier, Tyler J. Hodder, Martin Ross, Samuel E. Kelley, Andrew Rochester, and Phil McCausland. The subglacial mosaic of the laurentide ice sheet; a study of the interior region of southwestern hudson bay. *Quaternary Science Reviews*, 214:1–27, 6 2019. ISSN 0277-3791. doi: 10.1016/J.QUASCIREV.2019.04.015.

Michelle S. Gauthier, Samuel E. Kelley, and Tyler J. Hodder. Lake agassiz drainage bracketed holocene hudson bay ice saddle collapse. *Earth and Planetary Science Letters*, 544:116372, 8 2020. ISSN 0012-821X. doi: 10.1016/J.EPSL.2020.116372.

H. Goosse, V. Brovkin, T. Fichefet, R. Haarsma, P. Huybrechts, J. Jongma, A. Mouchet, F. Selten, P. Y. Barriat, J. M. Campin, E. Deleersnijder, E. Driesschaert, H. Goelzer, I. Janssens, M. F. Loutre, M. A. Morales Maqueda, T. Opsteegh, P. P. Mathieu, G. Munhoven, E. J. Pettersson, H. Renssen, D. M. Roche, M. Scha-

effer, B. Tartinville, A. Timmermann, and S. L. Weber. Description of the earth system model of intermediate complexity loveclim version 1.2. *Geoscientific Model Development*, 3:603–633, 2010. ISSN 1991959X. doi: 10.5194/gmd-3-603-2010.

K. M. Grant, E. J. Rohling, C. Bronk Ramsey, H. Cheng, R. L. Edwards, F. Florindo, D. Heslop, F. Marra, A. P. Roberts, M. E. Tamisiea, and F. Williams. Sea-level variability over five glacial cycles. *Nature Communications*, 5, 2014. ISSN 20411723. doi: 10.1038/ncomms6076.

J. M. Gregory, O. J.H. Browne, A. J. Payne, J. K. Ridley, and I. C. Rutt. Modelling large-scale ice-sheet-climate interactions following glacial inception. *Climate of the Past*, 8:1565–1580, 2012. ISSN 18149324. doi: 10.5194/cp-8-1565-2012.

Gerald H Haug, Andrey Ganopolski, Daniel M Sigman, Antoni Rosell-Mele, George E A Swann, Ralf Tiedemann, Samuel L Jaccard, Jörg Bollmann, Mark A Maslin, Melanie J Leng, and Geoffrey Eglinton. North pacific seasonality and the glaciation of north america 2.7 million years ago. *Nature*, 433:821–825, 2005. ISSN 1476-4687. doi: 10.1038/nature03332. URL `https://doi.org/10.1038/nature03332`.

Adam R. Herrington and Christopher J. Poulsen. Terminating the last interglacial: The role of ice sheet-climate feedbacks in a gcm asynchronously coupled to an ice sheet model. *Journal of Climate*, 25:1871–1882, 2012. ISSN 08948755. doi: 10.1175/JCLI-D-11-00218.1.

Hans Hersbach, Bill Bell, Paul Berrisford, Shoji Hirahara, András Horányi, Joaquín Muñoz-Sabater, Julien Nicolas, Carole Peubey, Raluca Radu, Dinand Schepers, Adrian Simmons, Cornel Soci, Saleh Abdalla, Xavier Abellan, Gianpaolo Balsamo,

Peter Bechtold, Gionata Biavati, Jean Bidlot, Massimo Bonavita, Giovanna De Chiara, Per Dahlgren, Dick Dee, Michail Diamantakis, Rossana Dragani, Johannes Flemming, Richard Forbes, Manuel Fuentes, Alan Geer, Leo Haimberger, Sean Healy, Robin J Hogan, Elías Hólm, Marta Janisková, Sarah Keeley, Patrick Laloyaux, Philippe Lopez, Cristina Lupu, Gabor Radnoti, Patricia De Rosnay, Iryna Rozum, Freja Vamborg, Sebastien Villaume, and Jean-Noël Thépaut. The era5 global reanalysis. *Q J R Meteorol Soc*, 146:1999–2049, 2020. doi: 10.1002/qj.3803. URL `https://rmets.onlinelibrary.wiley.com/doi/10.1002/qj.3803`.

Tyler J. Hodder, Michelle S. Gauthier, Martin Ross, and Olav B. Lian. Was there a nonglacial episode in the western hudson bay lowland during marine isotope stage 3? *Quaternary Research (United States)*, pages 148–161, 2023. ISSN 10960287. doi: 10.1017/qua.2023.35.

Christian Holme, Vasileios Gkinis, and Bo M Vinther. Molecular diffusion of stable water isotopes in polar firn as a proxy for past temperatures. *Geochimica et Cosmochimica Acta*, 225:128–145, 2018. ISSN 0016-7037. doi: https://doi.org/10.1016/j.gca.2018.01.015. URL `http://www.sciencedirect.com/science/article/pii/S0016703718300188`.

Aixue Hu, Gerald A Meehl, Weiqing Han, Ayako Abe-Ouchi, Carrie Morrill, Yusuke Okazaki, and Megume O Chikamoto. The pacific-atlantic seesaw and the bering strait. *Geophysical*, 39, 2012. doi: 10.1029/2011GL050567. URL `https://agupubs.onlinelibrary.wiley.com/doi/10.1029/2011GL050567`.

Aixue Hu, Gerald A. Meehl, Weiqing Han, Bette Otto-Bliestner, Ayako Abe-Ouchi,

and Nan Rosenbloom. Effects of the bering strait closure on amoc and global climate under different background climates. *Progress in Oceanography*, 132:174–196, 2015. ISSN 00796611. doi: 10.1016/j.pocean.2014.02.004. URL http://dx.doi.org/10.1016/j.pocean.2014.02.004.

Anna L.C. Hughes, Richard Gyllencreutz, Øystein S. Lohne, Jan Mangerud, and John Inge Svendsen. The last eurasian ice sheets - a chronological database and time-slice reconstruction, dated-1. *Boreas*, 45:1–45, 2016. ISSN 15023885. doi: 10.1111/bor.12142.

J Imbrie, A Berger, E A Boyle, S C Clemens, A Duffy, W R Howard, G Kukla, J Kutzbach, D G Martinson, A McIntyre, A C Mix, B Molfino, J J Morley, L C Peterson, N G Pisias, W L Prell, M E Raymo, N J Shackleton, and J R Toggweiler. On the structure and origin of major glaciation cycles 2. the 100,000-year cycle. *Paleoceanography*, 8:699–735, 1993. doi: https://doi.org/10.1029/93PA02751. URL https://agupubs.onlinelibrary.wiley.com/doi/abs/10.1029/93PA02751.

J.D. Ives. Glaciation of the torngat mountains, northern labrador. *Arctic*, 10:66, 1957. ISSN 0004-0843. doi: 10.14430/arctic3755.

Sigfus J. Johnsen, Dorthe Dahl-Jensen, Niels Gundestrup, Jrgen P. Steffensen, Henrik B. Clausen, Heinz Miller, Valerie Masson-Delmotte, Arny E. Sveinbjörnsdottir, and James White. Oxygen isotope and palaeotemperature records from six greenland ice-core stations: Camp century, dye-3, grip, gisp2, renland and northgrip. *Journal of Quaternary Science*, 16:299–307, 2001. ISSN 02678179. doi: 10.1002/jqs.622.

Jean Jouzel and Valerie Masson-Delmotte. Epica dome c ice core 800kyr deuterium data and temperature estimates, 2007. URL https://doi.org/10.1594/PANGAEA.683655. Supplement to: Jouzel, Jean; Masson-Delmotte, Valerie; Cattani, Olivier; Dreyfus, Gabrielle; Falourd, Sonia; Hoffmann, G; Minster, Bénédicte; Nouet, Julius; Barnola, Jean-Marc; Chappellaz, Jérôme A; Fischer, Hubertus; Gallet, J C; Johnsen, Sigfús Jóhann; Leuenberger, Markus Christian; Loulergue, Laetitia; Luethi, D; Oerter, Hans; Parrenin, Frédéric; Raisbeck, Grant M; Raynaud, Dominique; Schilt, Adrian; Schwander, Jakob; Selmo, Enricomaria; Souchez, Roland A; Spahni, Renato; Stauffer, Bernhard; Steffensen, Jørgen Peder; Stenni, Barbara; Stocker, Thomas F; Tison, Jean-Louis; Werner, Martin; Wolff, Eric William (2007): Orbital and millennial Antarctic climate variability over the past 800,000 years. Science, 317(5839), 793-797, https://doi.org/10.1126/science.1141038.

Masa Kageyama, S. Charbit, C. Ritz, M. Khodri, and G. Ramstein. Quantifying ice-sheet feedbacks during the last glacial inception. *Geophysical Research Letters*, 31:1–4, 2004. ISSN 00948276. doi: 10.1029/2004GL021339.

Masa Kageyama, Sandy P. Harrison, Marie L. Kapsch, Marcus Lofverstrom, Juan M. Lora, Uwe Mikolajewicz, Sam Sherriff-Tadano, Tristan Vadsaria, Ayako Abe-Ouchi, Nathaelle Bouttes, Deepak Chandan, Lauren J. Gregoire, Ruza F. Ivanovic, Kenji Izumi, Allegra N. Legrande, Fanny Lhardy, Gerrit Lohmann, Polina A. Morozova, Rumi Ohgaito, André Paul, W. Richard Peltier, Christopher J. Poulsen, Aurélien Quiquet, Didier M. Roche, Xiaoxu Shi, Jessica E. Tierney, Paul J. Valdes, Evgeny Volodin, and Jiang Zhu. The pmip4 last glacial maximum experiments: Preliminary

results and comparison with the pmip3 simulations. *Climate of the Past*, 17:1065–1089, 2021. ISSN 18149332. doi: 10.5194/cp-17-1065-2021.

D. S. Kaufman, N. E. Young, J. P. Briner, and W. F. Manley. Alaska paleo-glacier atlas (version 2). *Quaternary Glaciations Extent and Chronology, Part IV: A Closer Look*, 15:427–445, 2011.

Darrell S. Kauman and William F. Manley. Pleistocene maximum and late wisconsinan glacier extents across alaska, u.s.a. *Developments in Quaternary Science*, 2: 9–27, 1 2004. ISSN 1571-0866. doi: 10.1016/S1571-0866(04)80182-9.

M. Khodri, Y. Leclalnche, G. Ramstein, P. Braconnot, O. Marti, and E. Cortijo. Simulating the amplification of orbital forcing by ocean feedbacks in the last glaciation. *Nature*, 410:570–574, 2001. ISSN 00280836. doi: 10.1038/35069044.

Johan Kleman, Krister Jansson, Hernán De Angelis, Arjen P. Stroeven, Clas Hättestrand, Göran Alm, and Neil Glasser. North american ice sheet build-up during the last glacial cycle, 115–21 kyr. *Quaternary Science Reviews*, 29:2036–2051, 8 2010. ISSN 0277-3791. doi: 10.1016/J.QUASCIREV.2010.04.021.

R. M. Koerner. Instantaneous glacierization, the rate of albedo change, and feedback effects at the beginning of an ice age. *Quaternary Research*, 13:153–159, 3 1980. ISSN 0033-5894. doi: 10.1016/0033-5894(80)90025-3.

Claudia Kubatzki, Martin Claussen, Reinhard Calov, and Andrey Ganopolski. Sensitivity of the last glacial inception to initial and surface conditions. *Climate Dynamics*, 27:333–344, 9 2006. ISSN 09307575. doi: 10.1007/s00382-006-0136-6.

J. E. Kutzbach and H. E. Wright. Simulation of the climate of 18,000 years bp: Results for the north american/north atlantic/european sector and comparison with the geologic record of north america. *Quaternary Science Reviews*, 4:147–187, 1985. ISSN 02773791. doi: 10.1016/0277-3791(85)90024-1.

Valmore C LaMarche. Tree-ring evidence of past climatic variability. *Nature*, 276: 334–338, 1978. ISSN 1476-4687. doi: 10.1038/276334a0. URL https://doi.org/10.1038/276334a0.

Zhengyang Li, Tie Liu, Yue Huang, Jiabin Peng, and Yunan Ling. Evaluation of the cmip6 precipitation simulations over global land. *Earth's Future*, 10:1–21, 2022. ISSN 23284277. doi: 10.1029/2021EF002500.

Johan Liakka, Marcus Löfverström, and Florence Colleoni. The impact of the north american glacial topography on the evolution of the eurasian ice sheet over the last glacial cycle. *Climate of the Past*, 12:1225–1241, 5 2016. ISSN 1814-9332. doi: 10.5194/cp-12-1225-2016. URL https://cp.copernicus.org/articles/12/1225/2016/.

Jörg Lippold, Yiming Luo, Roger Francois, Susan E Allen, Jeanne Gherardi, Sylvain Pichat, Ben Hickey, and Hartmut Schulz. Strength and geometry of the glacial atlantic meridional overturning circulation. *Nature Geoscience*, 5:813–816, 2012. ISSN 1752-0908. doi: 10.1038/ngeo1608. URL https://doi.org/10.1038/ngeo1608.

Lorraine E. Lisiecki and Maureen E. Raymo. A pliocene-pleistocene stack of 57

globally distributed benthic d 18o records. *Paleoceanography*, 20:1–17, 2005. ISSN 08838305. doi: 10.1029/2004PA001071.

Marcus Lofverstrom and Johan Liakka. The influence of atmospheric grid resolution in a climate model-forced ice sheet simulation. *Cryosphere*, 12:1499–1510, 4 2018. ISSN 19940424. doi: 10.5194/TC-12-1499-2018.

Ryan Love, Heather J. Andres, Alan Condron, and Lev Tarasov. Freshwater routing in eddy-permitting simulations of the last deglacial: The impact of realistic freshwater discharge. *Climate of the Past*, 17:2327–2341, 11 2021. ISSN 18149332. doi: 10.5194/cp-17-2327-2021.

T.K. Lowenstein and B. Hönisch. The use of mg/ca as a seawater temperature proxy. *The Paleontological Society Papers*, 18:85–100, 2012. ISSN 1469817X. doi: 10.1017/S1089332600002564.

Jean Lynch-Stieglitz. The atlantic meridional overturning circulation and abrupt climate change, 1 2017. ISSN 19410611.

Dieter Lüthi, Martine Le Floch, Bernhard Bereiter, Thomas Blunier, Jean Marc Barnola, Urs Siegenthaler, Dominique Raynaud, Jean Jouzel, Hubertus Fischer, Kenji Kawamura, and Thomas F. Stocker. High-resolution carbon dioxide concentration record 650,000-800,000 years before present. *Nature*, 453:379–382, 2008. ISSN 14764687. doi: 10.1038/nature06949.

Isabelle McMartin, Pierre Marc Godbout, Janet E. Campbell, Tommy Tremblay, and Pouran Behnia. A new map of glacigenic features and glacial landsystems in

central mainland nunavut, canada. *Boreas*, 50:51–75, 2021. ISSN 15023885. doi: 10.1111/bor.12479.

Isabelle McMartin, Janet Campbell, Pierre-Marc Godbout, Pouran Behnia, Tommy Tremblay, and Philippe Normandeau. High-resolution mapping of glacial landscapes in the north-central portion of the laurentide ice sheet in nunavut and northwest territories. pages 145–165, 2023. doi: 10.4095/331423.

Martín Medina-Elizalde. A global compilation of coral sea-level benchmarks: Implications and new challenges. *Earth and Planetary Science Letters*, 362:310–318, 2013. ISSN 0012821X. doi: 10.1016/j.epsl.2012.12.001.

North Greenland Ice Core Project Members. 50 year means of oxygen isotope data from ice core ngrip, 2007. URL `https://doi.org/10.1594/PANGAEA.586886`. Supplement to: North Greenland Ice Core Project Members (2004): High-resolution record of Northern Hemisphere climate extending into the last interglacial period. Nature, 431, 147-151, https://doi.org/10.1038/nature02805.

L. Menviel, M. H. England, K. J. Meissner, A. Mouchet, and J. Yu. Atlantic-pacific seesaw and its role in outgassing co2 during heinrich events. *Paleoceanography*, 29: 58–70, 2014. ISSN 19449186. doi: 10.1002/2013PA002542.

Laurie C. Menviel, Luke C. Skinner, Lev Tarasov, and Polychronis C. Tzedakis. An ice–climate oscillatory framework for dansgaard–oeschger cycles. *Nature Reviews Earth and Environment*, 1:677–693, 2020. ISSN 2662138X. doi: 10.1038/s43017-020-00106-y.

Ute Merkel, Matthias Prange, and Michael Schulz. Enso variability and teleconnections during glacial climates. *Quaternary Science Reviews*, 29:86–100, 1 2010. ISSN 0277-3791. doi: 10.1016/J.QUASCIREV.2009.11.006.

M Milankovitch. Kanon der erdbestrahlung und seine anwendung auf das eiszeitproblem. *R. Serbian Acad. Spec. Publ.*, 132, 1941.

Gifford H. Miller and John T. Andrews. Hudson bay was not deglaciated during mis-3. *Quaternary Science Reviews*, 225:105944, 2019. ISSN 02773791. doi: 10.1016/j.quascirev.2019.105944. URL `https://doi.org/10.1016/j.quascirev.2019.105944`.

Juan Muglia and Andreas Schmittner. Glacial atlantic overturning increased by wind stress in climate models. *Geophysical Research Letters*, 42:9862–9869, 11 2015. ISSN 19448007. doi: 10.1002/2015GL064583.

Helene Muri, André Berger, Qiuzhen Yin, Aurore Voldoire, David Salas Y. Mélia, and Suchithra Sundaram. Sst and ice sheet impacts on the mis-13 climate. *Climate Dynamics*, 39:1739–1761, 2012. ISSN 09307575. doi: 10.1007/s00382-011-1216-9.

Per Möller, Grigorij Fedorov, Maxim Pavlov, Marit Solveig Seidenkrantz, and Charlotte Sparrenbom. Glacial and palaeoenvironmental history of the cape chelyuskin area, arctic russia. *Polar Research*, 27:222–248, 2008. ISSN 17518369. doi: 10.1111/j.1751-8369.2008.00066.x.

Per Möller, Helena Alexanderson, Svend Funder, and Christian Hjort. The taimyr peninsula and the severnaya zemlya archipelago, arctic russia: a synthesis of glacial history and palaeo-environmental change during the last glacial cycle (mis 5e–2).

Quaternary Science Reviews, 107:149–181, 1 2015. ISSN 0277-3791. doi: 10.1016/J.QUASCIREV.2014.10.018.

Per Möller, Ívar Örn Benediktsson, Johanna Anjar, Ole Bennike, Martin Bernhardson, S. Funder, Lena M. Håkansson, Geoffrey Lemdahl, Joseph M. Licciardi, Andrew S. Murray, and Marit Solveig Seidenkrantz. Data set on sedimentology, palaeoecology and chronology of middle to late pleistocene deposits on the taimyr peninsula, arctic russia. *Data in Brief*, 25:104267, 8 2019a. ISSN 2352-3409. doi: 10.1016/J.DIB.2019.104267.

Per Möller, Ívar Örn Benediktsson, Johanna Anjar, Ole Bennike, Martin Bernhardson, Svend Funder, Lena M. Håkansson, Geoffrey Lemdahl, Joseph M. Licciardi, Andrew S. Murray, and Marit Solveig Seidenkrantz. Glacial history and palaeoenvironmental change of southern taimyr peninsula, arctic russia, during the middle and late pleistocene. *Earth-Science Reviews*, 196:102832, 9 2019b. ISSN 0012-8252. doi: 10.1016/J.EARSCIREV.2019.04.004.

Sophie M.J. Nowicki, Anthony Payne, Eric Larour, Helene Seroussi, Heiko Goelzer, William Lipscomb, Jonathan Gregory, Ayako Abe-Ouchi, and Andrew Shepherd. Ice sheet model intercomparison project (ismip6) contribution to cmip6. *Geoscientific Model Development*, 9:4521–4545, 2016. ISSN 19919603. doi: 10.5194/gmd-9-4521-2016.

Dylan Oldenburg, Kyle C. Armour, Lu Anne Thompson, and Cecilia M. Bitz. Distinct mechanisms of ocean heat transport into the arctic under internal variability

and climate change. *Geophysical Research Letters*, 45:7692–7700, 8 2018. ISSN 19448007. doi: 10.1029/2018GL078719.

Lars Olsen, Harald Sveian, Bjørn Bergstrøm, Dag Ottesen, and Leif Rise. *Quaternary glaciations and their variations in Norway and on the Norwegian continental shelf*. 2013.

Francis O. Otieno and David H. Bromwich. Contribution of atmospheric circulation to inception of the laurentide ice sheet at 116 kyr bp. *Journal of Climate*, 22:39–57, 2009. ISSN 08948755. doi: 10.1175/2008JCLI2211.1.

F Parrenin, V Masson-Delmotte, P Köhler, D Raynaud, D Paillard, J Schwander, C Barbante, A Landais, A Wegner, and J Jouzel. Synchronous change of atmospheric co2 and antarctic temperature during the last deglacial warming. *Science*, 339:1060–1063, 2013. doi: 10.1126/science.1226368. URL `https://www.science.org/doi/abs/10.1126/science.1226368`.

Violet L Patterson, Lauren J Gregoire, Ruza F Ivanovic, Niall Gandy, Jonathan Owen, Oliver G Pollard, and Lachlan C Astfalck. Contrasting the penultimate and last glacial maxima (140 and 21 ka bp) using coupled climate-ice sheet modelling. *Climate of The Past Discussions*, 2024. doi: 10.5194/cp-2024-10. URL `https://doi.org/10.5194/cp-2024-10`.

W. Richard Peltier and Shawn Marshall. Coupled energy-balance/ice-sheet model simulations of the glacial cycle: A possible connection between terminations and terrigenous dust. *Journal of Geophysical Research*, 100:14269, 1995. ISSN 0148-0227. doi: 10.1029/95JD00015.

A. Persson, P. L. Langen, P. Ditlevsen, and B. M. Vinther. The influence of precipitation weighting on interannual variability of stable water isotopes in greenland. *Journal of Geophysical Research Atmospheres*, 116, 2011. ISSN 01480227. doi: 10.1029/2010JD015517.

Frerk Pöppelmeier, Jeemijn Scheen, Aurich Jeltsch-Thömmes, and Thomas F. Stocker. Simulated stability of the atlantic meridional overturning circulation during the last glacial maximum. *Climate of the Past*, 17:615–632, 3 2021. ISSN 1814-9332. doi: 10.5194/cp-17-615-2021. URL `https://cp.copernicus.org/articles/17/615/2021/`.

Maureen E. Raymo and Peter Huybers. Unlocking the mysteries of the ice ages. *Nature*, 451:284–285, 2008. ISSN 14764687. doi: 10.1038/nature06589.

Edward J. Rhodes. Optically stimulated luminescence dating of sediments over the past 200,000 years. *Annual Review of Earth and Planetary Sciences*, 39:461–488, 5 2011. ISSN 00846597. doi: 10.1146/annurev-earth-040610-133425.

Bjørg Risebrobakken, Trond Dokken, Odd Helge Otterå, Eystein Jansen, Yongqi Gao, and Helge Drange. Inception of the northern european ice sheet due to contrasting ocean and insolation forcing. *Quaternary Research*, 67:128–135, 2007. ISSN 00335894. doi: 10.1016/j.yqres.2006.07.007.

A T Roach, K Aagaard, C H Pease, S A Salo, T Weingartner, V Pavlov, and M Kulakov. Direct measurements of transport and water properties through the bering strait. *Journal of Geophysical Research: Oceans*, 100:18443–18457, 1995. doi: https:

//doi.org/10.1029/95JC01673. URL https://agupubs.onlinelibrary.wiley.com/doi/abs/10.1029/95JC01673.

Laura F Robinson, G M Henderson, H C Ng, and J F Mcmanus. Pa/th as a (paleo)circulation tracer: A north atlantic perspective. *Past Global Changes Magazine*, 27:2018–2019, 2019. ISSN 2411605X. doi: 10.22498/pages.27.2.56.

Gerard H. Roe. Orographic precipitation, 2005. ISSN 00846597.

Eelco J. Rohling, Fiona D. Hibbert, Felicity H. Williams, Katharine M. Grant, Gianluca Marino, Gavin L. Foster, Rick Hennekam, Gert J. de Lange, Andrew P. Roberts, Jimin Yu, Jody M. Webster, and Yusuke Yokoyama. Differences between the last two glacial maxima and implications for ice-sheet, d18o, and sea-level reconstructions. *Quaternary Science Reviews*, 176:1–28, 2017. ISSN 02773791. doi: 10.1016/j.quascirev.2017.09.009. URL https://doi.org/10.1016/j.quascirev.2017.09.009.

William F. Ruddiman. Orbital insolation, ice volume, and greenhouse gases. *Quaternary Science Reviews*, 22:1597–1629, 2003. ISSN 02773791. doi: 10.1016/S0277-3791(03)00087-8.

Audrey M. Rémillard, Guillaume St-Onge, Pascal Bernatchez, Bernard Hétu, Jan Pieter Buylaert, Andrew S. Murray, and Patrick Lajeunesse. Relative sea-level changes and glacio-isostatic adjustment on the magdalen islands archipelago (atlantic canada) from mis 5 to the late holocene. *Quaternary Science Reviews*, 171:216–233, 9 2017. ISSN 0277-3791. doi: 10.1016/J.QUASCIREV.2017.07.015.

Andreas Schmittner, Tiago A.M. Silva, Klaus Fraedrich, Edilbert Kirk, and Frank Lunkeit. Effects of mountains and ice sheets on global ocean circulation. *Journal of Climate*, 24:2814–2829, 2011. ISSN 08948755. doi: 10.1175/2010JCLI3982.1.

H Seroussi, S Nowicki, E Simon, A Abe-Ouchi, T Albrecht, J Brondex, S Cornford, C Dumas, F Gillet-Chaulet, H Goelzer, N R Golledge, J M Gregory, R Greve, M J Hoffman, A Humbert, P Huybrechts, T Kleiner, E Larour, G Leguy, W H Lipscomb, D Lowry, M Mengel, M Morlighem, F Pattyn, A J Payne, D Pollard, S F Price, A Quiquet, T J Reerink, R Reese, C B Rodehacke, N.-J. Schlegel, A Shepherd, S Sun, J Sutter, J Van Breedam, R S W van de Wal, R Winkelmann, and T Zhang. initmip-antarctica: an ice sheet model initialization experiment of ismip6. *The Cryosphere*, 13:1441–1471, 2019. doi: 10.5194/tc-13-1441-2019. URL `https://tc.copernicus.org/articles/13/1441/2019/`.

Sam Sherriff-Tadano and Marlene Klockmann. Pmip contributions to understanding the deep ocean circulation of the last glacial maximum. *Past Global Changes Magazine*, 29:84–85, 2021. ISSN 2411605X. doi: 10.22498/pages.29.2.84.

Rachel M Spratt and Lorraine E Lisiecki. A late pleistocene sea level stack. *Climate of the Past*, 12:1079–1092, 4 2016. ISSN 1814-9332. doi: 10.5194/cp-12-1079-2016. URL `http://dx.doi.org/10.5194/cp-12-1079-2016`.

John Inge Svendsen, Helena Alexanderson, Valery I. Astakhov, Igor Demidov, Julian A. Dowdeswell, Svend Funder, Valery Gataullin, Mona Henriksen, Christian Hjort, Michael Houmark-Nielsen, Hans W. Hubberten, Ólafur Ingólfsson, Martin Jakobsson, Kurt H. Kjær, Eiliv Larsen, Hanna Lokrantz, Juha Pekka Lunkka,

Astrid Lysså, Jan Mangerud, Alexei Matiouchkov, Andrew Murray, Per Möller, Frank Niessen, Olga Nikolskaya, Leonid Polyak, Matti Saarnisto, Christine Siegert, Martin J. Siegert, Robert F. Spielhagen, and Ruediger Stein. Late quaternary ice sheet history of northern eurasia. *Quaternary Science Reviews*, 23:1229–1271, 2004. ISSN 02773791. doi: 10.1016/j.quascirev.2003.12.008.

Finn Süfke. 231pa/230th records from the northwestern atlantic covering the period since heinrich stadial 2 until today, 2019. URL `https://doi.org/10.1594/PANGAEA.908156`.

Lev Tarasov and W Richard Peltier. Terminating the 100 kyr ice age cycle. *Journal of Geophysical Research: Atmospheres*, 102:21665–21693, 1997. doi: 10.1029/97JD01766. URL `https://agupubs.onlinelibrary.wiley.com/doi/abs/10.1029/97JD01766`.

Lev Tarasov, Arthur S. Dyke, Radford M. Neal, and W.R. Peltier. A data-calibrated distribution of deglacial chronologies for the north american ice complex from glaciological modeling. *Earth and Planetary Science Letters*, 315-316:30–40, 1 2012. ISSN 0012-821X. doi: 10.1016/J.EPSL.2011.09.010. URL `https://www.sciencedirect.com/science/article/pii/S0012821X11005243`.

D. J. Ullman, A. N. LeGrande, A. E. Carlson, F. S. Anslow, and J. M. Licciardi. Assessing the impact of laurentide ice sheet topography on glacial climate. *Climate of the Past*, 10:487–507, 3 2014. ISSN 1814-9332. doi: 10.5194/cp-10-487-2014. URL `https://cp.copernicus.org/articles/10/487/2014/`.

A. De Vernal, C. Causse, C. Hillaire-Marcel, R. J. Mott, and S. Occhietti. Palynos-

tratigraphy and th/u ages of upper pleistocene interglacial and interstadial deposits on cape breton island, eastern canada. *Geology*, 14:554–557, 1986. ISSN 00917613. doi: 10.1130/0091-7613(1986)14⟨554:PATAOU⟩2.0.CO;2.

G. Vettoretti and W. R. Peltier. Post-eemian glacial inception. part i: The impact of summer seasonal temperature bias. *Journal of Climate*, 16:889–911, 2003. ISSN 08948755. doi: 10.1175/1520-0442(2003)016⟨0889:PEGIPI⟩2.0.CO;2.

G. Vettoretti and W. R. Peltier. Sensitivity of glacial inception to orbital and greenhouse gas climate forcing. *Quaternary Science Reviews*, 23:499–519, 2 2004. ISSN 0277-3791. doi: 10.1016/J.QUASCIREV.2003.08.008.

S. M. Vicente-Serrano, R. García-Herrera, D. Peña-Angulo, M. Tomas-Burguera, F. Domínguez-Castro, I. Noguera, N. Calvo, C. Murphy, R. Nieto, L. Gimeno, J. M. Gutierrez, C. Azorin-Molina, and A. El Kenawy. Do cmip models capture long-term observed annual precipitation trends? *Climate Dynamics*, 58: 2825–2842, 5 2022. ISSN 0930-7575. doi: 10.1007/s00382-021-06034-x. URL `https://link.springer.com/10.1007/s00382-021-06034-x`.

Susanne L Weber. The utility of earth system models of intermediate complexity (emics). *WIREs Climate Change*, 1:243–252, 2010. doi: https://doi.org/10.1002/wcc.24. URL `https://wires.onlinelibrary.wiley.com/doi/abs/10.1002/wcc.24`.

Thomas L. Weiss, Braddock K. Linsley, Arnold L. Gordon, Yair Rosenthal, and Stefanie Dannenmann-Di Palma. Constraints on marine isotope stage 3 and 5 sea level

from the flooding history of the karimata strait in indonesia. *Paleoceanography and Paleoclimatology*, 37, 9 2022. ISSN 25724525. doi: 10.1029/2021PA004361.

Matteo Willeit, Andrey Ganopolski, Alexander Robinson, and Neil R. Edwards. The earth system model climber-x v1.0-part 1: Climate model description and validation. *Geoscientific Model Development*, 15:5905–5948, 7 2022. ISSN 19919603. doi: 10.5194/gmd-15-5905-2022.

Matteo Willeit, Reinhard Calov, Stefanie Talento, Ralf Greve, Jorjo Bernales, Volker Klemann, Meike Bagge, and Andrey Ganopolski. Glacial inception through rapid ice area increase driven by albedo and vegetation feedbacks. *EGUsphere [preprint]*, pages 1–41, 2023.

Isaac J Winograd, Tyler B Coplen, Jurate M Landwehr, Alan C Riggs, Kenneth R Ludwig, Barney J Szabo, Peter T Kolesar, and Kinga M Revesz. Continuous 500,000-year climate record from vein calcite in devils hole, nevada. *Science*, 258: 255–260, 1992. doi: 10.1126/science.258.5080.255. URL `https://www.science.org/doi/abs/10.1126/science.258.5080.255`.

Rebecca A Woodgate, Knut Aagaard, and Thomas J Weingartner. Interannual changes in the bering strait fluxes of volume, heat and freshwater between 1991 and 2004. *Geophysical Research Letters*, 33, 2006. doi: https://doi.org/10.1029/2006GL026931. URL `https://agupubs.onlinelibrary.wiley.com/doi/abs/10.1029/2006GL026931`.

M Yoshimori, A J Weaver, S J Marshall, and G K C Clarke. Glacial termination: sensitivity to orbital and co2 forcing in a coupled climate system model. *Climate*

Dynamics, 17:571–588, 2001. ISSN 1432-0894. doi: 10.1007/s003820000134. URL https://doi.org/10.1007/s003820000134.

M. Yoshimori, M. Reader, A. Weaver, and N. McFarlane. On the causes of glacial inception at 116 kabp. *Climate Dynamics*, 18:383–402, 2002. ISSN 09307575. doi: 10.1007/s00382-001-0186-8.

R. R. Young, J. A. Burns, D. G. Smith, L. D. Arnold, and R. B. Rains. A single, late wisconsin, laurentide glaciation, edmonton area and southwestern alberta. *Geology*, 22:683–686, 1994. ISSN 00917613. doi: 10.1130/0091-7613(1994)022⟨0683:ASLWLG⟩2.3.CO;2.

Appendix A

Appendix to Chapter 2

Video supplement: Ice sheet evolution of 15 NROY simulations for MIS 7e-6e and MIS 5e-4; https://doi.org/10.5446/66195

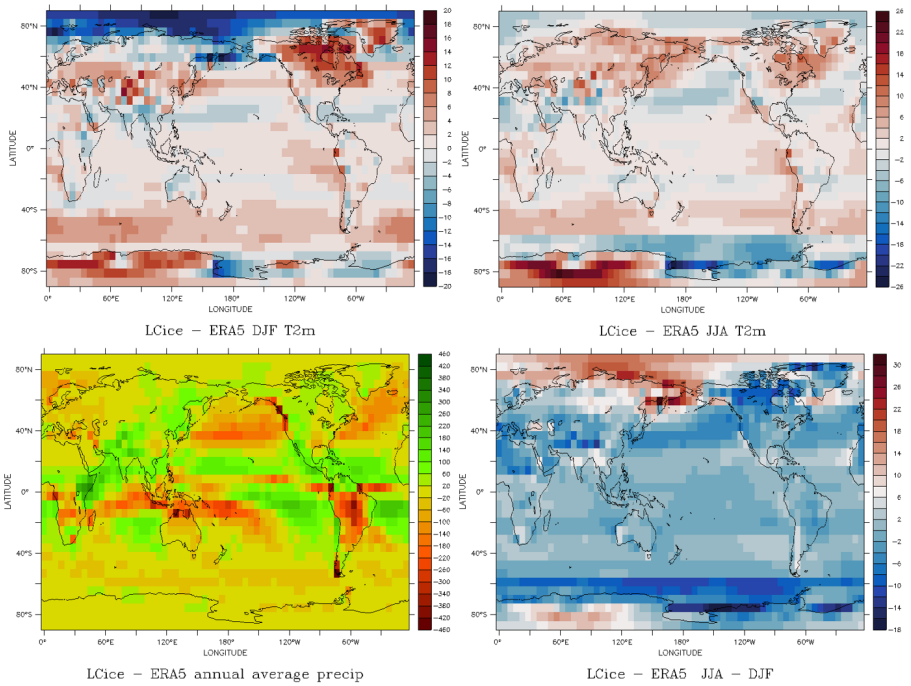

Figure A.1: Sub-ensemble mean seasonal temperature (DJF top left, JJA top right), annual precipitation (bottom left), and seasonal range (JJA-DJF temperature, bottom right) biases compared to ERA 5.

Table A.1: Mean LOVECLIM parameter values and standard deviation for the full ensemble ("all members"), the sub-ensemble passing sea-level filters for MIS 5d, 5c and 4 ("pass inc"), the sub-ensemble passing sea-level filters for MIS 7d, 7c and 6e ("pass peninc"), the sub-ensemble passing all filters, and the default values

Parameter	all members	pass inc	pass peninc	pass all filters	default
ampwir	0.9 ± 0.2	0.9 ± 0.2	0.8 ± 0.2	0.9 ± 0.1	1.0
ampeqir	1.8 ± 0.4	1.8 ± 0.5	1.8 ± 0.5	2.0 ± 0.4	1.8
expir	0.34 ± 0.06	0.33 ± 0.07	0.34 ± 0.07	0.35 ± 0.04	0.40
cdrag	0.0013 ± 0.0002	0.0013 ± 0.0003	0.0013 ± 0.0003	0.0013 ± 0.0001	0.0014
evfac	0.8 ± 0.1	0.8 ± 0.2	0.8 ± 0.2	0.80 ± 0.09	1.00
cwdrag	0.0017 ± 0.0006	0.0019 ± 0.0007	0.0017 ± 0.0006	0.0018 ± 0.0004	0.0021
ahu	99193 ± 23718	99929 ± 26863	96266 ± 25322	99673 ± 21792	100000
uv10rfx	0.78 ± 0.09	0.8 ± 0.1	0.8 ± 0.1	0.78 ± 0.04	0.80
relhmax	0.8 ± 0.1	0.8 ± 0.1	0.8 ± 0.1	0.81 ± 0.04	0.83
albet	0.13 ± 0.02	0.13 ± 0.03	0.13 ± 0.03	0.14 ± 0.02	0.13
albeg	0.21 ± 0.03	0.21 ± 0.03	0.21 ± 0.03	0.21 ± 0.01	0.20
albed	0.33 ± 0.05	0.32 ± 0.06	0.34 ± 0.07	0.33 ± 0.04	0.33
alphd	0.7 ± 0.1	0.7 ± 0.1	0.7 ± 0.1	0.72 ± 0.05	0.72
alphdi	0.57 ± 0.07	0.57 ± 0.10	0.57 ± 0.09	0.58 ± 0.03	0.62
alphs	0.50 ± 0.08	0.49 ± 0.10	0.48 ± 0.09	0.48 ± 0.05	0.53
albice	0.38 ± 0.07	0.37 ± 0.08	0.37 ± 0.08	0.37 ± 0.05	0.44
GHG	2.1 ± 0.4	2.2 ± 0.4	2.1 ± 0.4	2.2 ± 0.2	1.0

Table A.2: Parameter short names and description

ampwir	amplification factor longwave radiation
ampeqir	amplification factor longwave radiation equatorial region
expir	longwave radiation exponent to moisture
cdrag	coeff. in sensible and latent air-sea heat flux
evfac	max. evaporation factor over land
cwdrag	wind stress coeff.
ahu	ocean horizontal viscosity
uv10rfx	800 hPa wind speed reduction to 10 m
relhmax	precipitation threshold
albet	tree albedo
albeg	grass abledo
albed	dessert albedo
alphd	albedo of snow
alphdi	albedo of ice
alphs	albedo of melting snow

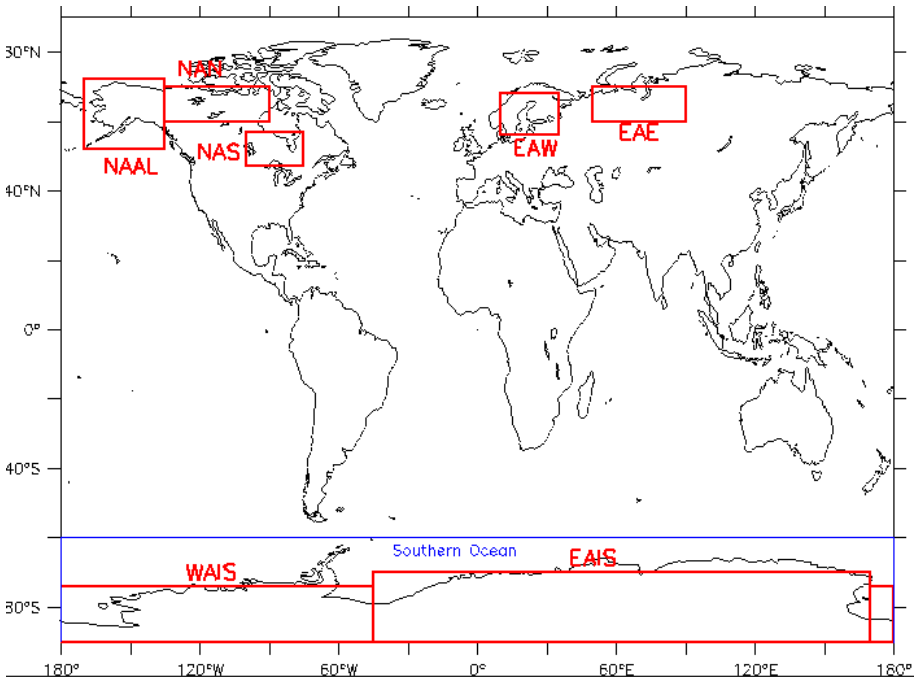

Figure A.2: Regions for filtering PD simulations against reanalysis

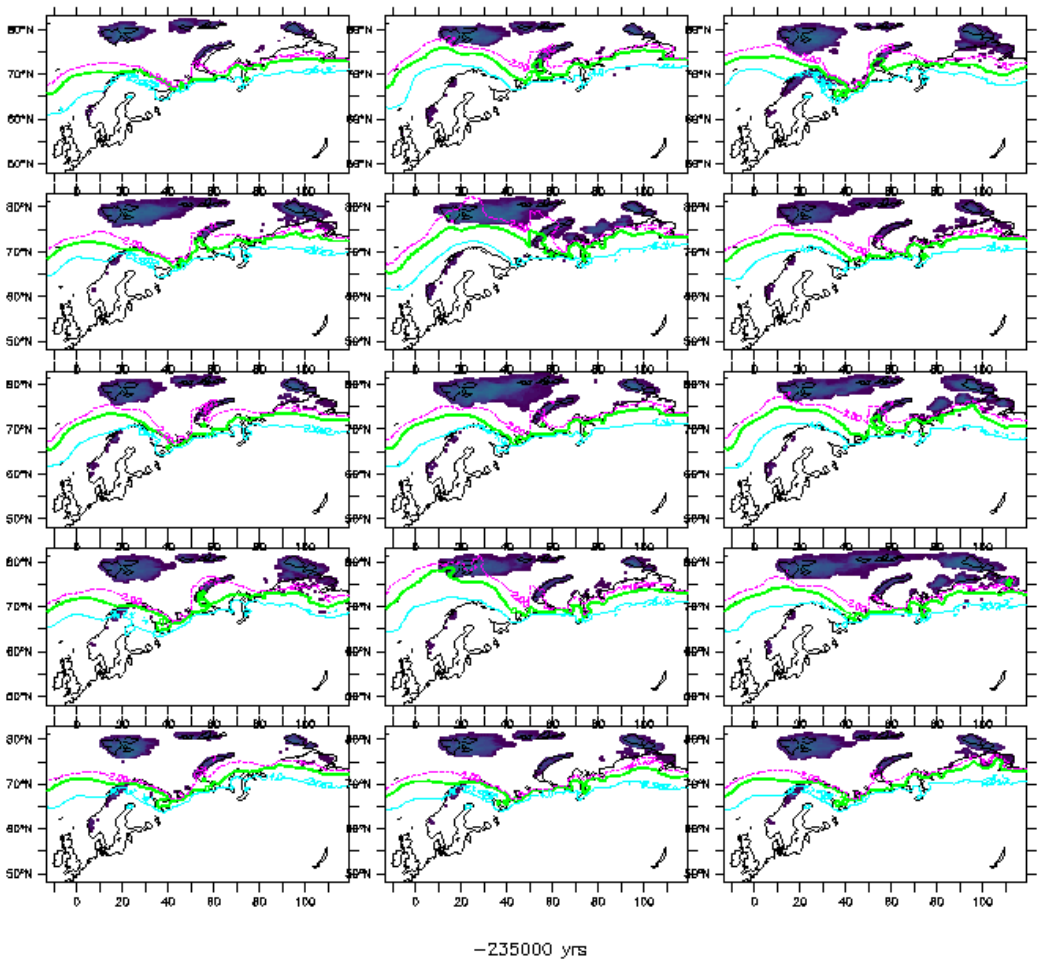

Figure A.3: Ice height and +4°(light blue), 0°(green), and -2°(pink) isotherms during Eurasian ice advance phase towards MIS 7d

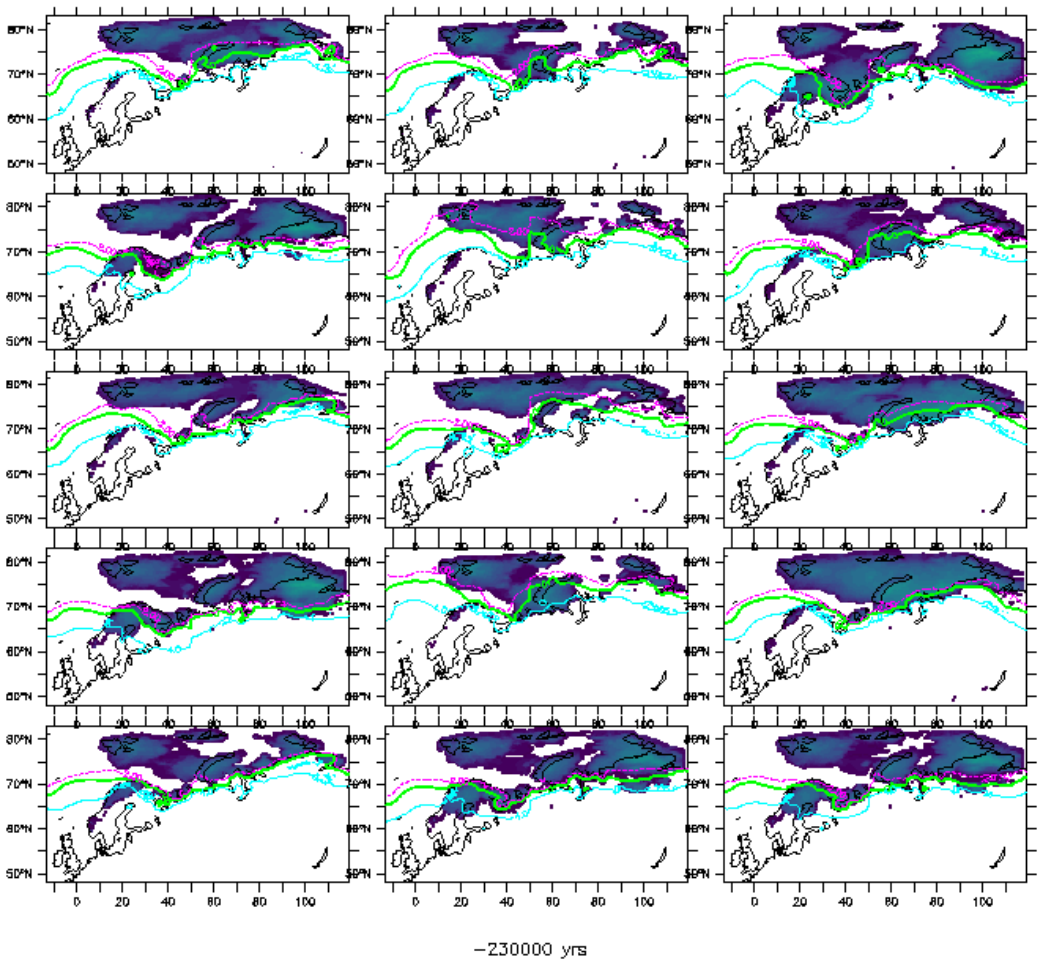

Figure A.4: Ice height and +4°(light blue), 0°(green), and -2°(pink) isotherms during Eurasian max. ice extent at MIS 7d

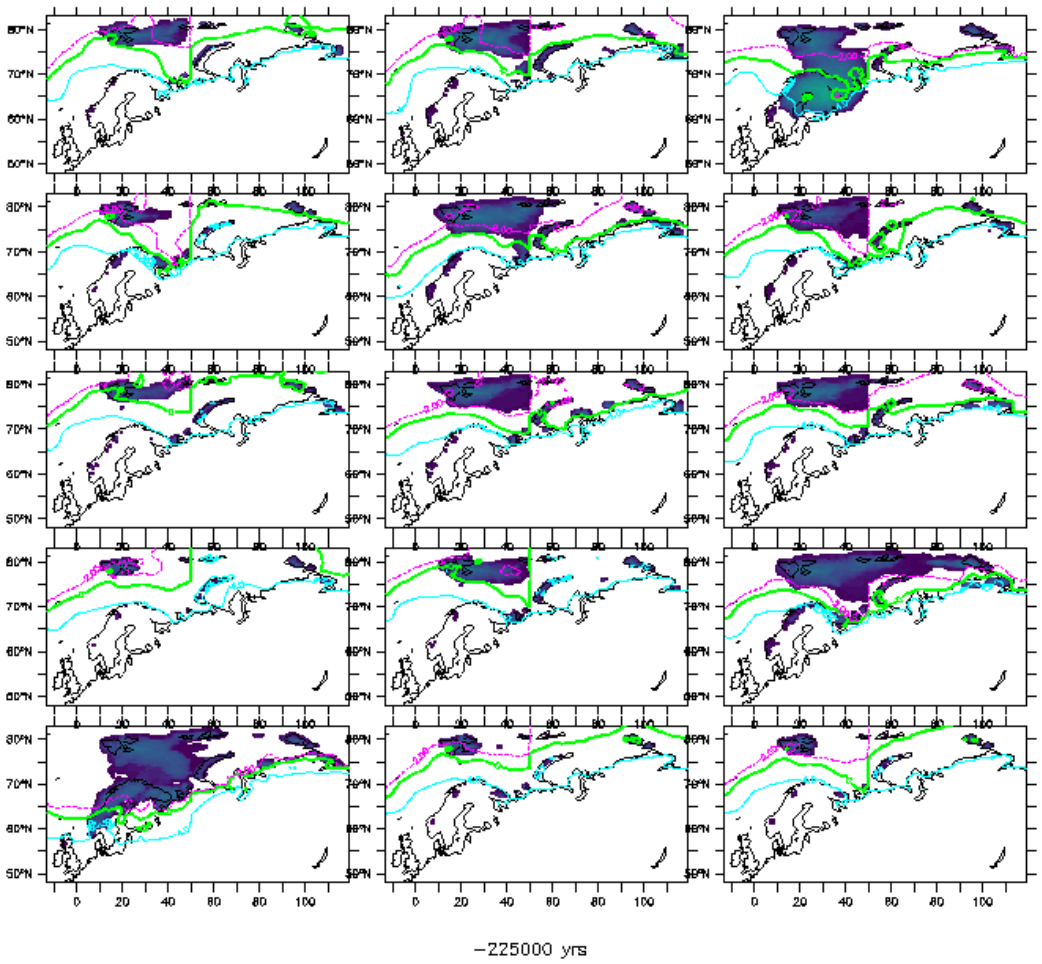

Figure A.5: Ice height and +4°(light blue), 0°(green), and -2°(pink) isotherms during Eurasian ice retreat phase after MIS 7d

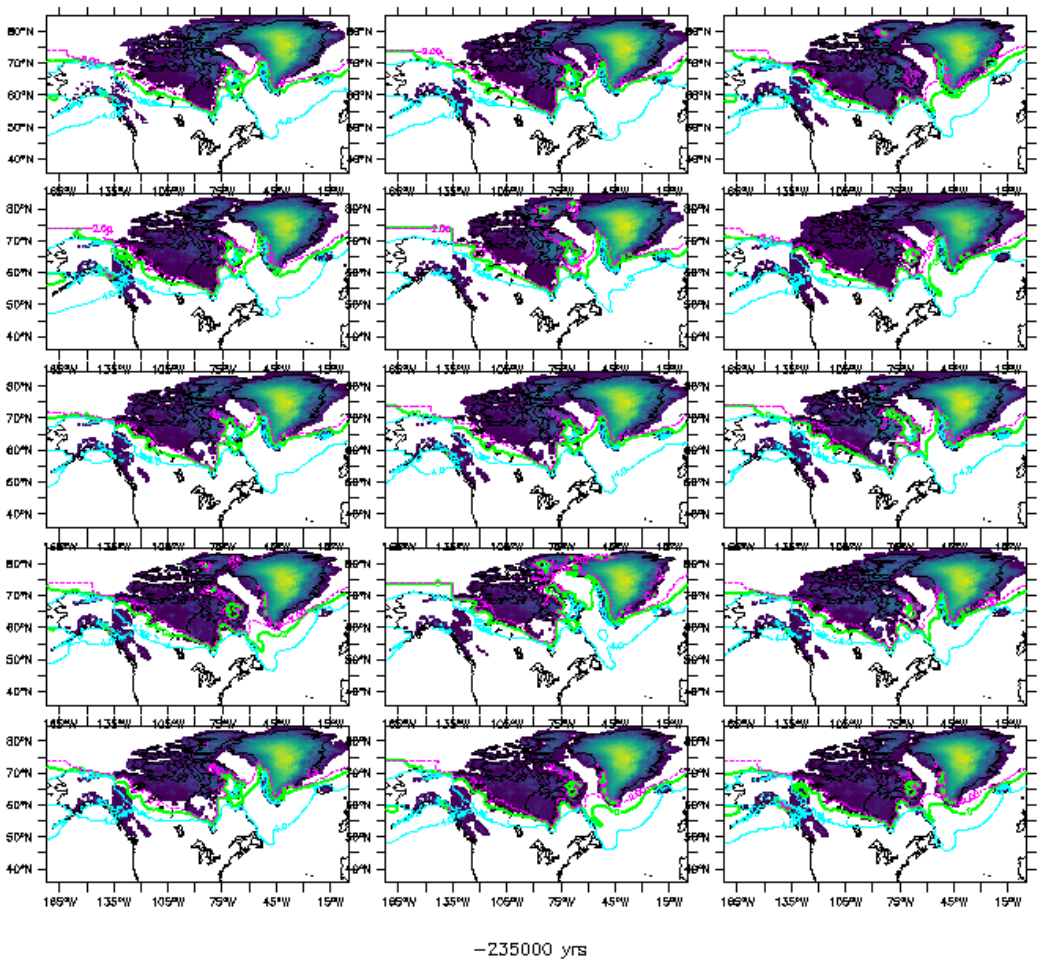

Figure A.6: Ice height and +4°(light blue), 0°(green), and -2°(pink) isotherms during North American ice advance phase towards MIS 7d

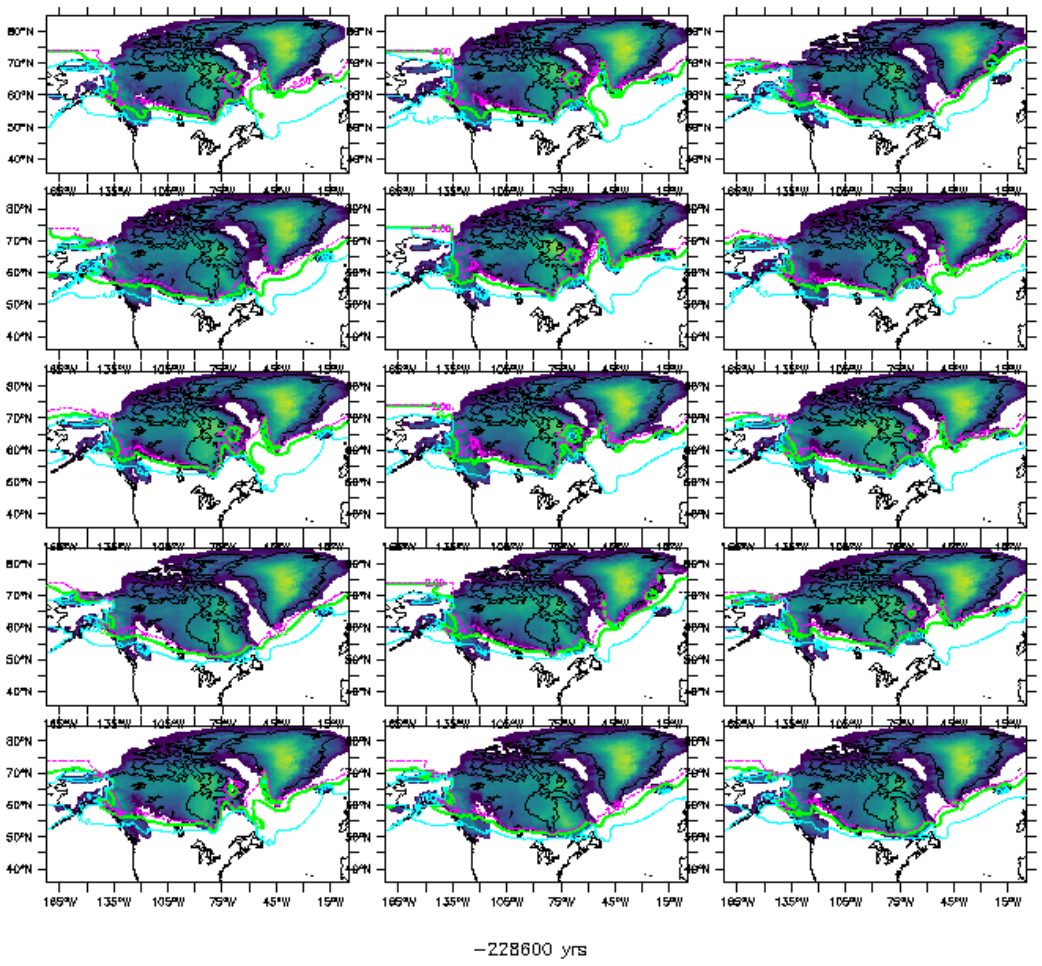

Figure A.7: Ice height and +4°(light blue), 0°(green), and -2°(pink) isotherms during North American max. ice extent at MIS 7d

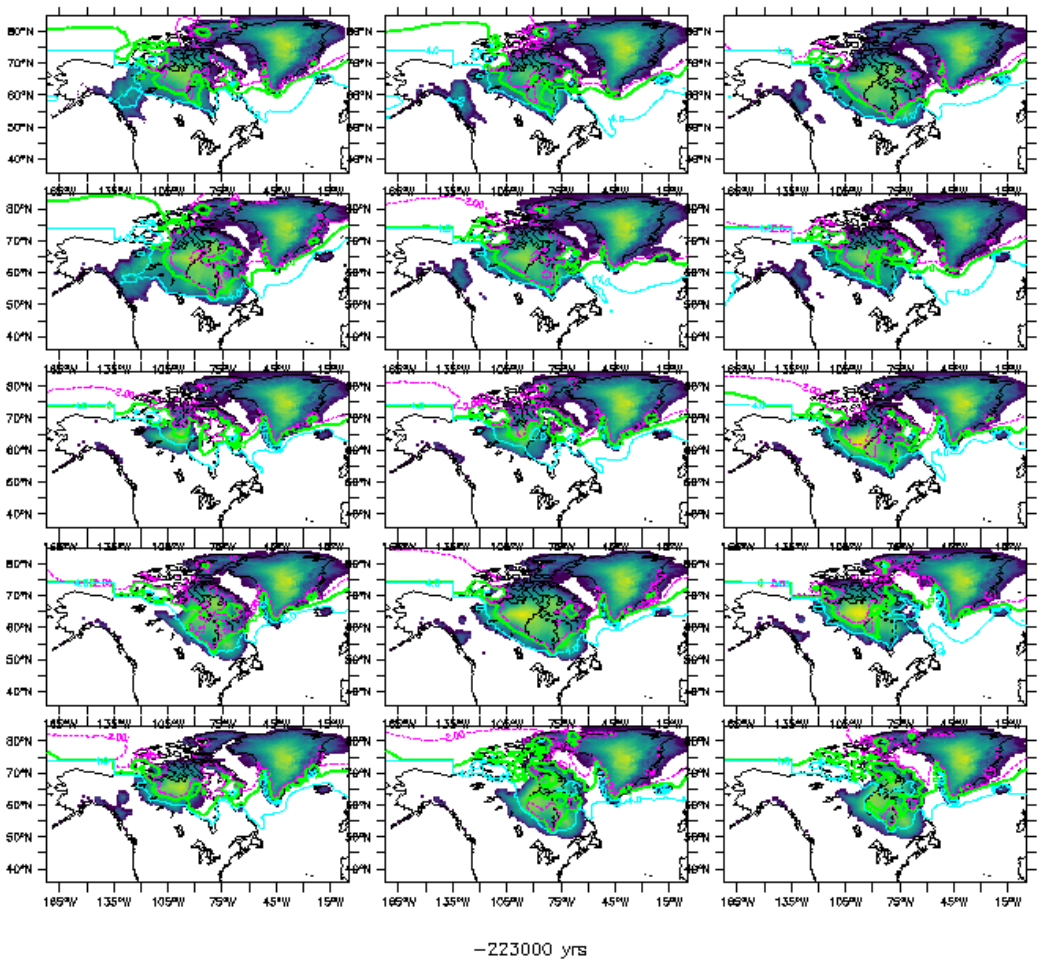

Figure A.8: Ice height and +4°(light blue), 0°(green), and -2°(pink) isotherms during North American ice retreat phase after MIS 7d

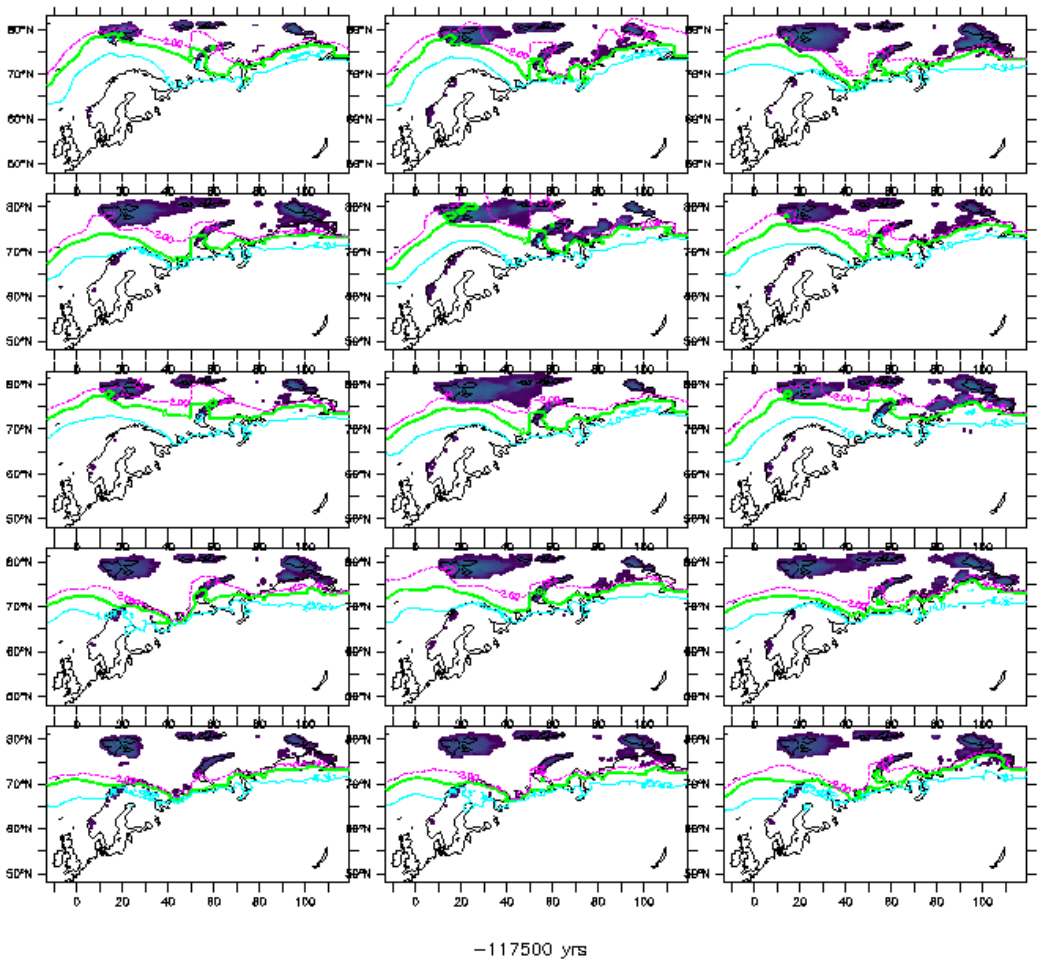

Figure A.9: Ice height and +4°(light blue), 0°(green), and -2°(pink) isotherms during Eurasian ice advance phase towards MIS 5d

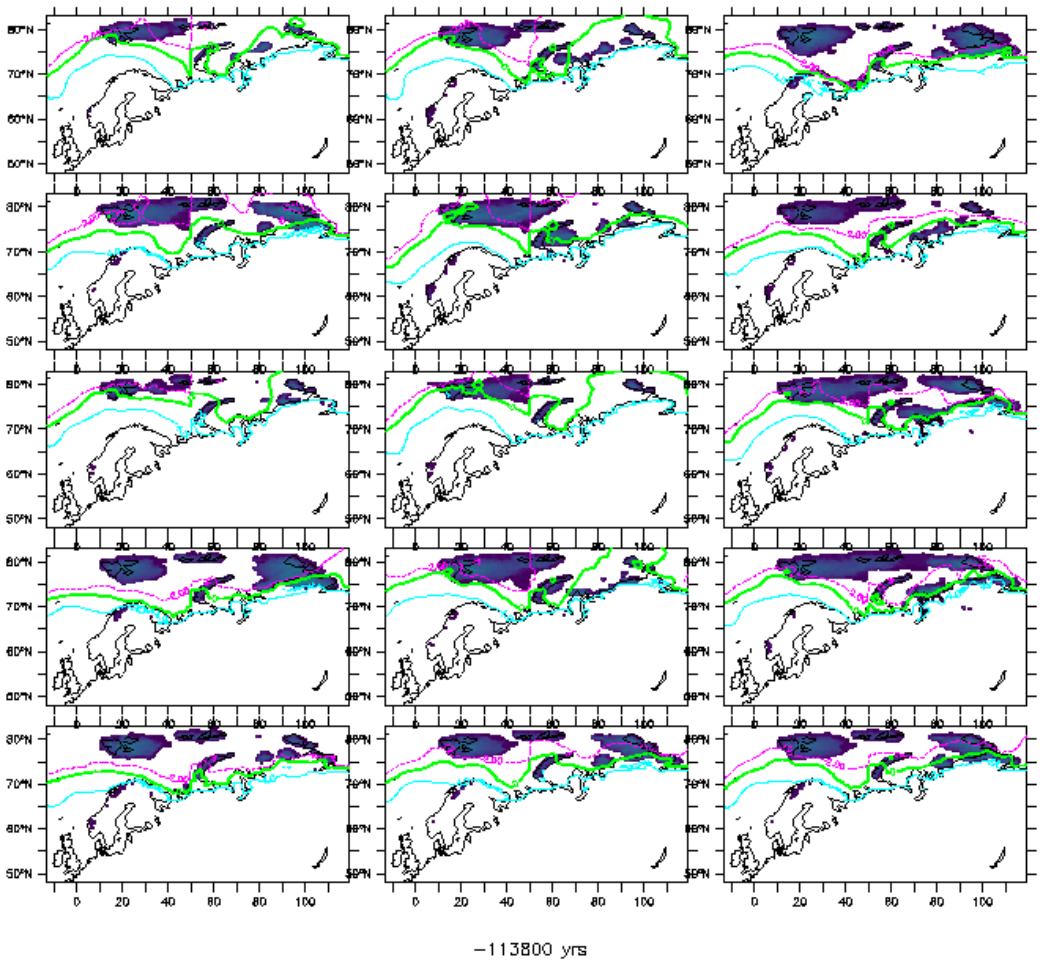

Figure A.10: Ice height and +4°(light blue), 0°(green), and -2°(pink) isotherms during Eurasian max. ice extent at MIS 5d

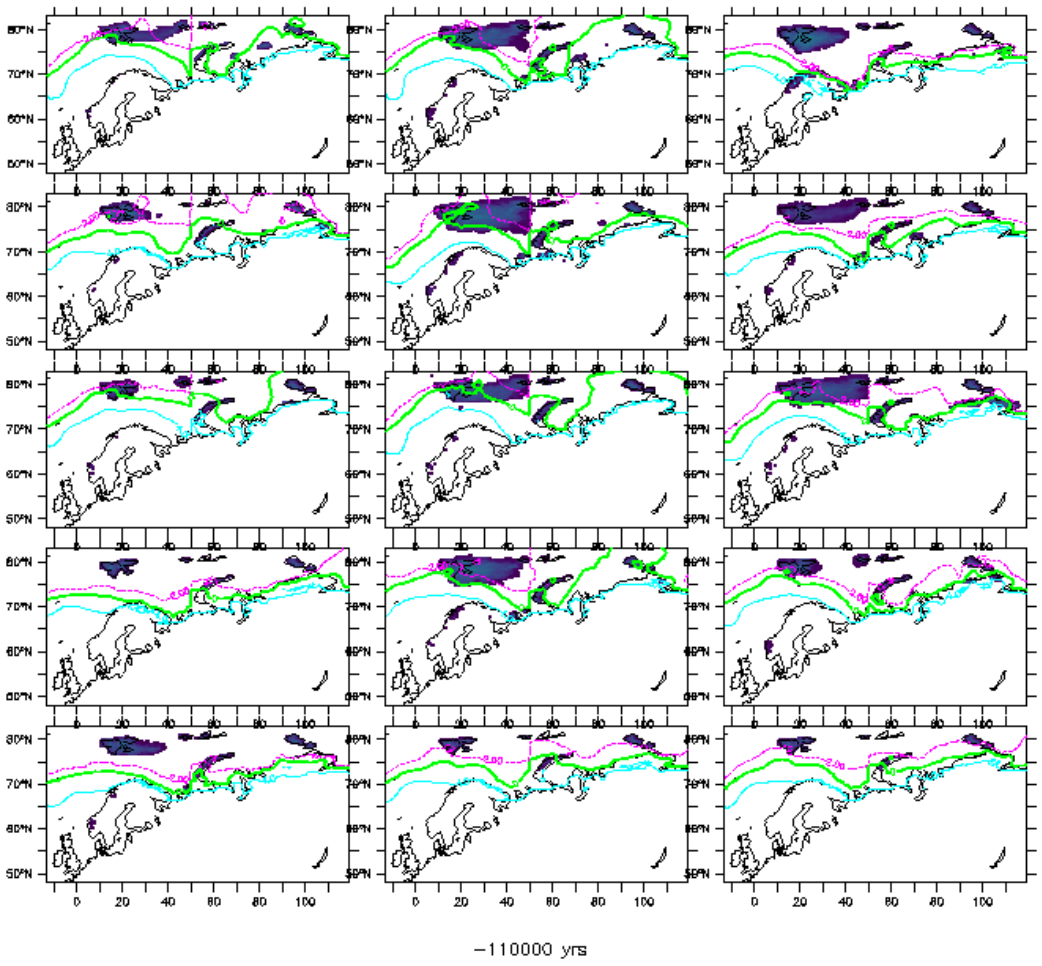

Figure A.11: Ice height and +4°(light blue), 0°(green), and -2°(pink) isotherms during Eurasian ice retreat phase after MIS 5d

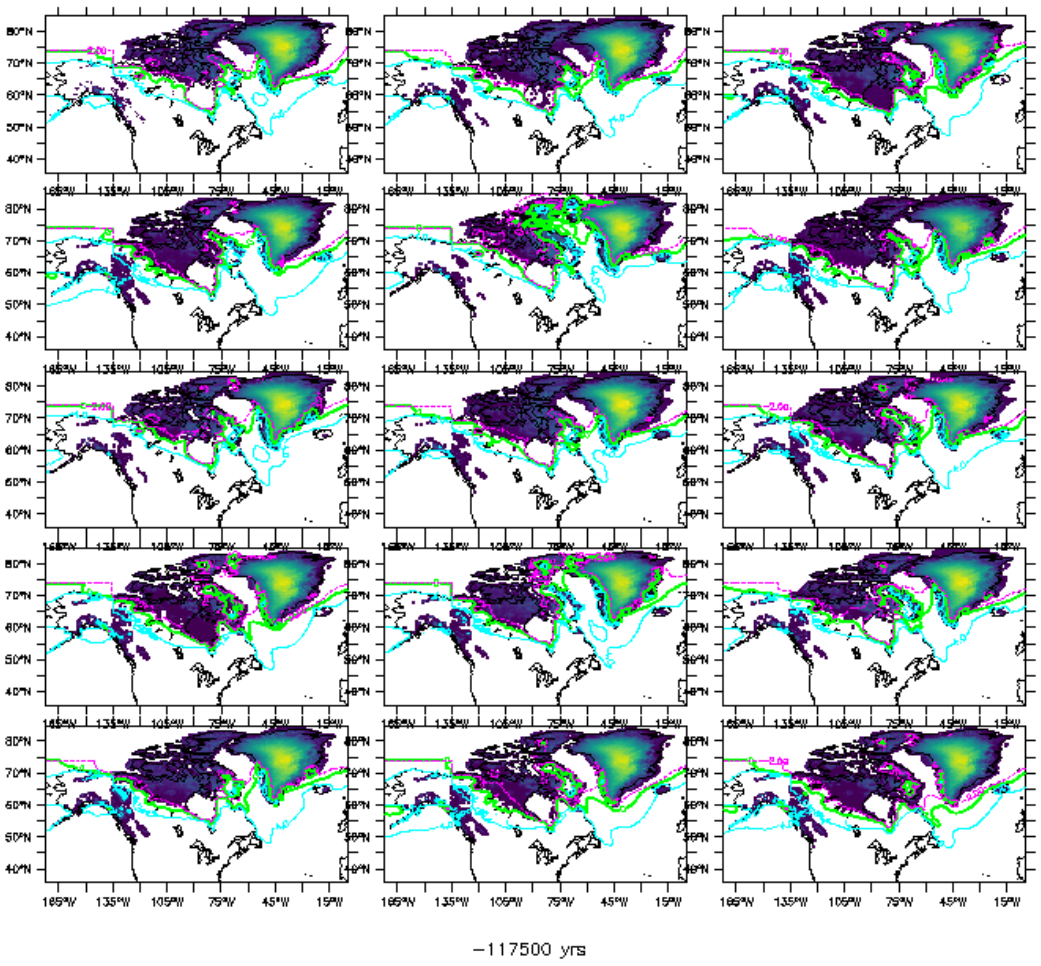

Figure A.12: Ice height and +4°(light blue), 0°(green), and -2°(pink) isotherms during North American ice advance phase towards MIS 5d

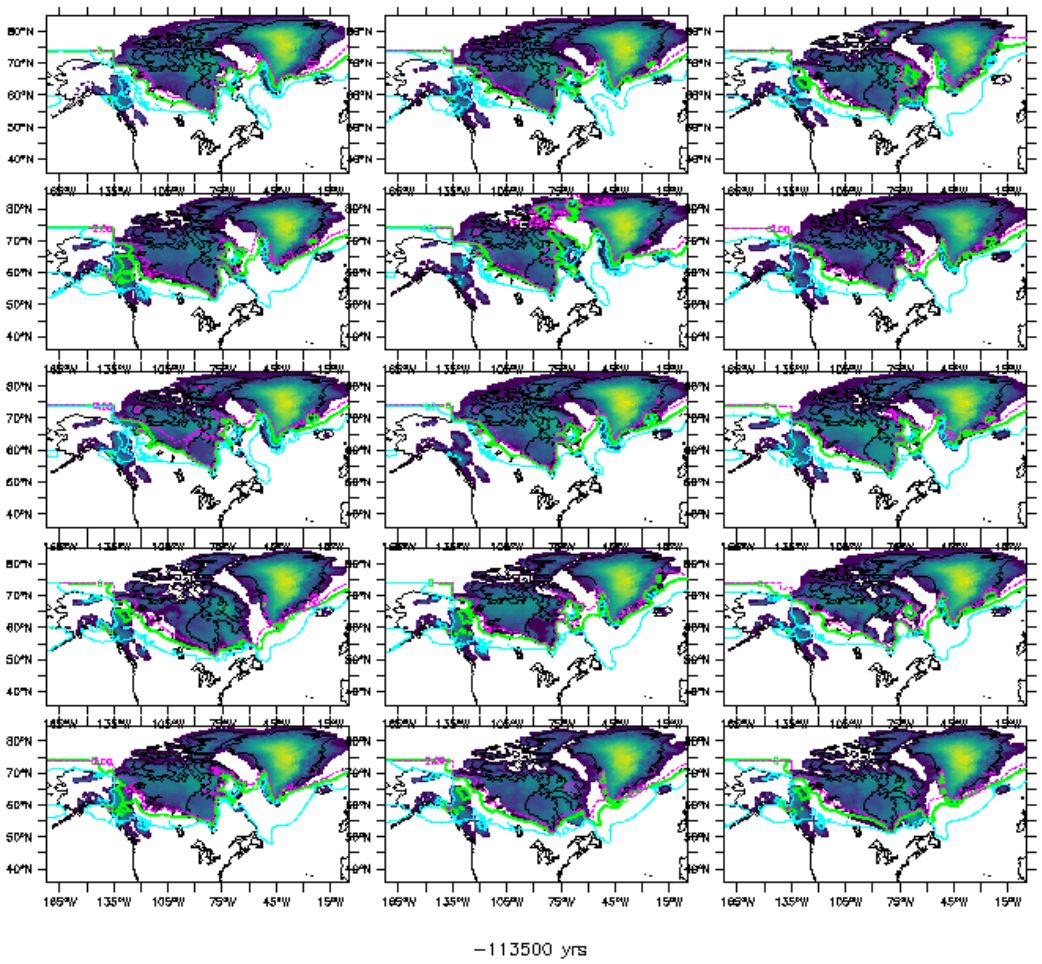

Figure A.13: Ice height and +4°(light blue), 0°(green), and -2°(pink) isotherms during North American max. ice extent at MIS 5d

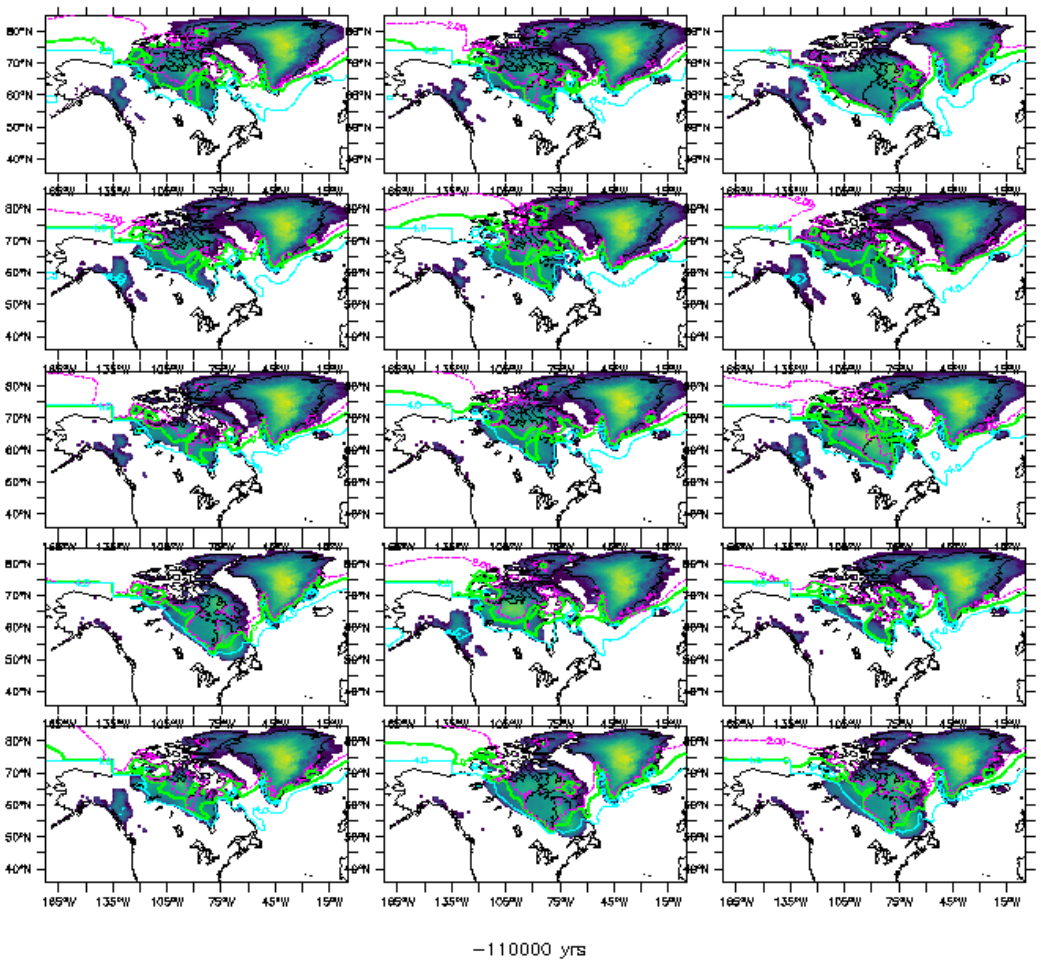

Figure A.14: Ice height and +4°(light blue), 0°(green), and -2°(pink) isotherms during North American ice retreat phase after MIS 5d

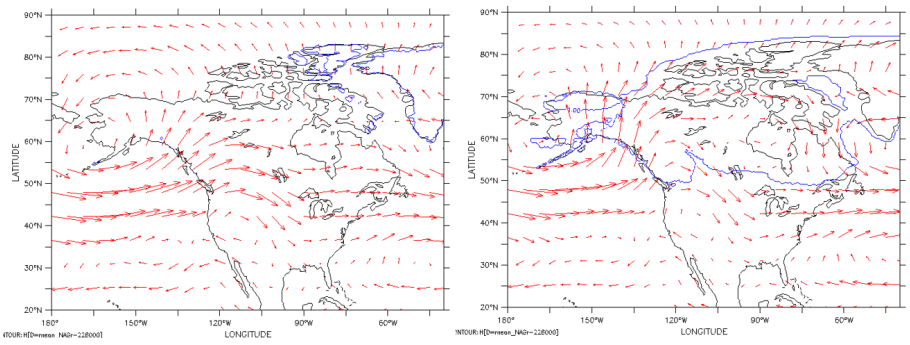

Figure A.15: Sub-ensemble mean 800 hPa January wind at simulation start (interglacial conditions, MIS 7e, left) and at MIS 7d (right)

Appendix B

Appendix to Chapter 4

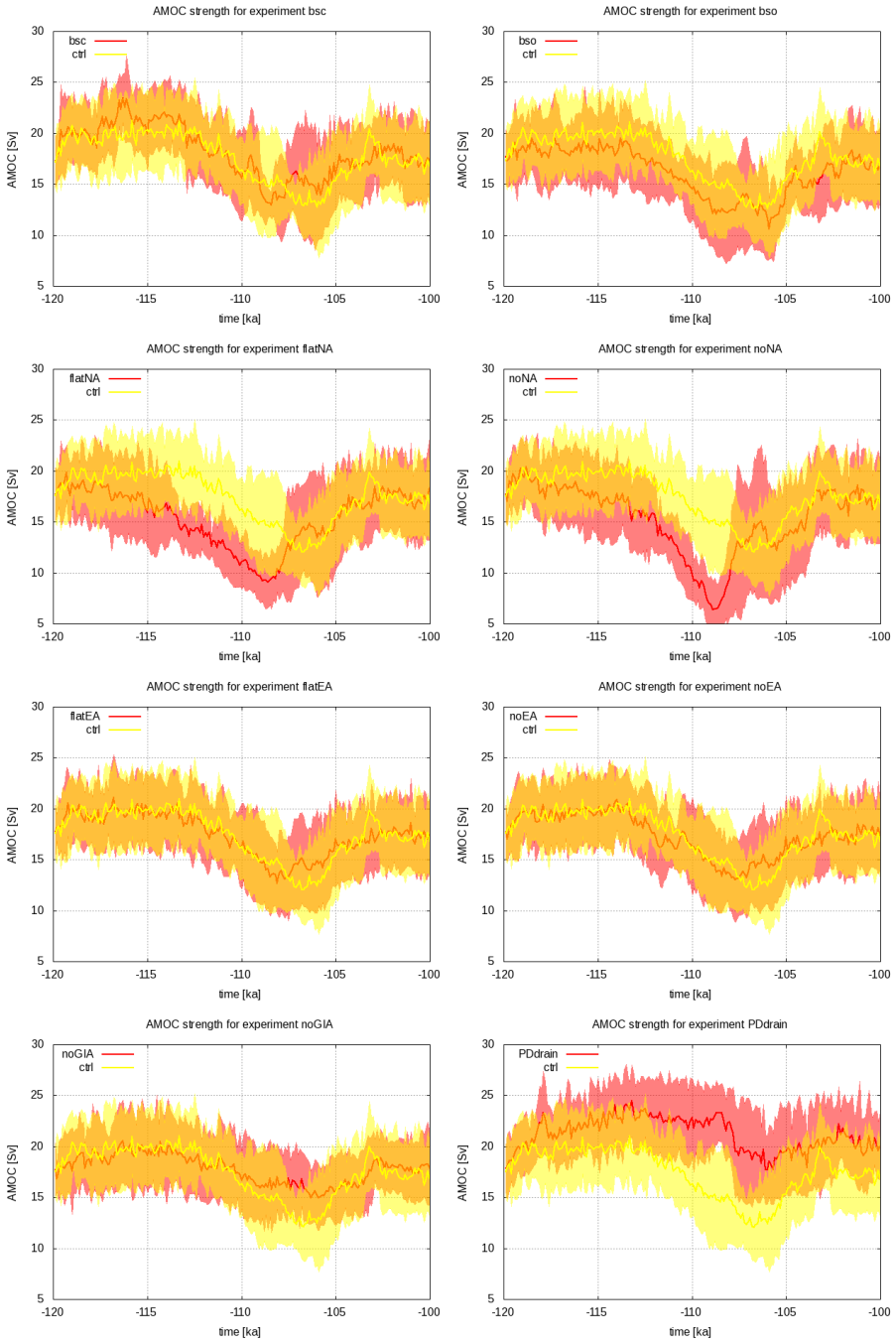

Figure B.1: Ensemble mean and Std Dev of AMOC strength for the MIS 5d interval. Red: sensitivity, yellow: ctrl, grey: excluded ensemble members

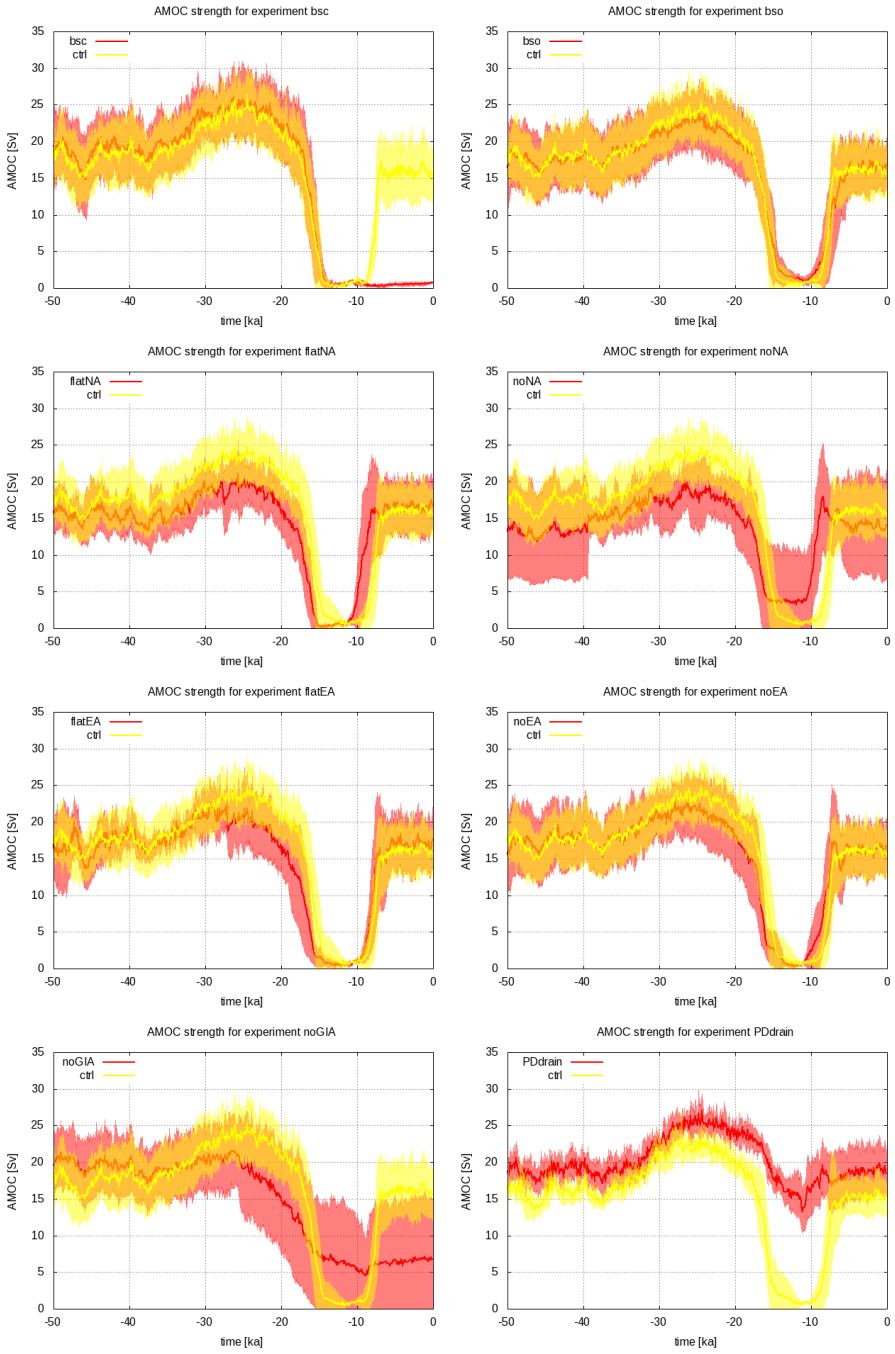

Figure B.2: Ensemble mean and Std Dev of AMOC strength for the MIS 3-1 interval. Red: sensitivity, yellow: ctrl, grey: excluded ensemble members

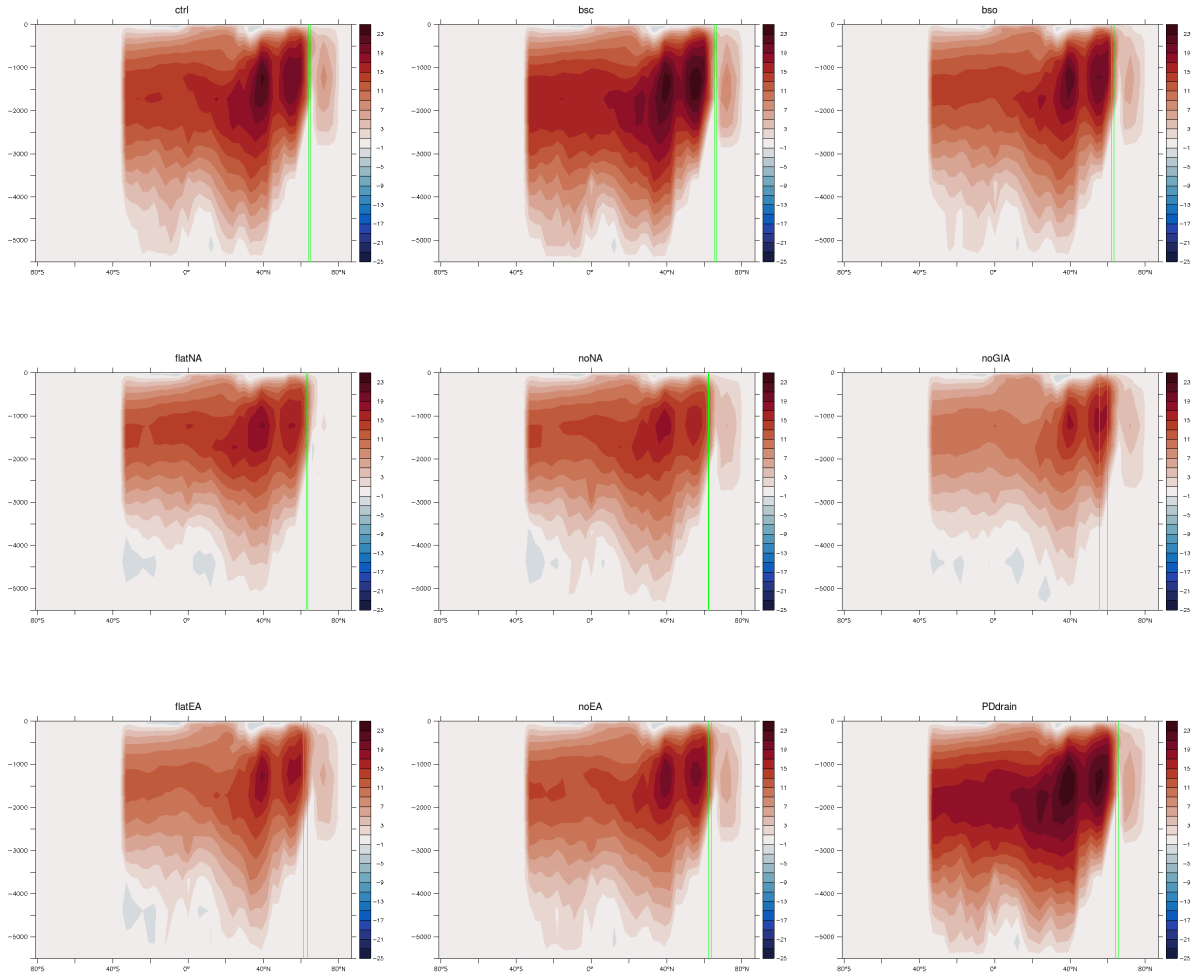

Figure B.3: North Atlantic streamfunction at 25 ka

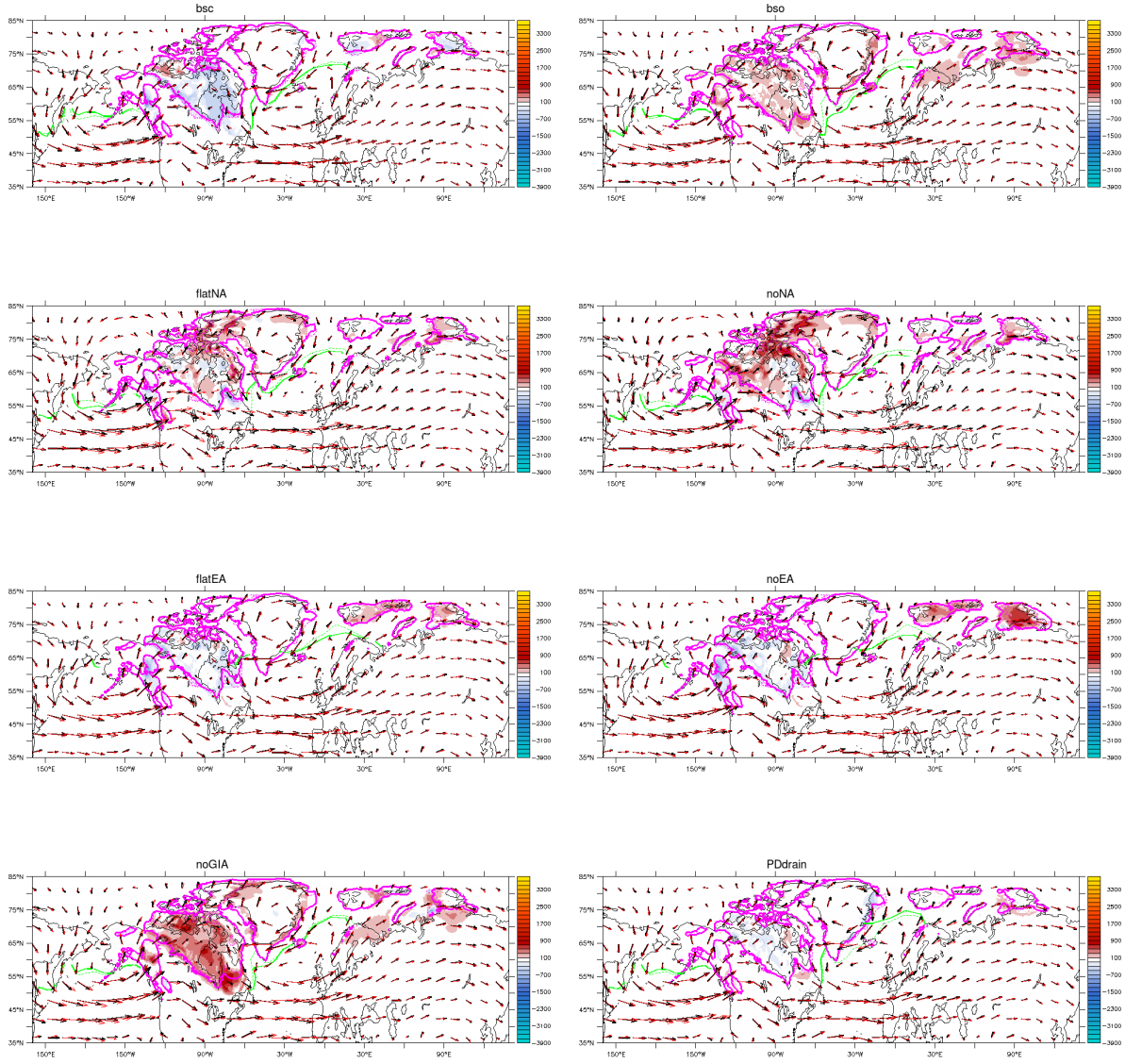

Figure B.4: DJF 800 hPa ensemble mean wind field and difference in ice height (sensitivity-ctrl) at MIS 5d. Black arrows: ctrl, red arrows: sensitivity. Green contour: April sea ice extent. Pink contour: ice sheet extent. Solid: sensitivity, dashed: ctrl

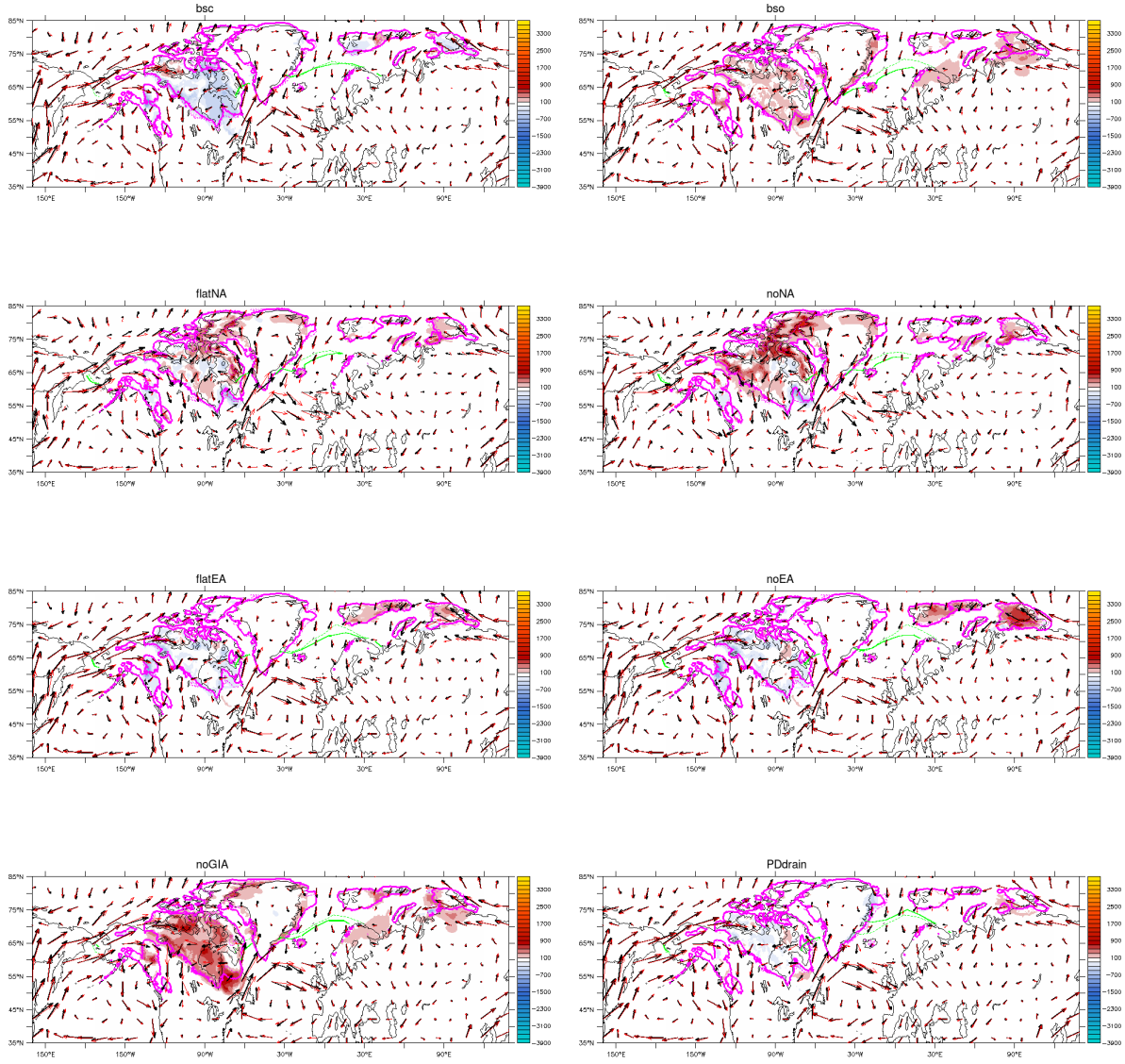

Figure B.5: JJA 800 hPa ensemble mean wind field and difference in ice height (sensitivity-ctrl) at MIS 5d. Black arrows: ctrl, red arrows: sensitivity. Green contour: October sea ice extent. Pink contour: ice sheet extent. Solid: sensitivity, dashed: ctrl

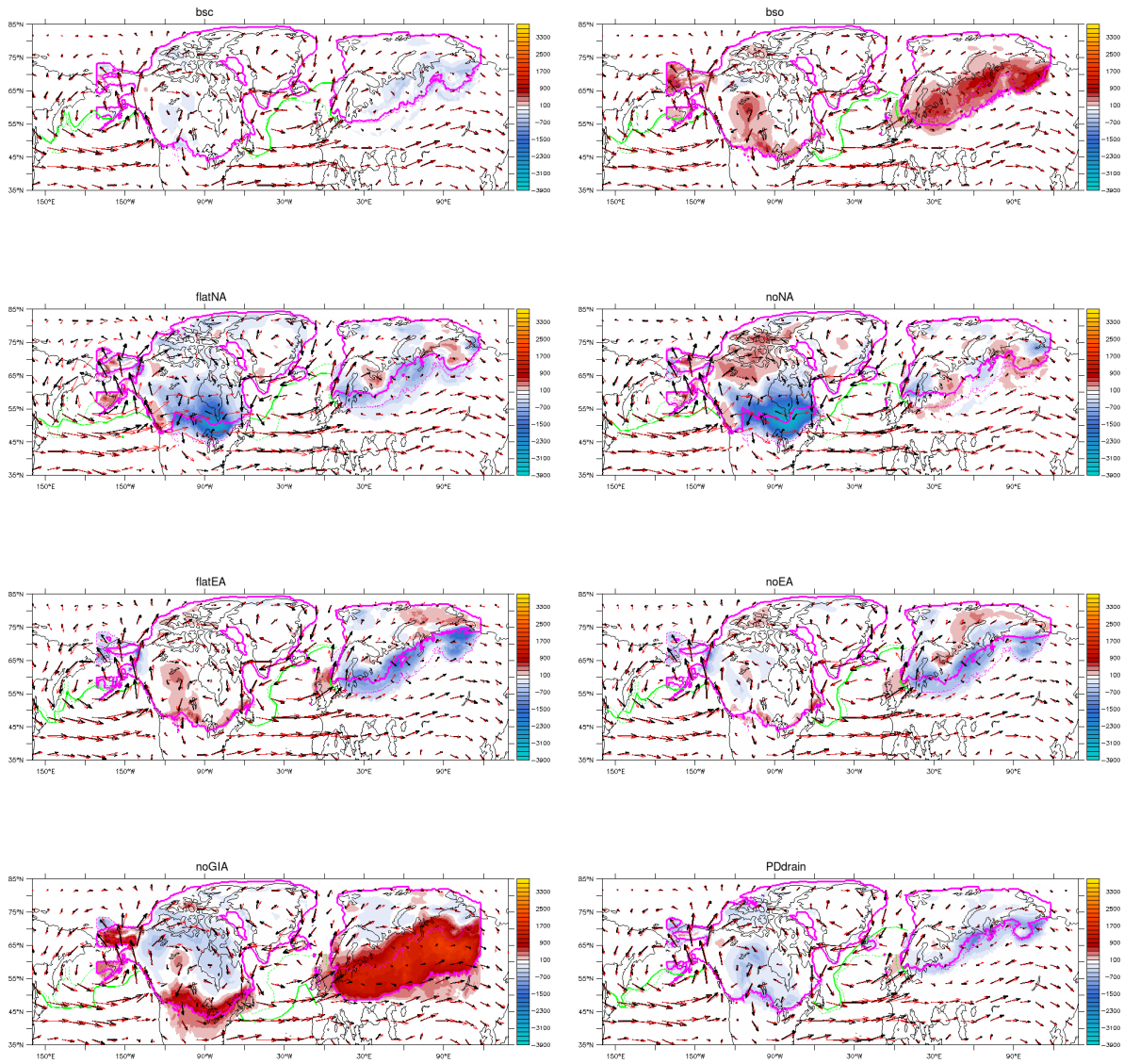

Figure B.6: DJF 800 hPa ensemble mean wind field and difference in ice height (sensitivity-ctrl) at LGM. Black arrows: ctrl, red arrows: sensitivity. Green contour: April sea ice extent. Pink contour: ice sheet extent. Solid: sensitivity, dashed: ctrl

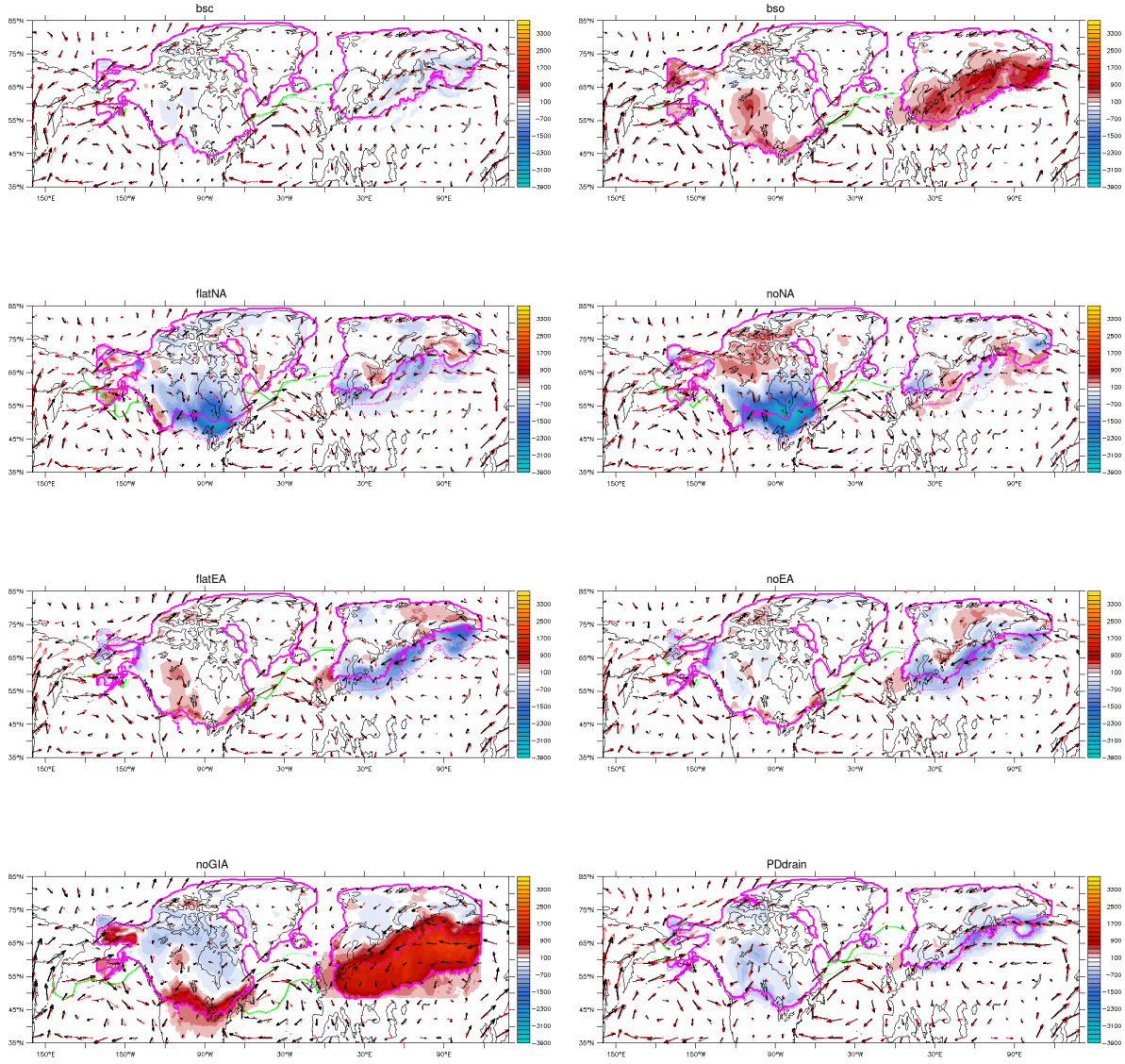

Figure B.7: JJA 800 hPa ensemble mean wind field and difference in ice height (sensitivity-ctrl) at LGM. Black arrows: ctrl, red arrows: sensitivity. Green contour: October sea ice extent. Pink contour: ice sheet extent. Solid: sensitivity, dashed: ctrl

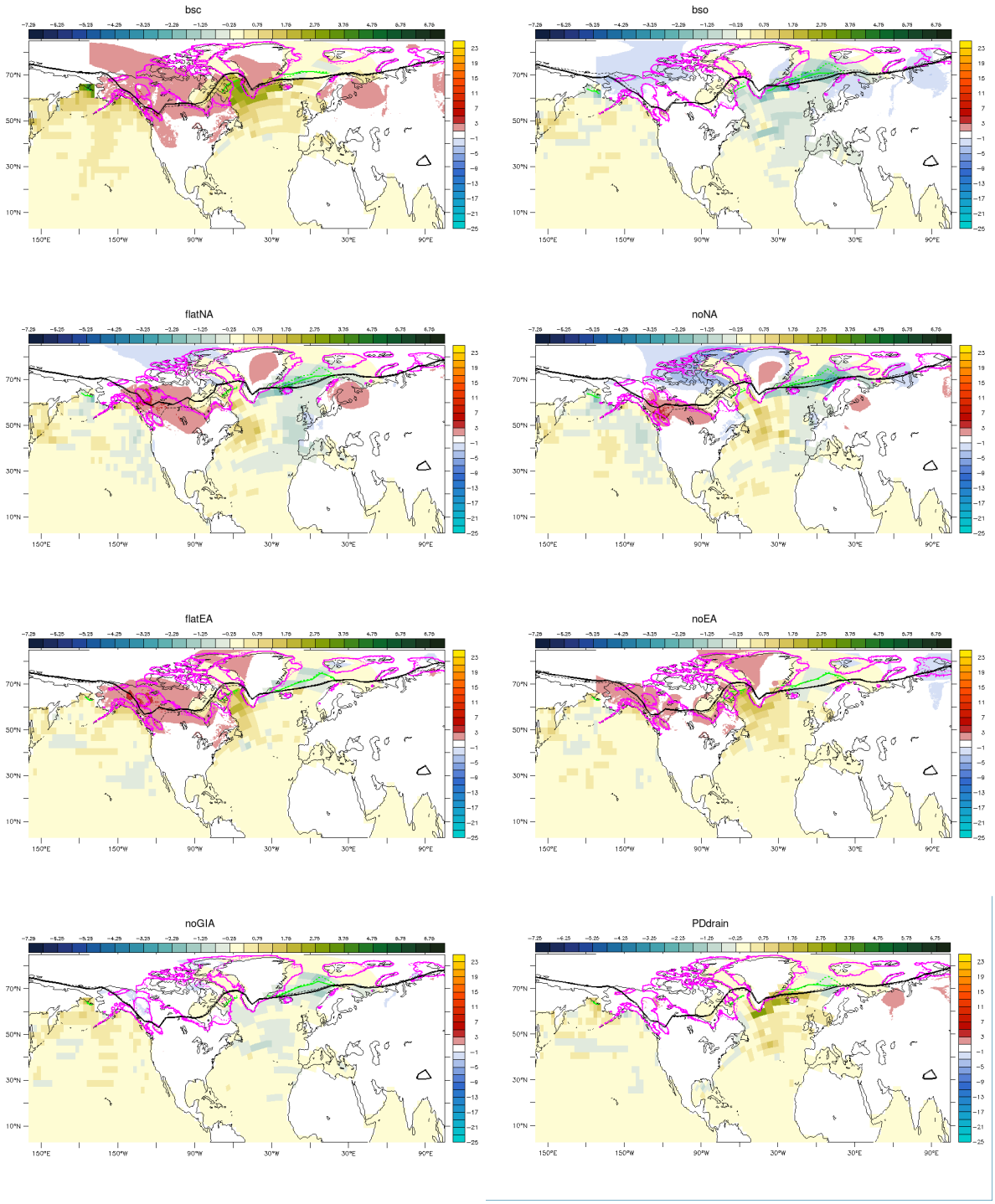

Figure B.8: Difference sensitivity-ctrl ensemble mean of October SST (blue-green shading) and GSM temperature over ice sheet domains scaled down to sea-level (cyan-yellow shading) at 115 ka. Black contour lines: ensemble mean LOVECLIM summer (JJA) 0 °isotherm, green contour lines: ensemble mean October sea ice extent, pink contour line: ensemble mean ice sheet extent, solid lines: sensitivity, dashed lines: ctrl

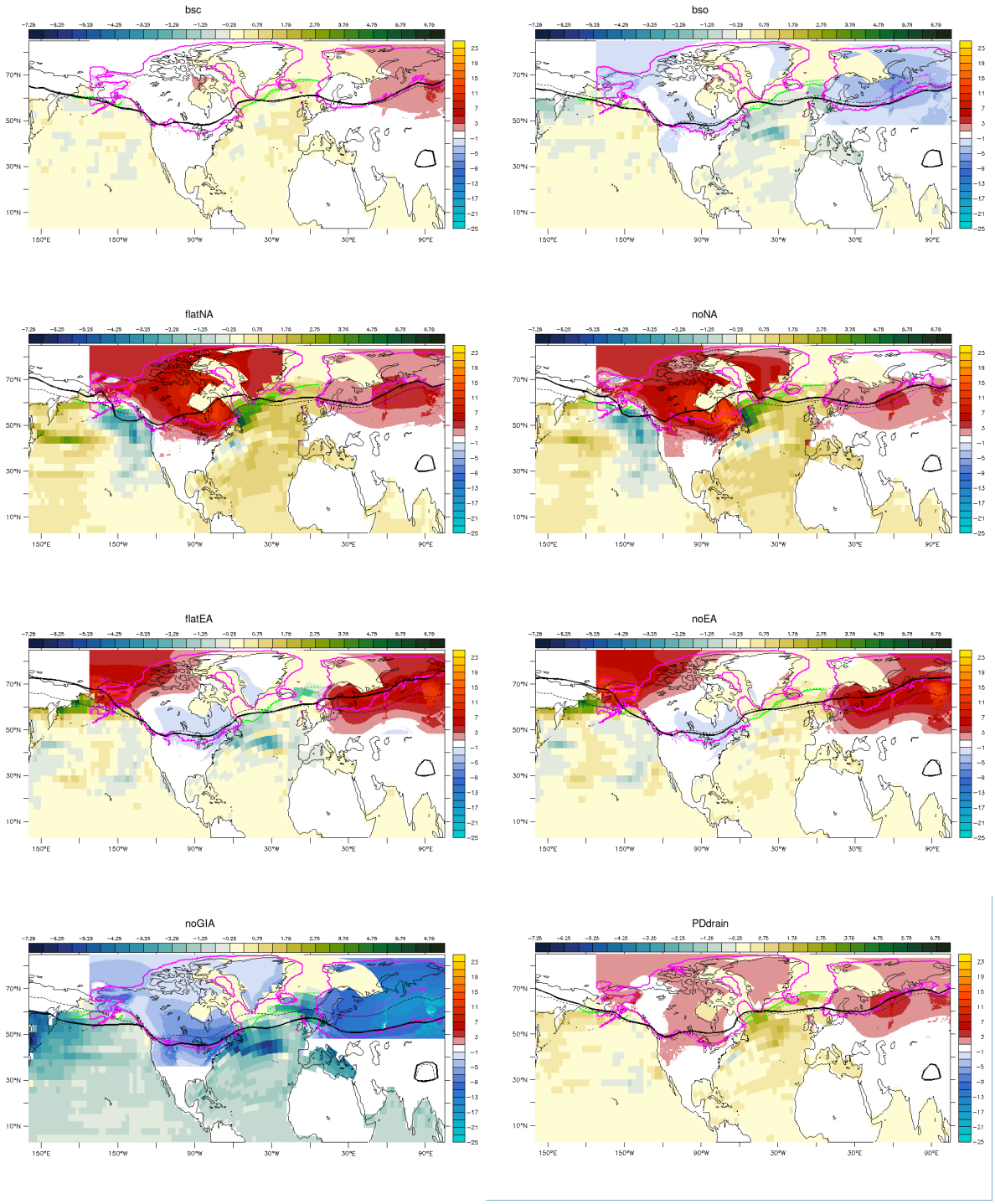

Figure B.9: Difference sensitivity-ctrl ensemble mean of October SST (blue-green shading) and GSM temperature over ice sheet domains scaled down to sea-level (cyan-yellow shading) at 21 ka. Black contour lines: ensemble mean LOVECLIM summer (JJA) 0 °isotherm, green contour lines: ensemble mean October sea ice extent, pink contour line: ensemble mean ice sheet extent, solid lines: sensitivity, dashed lines: ctrl

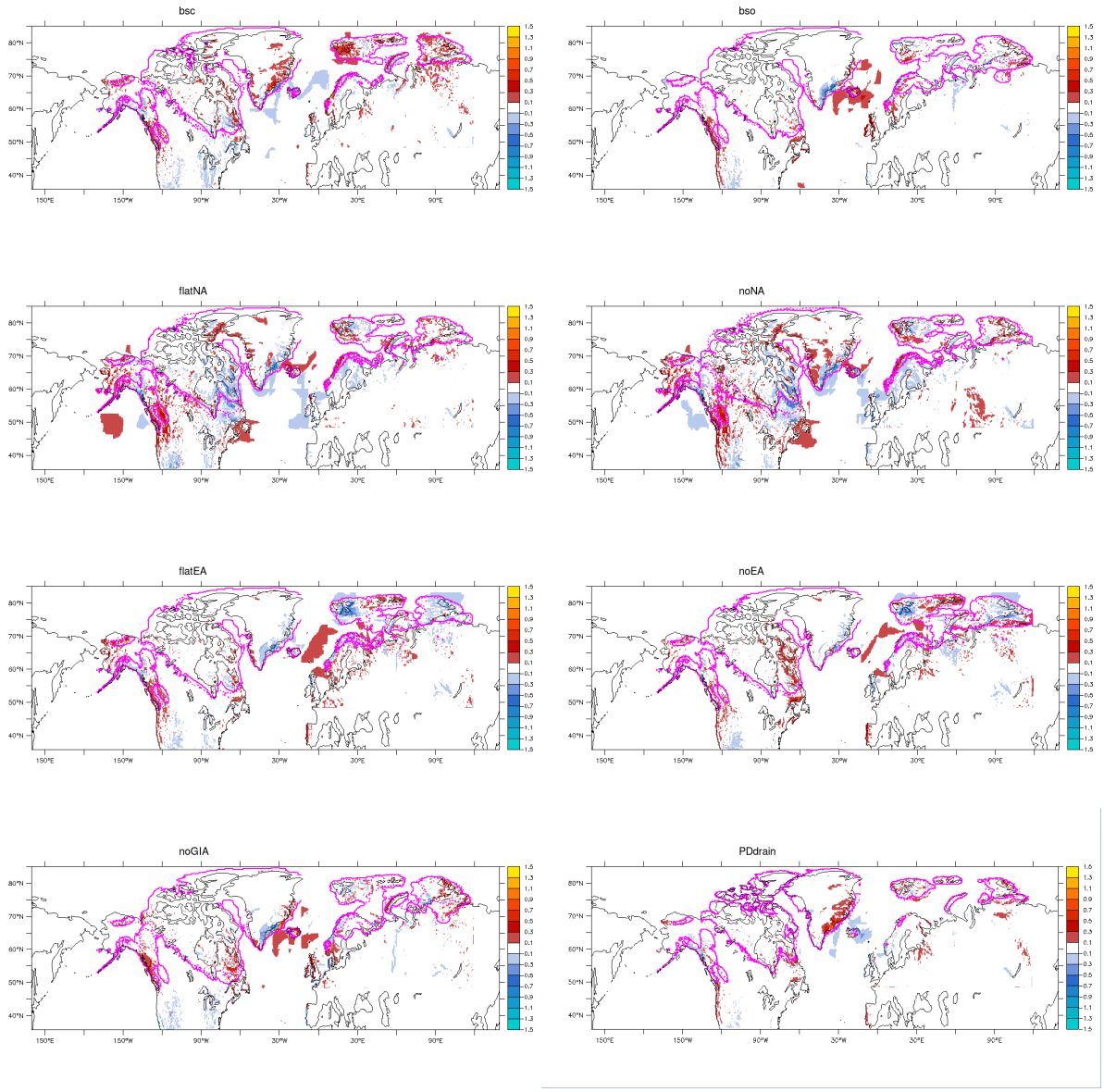

Figure B.10: Difference in ensemble mean precipitation at 114 ka sensitivity-ctrl, solid (dashed) pink contour line: sensitivity (ctrl) ice sheet extent

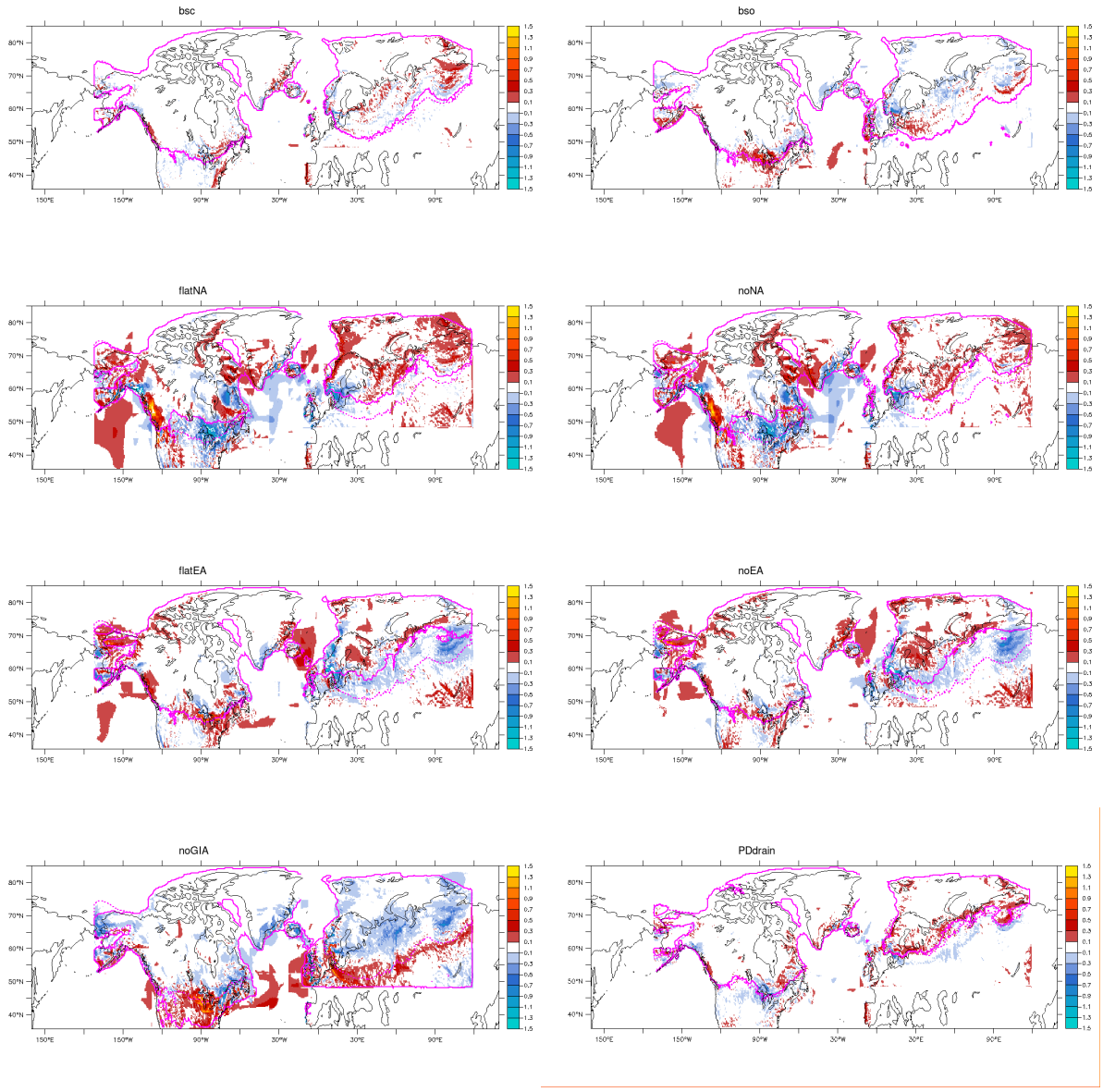

Figure B.11: Difference in ensemble mean precipitation at 21 ka sensitivity-ctrl, solid (dashed) pink contour line: sensitivity (ctrl) ice sheet extent